Stochastic gravitational wave backgrounds from primordial black holes

Fondos estocásticos de ondas gravitacionales a partir de agujeros negros primordiales

Memoria de Tesis Doctoral realizada por

Santiago Jaraba Gómez

presentada ante el Departamento de Física Teórica
de la Universidad Autónoma de Madrid
para optar al Título de Doctor en Física Teórica

Tesis Doctoral dirigida por

Prof. Juan García-Bellido Capdevila,

Catedrático de Física Teórica de la Universidad Autónoma de Madrid,

Dra. Sachiko Kuroyanagi,

Investigadora atracción de talento en el Instituto de Física Teórica

Departamento de Física Teórica
Universidad Autónoma de Madrid

Instituto de Física Teórica UAM-CSIC

Mayo de 2024

Agradecimientos

Esta tesis es resultado de 4 años de trabajo, que comenzó en 2020 desde casa, en plena pandemia de COVID. Afortunadamente, los últimos tres últimos años han transcurrido con mayor normalidad, permitiéndome participar en las actividades del IFT, conocer a mis compañeros y colaboradores, y realizar viajes para congresos, escuelas y estancias. Por ello, son muchas las personas a las que me gustaría agradecer por estos años.

Me gustaría comenzar agradeciendo a mis directores, Juan y Sachiko. De Juan me llevo su pasión por la Física, su capacidad de proponer nuevas ideas y su supervisión constante pero sin presión. De Sachiko quiero mencionar su trabajo riguroso, su guía dentro de LVK y su afán por crear nuevas y enriquecedoras colaboraciones científicas, en especial con la Universidad de Nagoya.

En este sentido, la mayor experiencia que me llevo de este doctorado es mi estancia de tres meses en Nagoya, que me ha permitido explorar varias ciudades de Japón y disfrutar de su cultura, sus paisajes y su gente. Quería agradecer en especial a Ryoto, cuya ayuda me facilitó enormemente mi tiempo en Nagoya, así como a Yurino, Takahiro y todas las personas que me acogieron allí, especialmente a Ichiki-san, Kato-san y Yokoyama-san. Asimismo, querría extender estos agradecimientos a quienes me acogieron en mi breve visita a la VUB en Bruselas, particularmente a Alba, pero también a Miguel, Alberto y Hannah.

De vuelta en Madrid, quiero agradecer a todos los que han formado parte de mi día a día en el IFT, muy especialmente a Gonzalo y Alexander, con quienes más tiempo y experiencias he podido compartir, así como a Marienza, Indira y Adrián, con quienes también he compartido muchos buenos momentos. Igualmente, estos agradecimientos van para todo el grupo de Cosmología, así como a mis colaboradores en LVK, especialmente a Leo por su dirección y su apoyo. Por último, si alguien me ha acompañado durante estos años han sido mis compañeros de despacho, empezando por Joan y Víctor y terminando por Dani y Alessandra, y acordándome especialmente de José Francisco, con quien mayor sintonía he tenido en la oficina.

En el lado más personal, me gustaría mencionar a mis amigos del colegio, Álvaro, Rubén, Alberto y Jacobo, y muy en especial a Borja, quien me ha acompañado incesantemente por las mañanas en el largo camino hasta el IFT. Asimismo, me quiero acordar también de mis amigos del doble grado en Matemáticas y Física, en especial de Clara, Patricia, Manu y Miguel, así como de Helena y Cristian, compañeros también de máster, y extender el agradecimiento a mis profesores de la universidad. En gran medida, la motivación para realizar este doctorado nace de aquellos 5 años en la Complutense que recuerdo con tanto cariño.

Por supuesto, a quien no puedo dejar de agradecer en esta tesis es a Clara, mi pareja de ya tantos años. A pesar de la distancia, gracias por estar a mi lado más que nadie durante todo este tiempo. Y en especial, gracias por recorrer medio mundo para verme unos días. Sin duda, Japón se disfruta mucho más en buena compañía.

Por último, quiero concluir agradeciendo a mi familia. Particularmente, a mi tía Ana y a mi prima Elena, que me han ayudado a desconectar del trabajo innumerables veces durante el doctorado, así como a mi tía Mari Carmen. Asimismo, a mis abuelos, Troadia y Valeriano, especialmente para mi abuela, que no ha podido ver el final de esta tesis y a quien va dedicada. Mención especial para mi hermana Cristina, con quien tanto he compartido durante estos años y quien más me ha aguantado cada día. Finalmente, a mis padres, Santiago y María Victoria, quienes me han dado la educación, recursos y motivación para poder llegar hasta aquí, y sin los cuales esta tesis no habría sido posible. Gracias.

A mi abuela Troadia

Abstract

The field of gravitational waves has made a huge progress over the last decade, especially since their first detection by LIGO in September 2015. Throughout this thesis, I will give an overview of some of the research lines where this progress is more tangible, all of them related in some way to the stochastic gravitational wave background or primordial black holes.

First, gravitational waves and stochastic gravitational wave backgrounds will be introduced, covering the standard formalisms, equations and data analysis tools, together with some works on anisotropies and constraints on theoretical models involving non-Gaussianities.

Then, we will study some of the phenomena related to hyperbolic encounters and primordial black holes, which are two of the areas that are progressively getting more attention as the number of detected gravitational-wave signals increases. In particular, hyperbolic encounters will be analyzed using Numerical Relativity, which is a key tool for the interpretation of these signals and, in this case, will be used to study the effect of spin induction in black holes.

Finally, the thesis will delve into the topic of stochastic gravitational wave backgrounds in different frequency ranges. After a brief overview, we will study how to set constraints for this background using astrometric data from astronomical surveys such as Gaia. This will illustrate that there is much more to gravitational waves than the work within the usual gravitational wave detectors, providing complementary information which is otherwise inaccessible. The thesis will ultimately conclude with some final remarks.

Resumen

El campo de las ondas gravitacionales ha experimentado un enorme progreso durante la última década, especialmente desde su primera detección por LIGO en septiembre de 2015. A lo largo de esta tesis, daré una visión general sobre algunas de las líneas de investigación en las que este progreso es más tangible, todas ellas relacionadas de alguna manera con el fondo estocástico de ondas gravitacionales o los agujeros negros primordiales.

En primer lugar, se introducirán las ondas gravitacionales y los fondos estocásticos de ondas gravitacionales, desarrollando los formalismos usuales, ecuaciones y herramientas para el análisis de datos, junto con algunos trabajos sobre anisotropías e imposición de límites en modelos teóricos que involucran no-Gaussianidades.

A continuación, estudiaremos algunos de los fenómenos relacionados con los encuentros hiperbólicos y los agujeros negros primordiales, que son dos de las áreas que progresivamente están recibiendo más atención a medida que aumenta el número de señales de ondas gravitacionales detectadas. En particular, los encuentros hiperbólicos se analizarán utilizando Relatividad Numérica, que es una herramienta clave para la interpretación de estas señales y, en este caso, se utilizará para estudiar el efecto de la inducción de espín en los agujeros negros.

Finalmente, la tesis desarrollará el estudio de los fondos estocásticos de ondas gravitacionales en diferentes rangos de frecuencia. Después de una breve descripción general, veremos cómo establecer límites sobre dicho fondo utilizando datos astrométricos de misiones astronómicas como Gaia. Esto servirá para ilustrar que las ondas gravitacionales abarcan mucho más que el trabajo relacionado con los detectores de ondas gravitacionales habituales, proporcionando información complementaria que sería de otro modo inaccesible. La tesis finalmente concluirá con algunas observaciones adicionales.

Declaration

This thesis collects original results obtained during the last four years at the Instituto de Física Teórica UAM-CSIC. Most of them have been published in the following articles:

[1] S. Jaraba and J. García-Bellido, *Black hole induced spins from hyperbolic encounters in dense clusters*, *Phys. Dark Univ.* **34** (2021) 100882 [2106.01436]

[2] J. García-Bellido, S. Jaraba and S. Kuroyanagi, *The stochastic gravitational wave background from close hyperbolic encounters of primordial black holes in dense clusters*, *Phys. Dark Univ.* **36** (2022) 101009 [2109.11376]

[3] L. Tsukada, S. Jaraba, D. Agarwal and E. Floden, *Bayesian parameter estimation for targeted anisotropic gravitational-wave background*, *Phys. Rev. D* **107** (2023) 023024 [2208.14421]

[4] S. Jaraba, J. García-Bellido, S. Kuroyanagi, S. Ferraiuolo and M. Braglia, *Stochastic gravitational wave background constraints from Gaia DR3 astrometry*, *Mon. Not. Roy. Astron. Soc.* **524** (2023) 3609–3622 [2304.06350]

[5] R. Inui, S. Jaraba, S. Kuroyanagi and S. Yokoyama, *Constraints on Non-Gaussian primordial curvature perturbation from the LIGO-Virgo-KAGRA third observing run*, 2311.05423

In particular, the final part of Chapter 2 is based on Ref. [5]. Chapter 3 is based on Ref. [3], Chapter 5 is based on Ref. [2], Chapter 7 is based on Ref. [1] and Chapters 9 and 10 are based on Ref. [4]. Some parts of Chapters 4 and 6 are also based on own, unpublished work, where specified. The contents of Chapters 1 and 8, as well as the remaining parts of Chapters 2, 4 and 6, are introductory reviews based on multiple references cited therein, on which no claim of originality is made. Chapter 11 gives concluding remarks and summarizes the results presented in the rest of the thesis. Finally, Appendix A is based on the appendix of [5], Appendix B is based on the appendix of [3], Appendix C is based on the appendix of [1] and Appendix D contains additional figures from [4].

The research that led to this thesis has been mainly funded by an FPI fellowship from the Spanish Ministry of Science (Ministerio de Ciencia e Innovación, MCIN) and the Spanish Research Agency (Agencia Estatal de investigación, AEI), MCIN/AEI/10.13039/501100011033, with code PRE2019-088741. I also received support from the the IFT Centro de Excelencia Severo Ochoa SEV-2016-0597 and CEX2020-001007-S funded by MCIN/AEI/10.13039/501100011033, as well as from Grants PGC2018-094773-B-C32 [MINECO-FEDER], PID2021-123012NB-C43 [MICINN-FEDER] and PID2020-118159GA-C42 [MCIN-AEI]. Part of the research was done during a 3-month research stay at Nagoya University in Japan, funded by the FPI PRE2019-088741 fellowship.

Santiago Jaraba Gómez
Madrid, May 2024

Contents

Abstract vii

Resumen ix

Introduction 1

Introducción 3

1 Gravitational wave theory 7

1.1 Gravitational wave formalism . . . 7

1.1.1 Linearized theory . . . 8

1.1.2 The harmonic gauge . . . 9

1.1.3 The transverse traceless gauge . . . 10

1.1.4 Plane waves . . . 12

1.1.5 Projection to TT gauge . . . 13

1.2 Generalization to curved backgrounds . . . 14

1.2.1 Propagation of gravitational waves . . . 16

1.2.2 Energy of a gravitational wave . . . 17

1.2.3 Quadrupole formulae . . . 20

1.3 Gravitational waves from a bound two-body system . . . 24

1.3.1 Keplerian dynamics . . . 25

1.3.2 Radiated power . . . 28

1.3.3 Gravitational waves and energy loss . . . 29

1.3.4 Energy spectrum . . . 33

1.4 Hyperbolic encounters . . . 37

1.4.1 Keplerian dynamics . . . 38
1.4.2 Radiated power . . . 40

2 Stochastic gravitational wave backgrounds 43
2.1 Stochastic gravitational wave background formalism . . . 45
2.2 Detection of gravitational waves . . . 47
2.2.1 Detector pattern functions . . . 47
2.2.2 SGWB data analysis . . . 49
2.3 Introduction to Bayesian inference . . . 55
2.3.1 The likelihood . . . 56
2.3.2 Sampling methods . . . 57
2.3.3 Post-processing techniques . . . 60
2.3.4 Parameter estimation of isotropic SGWB . . . 63
2.4 Constraints from LVK . . . 63
2.5 Constraints to non-Gaussianities from O3 data . . . 65
2.5.1 Introduction . . . 65
2.5.2 The model . . . 66
2.5.3 Data analysis . . . 68
2.5.4 Conclusions . . . 71

3 SGWB anisotropies 73
3.1 Formalism for anisotropic SGWB . . . 73
3.1.1 Basis decomposition . . . 75
3.1.2 Anisotropic SGWB data analysis . . . 77
3.2 Bayesian PE for targeted anisotropic GWB . . . 78
3.2.1 Introduction . . . 78
3.2.2 The formalism . . . 79
3.2.3 Model selection . . . 81
3.2.4 Conclusions . . . 84

4 Primordial black holes 87
4.1 Introduction . . . 87
4.2 PBH generation mechanisms . . . 87
4.2.1 Single-field inflation . . . 88

4.2.2 Non-Gaussianities . . . 90
4.3 Collapse of density perturbations . . . 91
4.3.1 The Misner-Sharp formalism . . . 92
4.3.2 Initial conditions . . . 95
4.3.3 Numerical simulations . . . 98
4.3.4 Numerical results . . . 101
4.3.5 Threshold dependence of equation of state . . . 102
4.4 Merger rates of primordial black holes . . . 104
4.4.1 Merger rates of PBH late binaries . . . 105

5 SGWBs from close hyperbolic encounters of PBHs 107
5.1 Introduction . . . 107
5.2 Stochastic background of GWs . . . 108
5.2.1 Binary BHs . . . 108
5.2.2 Close hyperbolic encounters . . . 109
5.2.3 Comparison between BBHs and CHEs . . . 112
5.3 Conclusions . . . 113

6 Numerical Relativity 115
6.1 Introduction to NR . . . 116
6.1.1 The 3+1 ADM formalism . . . 116
6.1.2 Initial conditions . . . 117
6.1.3 Adaptive mesh refinement . . . 119
6.2 Numerical simulations with the Einstein Toolkit . . . 120
6.2.1 The Einstein Toolkit . . . 121
6.2.2 Apparent horizons . . . 122
6.2.3 Gravitational-wave extraction . . . 125
6.2.4 Challenges: mass ratios, eccentricity, precession . . . 127
6.3 Hyperbolic encounters . . . 129

7 Spin induction on BHs from CHEs 133
7.1 Introduction . . . 133
7.2 Grid structure and initial conditions . . . 134
7.2.1 Equal mass case . . . 134

7.2.2 Changing the mass ratio . . . 135
7.3 Numerical results . . . 136
7.3.1 Error analysis . . . 136
7.3.2 General behavior of the simulations . . . 137
7.3.3 Equal masses, varying incidence angle . . . 138
7.3.4 Varying the mass ratio . . . 140
7.4 Towards lower mass ratios: the case of q=0.1 . . . 142
7.4.1 Issues with the Weyl scalar . . . 143
7.4.2 The spins . . . 143
7.5 Comparison with analytic expressions . . . 145
7.5.1 Trend for varying incidence angle . . . 145
7.5.2 Trend for varying mass ratio . . . 146
7.6 Conclusions . . . 146

8 Gravitational wave constraints from astrometry 149
8.1 The stochastic gravitational wave background in different frequencies . . . 149
8.2 Introduction to gravitational wave constraints from astrometry . . . 150
8.3 Minkowski spacetime . . . 151
8.3.1 Unperturbed case . . . 151
8.3.2 Perturbed case . . . 152
8.3.3 Observed angular deflection . . . 154
8.4 FLRW metric . . . 156
8.5 Further simplifications . . . 158
8.5.1 Plane waves and the distant source limit . . . 158
8.6 Angular deflection correlation . . . 160
8.6.1 Autocorrelation spectrum . . . 160
8.6.2 Frequency validity range . . . 163
8.6.3 Generalization to different directions . . . 164
8.7 Multipole decomposition . . . 168
8.7.1 Scalar spherical harmonics . . . 168
8.7.2 Vector spherical harmonics . . . 170
8.7.3 Contributions per mode and multipole . . . 173
8.7.4 Explicit computation of multipole power . . . 177

8.8 Data analysis . . . 179
8.8.1 Statistical significance . . . 181

9 The Gaia mission **185**
9.1 Introduction . . . 185
9.2 Generating clean datasets . . . 186
9.2.1 The QSO candidate sample . . . 186
9.2.2 Filtering and masking . . . 188
9.2.3 Gaia QSO selections . . . 189
9.3 Other datasets . . . 192
9.4 Queries of astronomical databases . . . 194
9.4.1 Gaia archive . . . 194
9.4.2 Cross-matching catalogs . . . 196
9.4.3 VLBA-based datasets . . . 198

10 SGWB constraints from Gaia DR3 **201**
10.1 Introduction . . . 201
10.2 Data analysis . . . 202
10.2.1 Likelihood . . . 202
10.2.2 Parameter estimation . . . 203
10.3 Results . . . 205
10.4 Future prospects . . . 208

11 Conclusions **209**

Conclusiones **211**

A Scalar-induced gravitational wave formalism **215**
A.1 Scalar induced gravitational waves . . . 215
A.2 Gravitational waves induced by non-Gaussian curvature perturbations . . . 217

B Derivation of dipole artifact due to Doppler shift **219**

C Analytic estimate of the induced spins **223**
C.1 Ring approximation . . . 223
C.2 Mass current . . . 225

C.3 From spin-orbit equations at PPN(1.5) 226
C.4 Differences between expressions 227

D Corner plots for SGWB constraints from Gaia DR3 **229**

List of Figures **240**

List of Tables **242**

Bibliography **243**

Introduction

Over the last decade, the field of gravitational waves (GW) has seen an astonishing evolution, from their first detection in 2015 by LIGO [6, 7] to the recent hints of a stochastic gravitational wave background (SGWB) from pulsar timing arrays (PTAs) [8, 9, 10, 11] in 2023. Just to mention some of the recent developments, new ground-based detectors have joined the observations (Virgo [12], KAGRA [13]), more than 90 signals from compact binary coalescences (CBCs) have officially been detected [14], the neutron star merger GW170817 has been observed jointly in GW and electromagnetic (EM) radiation [15], a merger between two black holes of masses 91 and 67 solar masses has been observed (GW190521) [16], standing as the most energetic astrophysical event ever observed, etc.

Next-generation detectors have also been proposed, where the ground-based ones, such as Einstein Telescope (ET) [17] and Cosmic Explorer (CE) [18], will dig drastically deeper into the Hz-kHz frequency band that LIGO-Virgo-KAGRA (LVK) [19] is already observing. Furthermore, the space missions (LISA [20], TianQin [21], Taiji [22], DECIGO [23]) will open up a new frequency band around the mHz, which will provide invaluable information we do not currently have access to.

All of this collaborative effort is expected to prove extremely fruitful for science in the coming decades. We anticipate more joint detections in GW and EM radiation, entering the era of multimessenger astronomy; a larger number of observations by orders of magnitude, due to the progressive increase in sensitivity and especially after LISA starts observing; long observations in mHz pointing to later observations in the LVK range (and in EM radiation) of the same sources, etc.

One of the possibilities is that small (under a solar mass) black holes (BHs) are detected, thus confirming the long theorized primordial black holes (PBHs) [24, 25, 26, 27], generated in the early universe without a star precursor. The overwhelming amount of signals will also allow to do black hole population analyses, constraining the abundance of these primordial black holes. This is especially relevant given that they are one of the candidates to be dark matter (DM), so these observations will potentially confirm them as one of the contributions to DM or rule them out, in any case providing invaluable evidence for one of the greatest problems in contemporary Physics.

Particularly interesting is the case of stochastic gravitational wave backgrounds, which could potentially play the role that the cosmic microwave background (CMB) has been playing in the last decades. A SGWB detection would, presumably, first consist on an astrophysical foreground from a superposition of CBC signals [28, 29, 30, 31, 32], but once technology is able to overcome that, we should be able to see the imprint of cosmological contributions. The data analysis of cosmological sources is assumed to be much more challenging, but the physical information we can gain from it

goes beyond recombination, thus providing unique cosmological insights of the moments closer to the CMB that no other messenger can deliver.

Together with the advancements on the experimental side, one of the key fields that had to be developed to properly analyze gravitational waves was Numerical Relativity (NR). It was not until 2005 that a successful numerical simulation of a binary black hole (BBH) merger was produced [33, 34, 35]. Since then, a lot of progress has been done on the analytic side and there are now various waveform models which can reproduce a real signal with a very high accuracy in a fraction of a second [36, 37]. In any case, Numerical Relativity is still relevant to calibrate them and test them, despite the heavy computational cost that these simulations have.

During this thesis, I will provide an overview of several of these fields: stochastic gravitational wave backgrounds, primordial black holes, hyperbolic encounters, numerical relativity and other probes of the SGWB in different frequency ranges.

The thesis is structured as follows. We will start by introducing the topic of gravitational waves in Chapter 1, continuing in Chapter 2 with the theory and data analysis formalism for an isotropic stochastic gravitational-wave background, and for its anisotropies in Chapter 3, presenting two of my works in this regard. In Chapter 4, I will give a brief introduction to primordial black holes, which will lead to a work on the SGWB produced by clustered PBH within hyperbolic encounters in Chapter 5. In Chapter 6, we will delve into Numerical Relativity from different perspectives: the critical collapse of a PBH and the more standard, binary black hole simulations, both from a CBC point of view and for hyperbolic encounters, concluding with our work on black hole spin induction within these interactions in Chapter 7. In Chapter 8, I will give a brief introduction to other probes of SGWB in different frequency ranges and develop the formalism relating this background to astrometric measurements, following with an overview of the Gaia mission and practical considerations to work with its data in Chapter 9 and concluding in Chapter 10 with our work constraining the SGWB amplitude below the nHz with Gaia data. Finally, I will outline some conclusions to this thesis in Chapter 11.

Introducción

Durante la última década, el campo de las ondas gravitacionales (GW) ha experimentado una sorprendente evolución, desde su primera detección en 2015 por LIGO [6, 7] hasta los recientes indicios de un fondo estocástico de ondas gravitacionales (SGWB) por parte de las matrices de medición temporal de púlsares (*pulsar timing arrays*, PTAs) [8, 9, 10, 11] en 2023. Solo por mencionar algunos de los desarrollos recientes, nuevos detectores terrestres se han sumado a las observaciones (Virgo [12], KAGRA [13]), se han detectado oficialmente más de 90 señales de coalescencias de binarias compactas (CBCs) [14], se ha detectado la fusión de estrellas de neutrones GW170817 observada conjuntamente en GW y radiación electromagnética (EM) [15], se ha observado una fusión entre dos agujeros negros de masas 91 y 67 masas solares (GW190521) [16], situándose como el evento astrofísico más energético que se ha observado, etc.

También se han propuesto detectores de próxima generación, donde los terrestres, como el Einstein Telescope (ET) [17] y Cosmic Explorer (CE) [18], profundizarán significativamente en la banda de frecuencia Hz-kHz que LIGO-Virgo-KAGRA (LVK) [19] ya está observando. Además, las misiones espaciales (LISA [20], TianQin [21], Taiji [22], DECIGO [23]) abrirán un nueva banda de frecuencia alrededor de los mHz, que proporcionará una valiosa información a la que actualmente no tenemos acceso.

Se prevé que todo este esfuerzo colaborativo resulte extremadamente fructífero para la ciencia en las próximas décadas. Se esperan más detecciones conjuntas en GW y radiación EM, entrando en la era de la astronomía multimensajero; un drástico aumento en el número de observaciones debido a la mejora progresiva de la sensibilidad y especialmente después de que LISA comience a observar; observaciones largas en mHz que indiquen observaciones posteriores en el rango de LVK (y en radiación EM) de las mismas fuentes, etc.

Una de las posibilidades es que se detecten agujeros negros (BH) pequeños (menores que una masa solar), confirmando así los llamados agujeros negros primordiales (PBH) que han sido teorizados durante mucho tiempo [24, 25, 26, 27], generados en el universo temprano sin una estrella precursora. La abrumadora cantidad de señales también permitirá realizar análisis de la población de agujeros negros, lo que pondrá límites observacionales a la abundancia de estos PBHs. Esto es especialmente relevante dado que son uno de los candidatos a materia oscura (DM), por lo que estas observaciones potencialmente los confirmarán como, al menos, parte de la DM, o bien los descartarán, proporcionando, en cualquier caso, una valiosa información sobre uno de los mayores problemas de la Física contemporánea.

Particularmente interesante es el caso de los fondos estocásticos de ondas gravitacionales, que podrían, potencialmente, desempeñar el papel que ha ocupado el fondo cósmico de microondas

(CMB) en las últimas décadas. Una detección de SGWB, en principio, consistiría primero en una señal astrofísica proveniente de una superposición de señales de CBCs [28, 29, 30, 31, 32]. Sin embargo, una vez que la tecnología sea capaz de indagar más allá de dicha señal, deberíamos poder ver la huella de las contribuciones cosmológicas. Se asume que el análisis de datos para estas fuentes cosmológicas será mucho más desafiante, pero la información física que podemos obtener de ellas va más allá de la recombinación, proporcionando así un conocimiento cosmológico único sobre los momentos más cercanos al CMB que ningún otro mensajero puede ofrecer.

Junto con los avances en el lado experimental, uno de los campos clave que hubo que desarrollar para analizar adecuadamente las ondas gravitacionales fue la Relatividad Numérica (NR). No fue hasta 2005 cuando se produjo una simulación numérica exitosa de una fusión de una binaria de agujeros negros (BBH) [33, 34, 35]. Desde entonces, se ha avanzado mucho en los desarrollos analíticos y actualmente existen múltiples modelos que pueden reproducir una señal real con una precisión muy alta en una fracción de segundo [36, 37]. En cualquier caso, la Relatividad Numérica sigue siendo relevante para calibrarlos y ponerlos a prueba, a pesar del alto coste computacional que tienen estas simulaciones.

A lo largo de esta tesis, proporcionaré una visión general de varios de estos campos: fondos estocásticos de ondas gravitacionales, agujeros negros primordiales, encuentros hiperbólicos, relatividad numérica y otras maneras de caracterizar el SGWB en diferentes rangos de frecuencia.

La tesis se estructura de la siguiente manera. Comenzaremos introduciendo el tema de las ondas gravitacionales en el Capítulo 1, continuando en el Capítulo 2 con la teoría y el formalismo del análisis de datos para un SGWB isotrópico, y para sus anisotropías en el Capítulo 3, presentando dos de mis trabajos al respecto. En el Capítulo 4, daré una breve introducción a los agujeros negros primordiales, lo que conducirá a un trabajo sobre el SGWB producido por encuentros hiperbólicos de PBHs en cúmulos en el Capítulo 5. En el Capítulo 6, profundizaremos en la Relatividad Numérica desde diferentes perspectivas: el colapso crítico de un PBH y las simulaciones de binarias de agujeros negros, tanto desde el punto de vista de CBCs como para encuentros hiperbólicos, y concluyendo con nuestro trabajo sobre la inducción de espín de agujeros negros en estas interacciones en el Capítulo 7. En el Capítulo 8, daré una breve introducción a otros métodos para caracterizar el SGWB en diferentes rangos de frecuencia y desarrollaré el formalismo que relaciona estos fondos con mediciones astrométricas, siguiendo con una descripción general de la misión Gaia y consideraciones prácticas para el manejo de sus datos en el Capítulo 9 y concluyendo en el Capítulo 10 con nuestro trabajo en el que utilizamos datos de Gaia para imponer límites a la amplitud del SGWB por debajo de los nHz. Finalmente, concluiremos con algunas observaciones sobre la tesis en el Capítulo 11.

Notation

In the context of General Relativity, we use the signature convention (-+++). We denote

$$x^\mu = (x^0, \vec{x}), \quad x^0 = ct, \tag{0.1}$$

with c the speed of light. We will use Greek indices for either time or space coordinates ($\mu = 0, 1, 2, 3$) and Latin indices to denote space coordinates ($i = 1, 2, 3$).

We will also use Einstein's summation convention over repeated indices, so that

$$a_\mu b^\mu \equiv \sum_{\mu=0}^{3} a_\mu b^\mu, \quad a_i b^i \equiv \sum_{i=1}^{3} a_i b^i (\equiv a_i b_i \equiv a^i b^i), \tag{0.2}$$

where the latter conventions for both spatial indices either raised or lowered only applies in the context of a Minkowskian metric. This is possible because, with our signature convention, $\eta_{ij} = \delta_{ij}$, so that $a_i = \eta_{ij} a^j = a^i$. This cannot be done for $\mu = 0$, for which lowering or raising indices generates an extra minus sign.

The convention for the Christoffel symbols will be

$$\Gamma^\mu_{\nu\rho} = \frac{1}{2} g^{\mu\sigma} \left(\partial_\nu g_{\sigma\rho} + \partial_\rho g_{\sigma\nu} - \partial_\sigma g_{\nu\rho} \right). \tag{0.3}$$

The Riemann tensor is then defined as

$$R^\mu{}_{\nu\rho\sigma} = \partial_\rho \Gamma^\mu_{\nu\sigma} - \partial_\sigma \Gamma^\mu_{\nu\rho} + \Gamma^\mu_{\alpha\rho} \Gamma^\alpha_{\nu\sigma} - \Gamma^\mu_{\alpha\sigma} \Gamma^\alpha_{\nu\rho}. \tag{0.4}$$

The Ricci tensor is defined as the contraction of the first and third indices of the Riemann tensor,

$$R_{\mu\nu} = R^\alpha{}_{\mu\alpha\nu}, \tag{0.5}$$

and, finaly, the Ricci scalar is the contraction of the Ricci tensor,

$$R = g^{\mu\nu} R_{\mu\nu}. \tag{0.6}$$

The convention for the n-dimensional Fourier transform of a certain function $f : \mathbb{R}^n \to \mathbb{R}$ will be

$$f(x) = \iint_{\mathbb{R}^n} \frac{d^n k}{(2\pi)^n} \tilde{f}(k) e^{ikx}, \tag{0.7}$$

while the inverse Fourier transform is then given by

$$\tilde{f}(k) = \iint_{\mathbb{R}^n} d^n x f(k) e^{-ikx}. \tag{0.8}$$

Then, for a function of time, the signature convention implies

$$f(t) = \iint_{-\infty}^{\infty} \frac{d\omega}{2\pi} \tilde{f}(\omega) e^{-i\omega t} \tag{0.9}$$

and, conversely,

$$\tilde{f}(\omega) = \iint_{-\infty}^{\infty} dt f(t) e^{i\omega t}, \tag{0.10}$$

matching the Landau-Lifshitz notation [38].

In addition, the Dirac delta satisfies

$$\delta(k) = \iint_{\mathbb{R}^n} \frac{d^n x}{(2\pi)^n} (k) e^{-ikx}, \tag{0.11}$$

so that, in one dimension,

$$\delta(f) = \iint_{-\infty}^{\infty} dt e^{-2\pi i f t}. \tag{0.12}$$

Chapter 1

Gravitational wave theory

In this first chapter of the thesis, it is necessary that we start by reviewing the most important aspects of Gravitational Wave theory. Despite the existence of much more complete introductions to the field in the scientific literature, it is more convenient to present here the needed theory and equations in a suitable way for the purposes of this thesis. In addition, even for a reader who is familiar with the topic, it is useful to review the basic concepts so that the ideas presented later in the thesis will become more clear to follow. All of this will also contribute to the thesis being more self-contained, which was one of the main intentions during the writing process, and it is the same philosophy which guided the rest of the chapters of this thesis.

In any case, this chapter does not mean to be a complete and thorough introduction to Gravitational Wave theory. Whenever possible, all equations will be properly derived and justified, but this is not always feasible when aiming for a reasonable extension of the thesis. Therefore, in some occasions, we will simply refer to other sources providing a more complete picture for the treated topic. In the first sections of this chapter, in particular, the main reference for consultation will be Michele Maggiore's books on Gravitational waves [39, 40], which provide an excellent introduction to the field.

1.1 Gravitational wave formalism

Gravitational waves can be studied as the tensor perturbations $h_{\mu\nu}$ of a background metric. In the context of Cosmology, arguably the most important metric is the Friedmann-Lemaître-Robertson-Walker (FLRW) metric, which has a line element

$$ds^2 = g_{\mu\nu}dx^\mu dx^\nu = -dt^2 + a(t)^2\left(\frac{dr^2}{1-kr^2} + r^2 d\Omega^2\right)\Bigg(\tag{1.1}$$

where Ω denotes the solid angle, $d\Omega^2 = d\theta^2 + \sin^2\theta d\varphi^2$.

Despite its simplicity, the FLRW metric is harder to work with than the Minkowski metric, with line element

$$ds^2 = \eta_{\mu\nu}dx^\mu dx^\nu = -dt^2 + \delta_{ij}dx^i dx^j. \tag{1.2}$$

As a result, it is usually a good idea to get familiar with gravitational waves within a Minkowski background metric, and then generalize to curved spacetimes as FLRW. In this case, we can add a small perturbation $h_{\mu\nu}$ to a Minkowski background, so that

$$g_{\mu\nu} = \eta_{\mu\nu} + h_{\mu\nu}, \quad |h_{\mu\nu}| \ll 1. \tag{1.3}$$

This perturbation is usually called *GW strain amplitude*, or simply *GW strain*, due to the effect it produces on matter and, in particular, in the arm lengths of GW detectors, as we will see.

The concept of "small perturbation" is frame-dependent, given that a coordinate transformation alters the metric and can increase the value of its components. More precisely, the rigorous statement of the previous equation is that there exists a reference system in which $|h_{\mu\nu}| \ll 1$ holds in a sufficiently large region of space. By choosing a reference frame, however, we are breaking one of the symmetries of General Relativity: the invariance under coordinate transformations. In the next subsections, we will continue making some choices regarding the reference system and gauge to reduce the non-physical degrees of freedom of the equations, until only the physically relevant information remains.

1.1.1 Linearized theory

Given that we consider $h_{\mu\nu}$ to be very small, we will compute the equations of motion to linear order, in a formalism which is called *linearized theory*. This means that we can raise and lower indices of quantities related to $h_{\mu\nu}$ with the Minkowski metric $\eta_{\mu\nu}$. As a result, Christoffel symbols in Eq. (0.3) can be obtained, to first order, as

$$\Gamma^{\mu}_{\nu\rho} = \frac{1}{2}\eta^{\mu\sigma}\left(\partial_\nu h_{\sigma\rho} + \partial_\rho h_{\sigma\nu} - \partial_\sigma h_{\nu\rho}\right). \tag{1.4}$$

Similarly, given that the Christoffel symbols are first order in $h_{\mu\nu}$, the Riemann tensor in Eq. (0.4) can be computed as the sum of just the first two terms:

$$R_{\mu\nu\rho\sigma} = \frac{1}{2}\left(\partial_\rho\partial_\nu h_{\mu\sigma} + \partial_\sigma\partial_\mu h_{\nu\rho} - \partial_\rho\partial_\mu h_{\nu\sigma} - \partial_\sigma\partial_\nu h_{\mu\rho}\right). \tag{1.5}$$

The Ricci tensor is then

$$R_{\mu\nu} = \frac{1}{2}\left(\partial^\rho\partial_\mu h_{\rho\nu} + \partial^\rho\partial_\nu h_{\mu\rho} - \Box h_{\mu\nu} - \partial_\mu\partial_\nu h\right), \tag{1.6}$$

with $\Box = \partial_\rho\partial^\rho$ the D'Alembertian operator and where we define h as the contraction of $h_{\mu\nu}$, $h = \eta^{\mu\nu}h_{\mu\nu}$. Finally, the Ricci scalar is

$$R = \partial^\rho\partial^\sigma h_{\rho\sigma} - \Box h. \tag{1.7}$$

In order to express Einstein's field equations,

$$R_{\mu\nu} - \frac{1}{2}g_{\mu\nu}R = \frac{8\pi G}{c^4}T_{\mu\nu}, \tag{1.8}$$

with G the universal gravitation constant and $T^{\mu\nu}$ the stress-energy tensor, we compute the Einstein tensor as

$$G_{\mu\nu} \equiv R_{\mu\nu} - \frac{1}{2} g_{\mu\nu} R = \frac{1}{2} \left(\partial^\rho \partial_\mu h_{\rho\nu} + \partial^\rho \partial_\nu h_{\mu\rho} - \Box h_{\mu\nu} - \partial_\mu \partial_\nu h - \eta_{\mu\nu} [\partial^\rho \partial^\sigma h_{\rho\sigma} - \Box h] \right), \tag{1.9}$$

which, for convenience, can be rewritten as

$$\begin{aligned} G_{\mu\nu} = \frac{1}{2} \Bigg(& \partial^\rho \partial_\mu \left[h_{\rho\nu} - \frac{1}{2} \eta_{\rho\nu} h \right] + \partial^\rho \partial_\nu \left[h_{\mu\rho} - \frac{1}{2} \eta_{\mu\rho} h \right] \Bigg(\\ & - \Box \left[h_{\mu\nu} - \frac{1}{2} \eta_{\mu\nu} h \right] - \eta_{\mu\nu} \partial^\rho \partial^\sigma \left[h_{\rho\sigma} - \frac{1}{2} \eta_{\rho\sigma} h \right] \Bigg) \Bigg(\end{aligned} \tag{1.10}$$

Thus, we can naturally define

$$\overline{h}_{\mu\nu} = h_{\mu\nu} - \frac{1}{2} \eta_{\mu\nu} h, \tag{1.11}$$

so that, using Eq. (1.10), the Einstein equations in Eq. (1.8) can be expressed as

$$\Box \overline{h}_{\mu\nu} + \eta_{\mu\nu} \partial^\rho \partial^\sigma \overline{h}_{\rho\sigma} - \partial^\rho \partial_\mu \overline{h}_{\rho\nu} - \partial^\rho \partial_\nu \overline{h}_{\mu\rho} = -\frac{16\pi G}{c^4} T_{\mu\nu}. \tag{1.12}$$

In the next subsection, we will simplify this equation by choosing a specific coordinate system.

1.1.2 The harmonic gauge

Even if we chose a reference system so that $|h_{\mu\nu}| \ll 1$, there is still some symmetry under the following transformation:

$$x^\mu \mapsto x'^\mu + \xi^\mu(x), \tag{1.13}$$

where $|\partial_\mu \xi_\nu| \lesssim |h_{\mu\nu}| \ll 1$. Using the tensor transformation rule for $g_{\mu\nu}$ under a coordinate change,

$$g'_{\mu\nu}(x') = \frac{\partial x^\rho}{\partial x'^\mu} \frac{\partial x^\sigma}{\partial x'^\nu} g_{\rho\sigma}(x), \tag{1.14}$$

we get that, under the transformation in Eq. (1.13),

$$h_{\mu\nu}(x) \mapsto h'_{\mu\nu}(x') = h_{\mu\nu(x)} - (\partial_\mu \xi_\nu + \partial_\nu \xi_\mu). \tag{1.15}$$

Therefore, if $|\partial_\mu \xi_\nu| \ll 1$ as we had imposed, then the condition $|h_{\mu\nu}| \ll 1$ still holds. This symmetry is usually referred to as *residual gauge freedom*.

We can use this freedom to impose the condition

$$\partial^\nu \overline{h}_{\mu\nu} = 0, \tag{1.16}$$

which is usually called the *harmonic gauge*, also named the Lorentz, Hilbert or De Donder gauge. The metric $\overline{h}_{\mu\nu}$ transforms as

$$\overline{h}_{\mu\nu}(x) \mapsto \overline{h}'_{\mu\nu}(x') = \overline{h}_{\mu\nu(x)} - (\partial_\mu \xi_\nu + \partial_\nu \xi_\mu - \eta_{\mu\nu} \partial_\rho \xi^\rho), \tag{1.17}$$

so its contracted derivative transforms as

$$\partial^\nu \overline{h}_{\mu\nu} \mapsto (\partial^\nu \overline{h}_{\mu\nu})' = \partial^\nu \overline{h}_{\mu\nu} - \Box \xi_\mu. \tag{1.18}$$

Thus, if $\partial^\nu \overline{h}_{\mu\nu}(x) = f_\mu(x)$ for a certain tensor function $f_\mu(x)$ which is not identically zero, we can make a coordinate change like Eq. (1.13) with a ξ_μ which satisfies

$$\Box \xi_\mu(x) = f_\mu(x), \tag{1.19}$$

so that, according to Eq. (1.18), then $(\partial^\nu \overline{h}_{\mu\nu})' = 0$ in the new coordinate system. It is known that an equation of the form of Eq. (1.19) always has solutions, given that there exist Green's functions of the D'Alembertian operator, meaning

$$\Box G(x - y) = \delta^4(x - y), \tag{1.20}$$

with y another point with coordinates independent of x and $\delta^4(x-y)$ the 4-dimensional Dirac delta function. For any given Green's function of the D'Alembertian, it is then immediate to show that a solution of Eq. (1.19) is given by

$$\xi_\mu(x) = \iint d^4 y G(x - y) f_\mu(y). \tag{1.21}$$

Thus, it is always possible to choose a coordinate system in which the harmonic condition (1.16) holds. In this case, the second to fourth terms in Eq. (1.12) vanish, and we get the simpler expression

$$\Box \overline{h}_{\mu\nu} = -\frac{16\pi G}{c^4} T_{\mu\nu}. \tag{1.22}$$

It is worth noting that the harmonic condition (1.16) gives four independent equations. Given that a 4-dimensional metric has 10 independent components due to the symmetry, the harmonic gauge restricts the remaining degrees of freedom to just 6. In the next subsection, we will see how they can be reduced to just 2 outside a source, in vacuum.

1.1.3 The transverse traceless gauge

The previous Equation (1.22) shows the dynamics of a perturbation $h_{\mu\nu}$ in any context, with a generic stress-energy tensor $T_{\mu\nu}$. However, for the propagation of gravitational waves, we are interested in what happens in vacuum, outside any source. In this case, the stress-energy momentum vanishes and Eq. (1.22) is reduced to

$$\Box \overline{h}_{\mu\nu} = 0. \tag{1.23}$$

Given that the D'Alembertian is given by

$$\Box = \eta^{\mu\nu} \partial_\mu \partial_\nu = -\frac{1}{c^2} \partial_t + \nabla^2, \tag{1.24}$$

with $\nabla = (\partial_x, \partial_y, \partial_z)$, Eq. (1.23) is a standard wave equation with propagation speed c, which means that gravitational waves propagate at the speed of light.

Because the right-hand side in Eq. (1.23) is now zero, then there is some extra gauge freedom, so that the condition $\partial^\nu \overline{h}_{\mu\nu} = 0$ does not completely determine the gauge. Indeed, an additional transformation of the form of Eq. (1.13) will preserve the condition $\partial^\nu \overline{h}_{\mu\nu} = 0$ as long as it satisfies

$$\Box \xi_\mu = 0, \tag{1.25}$$

something which can be deduced from Eq. (1.19). In addition, the extra term arising from this coordinate change in $\overline{h}_{\mu\nu}$, shown in Eq. (1.17), has a zero D'Alembertian under the condition (1.25),

$$\Box(\partial_\mu \xi_\nu + \partial_\nu \xi_\mu - \eta_{\mu\nu}\partial_\rho \xi^\rho) = 0, \tag{1.26}$$

due to the fact that the derivatives commute. This means that, under a coordinate change of the form (1.13) with the condition (1.25), the metric will satisfy the Einstein equation in the form (1.23). Then, we have the freedom to choose these functions ξ_μ to impose 4 independent conditions on $\overline{h}_{\mu\nu}$ via Eq. (1.17).

The first of the conditions we will impose is the *traceless* condition, that is

$$\overline{h} = 0. \tag{1.27}$$

From its definition in Eq. (1.11), the previous equation implies $\overline{h}_{\mu\nu} = h_{\mu\nu}$. Thus, we can forget about the bars from now on.

The three remaining conditions will be used to impose the *transversality* conditions,

$$h_{i0} = 0. \tag{1.28}$$

Under these equations, the harmonic condition (1.16) for $\mu = 0$ simplifies to

$$\partial^0 h_{00} = 0, \tag{1.29}$$

which means h_{00} is constant in time. This static contribution corresponds to the gravitational potential of the source. However, since we are studying gravitational waves, which correspond to the time-dependent part of the metric, we can safely ignore the static contribution and write

$$h_{00} = 0. \tag{1.30}$$

All the conditions we imposed up to now, including also the harmonic condition (1.16) for spatial indices, define the *transverse-traceless* (TT) gauge:

$$h_{0\mu} = 0, \quad h^i_i = 0, \quad \partial^j h_{ij} = 0. \tag{1.31}$$

In this gauge, we have used four extra conditions over the 6 degrees of freedom that we had from the harmonic gauge. Therefore, only 2 degrees of freedom remain.

In the next subsection, we will use this gauge to get the plane wave solutions to Eq. (1.23) in a physically meaningful form.

1.1.4 Plane waves

Given that the Einstein equations in the harmonic gauge take the form of a D'Alembert equation (1.23), they admit plane wave solutions. In the TT gauge, the time components $h_{\mu 0}$ vanish, so any metric is fully characterized by its spatial components. Thus, a plane wave solution takes the form

$$h_{ij}(x) = A_{ij}(\vec{k}) e^{ik_\mu x^\mu}, \tag{1.32}$$

where $\vec{k}$ is the wave vector carrying information of the direction of propagation $\vec{n} \equiv \vec{k}/|\vec{k}|$, wavelength $\lambda \equiv 2\pi/|\vec{k}|$ and, using the propagation speed c, also its frequency $\omega = c|\vec{k}|$; $A_{ij}(\vec{k})$ is the amplitude, which depends on $\vec{k}$, and $k^\mu \equiv (\omega/c, \vec{k})$ is the wave 4-vector, which is a light-like 4-vector by definition.

In order to better study these plane waves, we fix the propagation direction to be the z axis. We now use the conditions defining the TT gauge in Eq. (1.31) to simplify the previous equation.

First, the condition $\partial^i h_{ij} = 0$ implies $n^i h_{ij} = 0$. In this case, since we take $\vec{n} = (0, 0, 1)$, then the three A_{i3} in Eq. (1.32) vanish. With this constraint, the transversality condition remains $A_{11} + A_{22} = 0$, so we can define $h_+ \equiv A_{11} = -A_{22}$. Taking into account the metric symmetry, the only remaining component is A_{12}, which we define as $h_\times$. Thus, Eq. (1.32) can be written in matrix form as

$$h_{ij}(t, z) = \begin{pmatrix} h_+ & h_\times & 0 \\ h_\times & -h_+ & 0 \\ 0 & 0 & 0 \end{pmatrix}_{ij} e^{i\omega(t - z/c)}. \tag{1.33}$$

This equation clearly exposes the two remaining degrees of freedom of the TT gauge, mentioned in the previous subsection. The subindices $+$ and $\times$ denote the "plus" and "cross" polarizations. They have these names because of the effect they produce on test masses, which can be observed in Fig. 1.1.

In this case, where $\vec{n} = \hat{z}$, the basis tensors for these modes are given by

$$e^+_{ab} = \begin{pmatrix} 1 & 0 \\ 0 & -1 \end{pmatrix}_{ab}, \quad e^\times_{ab} = \begin{pmatrix} 0 & 1 \\ 1 & 0 \end{pmatrix}_{ab}, \tag{1.34}$$

where $a, b = 1, 2$, given that the rest of the components are zero. More generally, for an arbitrary direction of propagation $\vec{n}$, these basis tensors can be expressed as

$$e^+_{ij}(\vec{n}) = u_i u_j - v_i v_j, \quad e^\times_{ij}(\vec{n}) = u_i v_j + v_i u_j, \tag{1.35}$$

with $\vec{u}$, $\vec{v}$ unitary vectors orthogonal to each other and to the propagation direction $\vec{n}$.

Since the solution of Eq. (1.23) can be expressed as a superposition of plane waves, and given the previous definitions under the TT gauge, the most general solution of Eq. (1.23) is

$$h_{ij}(t, \vec{x}) = \sum_{A=+,\times} \left(\int_0^\infty df \int d^2\Omega \, \tilde{h}_A(f, \vec{n}) e^A_{ij}(\vec{n}) e^{-2\pi i f(t - \vec{n}\cdot\vec{x}/c)} + c.c., \right. \tag{1.36}$$

where the negative frequencies are unphysical and are therefore not included. However, in order to avoid adding the complex conjugate term, a common "trick" is to define, for negative frequencies,

$$\tilde{h}_A(-f, \vec{n}) = \tilde{h}^*_A(f, \vec{n}), \tag{1.37}$$

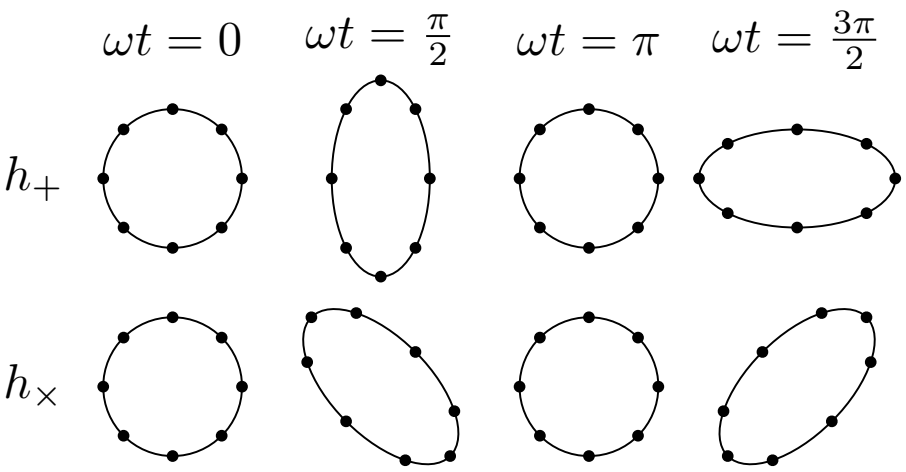

Figure 1.1: Effect of the polarizations plus (+) and cross (×) on a circle consisting of test masses.

where the notation * denotes complex conjugate. In this case, the complex conjugate term can be included into the first integral occupying the negative frequencies, so that Eq. (1.36) can be rewritten as

$$h_{ij}(t,\vec{x}) = \sum_{A=+,\times}\left(\int_{-\infty}^{\infty} df \int d^2\Omega\, \tilde{h}_A(f,\vec{n}) e^A_{ij}(\vec{n}) e^{-2\pi i f(t-\vec{n}\cdot\vec{x}/c)} + c.c. \right. \tag{1.38}$$

1.1.5 Projection to TT gauge

Related to the TT gauge, it is convenient to introduce a special tensor which will be used later. First, we define the projection tensor onto the plane orthogonal to the direction $\vec{n}$:

$$P_{ij}(\vec{n}) \equiv \delta_{ij} - n_i n_j. \tag{1.39}$$

This is a projector ($P_{ik}P_{kj} = P_{ij}$), it is symmetric and transverse ($n^i P_{ij}(\vec{n}) = 0$), and it has a trace $\delta^{ij}P_{ij} = 2$. Based on it, we construct the following projection tensor:

$$\Lambda_{ij,kl}(\vec{n}) = P_{ik}P_{il} - \frac{1}{2}P_{ij}P_{kl}. \tag{1.40}$$

This is again a projector ($\Lambda_{ij,kl}\Lambda_{kl,mn} = \Lambda_{ij,mn}$), transverse in its projected indices ($n^i\Lambda_{ij,kl} = n^j\Lambda_{ij,kl} = 0$), traceless in the first and second pair of indices ($\delta^{ij}\Lambda_{ij,kl} = \delta^{kl}\Lambda_{ij,kl} = 0$) and invariant under the change $(i,j) \leftrightarrow (k,l)$. Substituting Eq. (1.39) into Eq. (1.40), we get the explicit expression

$$\begin{aligned}\Lambda_{ij,kl}(\vec{n}) =& \delta_{ik}\delta_{jl} - \frac{1}{2}\delta_{ij}\delta_{kl} - n_j n_l \delta_{ik} - n_i n_k \delta_{jl} \\ &+ \frac{1}{2}(n_k n_l \delta_{ij} + n_i n_j \delta_{kl} + n_i n_j n_k n_l).\end{aligned} \tag{1.41}$$

Then, for a certain plane wave $h_{\mu\nu}$ in the harmonic gauge (1.16) propagating in the direction $\vec{n}$ which is not necessarily in the TT gauge, the projected metric with spatial components

$$h_{ij}^{TT} = \Lambda_{ij,kl} h_{kl}, \tag{1.42}$$

being the rest of them null, is a plane wave in the TT gauge. As just mentioned, the resulting metric is transverse, traceless and, if it was previously in the harmonic gauge (1.16) and a solution of the Einstein equations (1.23), then the projection does not spoil these conditions, as it also happens with the symmetry.

In general, the transverse-traceless projection of any symmetric tensor S_{ij} will be given by

$$S_{ij}^{\mathrm{TT}} = \Lambda_{ij,kl} S_{kl}. \tag{1.43}$$

1.2 Generalization to curved backgrounds

We now want to generalize the previous results for plane gravitational waves to an arbitrary background. Among other things, this is necessary to see how gravitational waves curve the spacetime. For this purpose, we decompose the metric as

$$g_{\mu\nu}(x) = \overline{g}_{\mu\nu}(x) + h_{\mu\nu}(x), \quad \overline{g}_{\mu\nu} = O(1), \quad |h_{\mu\nu}| \ll 1, \tag{1.44}$$

where taking the background metric as $O(1)$ is something we can always do in a region of spacetime under a change of coordinates, if necessary. However, since both terms are now dependent on x (unlike the background Minkowskian case), it is more subtle to argue how to decompose the metric into these two terms. In a general situation, this is not possible, but there is a natural way to divide the metric whenever there is a clear separation of either length scales or frequencies. If we denote the background length scale as L_B, then it is possible to clearly separate small perturbations if their wavelength λ is much smaller than L_B. Similarly, it is possible to disentangle a perturbation in the frequency spectrum if its frequency f is much higher than the one of the background, f_B. To summarize, we need either

$$\lambda\!\!\!^{-} \ll L_B \quad \text{or} \quad f \gg f_B, \tag{1.45}$$

where $\lambda\!\!\!^{-}$ is the reduced wavelength $\lambda\!\!\!^{-} = \lambda/(2\pi)$, which represents the physical scale associated to the wavelength λ. From now on, we will discuss only in terms of either λ or f, depending on what is more convenient for each argumentation. Both situations are analogous due to the fact that $f \propto \lambda^{-1}$, but it may be more clear to use one or the other in different contexts.

Now, we need to rewrite the Einstein equations up to second order in h, where h is loosely used as a synonym of $h_{\mu\nu}$ with any indices. First, we rewrite Eq. (1.8) as

$$R_{\mu\nu} = \frac{8\pi G}{c^4}\left(T_{\mu\nu} - \frac{1}{2} g_{\mu\nu} T\right)\Bigg(\tag{1.46}$$

Now, we need to separate this equation into its low and high-frequency parts. For this purpose, first we decompose the Ricci tensor up to $O(h^2)$. To avoid the explicit computations and just

illustrate the general procedure, we define $\overline{R}_{\mu\nu}$ as the part of the Ricci tensor dependent only on $\overline{g}_{\mu\nu}$ (the zero-th order in h) and $R^{(i)}_{\mu\nu}$ the i-th order in h. Thus, up to second order, we have

$$R_{\mu\nu} = \overline{R}_{\mu\nu} + R^{(1)}_{\mu\nu} + R^{(2)}_{\mu\nu}. \tag{1.47}$$

By construction, the term $\overline{R}_{\mu\nu}$ is only dependent on low frequencies and $R^{(1)}_{\mu\nu}$, on high ones, given that it is linear on h. However, the second order term $R^{(2)}_{\mu\nu}$ depends on both, since it is quadratic on h, and two high wave vectors $\vec{k}_1, \vec{k}_2$ can combine to give a low one if $\vec{k}_2 \approx -\vec{k}_1$. Then, $\overline{R}_{\mu\nu}$ will only appear in the low-frequency part of Eq. (1.46) and $R^{(1)}_{\mu\nu}$ in the high-frequency one, while $R^{(2)}_{\mu\nu}$ will appear in both. Thus, the low-frequency part of Eq. (1.46) can be written as

$$\overline{R}_{\mu\nu} = -\langle R^{(2)}_{\mu\nu}\rangle + \frac{8\pi G}{c^4}\langle T_{\mu\nu} - \frac{1}{2}g_{\mu\nu}T\rangle, \tag{1.48}$$

where $\langle\ \rangle$ denotes temporal average over many $1/f$, but much less than $1/f_B$ or, for the discussion in terms of λ, spatial average over many λ, but much less than one L_B. From now on, we denote

$$\overline{T}_{\mu\nu} = \langle T_{\mu\nu}\rangle. \tag{1.49}$$

In practice, if $T_{\mu\nu}$ comes from a macroscopic matter distribution, it will have a long wavelength, so that the trace of $\overline{T} \equiv \overline{g}^{\mu\nu}\overline{T}_{\mu\nu}$ will satisfy

$$\langle T_{\mu\nu} - \frac{1}{2}g_{\mu\nu}T\rangle = \overline{T}_{\mu\nu} - \frac{1}{2}\overline{g}_{\mu\nu}\overline{T}. \tag{1.50}$$

Notice that, if $T_{\mu\nu}$ had a high-frequency component, there could be terms in $g_{\mu\nu}T$ combining high frequencies in $g_{\mu\nu}$ and T so that the result is a low frequency, as argued before. Thus, the previous Eq. (1.50) would not hold with the definition (1.49), and then Eq. (1.50) would have to be imposed as a definition, as it is done in [39]. This is less natural, but applies for a wider range of contexts.

Next, we also define

$$t_{\mu\nu} = -\frac{c^4}{8\pi G}\langle R^{(2)}_{\mu\nu} - \frac{1}{2}\overline{g}_{\mu\nu}R^{(2)}\rangle, \tag{1.51}$$

with $R^{(2)} = \overline{g}^{\mu\nu}R^{(2)}_{\mu\nu}$, so that its trace satisfies

$$t = \overline{g}^{\mu}\nu t_{\mu\nu} = \frac{c^4}{8\pi G}\langle R^{(2)}\rangle. \tag{1.52}$$

With these definitions, we can express the term $-\langle R^{(2)}_{\mu\nu}\rangle$ in Eq. (1.48) as

$$-\langle R^{(2)}_{\mu\nu}\rangle = \frac{8\pi G}{c^4}\left(t_{\mu\nu} - \frac{1}{2}\overline{g}_{\mu\nu}t\right)\Bigg(\tag{1.53}$$

so that Eq. (1.48) can be rewritten, with the previous definitions, as

$$\overline{R}_{\mu\nu} = \frac{8\pi G}{c^4}\left(\Bigg(t_{\mu\nu} - \frac{1}{2}\overline{g}_{\mu\nu}t\right)\Bigg(+ \frac{8\pi G}{c^4}\left(\Bigg(\overline{T}_{\mu\nu} - \frac{1}{2}\overline{g}_{\mu\nu}\overline{T}\right)\Bigg(\tag{1.54}$$

Recast in the usual form of the Einstein equations, we get

$$\overline{R}_{\mu\nu} - \frac{1}{2}\overline{g}_{\mu\nu}\overline{R} = \frac{8\pi G}{c^4}(\overline{T}_{\mu\nu} + t_{\mu\nu}). \tag{1.55}$$

In this form, we can see $t_{\mu\nu}$ as an effective energy-momentum tensor coming from the perturbation $h_{\mu\nu}$, and quadratic in this field. This equation very clearly showcases how a gravitational wave can act as a source to curve spacetime through $t_{\mu\nu}$, similar to the behavior of a usual matter field through its energy-momentum tensor $T_{\mu\nu}$.

In fact, we can get a conservation rule from Eq. (1.55). Due to the contracted Bianchi identities [41],

$$\nabla^\rho R_{\rho\mu} = \frac{1}{2}\nabla_\mu R, \tag{1.56}$$

where ∇_μ denotes covariant derivative, then, the left-hand side of Eq. (1.55) vanishes under contraction with the covariant derivative with respect to $\overline{g}_{\mu\nu}$, which we denote by $\overline{\nabla}_\mu$. Then, the right-hand side of Eq. (1.55), which leaves

$$\overline{\nabla}^\mu(\overline{T}_{\mu\nu} + t_{\mu\nu}) = 0. \tag{1.57}$$

The previous expression implies that the energy-momentum tensor $\overline{T}_{\mu\nu}$ is not conserved anymore, but rather, its sum with $t_{\mu\nu}$. This illustrates how both matter and gravitational waves exchange energy and momentum, given that these are the quantities to remain invariant. In addition, outside the source, $\overline{T}_{\mu\nu}$, and for the limit of large distances, the background metric is approximately flat again and the covariant derivative reduces to the ordinary one. Thus, in this regime, we get the conservation law

$$\partial^\mu t_{\mu\nu} = 0. \tag{1.58}$$

In Subsec. 1.2.2, we will better study the properties of $t_{\mu\nu}$ to characterize the energy that gravitational waves carry, as well as their energy flux. This will be needed in later chapters of the thesis. However, before that, it is worth commenting on the other equation we have ignored in this process, which is the high-frequency version of Eq. (1.48).

1.2.1 Propagation of gravitational waves

As discussed before, the background Ricci tensor $\overline{R}_{\mu\nu}$ will not appear in the high-frequency part of Eq. (1.46), due to it being purely low-frequency. However, $R^{(1)}_{\mu\nu}$, which is purely high-frequency, will appear, as well as the corresponding component of $R^{(2)}_{\mu\nu}$. Thus, we get the equation

$$R^{(1)}_{\mu\nu} = -\left(R^{(2)}_{\mu\nu}\right)^{\text{High}} + \frac{8\pi G}{c^4}\left(T_{\mu\nu} - \frac{1}{2}g_{\mu\nu}T\right)^{\text{High}}, \tag{1.59}$$

where the "High" superscript denotes the projection on the high frequencies, similarly to how the averages $\langle\ \rangle$ acted before for low frequencies. The main quantity to be computed here is the first order of the Ricci tensor, which is

$$R^{(1)}_{\mu\nu} = \frac{1}{2}\left(\overline{\nabla}^\rho\overline{\nabla}_\mu h_{\nu\rho} + \overline{\nabla}^\rho\overline{\nabla}_\nu h_{\mu\rho} - \overline{\nabla}^\rho\overline{\nabla}_\rho h_{\mu\nu} - \overline{\nabla}_\mu\overline{\nabla}_\nu h\right), \tag{1.60}$$

with $\overline{\nabla}_\mu$ the covariant derivative with respect to $\overline{g}_{\mu\nu}$. We can see it is exactly the same as the one we obtained in linearized theory, Eq. (1.6), only with covariant derivatives instead of ordinary ones.

Studying the behavior of Eq. (1.54) in vacuum, $T_{\mu\nu} = 0$, the spacetime curvature is determined by the gravitational wave perturbation, that is,

$$\overline{R}_{\mu\nu} \sim (\partial h)^2. \tag{1.61}$$

We now recall that L_B is the typical scale of $\overline{g}_{\mu\nu}$, so that $\overline{R}_{\mu\nu} \sim \partial^2 g_{\mu\nu} \sim 1/L_B^2$ (since $\overline{g}_{\mu\nu} \sim 1$). On the other hand, $\lambda\!\!\!^{-}$ is the typical scale for h, so $\partial h \sim h/\lambda\!\!\!^{-}$. Then, Eq. (1.61) implies

$$h \sim \frac{\lambda\!\!\!^{-}}{L_B} \equiv \epsilon \ (\ll 1). \tag{1.62}$$

In this case, according to Eq. (1.60) and setting $L_B \sim 1$ for simplicity, the leading order in $R^{(1)}_{\mu\nu}$ is $\partial^2 h \sim h/\lambda\!\!\!^{-2} \sim 1/\epsilon$. Similarly, one can compute $R^{(2)}_{\mu\nu}$ to check that its dominant order is $\partial^2 h^2 \sim h^2/\lambda\!\!\!^{-2} \sim 1$ [39]. Thus, the leading order of Eq. (1.59) consists on the dominant order of $R^{(1)}_{\mu\nu}$ being null. Defining again $\overline{h}_{\mu\nu}$ as in Eq. (1.11) and using the harmonic gauge in Eq. (1.16), we get again the wave equation (1.23), recovering the results of linearized theory for gravitational wave propagation.

If, instead, we allow for a non-zero energy-momentum tensor, then the curvature is determined by it, dominating the gravitational wave contribution,

$$h \ll \frac{\lambda\!\!\!^{-}}{L_B}. \tag{1.63}$$

This time, we can stay at leading order in h and truncate the expansion in $\lambda\!\!\!^{-}/L_B$ at the next-to-leading order. In this case, Eq. (1.59) is simply $R^{(1)}_{\mu\nu} = 0$. By having a look at the form $R^{(1)}_{\mu\nu}$ in Eq. (1.60), we can simplify this equation with a similar gauge condition as the harmonic gauge in Eq. (1.16), only that with covariant derivatives instead of ordinary ones,

$$\overline{\nabla}^\nu \overline{h}_{\mu\nu} = 0, \tag{1.64}$$

Thus, the high-frequency Einstein equation (1.59) takes the final form

$$\overline{\nabla}^\rho \overline{\nabla}_\rho h_{\mu\nu} = 0, \tag{1.65}$$

again, completely analogous to Eq. (1.23) but with covariant derivatives. This generalizes the propagation of gravitational waves to a curved background for either of the conditions (1.45).

1.2.2 Energy of a gravitational wave

In order to properly study how gravitational waves interact with the background spacetime, which is a dynamics given by Eq. (1.55), we must study the behavior of the $t_{\mu\nu}$ tensor. Given its definition in Eq. (1.51), it is first necessary to compute the second-order of the Ricci tensor, $R^{(2)}_{\mu\nu}$. To simplify the analysis, we will study the energy and momentum of the gravitational waves at large distances from the source, which is how we detect them. This means we can go back to Minkowski spacetime.

In addition, one can apply several simplifications to the second-order Ricci tensor, involving gauge freedom reduction arguments similar to those in Sec. 1.1 which include setting the harmonic gauge condition (1.16), as well as arguments based on integration by parts inside the spatial or temporal averages in Eq. (1.51) (see the discussion in [39] for the full details). In this case, one can show that

$$\langle R^{(2)}_{\mu\nu}\rangle = -\frac{1}{4}\langle \partial_\mu h_{\alpha\beta}\partial_\nu h^{\alpha\beta}\rangle, \tag{1.66}$$

whose trace vanishes using $\Box h_{\mu\nu} = 0$. Then, $t_{\mu\nu}$ takes the form

$$t_{\mu\nu} = \frac{c^4}{32\pi G}\langle \partial_\mu h_{\alpha\beta}\partial_\nu h^{\alpha\beta}\rangle. \tag{1.67}$$

In Eq. (1.55), the tensor $t_{\mu\nu}$ plays the role of a usual energy-momentum tensor. Thus, the properties of a gravitational wave can be inferred from its components. On the one hand, the t^{00} component provides the energy density. From the Eq. (1.67), t^{00} takes a particularly simple expression in the TT gauge (1.31):

$$\frac{dE}{d^3V} \equiv t^{00} = \frac{c^2}{32\pi G}\langle \dot{h}^{TT}_{ij}\dot{h}^{TT}_{ij}\rangle, \tag{1.68}$$

or, in terms of the polarization amplitudes h_+ and $h_\times$,

$$\frac{dE}{d^3V} \equiv t^{00} = \frac{c^2}{16\pi G}\langle \dot{h}^2_+ + \dot{h}^2_\times\rangle. \tag{1.69}$$

On the other hand, the momentum flux in the direction k per unit time and surface can be obtained from the t^{0k} component:

$$\frac{dP^k}{d^2A\,dt} \equiv t^{0k} = -\frac{c^3}{32\pi G}\langle \dot{h}^{TT}_{ij}\partial^k h^{TT}_{ij}\rangle. \tag{1.70}$$

The main situation for physical interest is considering that the source is at the origin and the observer is very far away at a certain distance r. In this context, we want to compute how much momentum flux the gravitational wave carries away through the sphere of radius r. Then, we can write the surface element as $d^2A = r^2 d^2\Omega$, so that the total temporal momentum flux in the direction k which goes through the sphere of radius r can be written as

$$\frac{dP^k}{dt} \equiv t^{0k} = -\frac{c^3}{32\pi G}r^2 \iint d^2\Omega \langle \dot{h}^{TT}_{ij}\partial^k h^{TT}_{ij}\rangle. \tag{1.71}$$

In order to obtain the energy flux in the same situation, we can use the time derivative of the expression for the energy density in terms of t^{00} (1.68):

$$\frac{1}{c}\frac{dE}{d^3V\,dt} = \partial_0 t^{00} = -\partial_k t^{0k}, \tag{1.72}$$

where in the second step we have used the conservation law for $t^{\mu\nu}$ in Eq. (1.58). Using Stokes' theorem [42] and considering V the volume inside a sphere of radius r, we get

$$\frac{dE}{dt} = -c\int d^3V\partial_k t^{0k} = -c\iint d^2A n_k t^{0k}, \tag{1.73}$$

where A is the boundary of the volume V, i.e. the spherical surface of radius r, and n^k is the orthogonal unit vector to it in the outward direction, which means it is the radial unit vector $\hat{r}$. Then, using Eq. (1.67) in the TT gauge,

$$\frac{dE}{dt} = -\frac{c^5}{32\pi G}\langle \partial^0 h_{ij}^{\mathrm{TT}} \partial_r h_{ij}^{\mathrm{TT}} \rangle. \tag{1.74}$$

If our gravitational wave is propagating radially outward, we can assume the functional form

$$h_{ij}^{\mathrm{TT}}(t,r) = \frac{1}{r} f_{ij}\left(t - \frac{r}{c}\right) \tag{1.75}$$

for certain functions f_{ij}. As a result,

$$\partial_r h_{ij}^{\mathrm{TT}} = -\frac{1}{r^2} f_{ij}\left(t-\frac{r}{c}\right) + \frac{1}{r}\partial_r f_{ij}(t-r/c) = -\frac{1}{r^2} f_{ij}\left(t-\frac{r}{c}\right) - \frac{1}{c}\partial_t f_{ij}\left(t-\frac{r}{c}\right). \tag{1.76}$$

Assuming large distances, we can neglect the first term, so that $\partial_r h_{ij}^{\mathrm{TT}} \approx \partial^0 h_{ij}^{\mathrm{TT}}$, which, using Eq. (1.74), implies $t^{0r} = t^{00}$. Thus, Eq. (1.74) can be rewritten as

$$P = \frac{dE}{dt} = \frac{c^3 r^2}{32\pi G}\iint d^2\Omega \langle \dot{h}_{ij}^{\mathrm{TT}} \dot{h}_{ij}^{\mathrm{TT}} \rangle, \tag{1.77}$$

or, in terms of the polarization amplitudes h_+ and $h_\times$,

$$P = \frac{dE}{dt} = \frac{c^3 r^2}{16\pi G}\iint d^2\Omega \langle \dot{h}_+^2 + \dot{h}_\times^2 \rangle, \tag{1.78}$$

Then, in order to obtain the total flux of energy through $d^2A = r^2 d^2\Omega$ for all time, one would have to integrate the previous expression from $t \to -\infty$ to $t \to \infty$. In this case, we can first do this integral, which makes the averages $\langle\ \rangle$ unnecessary. Then, going back to the differential form per surface unit, we can write

$$\frac{dE}{d^2A} = \frac{c^3}{16\pi G}\int_{-\infty}^{\infty} dt \left(\dot{h}_+^2 + \dot{h}_\times^2\right). \tag{1.79}$$

We can now Fourier-decompose each of the polarizations, like

$$h_{+,\times}(t) = \iint_{-\infty}^{\infty} df \tilde{h}_{+,\times} e^{-2\pi i f t}, \tag{1.80}$$

so that the previous equation can be rewritten as

$$\frac{dE}{d^2A} = \frac{\pi c^3}{4G}\iint_{-\infty}^{\infty} df\, f^2 \left(|\tilde{h}_+|^2 + |\tilde{h}_\times|^2\right). \tag{1.81}$$

Using the parity symmetry $f \mapsto -f$, we can only integrate in positive frequencies, by multiplying the integral by a factor of 2. Then, we can write the energy flux per unit surface and unit frequency as

$$\frac{dE}{d^2A df} = \frac{\pi c^3}{2G} f^2 \left(|\tilde{h}_+|^2 + |\tilde{h}_\times|^2\right), \tag{1.82}$$

with the convention that dE/df is only defined for positive frequencies, giving the total energy when integrated over this range. Then, using again $d^2A = r^2 d^2\Omega$, we can integrate to get

$$\frac{dE}{df} = \frac{\pi c^3}{2G} f^2 r^2 \iint d^2\Omega \left(|\tilde{h}_+(f)|^2 + |\tilde{h}_\times(f)|^2\right). \tag{1.83}$$

1.2.3 Quadrupole formulae

The equations in the previous subsection relate the GW strain to the radiated energy. However, in order to know how much energy is emitted by a given physical system, we must relate these quantities to the source configuration, that is, to its energy-momentum tensor. Eq. (1.22) precisely relates these quantities, so in this subsection, we will solve it and derive important equations from its solution.

For this purpose, we first notice that Eq. (1.22) is formally identical to the the one obtained in Electromagnetism, so we can use the same procedure to solve it. First, we use that a Green's function for the D'Alembertian is given by

$$G(x-x') = -\frac{\delta(t-|\vec{x}-\vec{x}'|/c)}{4\pi|\vec{x}-\vec{x}'|}, \tag{1.84}$$

where the argument of the delta is usually called retarded time,

$$t_r = t - \frac{|\vec{x}-\vec{x}'|}{c}. \tag{1.85}$$

Then, applying this Green's function to Eq. (1.22), we get

$$\overline{h}_{\mu\nu}(t,\vec{x}) = \frac{4G}{c^4}\int\!\!\!\int d^3x' \frac{T_{\mu\nu}(t_r,\vec{x}')}{|\vec{x}-\vec{x}'|}. \tag{1.86}$$

As a result, the Fourier transform of $h_{\mu\nu}$ satisfies

$$\tilde{\overline{h}}_{\mu\nu}(\omega,\vec{x}) = \frac{4G}{c^4}\int\!\!\!\int d^3x' \frac{e^{i\omega|\vec{x}-\vec{x}'|}}{|\vec{x}-\vec{x}'|}\tilde{T}_{\mu\nu}(\omega,\vec{x}'). \tag{1.87}$$

For large distances from the source, we can assume that the distances involved at the source given by $|\vec{x}'|$ are negligible with respect to $|\vec{x}|$. Then, we can approximate $|\vec{x}-\vec{x}'| \approx |\vec{x}| \equiv r$ (see Fig. 1.2), so that the previous equation is

$$\tilde{\overline{h}}_{\mu\nu}(\omega,\vec{x}) = \frac{4G}{c^4}\frac{e^{i\omega r}}{r}\int\!\!\!\int d^3x' \tilde{T}_{\mu\nu}(\omega,\vec{x}'). \tag{1.88}$$

From the harmonic gauge condition (1.16) applied to $\tilde{\overline{h}}_{\mu\nu}$, $\partial_\mu \tilde{\overline{h}}^{\mu\nu} = 0$, we get

$$\tilde{\overline{h}}^{0\nu} = -\frac{i}{\omega}\partial_i \tilde{\overline{h}}^{i\nu}, \tag{1.89}$$

so, for $\nu = j$, the spatial components $\tilde{\overline{h}}^{ij}$ provide the mixed components $\tilde{\overline{h}}^{i\nu}$ and, for $\nu = 0$, these ones provide $\tilde{\overline{h}}^{00}$. Thus, it is only necessary to compute the spatial components from Eq. (1.88). Using the conservation of the energy-momentum tensor $\partial_\mu T^{\mu\nu} = 0$ within linearized theory, we can operate the integral as

$$\begin{aligned}\int d^3x\, \tilde{T}^{ij}(\omega,\vec{x}) &= \int\!\!\!\int d^3x\, \partial_k(x^i\tilde{T}^{kj}) - \int\!\!\!\int d^3x\, x^i\partial_k\tilde{T}^{kj} \\ &= \int d^3x\, x^i\partial_0\tilde{T}^{0j} = \frac{i\omega}{c}\int\!\!\!\int d^3x\, x^i\tilde{T}^{0j},\end{aligned} \tag{1.90}$$

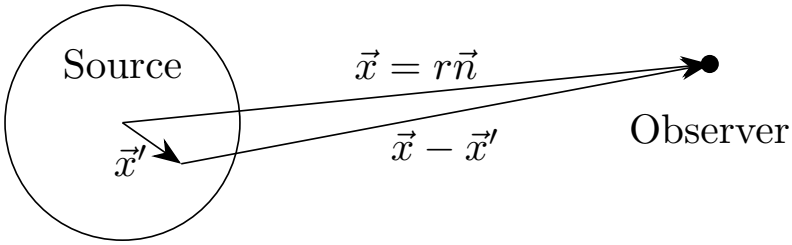

Figure 1.2: Illustration of the distances involved in Eqs. (1.86) and (1.87), where $\vec{x}$ is the distance from the source to the observer and $\vec{x}'$ is an internal distance of the source distribution. In the limit in which the distance from the source to the observer is much larger than the internal distances, $|\vec{x}| \gg |\vec{x}'|$, we can see how $\vec{x} - \vec{x}' \approx \vec{x}$.

where the second step uses that the surface integral vanishes at infinity. Then, using the symmetry of the energy-momentum tensor, we can get the symmetric part of the previous equation to write

$$\int d^3x\, \tilde{T}^{ij}(\omega, \vec{x}) = \frac{i\omega}{2c} \iint d^3x\, (x^i \tilde{T}^{0j} + x^j \tilde{T}^{0i}) = \frac{i\omega}{2c} \iint d^3x\, \left[\partial_l (x^i x^j \tilde{T}^{0l}) - x^i x^j \partial_l \tilde{T}^{0l}\right]$$
$$= \frac{i\omega}{2c} \int d^3x\, x^i x^j \partial_0 \tilde{T}^{00} = -\frac{\omega^2}{2c^2} \iint d^3x\, x^i x^j \tilde{T}^{00}. \tag{1.91}$$

We can then define the quantity

$$\rho(t, \vec{x}) \equiv \frac{T^{00}(t, \vec{x})}{c^2}, \tag{1.92}$$

which has dimensions of mass density and it is, in fact, the rest mass density at the leading order in v/c. This is inferred from the fact that ρ is the energy density divided by c^2. Then, we define the quadrupole moment of ρ as

$$I^{ij}(t) \equiv \iint d^3x\, x^i x^j \rho(t, \vec{x}) \tag{1.93}$$

Going back to Eq. (1.88), we get

$$\tilde{\bar{h}}_{ij}(\omega, \vec{x}) = -\frac{2G\omega^2}{c^4} \frac{e^{i\omega r}}{r} \tilde{I}_{ij}(\omega), \tag{1.94}$$

so taking the inverse Fourier transform,

$$\bar{h}_{ij}(t, \vec{x}) = \frac{2G}{c^4 r} \ddot{I}_{ij}(t_r), \tag{1.95}$$

which is the so-called *quadrupole formula* for the gravitational wave amplitude, first derived by Einstein in 1918.

We usually want to express this equation in the transverse-traceless gauge. Therefore, since I_{ij} has a certain trace $I \equiv \delta^{ij} I_{ij}$, it is sometimes more convenient to use the reduced quadrupole moment, which is a traceless quantity:

$$Q^{ij}(t) \equiv I^{ij}(t) - \frac{1}{3}\delta^{ij} I(t) = \int d^3x\, \rho(t, \vec{x}) \left(x^i x^j - \frac{1}{3} r^2 \delta^{ij}\right) \tag{1.96}$$

Thus, in the TT gauge, we can express Eq. (1.95) as

$$h_{ij}^{\mathrm{TT}}(t,\vec{x}) = \frac{2G}{c^4 r}\ddot{Q}_{ij}^{\mathrm{TT}}(t_r), \tag{1.97}$$

In practical terms, however, it is usually easier to compute the quadrupole moments I_{ij} in Eq. (1.93). It is therefore useful to compute the previous equation (1.97) in terms of the I_{ij} components. If we assume that the gravitational wave is propagating in the direction $\vec{n} = \hat{z}$, then it is easy to check that, applying the projector to the TT gauge in Eq. (1.40), we get

$$\ddot{Q}_{ij}^{\mathrm{TT}} = \Lambda_{ij,kl}\ddot{I}_{kl} = \begin{pmatrix} (\ddot{I}_{11} - \ddot{I}_{22})/2 & \ddot{I}_{12} & 0 \\ \ddot{I}_{12} & -(\ddot{I}_{11} - \ddot{I}_{22})/2 & 0 \\ 0 & 0 & 0 \end{pmatrix}. \tag{1.98}$$

In this tensor, we can clearly see the amplitudes of the plus and cross polarizations. Thus, substituting it in Eq. (1.97), we can get the gravitational wave amplitudes for each mode:

$$h_+(t,\vec{x}) = \frac{G}{c^4 r}(\ddot{I}_{11} - \ddot{I}_{22})(t_r), \tag{1.99}$$

$$h_\times(t,\vec{x}) = \frac{2G}{c^4 r}\ddot{I}_{12}(t_r). \tag{1.100}$$

By assuming that the gravitational wave propagates in direction $\vec{n} = \hat{z}$, we are not losing generality, since we can always apply a rotation so that this assumption is true, and then rotate back to recover the original reference system. However, there are cases in which it is easier to compute the quadrupole momenta in certain preferred axes, so it is useful to obtain Eqs. (1.99) and (1.100) for an arbitrary propagation direction.

In order to do this, we start from the quadrupole momentum tensor I_{ij} in its natural reference system S, with the additional hypothesis that the mass distribution is approximately flat in the z coordinate, so that $I_{i3} = 0$ for all i. This is to simplify the equations, given that during this thesis, all the systems considered will satisfy this assumption. We want to characterize a gravitational wave propagating in the direction $\vec{n} = (\sin\theta\cos\phi, \sin\theta\sin\phi, \cos\theta)$, so we define a rotated reference system S' such that its axis $\hat{z}'$ aligns with this direction. Note that there is still some freedom to define the reference system, given that a generic rotated reference system is characterized by three Euler angles: θ around the y axis, ϕ around the z axis and a third rotation around the z' axis determines the final orientation of the x' and y' axes. This third rotation would have the effect of shifting a fraction of the amplitude of one polarization to the other one, and vice versa, which is exactly the freedom we have when choosing the basis vectors $\vec{u}$ and $\vec{v}$ that define the polarization basis tensors e_{ij}^+ and $e_{ij}^\times$ in Eq. (1.35). Thus, since this is a question of definition rather than a physical effect, we do not consider it here and ignore this third rotation, so that our rotated system is characterized by the rotation matrix

$$R(\theta,\phi) = \begin{pmatrix} \cos\phi & -\sin\phi & 0 \\ \sin\phi & \cos\phi & 0 \\ 0 & 0 & 1 \end{pmatrix}\begin{pmatrix} \cos\theta & 0 & \sin\theta \\ 0 & 1 & 0 \\ -\sin\theta & 0 & \cos\theta \end{pmatrix}. \tag{1.101}$$

This rotation transforms the coordinates of S' to the coordinates of S, like

$$x_i = R_{ij}x'_j, \tag{1.102}$$

similar to how we obtain $\vec{n} = (\sin\theta\cos\phi, \sin\theta\sin\phi, \cos\theta)$ from $\hat{z}' = (0,0,1)$. The polarization tensor undergoes the same transformation, so that

$$I_{ij} = R_{ik}R_{jl}I'_{kl} \tag{1.103}$$

or, in matrix form,

$$I = RI'R^T \quad \Rightarrow \quad I' = R^T I R, \tag{1.104}$$

where we have used that rotations satisfy $R^{-1} = R^T$. We can then use the second equation to obtain the quadrupole momentum tensor I'_{ij} in the reference system S',

$$I'_{11} = (I_{11}\cos^2\phi + I_{22}\sin^2\phi)\cos^2\theta + I_{12}\cos^2\theta\sin(2\phi), \tag{1.105}$$

$$I'_{12} = \frac{I_{22} - I_{11}}{2}\cos\theta\sin(2\phi) + I_{12}\cos\theta\cos(2\phi), \tag{1.106}$$

$$I'_{22} = I_{11}\sin^2\phi + I_{22}\cos^2\phi - I_{12}\sin(2\phi). \tag{1.107}$$

In this system S', the z' axis and the direction of propagation of the gravitational wave coincide, so that Eqs. (1.99) and (1.100) hold. Thus, we can simply substitute the previous expressions for I'_{ij} to get the expressions for h_+ and $h_\times$ as functions of I_{ij},

$$h_+(t,\vec{x}) = \frac{G}{c^4 r}\Big[\ddot{I}_{11}(\cos^2\theta\cos^2\phi - \sin^2\phi) + \ddot{I}_{22}(\cos^2\theta\sin^2\phi - \cos^2\phi) + \ddot{I}_{12}\sin(2\phi)(1+\cos^2\theta)\Big] \tag{1.108}$$

$$h_\times(t,\vec{x}) = \frac{G}{c^4 r}\Big[(\ddot{I}_{22} - \ddot{I}_{11})\cos\theta\sin(2\phi) + 2\ddot{I}_{12}\cos\theta\cos(2\phi)\Big], \tag{1.109}$$

where the quantities at the right-hand side must be evaluated at t_r. Note that these expressions do not exactly match the ones in [39] due to the different choice of coordinates for $\vec{n}$.

To finish this section, we will compute the radiated power. For this purpose, we can substitute Eq. (1.97) into Eq. (1.77) to get

$$P = \frac{G}{8\pi c^5}\int d^2\Omega\, \langle \dddot{Q}^{\mathrm{TT}}_{ij}(t_r)\dddot{Q}^{\mathrm{TT}}_{ij}(t_r)\rangle. \tag{1.110}$$

In order to get this power from an arbitrary gauge, we can use the projection tensor $\Lambda_{ij,kl}(\vec{n})$ defined in Eq. (1.40) and apply Eq. (1.43) to $\ddot{Q}_{ij}$. In this case, Eq. (1.110) implies

$$P = \frac{G}{8\pi c^5}\int d^2\Omega\, \Lambda_{ij,kl}(\vec{n})\langle \dddot{Q}_{ij}(t_r)\dddot{Q}_{kl}(t_r)\rangle, \tag{1.111}$$

where the only dependence on the direction is in $\Lambda_{ij,kl}(\vec{n})$. Therefore, using its explicit expression in Eq. (1.41), we get

$$\begin{aligned}\int d^2\Omega\, \Lambda_{ij,kl}(\vec{n})\langle \dddot{Q}_{ij}(t_r)\dddot{Q}_{ij}(t_r)\rangle &= \frac{2\pi}{15}(11\delta_{ik}\delta_{jl} - 4\delta_{ij}\delta_{kl} + \delta_{il}\delta_{jk})\langle \dddot{Q}_{ij}(t_r)\dddot{Q}_{kl}(t_r)\rangle \\ &= \frac{8\pi}{5}\langle \dddot{Q}_{ij}(t_r)\dddot{Q}_{ij}(t_r)\rangle.\end{aligned} \tag{1.112}$$

Then, substituting back into Eq. (1.111), we get

$$P = \frac{G}{5c^5}\langle \dddot{Q}_{ij}(t_r)\dddot{Q}_{ij}(t_r)\rangle, \tag{1.113}$$

which is also called *quadrupole formula* for the radiated power, and was also derived by Einstein in 1918.

1.3 Gravitational waves from a bound two-body system

According to the first Kepler law, bound celestial bodies move following elliptical orbits around each other, in which the focus is located at the center of mass. In General Relativity, this is not true due to the energy emission in the form of gravitational waves. This energy loss causes the masses to become progressively closer to each other, in an inward spiral usually called *inspiral*. When they get too close, if both objects are massive enough, the two masses start *merging* into a common, final mass which suffers some oscillations until it stabilizes, in a final phase called *ringdown*. An example of trajectory is shown in the right panel of Fig. 1.3, while the three mentioned stages (inspiral, merger, ringdown) can clearly be distinguished from the qualitative behavior of the emitted gravitational waves shown in the left panel. These plots have been obtained from the numerical simulation in Sec. 6.2, to which one can refer for details on the plotted variables.

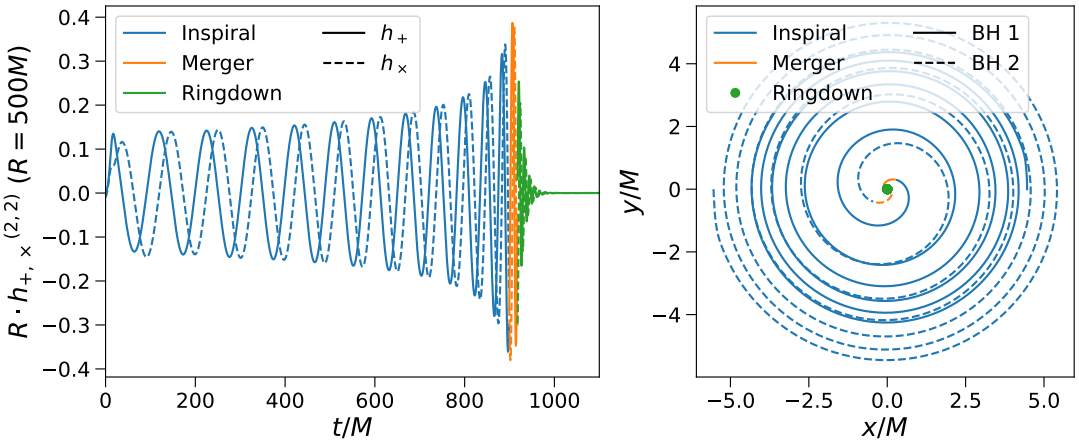

Figure 1.3: Gravitational-wave strain (left) and black hole trajectories (right) during a CBC, showing the inspiral, merger and ringdown in different colors.

The case of greatest interest for Astrophysics and Cosmology is that one in which both objects are *compact*, which is a term used to refer to neutron stars (NS) and black holes, due to the tremendous amount of energy they release within these interactions. The bound two-body systems they form can thus be binary black holes (BBHs), when both objects are black holes; binary neutron stars (BNS), if they are instead two neutron stars, and neutron star-black hole binaries (NSBH, or sometimes BHNS, binaries). The joint phenomenon of their inspiral, merger and ringdown is

called *compact binary coalescence* (CBC), and it represents the main source of gravitational-wave emission that we are able to detect with current GW detectors.

In general, the inspiral part of a CBC can be analytically treated, given that the distance from both masses is still large enough. This means that the interaction is still very similar to the Keplerian one, and it can be studied just by incorporating a first-order correction coming from the relativistic energy loss. This is exactly what we will do in this section, computing how much gravitational radiation these two-body systems emit, and how this affects to the evolution of their properties with time. As the masses get closer to each other, however, these approximations stop being valid and one has to resort to next-order corrections, following either post-Newtonian (PN, expansion in $1/c$) [43] or post-Minkowskian (PM, expansion in G) [44] approximations. For the post-Newtonian formalism, it is common to denote the expansion as PPN(n), or nPN, where PPN stands for *parameterized post-Newtonian* [45] and the n indicates the perturbative order. Refer to [45] for a very complete review on these approximations.

The ringdown can also be analytically modelled by using perturbation theory and studying the quasi-normal modes (QNMs) of black holes [46, 47]. However, at the stage of the merger, the dynamics is highly non-linear and no analytical approximation works accurately. One has then to resort to Numerical Relativity, which is further explained in Chapter 6.

For now, let us study the inspiral behavior by computing the power radiated by these two-body systems. We will do so by first reviewing the dynamics in the Keplerian case.

1.3.1 Keplerian dynamics

In order to study the elliptic motion of a two-body system, we should first define the geometrical elements of an ellipse, which are depicted in Fig. 1.4. In this figure, the relevant distances are the semi-major axis a, the semi-minor axis b and the distance c from the center of the ellipse to any of its foci. The ellipse is defined as the closed curve whose points satisfy that the sum of distances to the two foci is constant. From the points in the major (horizontal) axis, we have that this distance is $2a$, while for the ones in the minor (vertical) axis, we get that it is also $2\sqrt{b^2+c^2}$. Thus, c can be computed from a and b as

$$c = \sqrt{a^2 - b^2}. \tag{1.114}$$

Another important parameter is the eccentricity, defined as the ratio between c and a, so that

$$e = \frac{c}{a} = \sqrt{1 - \left(\frac{b}{a}\right)^2}, \quad \text{or} \quad b = a\sqrt{1-e^2}. \tag{1.115}$$

This parameter is defined in the range $[0, 1)$ and characterizes the similarity of the ellipse with a circumference, which corresponds to the case $e = 0$. For $e \to 1$, the ellipse would tend to a parabola, and beyond that, $e > 1$, the trajectory would be a hyperbola, with some parameters having to be redefined. We will study the hyperbolic case in Sec. 1.4.

An ellipse of fixed center and axis direction is fully characterized by two of these parameters, which are usually the semi-major axis a and eccentricity e. If we fix the center to be the right-most

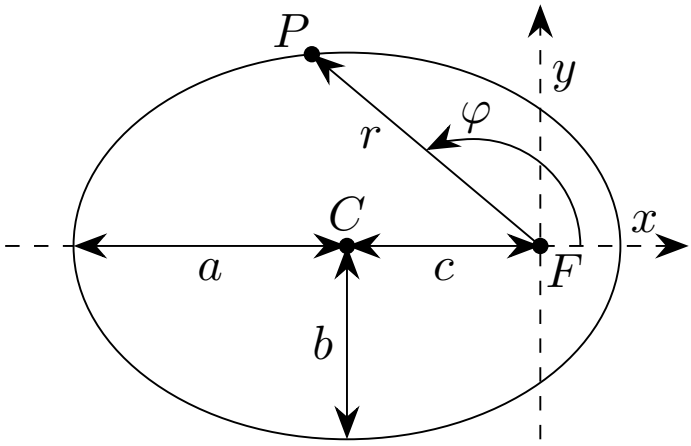

Figure 1.4: Ellipse with its relevant points, distances and angle. C indicates the center of the ellipse, while F indicates the focus which is taken as the origin of the coordinate system, while the other focus would be in the symmetric position. P indicates a generic point in the ellipse with radial coordinate r and phase φ. The semimajor and semiminor axes a and b are also shown, as well as the distance c from the center to the focus.

focus, the cartesian coordinates of the ellipse satisfy the equation

$$\left(\frac{(x+c)^2}{a}\right)^2 + \left(\frac{y}{b}\right)^2 = 1. \tag{1.116}$$

If we define a set of polar coordinates with the same center, related to the previous x and y with the usual equations,

$$\begin{cases} x = r\cos\varphi \\ y = r\sin\varphi \end{cases}, \tag{1.117}$$

then we can use Eq. (1.116) to derive the relation

$$r = \frac{a(1-e^2)}{1+e\cos\varphi}. \tag{1.118}$$

In Celestial Mechanics [48, 49], the parameter φ is called *true anomaly* and it is usually denoted by ν. Then, the periapsis and apoapsis are given by the maximum and minimum values of the denominator, $\cos\varphi = 1$ and $\cos\varphi = -1$, respectively, so that

$$r_p = a(1-e), \quad r_a = a(1+e). \tag{1.119}$$

When considering an ellipse in the context of an orbital trajectory, we have to introduce time, speed and other physical quantities to the picture, including the masses of the objects m_1 and m_2. As we know, we can treat the two-body problem as an effective one-body problem in the reference system of the center of mass, in which a particle of mass

$$\mu = \frac{m_1 m_2}{m_1 + m_2}, \tag{1.120}$$

which is called reduced mass, experiences a gravitational acceleration given by the universal gravitational law,

$$\ddot{\vec{r}} = -\frac{GM}{r^2}\hat{r}, \tag{1.121}$$

where $M = m_1 + m_2$ is the total mass. We can also write the conserved quantities, which are the orbital angular momentum $L = L_z$ and the energy E, given by

$$L = \mu|\vec{r}\times\vec{v}|, \quad E = \frac{1}{2}\mu v^2 - \frac{G\mu M}{r}, \tag{1.122}$$

or, using the expression for the velocity in polar coordinates, $\vec{v} = \dot{r}\hat{r} + r\dot{\varphi}\hat{\varphi}$,

$$L = \mu r^2\dot{\varphi}, \quad E = \frac{1}{2}\mu(\dot{r}^2 + r^2\dot{\varphi}^2) - \frac{G\mu M}{r}. \tag{1.123}$$

We can find explicit expressions for L and E in terms of the orbital parameters using the fact that they are conserved quantities. For this purpose, we evaluate them from Eq. (1.122) at the periapsis and apoapsis, and make the expressions at both points equal due to their conservation. At these points, the speed is perpendicular to the vector radius, so that

$$L_p = L_a \quad \Rightarrow \quad \mu r_p v_p = \mu r_a v_a \quad \Rightarrow \quad v_p = \frac{r_a}{r_p}v_a = \frac{1+e}{1-e}v_a, \tag{1.124}$$

where in the last step we have used the explicit expressions for r at the periapsis and apoapsis in Eq. (1.119). Repeating the process for the energy, we get

$$\begin{aligned} &E_p = E_a \quad \Rightarrow \quad \frac{1}{2}\mu v_p^2 - \frac{G\mu M}{r_p} = \frac{1}{2}\mu v_a^2 - \frac{G\mu M}{r_a} \\ \Rightarrow \quad &v_a^2\left[\left(\frac{1+e}{1-e}\right)^2 - 1\right] = \frac{2GM}{a}\left(\frac{1}{1-e} - \frac{1}{1+e}\right) \quad \Rightarrow \quad v_a^2 = \frac{GM}{a}\frac{1-e}{1+e}. \end{aligned} \tag{1.125}$$

Substituting this expression into the angular momentum and energy for the aphelion, we get

$$L = \mu\sqrt{GMa(1-e^2)}, \quad E = -\frac{G\mu M}{2a}. \tag{1.126}$$

Conversely, we can get the orbital parameters from the conserved quantities as

$$a = \frac{G\mu M}{2|E|}, \quad e^2 - 1 = \frac{2EL^2}{G^2M^2\mu^3}. \tag{1.127}$$

In particular, the fact that the expressions for the energy in Eqs. (1.122) and (1.126) are equal provides an easy way to compute the velocity,

$$v^2 = GM\left(\frac{2}{r} - \frac{1}{a}\right) \tag{1.128}$$

In Celestial Mechanics [48, 49], this expression is called the *vis-viva equation*.

Finally, the period of motion is given by Kepler's third law,

$$T^2 = \frac{4\pi^2}{GM}a^3. \tag{1.129}$$

1.3.2 Radiated power

We can now study the bound two-body problem in General Relativity by incorporating the energy loss arising from Einstein's equations. This energy loss is given by Eq. (1.113), which involves the reduced quadrupole moment Q_{ij} defined in Eq. (1.96). To simplify the computations, it is better to start from the quadrupole moment I_{ij} defined in Eq. (1.93), and then compute Q_{ij} by subtracting $1/3$ of the trace. From Eqs. (1.117) and assuming that the bodies are point masses, I_{ij} takes the form

$$I_{ij} = \mu r^2 \begin{pmatrix} \cos^2\varphi & \sin\varphi\cos\varphi & 0 \\ \sin\varphi\cos\varphi & \sin^2\varphi & 0 \\ 0 & 0 & 1 \end{pmatrix} = \frac{\mu a^2(1-e^2)^2}{(1+e\cos\varphi)^2} \begin{pmatrix} \cos^2\varphi & \sin\varphi\cos\varphi & 0 \\ \sin\varphi\cos\varphi & \sin^2\varphi & 0 \\ 0 & 0 & 1 \end{pmatrix}, \tag{1.130}$$

where we have used Eq. (1.118) so that this expression only depends on φ. In order to take the temporal derivatives, we can use the expression of $\dot{\varphi}$ from the angular momentum in Eq. (1.122)

$$\dot{\varphi} = \frac{L}{\mu r^2} = \sqrt{\frac{GM}{a^3(1-e^2)^3}}(1+e\cos\varphi)^2, \tag{1.131}$$

where we have used the expressions for L and r in Eqs. (1.126) and (1.118), respectively. Then, the third derivatives of the relevant matrix elements in Eq. (1.130) are

$$\dddot{I}_{11} = 2\mu\sqrt{\frac{G^3M^3}{a^5(1-e^2)^5}}(1+e\cos\varphi)^2[2\sin(2\varphi) + 3e\sin\varphi\cos^2\varphi], \tag{1.132}$$

$$\dddot{I}_{22} = 2\mu\sqrt{\frac{G^3M^3}{a^5(1-e^2)^5}}(1+e\cos\varphi)^2[-2\sin(2\varphi) - e\sin\varphi(1+3\cos^2\varphi)], \tag{1.133}$$

$$\dddot{I}_{12} = 2\mu\sqrt{\frac{G^3M^3}{a^5(1-e^2)^5}}(1+e\cos\varphi)^2[-2\cos(2\varphi) + e\cos\varphi(1-3\cos^2\varphi)]. \tag{1.134}$$

Instead of computing directly $\dddot{Q}_{ij} = \dddot{I}_{ij} - \delta_{ij}\dddot{I}/3$, it is easier to simplify the contraction as

$$\dddot{Q}_{ij}\dddot{Q}_{ij} = \dddot{I}_{ij}\dddot{I}_{ij} - \frac{1}{3}\dddot{I}^2 = \dddot{I}_{11}^2 + \dddot{I}_{22}^2 + 2\dddot{I}_{12}^2 - \frac{1}{3}(\dddot{I}_{11} + \dddot{I}_{22})^2 \tag{1.135}$$

$$= \frac{8G^3}{3}\frac{\mu^2M^3}{a^5(1-e^2)^5}(1+e\cos\varphi)^4[12(1+e\cos\varphi)^2 + e^2\sin^2\varphi]. \tag{1.136}$$

Using this expression in Eq. (1.113), we get to the result

$$P = \frac{8G^4}{15c^5}\frac{\mu^2M^3}{a^5(1-e^2)^5}\langle(1+e\cos\varphi)^4[12(1+e\cos\varphi)^2 + e^2\sin^2\varphi]\rangle. \tag{1.137}$$

We still have to do the time average over several periods, represented by the angle brackets $\langle\ \rangle$. For convenience, we will denote the argument of the average as $P(\varphi)$. Then, the radiated power is

$$P = \frac{1}{T}\int_0^T dt P(\varphi) = \frac{1}{T}\int_0^{2\pi}\frac{d\varphi}{\dot{\varphi}}P(\varphi). \tag{1.138}$$

Having a look at the expression of $\dot{\varphi}$ in Eq. (1.131) and at the period in Eq. (1.129), we can notice that multiplying them gets rid of most of the constants:

$$\dot{\varphi}T = 2\pi\frac{(1+e\cos\varphi)^2}{(1-e^2)^{3/2}}. \tag{1.139}$$

Then, we can substitute this into Eq. (1.138), together with $P(\varphi)$ in Eq. (1.137), to get

$$\begin{aligned} P &= \frac{4G^4}{15\pi c^5}\frac{\mu^2M^3}{a^5(1-e^2)^{7/2}}\int_0^{2\pi} d\varphi\,(1+e\cos\varphi)^2[12(1+e\cos\varphi)^2+e^2\sin^2\varphi] \\ &= \frac{G^4}{15c^5}\frac{\mu^2M^3}{a^5(1-e^2)^{7/2}}(96+292e^2+37e^4). \end{aligned} \tag{1.140}$$

This is the known expression for the radiated power first derived by Peters and Mathews [50], which is usually presented as

$$P = \frac{32G^4\mu^2M^3}{5c^5a^5}f(e), \tag{1.141}$$

where

$$f(e) = \frac{1}{(1-e^2)^{7/2}}\left(1+\frac{73}{24}e^2+\frac{37}{96}e^4\right)\Bigg(\tag{1.142}$$

This function $f(e)$ represents the enhancement due to the eccentricity, given that, for the circular case, $e=0$ implies $f(e)=1$, and Eq. (1.141) can be written changing a to R, representing the constant orbital radius.

1.3.3 Gravitational waves and energy loss

In the previous subsection, we arrived to an expression for the power radiated by a bound two-body system. We will continue this study by computing how this energy loss translates into gravitational waves, as well as how much time it takes the system to merge. Throughout this section, in order to match the notation in Subsec. 1.2.3, we denote the distance from the observer to the CBC (sometimes simply called *source*) by r, which must not be confused with the radial coordinate in Eq. (1.118).

We start by computing the gravitational wave amplitudes. First, from Eq. (1.130) for I_{ij} and using Eq. (1.131) for $\dot{\phi}$ again, we compute the derivatives of the quadrupole momenta,

$$\ddot{I}_{11} = -\frac{2G\mu M}{a(1-e^2)}[\cos(2\varphi)+e\cos^3\varphi], \tag{1.143}$$

$$\ddot{I}_{22} = \frac{2G\mu M}{a(1-e^2)}[\cos(2\varphi)+e\cos\varphi(1+\cos^2\varphi)+e^2], \tag{1.144}$$

$$\ddot{I}_{12} = -\frac{2G\mu M}{a(1-e^2)}[\sin(2\varphi)+e(1+\cos^2\varphi]. \tag{1.145}$$

Then, using Eqs. (1.108) and (1.109),

$$h_+(t) = -\frac{G^2\mu M}{c^4 r a(1-e^2)}(1+\cos^2\theta)\Big\{2\cos(2\varphi-2\phi) + e\left[\frac{\cos\varphi\sin^2\theta}{1+\cos^2\theta}+\frac{1}{2}(5\cos(\varphi-2\phi)+\cos(3\varphi-2\phi)\right] + e^2\left[\cos(2\phi)+\frac{\sin^2\theta}{1+\cos^2\theta}\right]\Big\}, \tag{1.146}$$

$$h_\times(t) = -\frac{G^2\mu M}{c^4 r a(1-e^2)}\cos\theta \quad \Big\{4\sin(2\varphi-2\phi) + e\left[5\sin(\varphi-2\phi)+\sin(3\varphi-2\phi)\right] - 2e^2\sin(2\phi)\Big\}, \tag{1.147}$$

where we must recall that the right-hand side quantities should be evaluated in the retarded time t_r in Eq. (1.85).

From now on, we will focus on the circular case, $e = 1$, due to the complexity of the equations. For more details on the elliptic case, see [51, 39]. In General Relativity, due to the energy loss, the radius of the trajectory R gets progressively smaller, so these trajectories receive the name of *quasi-circular orbits*. Furthermore, BBHs tend to reduce their eccentricity over time, in a phenomenon called *circularization* [51, 39]. Therefore, quasi-circular orbits are expected to be much more common than eccentric ones, so we are not losing much generality. In this case, the previous expressions greatly simplify:

$$h_+(t) = -\frac{4G^2\mu M}{c^4 r R}\frac{1+\cos^2\theta}{2}\cos(2\varphi-2\phi), \tag{1.148}$$

$$h_\times(t) = -\frac{4G^2\mu M}{c^4 r R}\cos\theta\sin(2\varphi-2\phi). \tag{1.149}$$

Furthermore, in the quasi-circular case, to first order, the trajectory can be parametrized as $\varphi(t) = \omega_0 t$, with ω_0 the angular frequency corresponding to the period in Eq. (1.129) for $a = T$,

$$\omega_0 = \frac{2\pi}{T} = \sqrt{\frac{GM}{R^3}}. \tag{1.150}$$

The angular frequency of the gravitational wave, however, doubles this number, given that it is 2φ what appears in the argument of the trigonometric functions. Thus, we define the gravitational wave frequency as

$$\omega_{\rm gw} = 2\omega_0 \quad \text{and, correspondingly,} \quad f_{\rm gw} = 2f_0 = \frac{\omega_0}{\pi}. \tag{1.151}$$

Particularly useful are the expressions relating $f_{\rm gw}$ and R,

$$\pi f_{\rm gw} = \sqrt{\frac{GM}{R^3}}, \quad R = \left(\frac{GM}{\pi^2 f_{\rm gw}^2}\right)^{1/3}, \tag{1.152}$$

where the last expression is particularly useful to get rid of R in favour of $f_{\rm gw}$. This is precisely what we do in Eqs. (1.148) and (1.149). Moreover, we can choose the initial setting of the system

to be at phase π, so that the corresponding trigonometric functions change sign and we can get rid of the global minus sign. With these changes, Eqs. (1.148) and (1.149) are now

$$h_+(t) = \frac{4\mu}{r}\left(\frac{G}{c^2}\right)^{5/3}\left(\frac{M\pi f_{\rm gw}}{c}\right)^{2/3}\frac{1+\cos^2\theta}{2}\cos(2\pi f_{\rm gw}t_r - 2\phi), \tag{1.153}$$

$$h_\times(t) = \frac{4\mu}{r}\left(\frac{G}{c^2}\right)^{5/3}\left(\frac{M\pi f_{\rm gw}}{c}\right)^{2/3}\cos\theta\sin(2\pi f_{\rm gw}t_r - 2\phi). \tag{1.154}$$

The amplitude dependence on the mass here is very important: if a gravitational wave is observed with a certain frequency $f_{\rm gw}$ at a certain distance r, from its amplitude we can derive a mass-related quantity. So that it has units of mass, this quantity, called *chirp mass*, is defined as

$$M_c = \mu^{3/5}M^{2/5} = \frac{m_1^{3/5}m_2^{3/5}}{(m_1+m_2)^{1/5}}, \tag{1.155}$$

so that the previous equations can be rewritten as

$$h_+(t) = \frac{4}{r}\left(\frac{GM_c}{c^2}\right)^{5/3}\left(\frac{\pi f_{\rm gw}}{c}\right)^{2/3}\frac{1+\cos^2\theta}{2}\cos(2\pi f_{\rm gw}t_r - 2\phi), \tag{1.156}$$

$$h_\times(t) = \frac{4}{r}\left(\frac{GM_c}{c^2}\right)^{5/3}\left(\frac{\pi f_{\rm gw}}{c}\right)^{2/3}\cos\theta\sin(2\pi f_{\rm gw}t_r - 2\phi). \tag{1.157}$$

In a typical case, we will not know the distance r at which this event was produced. Thus, the chirp mass will be degenerate with the distance.

Then, from Eq. (1.77), we can compute the radiated power per unit angle as

$$\frac{dP}{d^2\Omega} = \frac{c^3r^2}{16\pi G}\langle\dot{h}_+^2 + \dot{h}_\times^2\rangle, \tag{1.158}$$

so that, substituting Eqs. (1.156) and (1.157), we get

$$\frac{dP}{d^2\Omega} = \frac{2c^5}{\pi G}\left(\frac{GM_c\pi f_{\rm gw}}{c^3}\right)^{10/3}g(\theta), \tag{1.159}$$

with

$$g(\theta) = \left(\frac{1+\cos^2\theta}{2}\right)^2 + \cos^2\theta. \tag{1.160}$$

Integrating over the solid angle,

$$\int d^2\Omega g(\theta) = \frac{16\pi}{5}, \tag{1.161}$$

so that

$$P = \frac{32c^5}{5G}\left(\frac{GM_c\pi f_{\rm gw}}{c^3}\right)^{10/3}. \tag{1.162}$$

Using the definition of $f_{\rm gw}$, it is easy to check that this expression matches the one obtained for the elliptic case in Eq. (1.141) for $e = 1$.

Now, from Eq. (1.126), we have that the energy of the system is

$$E = -\frac{1}{2}\left(G^2 M_c^5 \pi^2 f_{\rm gw}^2\right)^{1/3}. \tag{1.163}$$

To first order, its negative (energy loss) time derivative is given by the radiated power in Eq. (1.162). Making both expressions equal,

$$\frac{\dot{f}_{\rm gw}}{3}\left(\frac{G^2 M_c^5 \pi^2}{f_{\rm gw}}\right)^{1/3} = \frac{32c^5}{5G}\left(\frac{GM_c \pi f_{\rm gw}}{c^3}\right)^{10/3}, \tag{1.164}$$

we can find an expression for the frequency time variation to first order,

$$\dot{f}_{\rm gw} = \frac{96}{5}\pi^{8/3}\left(\frac{GM_c}{c^3}\right)^{5/3} f_{\rm gw}^{11/3}. \tag{1.165}$$

Integrating, its solution is given by

$$f_{\rm gw}(t) = \left(\frac{5}{256}\frac{1}{C-t}\right)^{3/8}\left(\frac{GM_c}{c^3}\right)^{-5/8}, \tag{1.166}$$

with C an arbitrary function. Analyzing this expression, we can see it has a divergence precisely at time $t = C$. Physically speaking, the fact that the frequency $f_{\rm gw}$ is inversely proportional to a power of the orbital radius, $f_{\rm gw} \propto R^{-3/2}$ (Eq. (1.152)) means that, as time passes, the frequency gets higher as the orbital radius gets smaller. Therefore, the instant at which $f_{\rm gw} \to \infty$ corresponds to $R \to 0$. Thus, we denote this time by $t_{\rm coal}$, the time of coalescence, or merger. To be precise, both times should be the corresponding retarded times but, given the definition in Eq. (1.85) and the fact that the distance to the source is assumed to be the same at both times, then $t_{\rm coal,r} - t_r = t_{\rm coal} - t$. If we denote $\tau \equiv t_{\rm coal} - t$, which is the time to coalescence, we can express the previous equation as

$$f_{\rm gw}(\tau) = \frac{1}{\pi}\left(\frac{5}{256}\frac{1}{\tau}\right)^{3/8}\left(\frac{GM_c}{c^3}\right)^{-5/8}. \tag{1.167}$$

In an observational context, this means that, if we are able to detect a gravitational wave of a certain frequency and somehow determine its distance (so that the chirp mass is not degenerate with it), we can compute the time to coalescence as

$$\tau = \frac{5}{256}\left(\frac{GM_c}{c^3}\right)^{-5/3}(\pi f_{\rm gw})^{-8/3}. \tag{1.168}$$

We can express this equation in terms of more practical units. Using $c = 2.998 \times 10^5$ km/s and $2GM_\odot/c^2 = 2.95$ km, we get

$$\tau \approx 82 \text{ ms}\left(\frac{8.71M_\odot}{M_c}\right)^{5/3}\left(\frac{100 \text{ Hz}}{f_{\rm gw}}\right)^{8/3}, \tag{1.169}$$

where a chirp mass of $8.71M_\odot$ corresponds to two equal masses of $10M_\odot$. Of course, in a real event, we will not observe a divergence at this point. What happens is that our approximation to first order is not valid anymore, entering in a regime of strong gravity in which, first, post-Newtonian

approximations to higher orders have to be used and, later, even these approximations fail and one has to resort to Numerical Relativity. We will see more on NR in Chapter 6.

As a result of the changes in frequency, the waveforms in Eqs. (1.156) and (1.157) will vary over time. Assuming a null global phase at the initial moment for simplicity, we can compute the new phase as an integral over time,

$$\Phi(t) = \int_0^t dt' \omega_{\rm gw}(t'), \tag{1.170}$$

which coincides with the Keplerian case for a constant $\omega_{\rm gw}$. Using Eq. (1.167), we get that

$$\Phi(\tau) = -2\left(\frac{5}{256}\right)^{3/8}\left(\frac{GM_c}{c^3}\right)^{-5/8}\frac{8\tau^{5/8}}{5} + \Phi_0 = -2\left(\frac{5GM_c}{c^3}\right)^{-5/8}\tau^{5/8} + \Phi_0, \tag{1.171}$$

where the minus sign comes from the definition $\tau = t_{\rm coal} - t$ and $\Phi_0 = \Phi(\tau = 0)$ is the phase corresponding to the instant of coalescence. We cannot set it Φ_0 to zero since we already imposed $\Phi(t = 0) = 0$. Substituting this $\Phi(\tau)$ in Eqs. (1.156) and (1.157) as well as $f_{\rm gw}(\tau)$ from Eq. (1.167), we get

$$h_+(t) = \frac{1}{r}\left(\frac{GM_c}{c^2}\right)^{5/4}\left(\frac{5}{c\tau}\right)^{1/4}\frac{1+\cos^2\theta}{2}\cos\left[-2\left(\frac{c^3\tau}{5GM_c}\right)^{5/8} + \Phi_0\right] \tag{1.172}$$

$$h_\times(t) = \frac{1}{r}\left(\frac{GM_c}{c^2}\right)^{5/4}\left(\frac{5}{c\tau}\right)^{1/4}\cos\theta\sin\left[-2\left(\frac{c^3\tau}{5GM_c}\right)^{5/8} + \Phi_0\right]. \tag{1.173}$$

1.3.4 Energy spectrum

To finish this section, we are interested in the energy spectrum in frequency for the circular orbits. This is a key quantity to compute the stochastic gravitational wave background from astrophysical events. In Chapter 2, we will see the main formalism for SGWBs and, in Chapter 5, we will compute the contribution from these CBCs, as well as from hyperbolic encounters (see Sec. 1.4).

Stationary phase integration

In order to get the energy spectrum, we first need the Fourier transforms of Eqs. (1.172) and (1.173). We follow a similar procedure to the one in Maggiore's book [39], which is based on an integration technique called *stationary phase integration* [52]. The main idea is that, if we have an integral like

$$I(f) = \int_{-\infty}^{\infty} dt A(t) e^{i[2\pi f t - \Phi(t)]}, \tag{1.174}$$

then, the main contribution to the integral will be given by the point(s) that make the first derivative of the phase $\phi(t) = 2\pi f t - \Phi(t)$ vanish. We call these points *stationary points*.

Otherwise, in a certain point t_1 such that $\dot{\phi}(t_1) \neq 0$, the first order in the Taylor expansion will dominate the time evolution, $\phi(t) \approx \phi(t_1) + \dot{\phi}(t_1)(t - t_1)$ and the integral will be dominated by the oscillatory behavior of a factor of the form e^{ikt} for a certain constant k. The integral will then

rapidly oscillate, with a higher frequency as it goes away from a stationary point, so that, if $\ln A(t)$ varies slower than the phase, the contributions from $2\pi ft - \Phi(t) \in [2n\pi, (2n+1)\pi]$ will (at least partially) compensate the ones from $2\pi ft - \Phi(t) \in [(2n+1)\pi, (2n+2)\pi]$. This oscillatory behavior is the reason why the Fourier transform of 1, given by the Cauchy principal value or the integral of $e^{-2\pi ift}$ over the real numbers for t, is $\delta(f)$, which is zero for all frequencies except for the one ($f = 0$) that makes the exponential non-oscillatory.

For simplicity, we will assume there is just one stationary point, which we denote by t_*. We can then Taylor-expand the exponential phase around t_* up to order $(t - t_*)^2$, thus neglecting the contributions to third order. The third-order contributions and beyond only start to be relevant far away from t_*, for which we assume that the oscillatory suppression already dominates, so we can safely ignore them. Thus,

$$\phi(t) \approx 2\pi ft_* - \Phi(t_*) - \frac{1}{2}\ddot{\Phi}(t_*)(t - t_*)^2. \tag{1.175}$$

Assuming that the function $\log A(t)$ varies slower than $\phi(t)$ around t_*, we can approximate the integral as

$$I(f) \approx A(t_*)e^{i[2\pi ft_* - \Phi(t_*)]} \int_{-\infty}^{\infty} dt e^{-\frac{1}{2}i\ddot{\Phi}(t_*)(t-t_*)^2}. \tag{1.176}$$

We can now use

$$\int_{-\infty}^{\infty} dx e^{-x^2} = \sqrt{\pi} \quad \Rightarrow \quad \int_{-\infty}^{\infty} dt e^{-\frac{1}{2}i\ddot{\Phi}(t_*)(t-t_*)^2} = \sqrt{\frac{2\pi}{i\ddot{\Phi}(t_*)}} = \sqrt{\frac{2\pi}{\ddot{\Phi}(t_*)}} e^{-i\pi/4}, \tag{1.177}$$

so that our integral is

$$I(f) \approx A(t_*)\sqrt{\frac{2\pi}{\ddot{\Phi}(t_*)}} e^{i[2\pi ft_* - \Phi(t_*) - \pi/4]}. \tag{1.178}$$

Fourier transform of polarization amplitudes

Using the stationary phase integration method described above, we will compute the Fourier transform of h_+ and $h_\times$ in Eqs. (1.172) and (1.173). Following our criterion in Subsec. 1.1.4 (Eq. (1.38)), we will only consider positive frequencies. Starting by h_+, its Fourier transform is given by

$$\begin{aligned}\tilde{h}_+(f) &= \int_{-\infty}^{\infty} dt\, h_+(t) e^{2\pi ift} \\ &= \int_{-\infty}^{\infty} dt\, \frac{1}{r}\left(\frac{GM_c}{c^2}\right)^{5/4} \left(\frac{5}{c(t_{\rm coal,r} - t_r)}\right)^{1/4} \frac{1 + \cos^2\theta}{2} \cos\Phi(t_r) e^{2\pi ift},\end{aligned} \tag{1.179}$$

with Φ defined in Eq. (1.170), so that $\dot{\Phi}(t_r) = \omega_{\rm gw}(t_r)$. In this equation, the distinction between t and t_r is now important. In previous equations, given that $h_+(t)$ only depends on the difference $\tau = t_{\rm coal,r} - t_r = t_{\rm coal,r} - t_r$, we could use either t or t_r indistinctly as long as the coalescence time was the corresponding non-retarded or retarded version. Now, however, the integrand has an extra factor dependent on t, to which this simplification cannot be applied. Additionally, the integral range should not be the full real numbers, but there should be a cutoff at the time of coalescence.

Otherwise, the integrand will diverge. However, due to the integration method we will use, which approximates the integral by an expression in terms of local quantities, this will not be a problem.

For simplicity, we define

$$A(t_r) = \frac{1}{r}\left(\frac{GM_c}{c^2}\right)^{5/4}\left(\frac{5}{c(t_{\rm coal,r}-t_r)}\right)^{1/4}\frac{1+\cos^2\theta}{2}, \tag{1.180}$$

so that Eq. (1.179) can be rewritten as

$$\tilde{h}_+(f) = e^{2\pi i f r/c}\int_{-\infty}^{\infty} dt_r\, A(t_r)\cos\Phi(t_r)e^{2\pi i f t_r}, \tag{1.181}$$

where the extra factor $e^{2\pi i f r/c}$ compensates the $e^{2\pi i f r/c}$ factor inside the integral that has been reabsorbed to express the exponential in terms of t_r. Now that everything is expressed in terms of t_r, we drop the index to simplify the equations, but we should keep in mind that the t from now on has to be understood as a t_r, until we finish the integration and recover the notation. Thus, we can write Eq. (1.181) as

$$\tilde{h}_+(f) = \frac{1}{2}e^{2\pi i f r/c}\int_{-\infty}^{\infty} dt A(t)\left[e^{i\Phi(t)}+e^{-i\Phi(t)}\right]e^{2\pi i f t}, \tag{1.182}$$

where we have expressed the cosine as a sum of imaginary exponentials. Of these two terms, the first one has a phase without stationary points: since $\dot{\Phi}(t) = \omega_{\rm gw}(t) > 0$ and we are considering only positive frequencies, then the time derivative of this phase is $\omega_{\rm gw}(t)+2\pi f$, which is positive for all times. Thus, this term will rapidly oscillate and can be neglected over the second one, which will have stationary points that dominate the integral. This second term has a phase with stationary point t_* such that

$$\omega_{\rm gw}(t_*) = 2\pi f. \tag{1.183}$$

We also have that $\ln A(t)$ varies slower than the phase, given that it is a power law of exponent $-1/4$, so we are under the conditions to apply Eq. (1.178). Accounting for the extra factor $e^{2\pi i f r/c}/2$, we get

$$\tilde{h}_+(f) \approx \frac{1}{2}A(t_*)\sqrt{\frac{2\pi}{\ddot{\Phi}(t_*)}}e^{i[2\pi f(t_*+r/c)-\Phi(t_*)-\pi/4]}. \tag{1.184}$$

At this point, we can get back to the discussion on the subscript for t_r. Both A and Φ only depend on τ, so we can work with this variable regardless of whether it is defined with both the usual and coalescence time in their retarded forms or not. The only place where this distinction matters is in the phase, where t_* should be interpreted as retarded. Moreover, we can get rid of this quantity in favour of f using Eq. (1.183). For this purpose, we can use the expression for $f_{\rm gw}(t)$ in Eq. (1.167), so that

$$f = \frac{1}{\pi}\left(\frac{5}{256}\frac{1}{\tau_*}\right)^{3/8}\left(\frac{GM_c}{c^3}\right)^{-5/8} \quad\Rightarrow\quad \tau_* = \frac{5}{256}\left(\frac{GM_c}{c^3}\right)^{-5/3}(\pi f)^{-8/3}, \tag{1.185}$$

where t_* is computed as $t_{\rm coal,r}-\tau_*$, given that it refers to a retarded time. Conveniently, the extra factor $-r/c$ in $t_{\rm coal,r}$ will cancel out with the $+r/c$ of the phase shown in Eq. (1.184), so the final expression will not depend on any retarded quantity. For $\Phi(t_*)$, we use that it is the integral

with respect to t of $\omega_{\rm gw}$ as shown in Eq. (1.170). Since $\omega_{\rm gw} \propto \tau^{-3/8}$ and we already defined the integration constant as Φ_0, we have

$$\Phi(t_*) = -\frac{8}{5} 2\pi f \tau_* + \Phi_0 = -2\pi f \frac{1}{32} \left(\frac{GM_c}{c^3}\right)^{-5/3} (\pi f)^{-8/3} + \Phi_0, \tag{1.186}$$

which, aside from the global phase Φ_0, is identical to the term coming from $2\pi f t_*$ but with a different numerical factor. As a result, the final phase in Eq. (1.184) is

$$\Psi_+(f) = 2\pi f t_{\rm coal} - \Phi_0 - \frac{\pi}{4} + \frac{3}{128} \left(\frac{GM_c}{c^3}\pi f\right)^{-5/3}. \tag{1.187}$$

To compute $\ddot{\Phi}(t_*)$, we can use that it is the derivative with respect to t of $\omega_{\rm gw}$ and, again, that $\omega_{\rm gw} \propto \tau^{-3/8}$, so that

$$\begin{aligned} \ddot{\Phi}(t_*) &= \frac{3}{8}\frac{2\pi f}{\tau_*} = 2\pi f \frac{96}{5} \left(\frac{GM_c}{c^3}\right)^{5/3} (\pi f)^{8/3} \\ \Rightarrow \quad \sqrt{\frac{2\pi}{\ddot{\Phi}(t_*)}} &= \sqrt{\frac{5}{96}} \left(\frac{GM_c}{c^3}\right)^{-5/6} \pi^{-4/3} f^{-11/6}, \end{aligned} \tag{1.188}$$

while for $A(t_*)$, we can simply substitute τ_* in Eq. (1.185) into the expression for $A(t_r)$ in Eq. (1.180):

$$A(t_*) = \frac{4c}{r} \left(\frac{GM_c}{c^3}\right)^{5/3} (\pi f)^{2/3} \frac{1+\cos^2\theta}{2}. \tag{1.189}$$

Multiplying the two last equations by $1/2$, we get the amplitude in Eq. (1.184),

$$\frac{1}{\pi^{2/3}} \sqrt{\frac{5}{24}} \frac{c}{r} \left(\frac{GM_c}{c^3}\right)^{5/6} \frac{1+\cos^2\theta}{2}. \tag{1.190}$$

Then, the Fourier transform of the plus polarization is finally

$$\tilde{h}_+(f) = \frac{1}{\pi^{2/3}} \sqrt{\frac{5}{24}} \frac{c}{r} \left(\frac{GM_c}{c^3}\right)^{5/6} \frac{1+\cos^2\theta}{2} \frac{e^{i\Psi_+(f)}}{f^{7/6}}, \tag{1.191}$$

with the phase Ψ_+ defined in Eq. (1.187).

Similarly, one can go through the same procedure to find $\tilde{h}_\times$. Aside from the different factors in the definition of $A(t_r)$ coming from the different prefactors in Eqs. (1.172) and (1.173), the main difference is that the trigonometric function dependent on Φ is now a sine instead of a cosine. Thus, at the step (1.182), the negative exponential term, which is the only relevant one, would have an extra $-1/i = i = e^{i\pi/2}$ factor. This translates into an additional global phase $\pi/2$, but the rest of the computation is identical. Thus, we would get to the equation

$$\tilde{h}_\times(f) = \frac{1}{\pi^{2/3}} \sqrt{\frac{5}{24}} \frac{c}{r} \left(\frac{GM_c}{c^3}\right)^{5/6} \cos\theta \frac{e^{i\Psi_\times(f)}}{f^{7/6}}, \tag{1.192}$$

with $\Psi_\times = \Psi_+ + \pi/2$, that is,

$$\Psi_\times(f) = 2\pi f t_{\rm coal,r} - \Phi_0 + \frac{\pi}{4} + \frac{3}{128} \left(\frac{GM_c}{c^3}\pi f\right)^{-5/3}. \tag{1.193}$$

Computation of energy spectrum

Having computed the polarization amplitudes (1.191) and (1.192), we can use Eq. (1.83) to get

$$\frac{dE}{df d^2\Omega} = \frac{5}{48}\frac{1}{\pi^{1/3}G}\left(GM_c\right)^{5/3} f^{-1/3} g(\theta), \tag{1.194}$$

with the same $g(\theta)$ as the one defined in Eq. (1.160). Using that its integral over the solid angle is $16\pi/5$, as stated in Eq. (1.161), then the energy spectrum is finally

$$\frac{dE}{df} = \frac{\pi^{2/3}}{3G}\left(GM_c\right)^{5/3} f^{-1/3}, \tag{1.195}$$

which is more commonly used as the energy derivative per logarithmic frequency bin,

$$\frac{dE}{d(\ln f)} = \frac{\pi^{2/3}}{3G}\left(GM_c\right)^{5/3} f^{2/3}. \tag{1.196}$$

The reason to use the frequency logarithm is that it is more natural when discussing in terms of different orders of magnitude. Furthermore, $\ln f$ is a dimensionless quantity, so the spectrum per logarithmic frequency bin has units of energy. In addition, it will also appear in this form when computing the SGWB from CBCs and hyperbolic encounters, as we will see in Chapter 5.

Before finishing this section, we should recall that these equations are only valid as a first approach. We have been using Keplerian expressions for the relations between the orbital parameters, masses, etc., and computed the quadrupole radiated power using them but, in General Relativity, this radiated energy would have an impact on the spacetime geometry, which would, in turn, alter the GW energy again. This kind of effect is usually called *backreaction*. To be precise, one would have to take into account the variation of the orbital parameters with time, which is linked to the energy loss. This inter-dependence makes this problem difficult to treat, so that post-Newtonian approximations or Numerical Relativity have to be used. Nevertheless, when both masses are still far from merging, this first-approach approximation is usually precise enough. The problem arises close to the merger and, of course, during it and the ringdown.

In the next section, we will study what happens when the two bodies are not bound, but they have enough energy to escape from each other.

1.4 Hyperbolic encounters

In the Keplerian regime, it is known that the two-body problem describes a conical curve trajectory, which can either be an ellipse ($e < 1$, circumference if $e = 0$) if both masses are bound, as studied in the previous section, or a hyperbola ($e > 1$) if their kinetic energy is enough to overcome the gravitational pull. Between both cases, there is the parabolic limit for which $e = 1$, but this is more a theoretical limit than a practical case.

The gravitational wave theory is better developed for the elliptic case given its practical application: because their interaction is strong during a lot of orbits, the integrated sensitivity over time for this events is much larger. A hyperbolic interaction generates an energy burst when both masses

are closest to each other, but it disappears shortly after. In addition, the merger between two black holes or neutron stars generates a tremendous amount of energy, which is not really comparable to the one that they can release due to a hyperbolic interaction.

Thus, it is no wonder that elliptic orbits, particularly CBCs, attract the main attention of scientists. Nevertheless, hyperbolic encounters should also be there and, when they are close enough (*close hyperbolic encounters*, CHEs), produce a non-negligible amount of energy, which should be detectable with either current or future detectors depending on the specifics of the black hole and neutron star populations. Over the last years, the number of articles on hyperbolic encounters has increased [53, 54, 55, 56, 57, 58, 59, 60, 61, 62, 63, 64], a growth we contributed to with our articles [1, 2]. It is therefore useful to make the analogous computations to the elliptic/circular case.

1.4.1 Keplerian dynamics

Again, we start by recalling the relevant equations of the hyperbolic motion within the Newtonian regime. As we can see in Fig. 1.5, the semi-major axis a represents the distance from the center of the hyperbola to its vertex, similar to the elliptic case. As in the elliptic case, c is the distance from the center to the focus and its ratio with a is the eccentricity,

$$e = \frac{c}{a}. \tag{1.197}$$

One can also define a "semi-minor axis" b which, as we can see in Fig. 1.5, it is related to a and e as

$$b^2 = c^2 - a^2 \quad \Rightarrow \quad b = a\sqrt{e^2 - 1} \tag{1.198}$$

similarly to Eq. (1.115). This parameter measures the distance from the focus to the asymptote. In Physics, this is a relevant quantity in any scattering problem and it is more commonly referred to as *impact parameter*. As a particle tends to go towards $t \to \infty$, the impact parameter represents the projection of the vector radius over the orthogonal axis to its velocity. Therefore, the angular momentum can be expressed as

$$L = \mu b v_\infty, \tag{1.199}$$

with v_∞ the limit of the particle speed at an infinite time.

Similarly to Eq. (1.118), the orbital radius is now given by

$$r = \frac{a(e^2 - 1)}{1 + e\cos\varphi}, \tag{1.200}$$

where the denominator is now only defined for $1 + e\cos\varphi > 0$ (or < 0, but not both due to the discontinuity at 0), so that

$$\varphi \in (-\varphi_0, \varphi_0), \quad \varphi \equiv \arccos\left(-\frac{1}{e}\right)\Bigg(\tag{1.201}$$

where we take the arccosine image to range from 0 to π. This angle φ_0 is also shown in Fig. 1.5. In Physics, most references [54, 65, 66, 67, 68] take a rotated reference system with an angle φ_0,

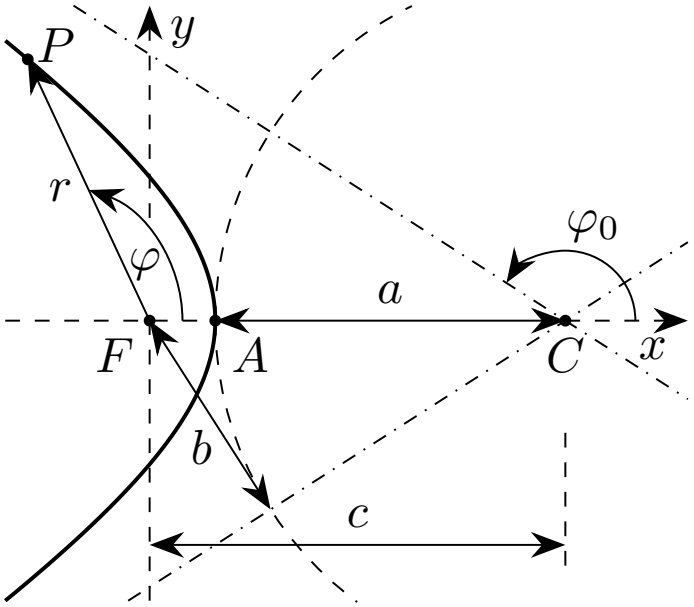

Figure 1.5: Left branch of a hyperbola with its relevant points, distances and angles. C indicates the center of the hyperbola, A is the branch vertex and F its focus, which is taken as the origin of the coordinate system. P indicates a generic point in the left branch with radial coordinate r and phase φ. The semimajor axis a is also shown, representing the distance from the center to the vertex, as well as the distance c from the center to the focus. The dash-dotted lines represent the asymptotes of the hyperbola, while φ_0 is the angle they form with the major axis. Finally, the impact parameter b indicates the distance from the focus to the asymptotes.

so that one of the asymptote is at the x axis, showing that the particle originally has a horizontal velocity, which is then bent due to the interaction. Nevertheless, I decided to keep this orientation, more standard in Mathematics, due to its better analogy with the elliptic case and the better explainability of its geometrical elements.

The periapsis is given by the value that maximizes the denominator, which is $\varphi = 0$, so that

$$r_p = a(e-1), \tag{1.202}$$

while there is no apoapsis, since the distance can be arbitrarily large since the denominator can be arbitrarily close to zero.

We now turn our attention to speeds. We denote v_0 the speed at the periapsis. On the one hand, the angular momentum at infinity is given by $\mu b v_\infty$ (Eq. (1.199)) and, for the one at the periapsis, the speed and vector radius are orthogonal. The fact that both are equal indicates

$$bv_\infty = a(e-1)v_0 \quad \Rightarrow v_0 = \sqrt{\frac{e+1}{e-1}}v_\infty, \tag{1.203}$$

where we have used the equation for the periapsis radius in Eq. (1.202) and the expression of b from a and e in Eq. (1.198).

On the other hand, the gravitational energy vanishes at infinity. Making the energies at infinity and at the periapsis equal, we get

$$\frac{1}{2}v_\infty^2 = \frac{1}{2}v_0^2 - \frac{GM}{a(e-1)} \quad \Rightarrow \quad \left(\frac{e+1}{e-1} - 1\right)v_\infty^2 = \frac{2GM}{a(e-1)} \quad \Rightarrow \quad v_\infty^2 = \frac{GM}{a}, \tag{1.204}$$

so the velocities at infinity and the periapsis are, respectively,

$$v_\infty = \sqrt{\frac{GM}{a}}, \quad v_0 = \sqrt{\frac{e+1}{e-1}\frac{GM}{a}}. \tag{1.205}$$

Then, the angular momentum and energy can be computed as

$$L = \mu b\sqrt{\frac{GM}{a}} = \mu\sqrt{GMa(e^2-1)}, \quad E = \frac{GM}{2a}. \tag{1.206}$$

From the expression of the energy (which is positive, unlike in the elliptic case), we can again compute an expression for the velocity (vis-viva equation) using the fact that it is a conserved quantity,

$$v^2 = GM\left(\frac{2}{r} + \frac{1}{a}\right) \tag{1.207}$$

As we can see, most of the expressions are essentially equal to the elliptic ones, only that with $a \mapsto -a$. In practice, this can better be noticed in that all the factors $1-e$ which appeared before in the elliptic case now appear as $e-1$, being positive in either of the cases.

1.4.2 Radiated power

The radiated power can be obtained very similarly to the elliptic case. First, the quadrupole moment is

$$I_{ij} = \mu r^2 \begin{pmatrix} \cos^2\varphi & \sin\varphi\cos\varphi & 0 \\ \sin\varphi\cos\varphi & \sin^2\varphi & 0 \\ 0 & 0 & 1 \end{pmatrix} = \frac{\mu a^2(e^2-1)^2}{(1+e\cos\varphi)^2} \begin{pmatrix} \cos^2\varphi & \sin\varphi\cos\varphi & 0 \\ \sin\varphi\cos\varphi & \sin^2\varphi & 0 \\ 0 & 0 & 1 \end{pmatrix} \tag{1.208}$$

which is very similar to the elliptic one, Eq. (1.130), but with $1-e \mapsto e-1$. From the conservation of angular momentum, we can also get an expression for $\dot{\varphi}$ similar to (1.131),

$$\dot{\varphi} = \frac{L}{\mu r^2} = \sqrt{\frac{GM}{a^3(e^2-1)^3}}(1+e\cos\varphi)^2. \tag{1.209}$$

We need this expression to compute the third derivative of the quadrupole moment in Eq. (1.208), which are

$$\dddot{I}_{11} = 2\mu\sqrt{\frac{G^3M^3}{a^5(e^2-1)^5}}(1+e\cos\varphi)^2[2\sin(2\varphi) + 3e\sin\varphi\cos^2\varphi], \tag{1.210}$$

$$\dddot{I}_{22} = 2\mu\sqrt{\frac{G^3M^3}{a^5(e^2-1)^5}}(1+e\cos\varphi)^2[-2\sin(2\varphi) - e\sin\varphi(1+3\cos^2\varphi)], \tag{1.211}$$

$$\dddot{I}_{12} = 2\mu\sqrt{\frac{G^3M^3}{a^5(e^2-1)^5}}(1+e\cos\varphi)^2[-2\cos(2\varphi) + e\cos\varphi(1-3\cos^2\varphi)]. \tag{1.212}$$

Using the expression for $\dddot{Q}_{ij}\dddot{Q}_{ij}$ in terms of $\dddot{I}_{ij}$ in Eq. (1.135), we get

$$\begin{aligned}\dddot{Q}_{ij}\dddot{Q}_{ij} &= \dddot{I}_{ij}\dddot{I}_{ij} - \frac{1}{3}\dddot{I}^2 = \dddot{I}_{11}^2 + \dddot{I}_{22}^2 + 2\dddot{I}_{12}^2 - \frac{1}{3}(\dddot{I}_{11} + \dddot{I}_{22})^2 \\ &= \frac{8G^3}{3}\frac{\mu^2 M^3}{a^5(e^2-1)^5}(1+e\cos\varphi)^4[12(1+e\cos\varphi)^2 + e^2\sin^2\varphi],\end{aligned} \tag{1.213}$$

so that, substituting this expression in Eq. (1.113), we get to the result

$$P(\varphi) = \frac{8G^4}{15c^5}\frac{\mu^2 M^3}{a^5(e^2-1)^5}(1+e\cos\varphi)^4[12(1+e\cos\varphi)^2 + e^2\sin^2\varphi], \tag{1.214}$$

which exactly matches the one for the elliptic case in Eq. (1.137) except for the mentioned change in eccentricity. With the corresponding variable changes, it also matches other expressions in the literature [66], also when shown as functions of φ_0 [67, 68].

Finally, in the elliptic case, we computed the power averaged in a period. In a hyperbolic orbit, there is no periodicity, so what we can do instead is computing the energy loss in the full orbit. For this purpose, we have to integrate over time or, equivalently, over φ if we divide by $\dot{\varphi}$ in Eq. (1.209), using the chain rule. In this case, the integral range goes from $\varphi \to -\varphi_0$ to $\varphi \to \varphi_0$, corresponding to the past and future infinity, respectively, as explained in the previous subsection. We will denote $\varphi_0 = \arccos(-1/e)$ Thus,

$$\begin{aligned}\Delta E &= \int_{-\infty}^{\infty} dt P(\varphi) = \int_{-\varphi_0}^{\varphi_0}\frac{d\varphi}{\dot{\varphi}}P(\varphi) \\ &= \frac{8G^{7/2}}{15c^5}\frac{\mu^2 M^{5/2}}{a^{7/2}(e^2-1)^{7/2}}\int_{-\varphi_0}^{\varphi_0} d\varphi\,(1+e\cos\varphi)^2[12(1+e\cos\varphi)^2 + e^2\sin^2\varphi].\end{aligned} \tag{1.215}$$

Solving this integral yields the result

$$\Delta E = \frac{2G^{7/2}}{45c^5}\frac{\mu^2 M^{5/2}}{a^{7/2}(e^2-1)^{7/2}}\left[\sqrt{e^2-1}(602+673e^2) + 3(96+292e^2+37e^4)\phi_0\right]\left(\tag{1.216}$$

where the second term matches the expression for the elliptic case (1.141) except for the mentioned changes in the eccentricity and the presence of ϕ_0. Using the relation between r_p and a in Eq. (1.202), this expression is usually presented in the literature [54, 69, 68, 2] as

$$\Delta E = \frac{8G^{7/2}}{15c^5}\frac{m_1^2 m_2^2 M^{1/2}}{r_p^{7/2}}f(e) \tag{1.217}$$

with

$$f(e) = \frac{1}{(e+1)^{7/2}}\left[24\arccos\left(-\frac{1}{e}\right)\left(1+\frac{73}{24}e^2+\frac{37}{96}e^4\right) + \sqrt{e^2-1}\left(\frac{301}{6}+\frac{673}{12}e^2\right)\right], \tag{1.218}$$

which also matches similar expressions in the literature as functions of φ_0 [68, 67].

We will use this equation later in Chapter 5. In this chapter, we compute the stochastic gravitational wave backgrounds that these hyperbolic encounters produce under certain hypotheses. In the next section, these stochastic gravitational wave backgrounds will be introduced.

In order to compute the gravitational wave backgrounds from hyperbolic encounters, as in the circular case, we also need their energy spectrum, similar to Eq. (1.196) but for a hyperbolic trajectory. The computation in that case was somewhat tedious despite being in the simplified case of circular motion. In the elliptic case or, in this case, the hyperbolic, the computation is even harder, so we just indicate the equation here and refer to [54, 68] for the derivation. Expressed as in our article [2],

$$\frac{dE}{d(\ln f)} = \nu \frac{dE}{d\nu} = \frac{4\pi}{45} \frac{G^3 m_1^2 m_2^2}{a^2 c^5 \nu_0} \nu^5 F_e(\nu)\,, \tag{1.219}$$

with $\nu = 2\pi\nu_0 f$, ν_0 being a constant that makes ν dimensionless,

$$\nu_0 = \sqrt{\frac{a^3}{GM}}, \tag{1.220}$$

and with $F_e(\nu)$ a function of frequency and eccentricity that can be approximated at low eccentricities as [54]

$$\begin{aligned} \nu^5 F_e(\nu) &\simeq \frac{12 F(\nu)}{\pi\, y\, (1+y^2)^2}\, e^{-2\nu\,\xi(y)}\,, \\ F(\nu) &= \nu^2 \left(1 - y^2 - 3\,\nu\, y^3 + 4\, y^4 + 9\,\nu\, y^5 + 6\,\nu^2 y^6\right)\,, \\ \xi(y) &= y - \tan^{-1} y\,, \\ y &= \sqrt{e^2 - 1}\,. \end{aligned} \tag{1.221}$$

Taking the numerical constants $(12/\pi)$ and the leading order of the frequency (ν^2) outside $F_e(\nu)$, we can rewrite Eq. (1.219) in a more comparable way to the circular case,

$$\frac{dE}{d(\ln f)} = \frac{64\pi^2}{15 c^5 G} \frac{(GM)^{3/2}\mu^2}{a^{1/2}} f^2\, g_e(f), \tag{1.222}$$

where $g_e(f) = 1/y$ at the leading order in f and y. This expression is somewhat differently to the one for the circular case in Eq. (1.196), mainly due to its frequency dependence. The hyperbolic case goes like f^2 and the circular one, as $f^{2/3}$. In Chapter 5, we will see why this difference in the frequency dependence, coming from the different behaviors of the orbits, is something which will be of great observational interest, given that it allows to clearly distinguish both types of signal.

Chapter 2

Stochastic gravitational wave backgrounds

In the previous chapter, we have studied the general formalism for gravitational waves and focused on signals coming from 2-body interactions. In this chapter, we will instead focus on another type of signal which gives name to the title of the thesis: the *stochastic gravitational wave background*. This is a background signal consisting of the superposition of gravitational waves, which should be below the signals we observe with the current detectors, similar to the role of the cosmic microwave background for electromagnetic radiation.

There are a lot of sources which generate a stochastic gravitational wave background, usually classified in two types: astrophysical or cosmological.

The astrophysical signals are the ones which undoubtedly exist, constituted by the superposition of weak gravitational waves coming from CBCs or other astrophysical sources. Those signals with a high enough amplitude stand out above the background and noise and we can observe them with current or future detectors. However, similar to these ones, there should be many more with smaller amplitudes which fall below the noise and, even with very precise detectors, the fact that they are so many would make it impossible to resolve them. Thus, this superposition of unresolved, incoherent gravitational waves will constitute one of the contributions to the SGWB. In fact, it is expected to be the dominant one, at least at LVK-like frequencies [28, 29].

In addition to the contribution from CBCs, there are other astrophysical sources such as hyperbolic encounters (see Chapter 5), supernovae [70, 71, 72, 73] or Galactic binaries [74, 75].

The cosmological signals are more difficult to be detected, given that they usually have smaller amplitudes. Some examples include inflation [76, 77], cosmic strings [78, 79] or phase transitions [80], as Fig. 2.1 shows, as well as axion-gauge inflation [81, 82, 83, 84, 85, 86, 87] and scalar-induced gravitational waves [88, 89, 90, 91, 92, 93, 94, 95, 96, 97] (see also Sec. 2.5). In this figure, we can also see that the cosmological sources spread over all the frequency spectrum, which is also true for the astrophysical ones. In Chapter 10, we will elaborate a bit more on the different constraining methods.

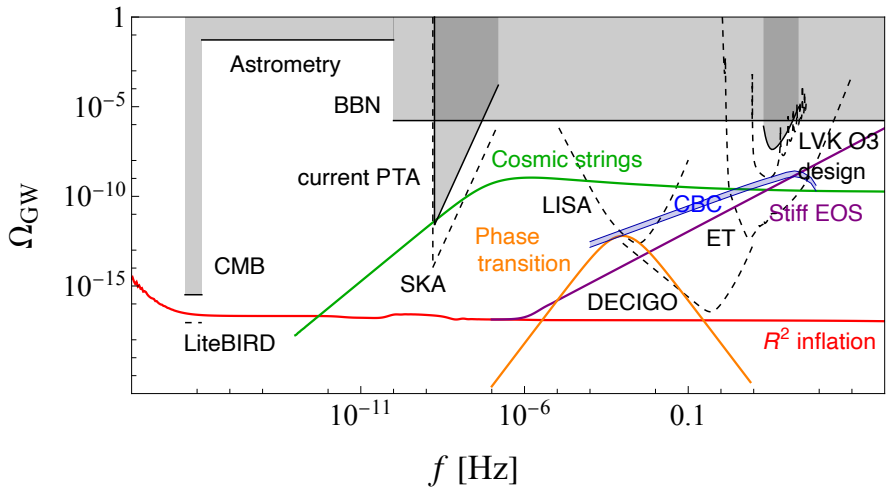

Figure 2.1: SGWB spectra for several cosmological models (colored solid curves) compared to current upper limits (shaded in gray) and expected sensitivities of future experiments (black dashed lines), taken from [98]. The figure includes signals from inflation (R^2 inflation [76]) along with their modification by a stiff equation of state [77], but one should note that the amplitude and spectral behavior of these signals heavily depend on the model parameters. The GW spectrum of cosmic string loops [78, 79] is also presented, as well as the electroweak phase transition [80]. Current constraints include the Advanced-LIGO O3 upper limit [28], constraints based on Big Bang nucleosynthesis and CMB observations [99], pulsar timing, the astrometric measurements by Gaia explained in Chapter 10, CMB temperature and polarization observations [100], and pulsar timing arrays [11]. Future expected sensitivities include the final sensitivity of Advanced-LIGO [101], ET [102], DECIGO [23], LISA [103], SKA [104], and LiteBIRD [105]. An observing period of 3 years is assumed for interferometer experiments and 20 years for SKA. The blue-shaded band indicates the expected amplitude of the SGWB due to the cosmic population of CBCs, based on the observed individual events in the O3 catalog [106], while the expected spectral amplitude is extrapolated to the LISA frequency band assuming the $f^{2/3}$ dependence of the inspiral phase (Eq. (1.196)). However, the lower frequencies could be modified by the effects of eccentricity and precession at the time of binary formation [107, 108].

We will begin this chapter by computing the general equations to work with a SGWB, where some useful references include [39, 109, 110, 111, 112].

2.1 Stochastic gravitational wave background formalism

We start from the general decomposition of a gravitational wave in different propagation directions, frequencies and polarizations in Eq. (1.38), which we rewrite here for convenience:

$$h_{ij}(t,\vec{x}) = \sum_{A=+,\times}\left(\int_{-\infty}^{\infty} df \int d^2\Omega\, \tilde{h}_A(f,\vec{n}) e^A_{ij}(\vec{n}) e^{-2\pi i f(t-\vec{n}\cdot\vec{x}/c)}, \tag{2.1}$$

The word *stochastic* is used to describe the fact that the amplitudes $\tilde{h}_A(f,\vec{n})$ are random variables. Therefore, we can characterize them by their ensemble averages, for which we use temporal averages, similarly to other fields in Cosmology. Statistically speaking, under the assumptions which we will discuss below, the quantity in Eq. (2.1) averages out to zero, so the one-point correlator $\langle \tilde{h}_A(f,\vec{n})\rangle$ is also zero for all frequencies.

We are therefore interested in characterizing the correlators $\langle \tilde{h}^*_A(f,\vec{n})\tilde{h}_{A'}(f',\vec{n}')\rangle$. If we assume that the background is Gaussian, these are the only useful correlators, given that any other N-point correlator can be reduced to it. This assumption is justified by the Central Limit Theorem [113] for unresolved sources, but it fails for other sources such as axion-gauge inflation [81, 82, 83, 84, 85, 86, 87]. For simplicity in the exposition, however, we will keep this assumption, as well as make other ones which are standard in SGWB theory. These can generally be relaxed and obtain different formalisms, such as assuming the presence of anisotropies. Nevertheless, we follow these assumptions as a first step, for simplicity:

- Stationarity: we assume that the correlators will only depend on time differences $t-t'$, but not on the absolute values of time. This means that, even if the background has a certain time dependence, it is only local rather than something on larger time scales. In practice, this is needed so that we can assume $\langle \tilde{h}^*_A(f,\vec{n})\tilde{h}_{A'}(f',\vec{n}')\rangle \propto \delta(f-f')$.
- No polarization: we assume that the background is unpolarized, so that $\langle \tilde{h}^*_A(f,\vec{n})\tilde{h}_{A'}(f',\vec{n}')\rangle \propto \delta_{AA'}$. Again, some sources such as axion-gauge inflation do not satisfy this, producing a chiral background [114].
- Isotropy: similarly to the CMB, we assume the background is statistically isotropic at first order, so that $\langle \tilde{h}^*_A(f,\vec{n})\tilde{h}_{A'}(f',\vec{n}')\rangle \propto \delta^2(\vec{n},\vec{n}')$, which is a Dirac delta over the two-sphere,

  $$\delta^2(\vec{n},\vec{n}') = \delta(\phi-\phi')\delta(\cos\theta-\cos\theta'). \tag{2.2}$$

  Of course, just as the CMB, the real background will have anisotropies. For the treatment of an anisotropic SGWB, see Chapter 3.

Under these assumptions, the two-point correlator can be expressed as

$$\langle \tilde{h}^*_A(f,\vec{n})\tilde{h}_{A'}(f',\vec{n}')\rangle = \delta(f-f')\frac{\delta^2(\vec{n},\vec{n}')}{4\pi}\delta_{AA'}\frac{1}{2}S_h(f), \tag{2.3}$$

for a certain function $S_h(f)$ which is called *power spectral density* (PSD). The factor $1/2$ is chosen to be there when the frequency integral covers the full real numbers, while it should be removed if we integrate just the positive range $f>0$. Additionally, the 4π is a normalization factor which

compensates for the one arising from the integral over the spheres for $\vec{n}$ and $\vec{n}'$. Using this expression for the second correlator of h_{ij} in Eq. (2.1), we get

$$\langle h_{ij}(t,\vec{x})h^{ij}(t,\vec{x})\rangle = 4\int_0^\infty df\, S_h(f), \tag{2.4}$$

where the factor 4 comes from the contraction of the polarization tensors defined in Eq. (1.35):

$$e^+_{ij}e^+_{ij} = |\vec{u}|^4 + |\vec{v}|^4 = 2, \quad e^\times_{ij}e^\times_{ij} = 2|\vec{u}|^2|\vec{v}|^2 = 2 \quad \Rightarrow \quad \sum_{A=+,\times} e^A_{ij}e^A_{ij} = 4. \tag{2.5}$$

We also note that this is the step where we lose the position dependence. In Eq. (2.4), both $h_{ij}(t,\vec{x})$ depend on the position only through their exponentials. Given that one of them must be conjugate, both exponentials cancel out and the result is position-independent, as a background should be.

From Eq. (1.68), we also know that the energy density of gravitational waves is related to the strain amplitude as

$$\rho_{\rm gw} = \frac{c^2}{32\pi G}\langle \dot{h}^{TT}_{ij}\dot{h}^{TT}_{ij}\rangle. \tag{2.6}$$

Substituting h_{ij} in Eq. (2.1) into this equation, we get

$$\rho_{\rm gw} = \frac{c^2}{8\pi G}\int_1^\infty df(2\pi f)^2 S_h(f) = \frac{\pi c^2}{2G}\int_1^\infty df\, f^2 S_h(f). \tag{2.7}$$

In Cosmology, the common practice is to indicate these densities with the density parameter,

$$\Omega_{\rm gw} = \frac{\rho_{\rm gw}}{\rho_c}, \tag{2.8}$$

where ρ_c is the critical density, defined as

$$\rho_c = \frac{3c^2H_0^2}{8\pi G}, \tag{2.9}$$

with H_0 the Hubble constant. Throughout this thesis, we will, in general, use its normalization

$$H_0 = 70\ h_{70}\ \text{km/s/Mpc}. \tag{2.10}$$

Given that the contributions to the density come from different frequencies spread over several orders of magnitude,

$$\rho_{\rm gw} = \int_1^\infty d(\ln f)\frac{d\rho_{\rm gw}}{d(\ln f)}, \tag{2.11}$$

we are interested in the energy density parameter as a function of frequency, so we define

$$\Omega_{\rm gw}(f) = \frac{1}{\rho_c}\frac{d\rho_{\rm gw}}{d(\ln f)}, \tag{2.12}$$

where the dependence indication (f) will mark if we are referring to the first definition (2.8) or the second one (2.12), in an abuse of notation which is common practice in the literature. By definition, both are then related as

$$\Omega_{\rm gw} = \int_1^\infty d(\ln f)\Omega_{\rm gw}(f). \tag{2.13}$$

From the expression for $\rho_{\rm gw}$ as a function of $S_h(f)$ in Eq. (2.7) and Eq. (2.11), we get

$$\frac{d\rho_{\rm gw}}{d(\ln f)} = \frac{\pi c^2}{2G} f^3 S_h(f), \tag{2.14}$$

so that, from the definition of $\Omega_{\rm gw}(f)$ in Eq. (2.12) and the critical density ρ_c in Eq. (2.9), we have

$$\Omega_{\rm gw}(f) = \frac{4\pi^2}{3H_0^2} f^3 S_h(f). \tag{2.15}$$

2.2 Detection of gravitational waves

Up until now, we have studied gravitational waves in space, but at the end of this chapter and the next one, we want to do data analysis with actual data. Thus, we first need to know how the picture changes when we get the observational data with a detector.

Current gravitational-wave detectors like LIGO [6], Virgo [12] or KAGRA [13] consist on a Michelson interferometer with two orthogonal arms. In the future, detectors like LISA [20] and Cosmic Explorer [18] will have different configurations, while it is still unclear whether Einstein Telescope [17] will have a similar design to the current detectors or not. If a gravitational wave goes through a detector, propagating orthogonally to the plane defined by its arms, their lengths are contracted or expanded according to the wave polarization, following the patterns in Fig. 1.1. This tiny length change makes the optical path of both arms differ, so that these slight variations of the system configuration can be detected through interferometry.

In this section, we will see how the detector's response changes for a general orientation and how we can apply the output signal to derive the properties of a stochastic gravitational wave background. Useful references for the first Subsec. 2.2.1 include [39, 112, 115], while for the data analysis part in Subsec. 2.2.2, one can refer to [73, 116, 28, 112, 117, 110].

2.2.1 Detector pattern functions

Whenever a gravitational wave goes through a detector, which we will denote with an index I, the output signal it will produce cannot be the gravitational wave itself, which is a tensor. For now, we will assume there is no noise and the detector is perfectly able to react to all frequencies equally, with zero loss. Then, its output signal will be given by

$$h_I(t) = D_I^{ij} h_{ij}(t), \tag{2.16}$$

where D_I^{ij} is the *detector tensor*, characterizing the effect that a gravitational wave with a given propagation direction and polarization will have in the detector, due to its orientation and geometry.

We consider a gravitational wave propagating in direction $\vec{n}$ given by (θ, ϕ) with frequency f and arbitrary polarization,

$$h_{ij}(t) = \sum_{A=+,\times} h_A(t) e_{ij}^A(\vec{n}), \tag{2.17}$$

where we drop the spatial dependence for now, assuming that all the detector can be assigned roughly the same position $\vec{x} = 0$. Then, the output signal in Eq. (2.16) can be expressed as

$$h_I(t) = h_+(t) F_I^+(\theta, \phi) + h_\times(t) F_I^\times(\theta, \phi), \tag{2.18}$$

where we have defined the *detector pattern functions*, or *antenna patterns* $F_I^A(\vec{n})$, as

$$F_I^A(\vec{n}) = D_I^{ij} e_{ij}^A(\vec{n}). \tag{2.19}$$

We can characterize them by first studying a simpler case, which is the one in which the gravitational wave propagates in the orthogonal direction to the detector plane. In this case, if we define the polarization h_+ so that its base directions coincide with the arms, the detector will be fully able to measure h_+, but it will not react to the polarization $h_\times$. Thus, the response function in this case is $F_I^+ = 1$, $F_I^\times = 0$. In other words, for a detector whose base directions are $\hat{u}$ and $\hat{v}$, the detection tensor is given by

$$D_I^{ij} = \frac{1}{2}\left(u^i u^j - v^i v^j\right), \tag{2.20}$$

so that $F_I^+ = D_I^{ij} e_{ij}^A = \delta^{A+}$, with the definitions in Eq. (1.35). By knowing this, we can compute the response function for an arbitrary direction with an auxiliary rotated reference system, similar to how we did in Subsec. 1.2.3.

Again, the reference system S' will be defined by the rotation in Eq. (1.101), where the propagation direction $\vec{n}$ of our gravitational wave will coincide with $\hat{z}'$. Once again, we could define a third rotation around $\vec{n}$ which alters the polarization definitions, but we disregard this degree of freedom. In S', since the wave propagates in the direction $\hat{z}'$, then h'_{ij} is simply

$$h'_{ij} = \begin{pmatrix} h'_+ & h'_\times & 0 \\ h'_\times & -h'_+ & 0 \\ 0 & 0 & 0 \end{pmatrix}_{ij}. \tag{2.21}$$

We now have to evaluate how this perturbation is observed in S, for which we apply Eq. (1.104). Note that, while in that case, we wanted to get I' from I, now we want the opposite: obtaining h_{ij} from h'_{ij}, so we use the first equation in Eq. (1.104) rather than the second. Additionally, from that equation we will obtain h_{ij} in an arbitrary gauge, for which we will then need to project to the TT gauge. This projection means setting all h_{i3} components to zero and subtracting the trace, so that

$$h_+ = h_{11}^{\mathrm{TT}} = \frac{1}{2}(h_{11} - h_{12}). \tag{2.22}$$

Thus, it is enough to compute h_{11} and h_{22} from Eq. (1.104), which gives

$$h_{11} = h'_+(\cos^2\theta\cos^2\phi - \sin^2\phi) - h'_\times \cos\theta \sin(2\phi), \tag{2.23}$$

$$h_{22} = h'_\times(\cos^2\theta\sin^2\phi - \cos^2\phi) + h'_\times \cos\theta \sin(2\phi), \tag{2.24}$$

where the second sign of both equations differs from [39] due to the different definitions for ϕ, where a transformation $\phi \mapsto -\phi$ converts from one system to the other. Therefore, the plus polarization (which, as we saw, is the only one that the detector lets pass) is

$$h_+ = \frac{1}{2}(h_{11} - h_{12}) = \frac{1}{2}h'_+(1+\cos^2\theta)\cos(2\phi) - h'_\times \cos\theta \sin(2\phi), \tag{2.25}$$

where the minus sign can actually be absorbed by redefining $\phi \mapsto -\phi$. From this equation and Eq. (2.18), we can read the antenna patterns as the coefficients for h'_+ and $h'_\times$,

$$F_I^+(\theta,\phi) = \frac{1}{2}(1+\cos^2\theta)\cos(2\phi), \tag{2.26}$$

$$F_I^\times(\theta,\phi) = -\cos\theta\sin(2\phi). \tag{2.27}$$

We can see from this equation that the detector maximally detects gravitational waves in some directions and polarizations, while it completely misses them in other cases. In particular, for $h_\times$, the signals have maximal amplitude (either positive or negative) when $\theta = 0, \pi$ (ϕ in this case represents the extra rotation we disregard) and the detector is blind to them for $\phi = \pi/4 + n\pi/2$, which is also true for $h_\times$ in the particular case $\theta = \pi/2$. These blind spots are completely reasonable when one takes into account the effect outlined in Fig. 1.1, given that they coincide with a null effect on both arms or the exact same, non-null effect on both of them, so that the difference in optical length between them is null.

Finally, we should note that the antenna patterns just characterize the signal the detector observes due to its relative position and configuration. However, even neglecting the noise, its output signal will not be directly given by this $h_I(t)$, which is going through a complex system that produces the output. This process will be more sensitive to certain frequencies and not to others at all, which is something that is characterized by a transfer function $T(f)$. Therefore, as a function of frequency, the output we will observe is given by

$$\tilde{h}_I^{\text{out}}(f) = T(f)\tilde{h}_I(f), \tag{2.28}$$

plus, of course, the noise going into the detector from any possible source able to cause a displacement on the interferometer arms.

2.2.2 SGWB data analysis

For a SGWB, the picture outlined in Sec. 2.1 changes in the context of a detector. We have seen how a detector measures a gravitational wave propagating in direction $\vec{n}$ with frequency f is given by Eq. (2.18). Thus, the decomposition in Eq. (2.1) for a generic gravitational wave is now

$$h_I(t) = \sum_{A=+,\times}\left(\int_{-\infty}^{\infty} df \int d^2\Omega\, \tilde{h}_A(f,\vec{n}) F_I^A(\vec{n}) e^{-2\pi i f(t-\vec{n}\cdot\vec{x}_I/c)}, \right. \tag{2.29}$$

where $\vec{x}_I$ is the position of the I detector. The main change with respect to Eq. (2.1) is that, under the contraction with the detector tensor D_{ij}, the polarization basis tensors $e_{ij}^A(\vec{n})$ must be replaced by the detector pattern functions $F_A(\vec{n})$.

However, there is one more important change when dealing with real data: noise. In particular, in a gravitational-wave detector, the output is mostly dominated by noise. Therefore, if we divide the detector signal $s_I(t)$ as the sum of the gravitational wave strain $h_I(t)$ and a noise component $n_I(t)$[1],

$$s_I(t) = h_I(t) + n_I(t), \quad \langle n_I(t) n_I(t)\rangle \gg \langle h_I(t) h_I(t)\rangle, \tag{2.30}$$

then the noise will dominate the signal two-point correlator. We call this regime the *weak-signal limit*. In order to avoid this, what we do is correlating the signal obtained by two different detectors, where we will denote the second one by $J \neq I$. The idea is that the noise is completely uncorrelated between two different detectors, as well as uncorrelated from any of the GW signals h_I. In practice, there are some sources of noise which are correlated, the most relevant of which are the *Schumann resonances* in the Earth's magnetic field, caused by lightning strikes and covering thousands of kilometers [118, 119, 120, 121, 112]. Nevertheless, for simplicity in the explanation, we will keep the assumption of no correlation between detectors, while we refer to [112] for additional information on correlated sources and to [118, 119, 120, 121] for more details of Schumann resonances. Under this assumption, the following approximation holds:

$$\langle s_I(t) s_J(t)\rangle = \langle h_I(t) h_J(t)\rangle + \langle h_I(t) n_J(t)\rangle + \langle n_I(t) h_J(t)\rangle + \langle n_I(t) n_J(t)\rangle \approx \langle h_I(t) h_J(t)\rangle, \tag{2.31}$$

so we will use $\langle s_I(t) s_J(t)\rangle$ and $\langle h_I(t) h_J(t)\rangle$ interchangeably.

When correlating different detectors, Eq. (2.3) still holds, since it only depends on $\tilde{h}_A$, but the e^A_{ij} contraction in Eq. (2.5) must now be replaced by the contraction between the detector pattern functions $F^A_I(\vec{n})$. Thus, Eq. (2.4) now takes the form

$$\langle s_I(t) s_J(t)\rangle = \frac{1}{4\pi} \sum_{A=+,\times} \int_0^\infty df \int d^2\Omega\, F^A_I(\vec{n}) F^A_J(\vec{n}) S_h(f) e^{2\pi i f \vec{n}\cdot(\vec{x}_I - \vec{x}_J)/c}. \tag{2.32}$$

When we were correlating a signal with itself, this exponential factor dependent on the position did not appear, since both positions were the same and the factor cancelled out. Now, however, this factor cannot be simplified. Related to it, it is useful to define the so-called *overlap reduction function* (ORF) as

$$\gamma_{IJ}(f) \equiv \frac{5}{8\pi} \sum_{A=+,\times} \int d^2\Omega\, F^A_I(\vec{n}) F^A_J(\vec{n}) S_h(f) e^{2\pi i f \vec{n}\cdot(\vec{x}_I - \vec{x}_J)/c}, \tag{2.33}$$

where the normalization factor $5/(8\pi)$ is chosen so that the self-ORF $\gamma_{II}(f) = 1$. This factor can easily be computed by using the explicit form of F^A_I in Eqs. (2.26) and (2.27), so that

$$\begin{aligned} \int d^2\Omega \left[(F^+_I)^2 + (F^\times_I)^2\right] &= \int_0^\pi d\theta \int_0^{2\pi} d\phi \sin\theta \left[\frac{1}{4}(1+\cos^2\theta)^2 \cos^2(2\phi) + \cos^2\theta \sin^2(2\phi)\right] \\ &= \pi\left[\frac{14}{15} + \frac{2}{3}\right] = \frac{8\pi}{5}. \end{aligned} \tag{2.34}$$

[1] In this thesis, we keep the name *strain* for h in the context of a detector, while its sum with the noise is called *signal*. However, in other texts, *signal* is used to refer to the real signal coming from GW, as opposed to the noise, while *strain* is used for its sum with the noise. In any case, any possible confusion is cleared up with the variable names s, h and n, such that $s = h + n$ (Eq. (2.30)).

Therefore, Eq. (2.32) can now be written as

$$\langle s_I(t)s_J(t)\rangle = \frac{2}{5}\int_0^\infty df\,\gamma_{IJ}(f)S_h(f). \tag{2.35}$$

Additionally, using the relation between $S_h(f)$ and $\Omega_{\rm gw}$ in Eq. (2.15), we get

$$\langle s_I(t)s_J(t)\rangle = \frac{3H_0^2}{10\pi^2}\int_0^\infty df\,\gamma_{IJ}(f)\frac{\Omega_{\rm gw}(f)}{f^3}. \tag{2.36}$$

We usually work with time segments of duration T, so that, for the time segment centered in t, we define

$$Y_{IJ}(t) = \int_{t-T/2}^{t+T/2} dt\, s_I(t)s_J(t). \tag{2.37}$$

In this text, we will assume these time segments do not overlap, that is, that the distance between one center t and the following one is exactly T. In the real analysis by LVK, these centers are separated by $T/2$, so their first half completely overlaps with the last half of the previous segment, and similarly for the second half with the next segment. For details of how to deal with this analysis, see [110].

Using Eq. (2.36), we obtain that the expected value for $Y_{IJ}(t)$ in Eq. (2.37) is

$$\begin{aligned}\langle Y_{IJ}(t)\rangle &= \int_{t-T/2}^{t+T/2} dt\,\langle s_I(t)s_J(t)\rangle = T\frac{3H_0^2}{10\pi^2}\int_0^\infty df\,\gamma_{IJ}(f)\frac{\Omega_{\rm gw}(f)}{f^3}\\ &\equiv T\int_0^\infty df\,\gamma_{IJ}(f)S_0(f)\Omega_{\rm gw}(f),\end{aligned} \tag{2.38}$$

where we have defined

$$S_0(f) = \frac{3H_0^2}{10\pi^2 f^3}, \tag{2.39}$$

matching the notation in [110]. This way, $Y_{IJ}(t)$ constitutes an unbiased estimator for the right-hand side quantity in Eq. (2.38).

We now divide the integral frequency range into a discrete range of frequencies with resolution Δf, in order to get an estimate for $\Omega_{\rm gw}(f)$ in each of these frequencies. This is called the *narrow-band* analysis. In order to be coherent with the resolutions, we note that T imposes a minimum characterized frequency, $f_{\rm min} = 1/T$. Therefore, we must choose T and Δf so that they satisfy $T\Delta f > T\times 1/T = 1$. In LVK, we usually work with $T = 192$ s, which corresponds to a frequency of 0.0052 Hz, while the typical resolution is $1/32 \approx 0.031$ Hz. Thus, $T\Delta f = 6 > 1$, so the analysis is coherent.

For the narrowband analysis, we have to take Eq. (2.38) and divide into frequency bins. For this purpose, if is useful to go to Fourier space, but note that the time integration only goes from $t - T/2$ to $t + T/2$. Thus, we define the *short-time Fourier transform* of $s_I(t)$ over a period T as

$$\tilde{s}_I(f,t) = \int_{t-T/2}^{t+T/2} dt' s_I(t')e^{2\pi i f t'}, \tag{2.40}$$

where the t does not indicate a real dependence, but rather, it can be thought of as a tag which points to the time segment of length T that has been used to compute $\tilde{s}_I(f,t)$.

Short-time Fourier transforms essentially behave as usual Fourier transforms with some properties slightly changed. One of them is the associated Dirac delta function, which is now

$$\delta_T(f-f') = \int_{t-T/2}^{t+T/2} e^{-2\pi i(f-f')t} = T\,\mathrm{sinc}[\pi T(f-f')], \tag{2.41}$$

with $\mathrm{sinc}(x) = \sin(x)/x$ for $x \neq 0$ and $\mathrm{sinc}(0) = 1$ for continuity in all real numbers. In particular, we notice that $\delta_T(0) = T$, which is a finite value. As $T \to \infty$, we would recover the standard Dirac delta function, just as the short-time Fourier transform tends to the standard one.

This way, $Y_{IJ}(t)$ in Eq. (2.37) can be expressed as

$$\begin{aligned} Y_{IJ}(t) &= \int_{-\infty}^{\infty} df \int_{-\infty}^{\infty} df' \int_{t-T/2}^{t+T/2} dt\, e^{2\pi i(f-f')t} \tilde{s}_I^*(f,t)\tilde{s}_J(f,t) \\ &= \int_{-\infty}^{\infty} df \int_{-\infty}^{\infty} df' \delta_T(f-f')\tilde{s}_I^*(f,t)\tilde{s}_J(f',t) \qquad (2.42) \\ &= \int_{-\infty}^{\infty} df \tilde{s}_I^*(f,t)\tilde{s}_J(f,t) = 2\int_{0}^{\infty} df \tilde{s}_I^*(f,t)\tilde{s}_J(f,t), \qquad (2.43) \end{aligned}$$

where the $\delta_T(f-f')$ has been used as a standard Dirac delta. If we discretize in frequency bins of resolution Δf, using Eq. (2.43), Eq. (2.38) can be expressed as

$$2\Delta f \sum_f \langle \tilde{s}_I^*(f,t)\tilde{s}_J(f,t)\rangle = T\Delta f \sum_f \gamma_{IJ}(f)S_0(f)\Omega_{\mathrm{gw}}(f). \tag{2.44}$$

Making the contributions per frequency bin at both sides equal and solving for $\Omega_{\mathrm{gw}}(f)$, we get its narrowband estimate for each time segment and baseline,

$$\hat{\Omega}_{\mathrm{gw}}^{IJ}(f,t) = \frac{2}{T}\frac{\mathrm{Re}[\tilde{s}_I^*(f,t)\tilde{s}_J(f,t)]}{\gamma_{IJ}(f)S_0(f)}, \tag{2.45}$$

where the hat denotes estimator and we take the real part to avoid complex-valued estimators. Based on this equation, we define the cross-spectral density (CSD) [73, 116, 117, 28, 110] C_{IJ} as

$$C_{IJ}(f,t) = \frac{2}{T}\tilde{s}_I^*(f,t)\tilde{s}_J(f,t), \tag{2.46}$$

so that Eq. (2.45) can finally be expressed as

$$\hat{\Omega}_{\mathrm{gw}}^{IJ}(f,t) = \frac{\mathrm{Re}[C_{IJ}(f,t)]}{\gamma_{IJ}(f)S_0(f)}. \tag{2.47}$$

It is also important to get an associated error for these estimates. We first start by estimating the variance for $Y_{IJ}(t)$, in the form of Eq. (2.43). Given that its mean involves a two-point correlator, the variance $\sigma^2_{Y,IJ}(t) = \langle Y_{IJ}(t)^2\rangle - \langle Y_{IJ}(t)\rangle^2$ will involve four-point correlators. In the weak-signal limit, given by the condition $\langle h_I^2\rangle \ll \langle n_I^2\rangle$, there will be terms in which the signal from a detector

combines with itself, getting that $\langle s_I^2\rangle \approx \langle n_I^2\rangle$. Thus, these terms will dominate the ones proportional to h^2, particularly $\langle Y_{IJ}(t)\rangle^2$, so that we can assume $\sigma^2_{Y,IJ}(t) \approx \langle Y_{IJ}(t)^2\rangle$. We can also substitute all s_I by the noise n_I, so that

$$\sigma^2_{Y,IJ}(t) \approx \int_{-\infty}^{\infty} df \int_{-\infty}^{\infty} df' \iint_{-\infty}^{\infty} df'' \int_{-\infty}^{\infty} df''' \, \delta_T(f-f')\delta_T(f''-f''') \times \langle \tilde{n}_I^*(f,t)\, \tilde{n}_J(f',t)\, \tilde{n}_I(f'',t)\, \tilde{n}_J^*(f''',t)\rangle. \tag{2.48}$$

Assuming that the noise is uncorrelated between different detectors, we can express

$$\begin{aligned}\langle \tilde{n}_I^*(f,t)\, \tilde{n}_J(f',t)\, \tilde{n}_I(f'',t)\, \tilde{n}_J^*(f''',t)\rangle &= \langle \tilde{n}_I^*(f,t)\tilde{n}_J(f',t)\rangle \langle \tilde{n}_I(f'',t)\, \tilde{n}_J^*(f''',t)\rangle \\ &+ \langle \tilde{n}_I^*(f,t)\, \tilde{n}_I(f'',t)\rangle \langle \tilde{n}_J(f',t)\, \tilde{n}_J^*(f''',t)\rangle \\ &+ \langle \tilde{n}_I^*(f,t)\, \tilde{n}_J^*(f''',t)\rangle \langle \tilde{n}_J(f',t)\, \tilde{n}_I(f'',t)\rangle \\ &\approx \langle \tilde{n}_I^*(f,t)\, \tilde{n}_I(f'',t)\rangle \langle \tilde{n}_J(f',t)\, \tilde{n}_J^*(f''',t)\rangle. \end{aligned} \tag{2.49}$$

Substituting this into Eq. (2.48) and integrating over f' and f''' using the delta functions,

$$\sigma^2_{Y,IJ}(t) \approx \iint_{-\infty}^{\infty} df \iint_{-\infty}^{\infty} df'' \, \langle \tilde{n}_I^*(f,t)\, \tilde{n}_I(f'',t)\rangle \langle \tilde{n}_J(f,t)\, \tilde{n}_J^*(f'')\rangle. \tag{2.50}$$

At this point, similar to Eq. (2.3), we define the *one-sided power spectral density* $P_I(f)$ as

$$\langle \tilde{n}_I(f)\, \tilde{n}_I(f')\rangle = \frac{1}{2}\delta(f-f')P_I(f) \quad (= \langle \tilde{s}_I(f)\, \tilde{s}_I(f')\rangle), \tag{2.51}$$

where the tilde indicates a standard Fourier transform in this case, and the last equality is a consequence of the weak-signal limit. The short-time Fourier transforms satisfy a similar relation,

$$\langle \tilde{n}_I(f,t)\, \tilde{n}_I(f',t)\rangle = \frac{1}{2}\delta_T(f-f')P_I(f), \tag{2.52}$$

where these $P_I(f)$ can be estimated for each time segment as

$$P_I(f,t) = \frac{2}{T} s_I^*(f,t) s_I(f,t), \tag{2.53}$$

similar to how we did for $\Omega_{\rm gw}(f)$ in Eq. (2.47). From the previous expression, we can see that $P_I(f,t)$ is actually just $C_{IJ}(f,t)$ in Eq. (2.46) for the particular case $I=J$. Now, substituting Eq. (2.52) into Eq. (2.50), we get

$$\begin{aligned}\sigma^2_{Y,IJ}(t) &\approx \frac{1}{4}\int_{-\infty}^{\infty} df \iint_{-\infty}^{\infty} df'' \delta_T^2(f-f'')P_I(f)P_J(f'') = \frac{1}{4}\int_{-\infty}^{\infty} df \delta_T(0) P_I(f)P_J(f) \\ &= \frac{T}{2}\iint_{0}^{\infty} df P_I(f)P_J(f), \end{aligned} \tag{2.54}$$

where we have used one of the $\delta_T(f-f'')$ as a standard delta function, for the integration in f'', and the other one has been evaluated at zero. This expression coincides with the expression in [73], and we can see that this result, which is an expected value, is independent of t. In order to get our

estimate for $\sigma^2_{Y,IJ}$, we only have to add the time dependence due to estimating $P_I(f)$ and $P_J(f)$ via Eq. (2.53). Thus,

$$\hat{\sigma}^2_{Y,IJ}(t) = \frac{T}{2}\int_0^\infty df P_I(f,t)P_J(f,t), \tag{2.55}$$

which satisfies $\langle\hat{\sigma}^2_{Y,IJ}(t)\rangle = \sigma^2_{Y,IJ}(t)$. This is the final expression we were looking for in the case of $Y_{IJ}(t)$.

For the narrowband estimator for $\Omega_{\rm gw}(f)$, first we write, from Eq. (2.38) and the discretization in later equations,

$$Y_{IJ}(t) = T\Delta f \sum_f \gamma_{IJ}(f)S_0(f)\hat{\Omega}^{IJ}_{\rm gw}(f,t). \tag{2.56}$$

Therefore, its variance satisfies

$$\begin{aligned}\sigma^2_{Y,IJ} = \langle Y_{IJ}(t)^2\rangle &= T^2(\Delta f)^2\sum_f\sum_{f'}\delta_{ff'}\gamma_{IJ}(f)S_0(f)\gamma_{IJ}(f')S_0(f')\langle\hat{\Omega}^{IJ}_{\rm gw}(f,t)\hat{\Omega}^{IJ}_{\rm gw}(f',t)\rangle \\ &= T^2(\Delta f)^2\sum_f\gamma^2_{IJ}(f)S_0^2(f)\langle(\hat{\Omega}^{IJ}_{\rm gw}(f,t))^2\rangle \\ &= T^2(\Delta f)^2\sum_f\gamma^2_{IJ}(f)S_0^2(f)\sigma^2_{IJ}(f),\end{aligned} \tag{2.57}$$

where we denote the variance of the $\hat{\Omega}^{IJ}_{\rm gw}(f,t)$ estimate by $\sigma^2_{IJ}(f)$. If we now make this equation equal to the discretized version of Eq. (2.54),

$$T^2(\Delta f)^2\sum_f\gamma^2_{IJ}(f)S_0^2(f)\sigma^2_{IJ}(f) = \frac{T}{2}\Delta f\sum_f P_I(f)P_J(f), \tag{2.58}$$

we get, solving for $\sigma^2_{IJ}(f)$,

$$\sigma^2_{IJ}(f) = \frac{1}{2T\Delta f}\frac{P_I(f)P_J(f)}{\gamma^2_{IJ}(f)S_0^2(f)}, \tag{2.59}$$

which coincides with the expressions in the literature [116, 122, 110]. Thus, the corresponding estimate is

$$\hat{\sigma}^2_{IJ}(f,t) = \frac{1}{2T\Delta f}\frac{P_I(f,t)P_J(f,t)}{\gamma^2_{IJ}(f)S_0^2(f)}, \tag{2.60}$$

which is our final result for the narrow-band analysis.

With this formalism, we have an independent estimator for $\Omega_{\rm gw}(f)$ per time segment, which is useful to see their variability and address possible problems. In particular, this helps to remove the worst-quality time segments, improving the quality of a combined estimator for all time data. The estimation of these variances is therefore essential, given that they can be used to weigh how much each time segment should contribute. The usual criterion is to do an inverse-noise-weighted average, like

$$\hat{\Omega}^{IJ}_{\rm gw}(f) = \frac{\sum_t \hat{\Omega}^{IJ}_{\rm gw}(f,t)\sigma^{-2}_{IJ}(f,t)}{\sum_t \sigma^{-2}_{IJ}(f,t)}, \tag{2.61}$$

with the estimated uncertainty given by

$$\hat{\sigma}^2_{IJ}(f) = \left(\sum_t \sigma^{-2}_{IJ}(f,t) \right)^{-1} . \tag{2.62}$$

These estimates for $\Omega_{\rm gw}$ and σ are used to do parameter estimation and model selection, as we will see in Secs. 2.4 and 2.5, as well as in Chapter 3. Before going into these topics, however, there is another type of estimate we can build with the ones defined up to now.

If we applied a similar average for $\hat{\Omega}^{IJ}_{\rm gw}(f)$ and its variance over frequency, we would get a joint estimate for the amplitude of a flat $\Omega_{\rm gw}(f)$. We can generalize this idea for a power-law functional form for $\Omega_{\rm gw}(f)$,

$$\Omega_{\rm gw}(f) = \Omega_\alpha \left(\frac{f}{f_{\rm ref}} \right)^\alpha , \tag{2.63}$$

where $\Omega_\alpha = \Omega_{\rm gw}(f = f_{\rm ref})$ for a certain reference frequency $f_{\rm ref}$. If we define

$$H_{\rm ref}(f) = \left(\frac{f}{f_{\rm ref}} \right)^\alpha , \tag{2.64}$$

then, an estimator for Ω_α is given by

$$\hat{\Omega}^{IJ}_\alpha = \frac{\sum_f H_{\rm ref}(f) \hat{\Omega}^{IJ}_{\rm gw}(f) \hat{\sigma}^{-2}_{IJ}(f)}{\sum_f H^2_{\rm ref}(f) \hat{\sigma}^{-2}_{IJ}(f)}, \tag{2.65}$$

which is called *broad-band* estimator. In addition, the associated uncertainty can be estimated as

$$\hat{\sigma}^2_{\alpha,IJ} = \left(\sum_f H^2_{\rm ref}(f) \hat{\sigma}^{-2}_{IJ}(f) \right)^{-1} . \tag{2.66}$$

In fact, similar estimators can be used for the amplitudes of arbitrary $H_{\rm ref}(f)$ (not necessarily given by Eq. (2.63)), as long as they have no other free parameter than a global amplitude.

We also note that all the estimates depend on the baseline IJ that we are using. When we have several baselines, the broadband estimators in Eqs. (2.65) and Eq. (2.66) have the same definition with an additional sum over the baselines.

In the next section, we will see an introduction to Bayesian inference, which, together with the narrowband and broadband formalisms, will then be used in Sections 2.4 and 2.5, as well as in Chapter 3, to get constraints on models from gravitational-wave data.

2.3 Introduction to Bayesian inference

Whenever we have some data and we want to extract its physical information, we usually assume it follows some model M with certain parameters $\vec{\theta}$. Under this hypothesis, the main task is then

inferring the values of these parameters from the data, a procedure that is usually called *parameter estimation*.

There are many ways to do parameter estimation using statistical tools, including frequentist and Bayesian methods (see [123] for further details on the topic). In this thesis, I will focus on the latter, which are the most used in the field of Gravitational Waves [28, 124, 14, 8].

The main idea of Bayesian inference is that the parameters are random variables with some unknown distribution we aim to determine. For this purpose, we use our data D. It is also necessary to assume some *a priori* distribution for $\vec{\theta}$, or *prior* $P(\vec{\theta})$ (sometimes denoted $\pi(\vec{\theta})$), as a starting point, where P denotes probability. Then, using Bayes' theorem, we can get the probability distribution for our parameters conditioned to the data, or *posterior distribution* $P(\vec{\theta}|D, M)$,

$$P(\vec{\theta}|D, M) = \frac{P(D|\vec{\theta}, M)P(\vec{\theta})}{P(D|M)}, \tag{2.67}$$

where $P(D|\vec{\theta}, M)$ measures how likely it is to obtain the data with the model M for a given set of parameters $\vec{\theta}$. Due to this definition, this quantity is usually called *likelihood*, which we will denote by $\mathcal{L}(\vec{\theta})$ throughout the thesis. Additionally, $P(D|M)$ is the total probability to obtain the data given the model M. Due to the law of total probability, it is marginalization of the numerator over all parameter space. It is usually called the model *evidence* and denoted by Z,

$$Z(M) = P(D|M) = \int d\vec{\theta} P(D|\vec{\theta}, M)P(\vec{\theta}) = \iint\!\!\!\!\!\!\int d\vec{\theta}\mathcal{L}(\vec{\theta})\pi(\vec{\theta}). \tag{2.68}$$

When we have two different models M_1 and M_2 for the same problem, the evidence can be used to decide which one of them is favoured by the data. The natural tool to see which of them is more likely is the *odds ratio*,

$$\mathcal{O}^{M_1}_{M_2} = \frac{P(M_1|D)}{P(M_2|D)} = \frac{P(D|M_1)\pi(M_1)}{P(D|M_2)\pi(M_2)}, \tag{2.69}$$

where in the second step we have used Bayes' theorem (2.67) applied to models rather than parameters. If we assume that none of the models is preferred, so that $\pi(M_1) = \pi(M_2)$, then the odds ratio reduces to the *Bayes factor*,

$$\mathcal{B}^{M_1}_{M_2} = \frac{P(D|M_1)}{P(D|M_2)} = \frac{Z(M_1)}{Z(M_2)}, \tag{2.70}$$

which is just the ratio of evidences defined in Eq. (2.68). It is commonly agreed that the evidence in favour of M_1 is strong for $\mathcal{B}^{M_1}_{M_2} \gtrsim 10$ and conclusive for $\mathcal{B}^{M_1}_{M_2} \gtrsim 100$ [125], although the exact numbers and statements may vary in different references. Using these statistical tools to distinguish between two models, one of which is preferred by the data, is called *model selection*.

With the formalism defined, all that remains is to choose a suitable likelihood and characterize the numerator of Eq. (2.67) in a sufficiently large area of the parameter space, which is a procedure called *sampling*.

2.3.1 The likelihood

Suppose we have a set of points $\{x_i\}$, $i = 1, \ldots, N$, where we measure the value of the quantity y with certain experimental errors σ_i. According to our model M, y is given by a function f

depending on some parameters $\vec{\theta}$, so that $y = f(x, \vec{\theta})$. Thus, we should expect a value close enough to $\mu_i = f(x_i, \vec{\theta})$ for each i, where the measurement of how close it is depends on the error scale σ_i. Then, for a single measurement i, we can approximate the expected probability distribution of y_i by a Gaussian with mean $\mu_i = f(x_i, \vec{\theta})$ and width σ_i, $y_i \sim N(\mu_i, \sigma_i)$, so that its probability density function (PDF) is

$$P(y_i|\vec{\theta}, M) = \frac{1}{\sqrt{2\pi}\sigma_i} \exp\left[-\frac{1}{2}\left(\frac{y_i - \mu_i}{\sigma_i}\right)^2\right]. \tag{2.71}$$

If all the measurements are independent, their joint PDF is the product of all the individual PDFs. If the Gaussian hypothesis holds for all points, then the joint probability for $\vec{y} = (y_1, \dots y_N)$ is given by

$$P(\vec{y}|\vec{\theta}, M) = \frac{1}{(2\pi)^{N/2}} \left.\prod_{i=1}^{N} \sigma_i\right)^{-1} \exp\left[-\frac{1}{2}\sum_{i=1}^{N}\left(\frac{y_i - \mu_i}{\sigma_i}\right)^2\right]\Bigg(\tag{2.72}$$

This is the standard Gaussian likelihood used in the majority of parameter estimations. However, as we will see in Chapter 10, there are other likelihoods which are also acceptable under different hypotheses. For the first chapters, however, we will always use Gaussian likelihoods.

The Gaussian likelihood has a quadratic exponential dependence on the model, which implicitly appears in the μ_i terms. As we know, exponentials are very sensitive to changes in their exponents, so it is more natural to work with the logarithm of the likelihood to avoid this issue. In this case, the products appearing in Eq. (2.72) can now be expressed as sums.

In general, the samplers which will characterize the product of the likelihood and priors (the numerator in Eq. (2.67)) will only care about the shape of this function and disregard its normalization constant. Therefore, from Eq. (2.72), it is enough to know that

$$\mathcal{L} \propto \exp\left[-\frac{1}{2}\sum_{i=1}^{N}\left(\frac{y_i - \mu_i}{\sigma_i}\right)^2\right]\Bigg(\tag{2.73}$$

or, in terms of the log-likelihood,

$$\ln \mathcal{L} = -\frac{1}{2}\sum_{i=1}^{N}\left(\frac{y_i - \mu_i}{\sigma_i}\right)^2 + \text{const.} \tag{2.74}$$

2.3.2 Sampling methods

In order to evaluate the shape of the posterior in Eq. (2.67), it is necessary to evaluate the likelihood and prior at a large region of the parameter space. For a problem with moderate or high dimensionality, it is not possible to explore the parameter space with a uniform grid or similar "brute force" methods. Thus, we need a more sophisticated algorithm that helps us with this exploration, which is what we call a *sampler*.

There are two main families of sampler which are widely used: Markov chain Monte Carlo (MCMC) sampling and nested sampling, both of which are based on some random process which explores the parameter space based on where the likelihood is higher. We will briefly comment on both methods, where a good review can be consulted in [126].

Markov chain Monte Carlo sampling

MCMC sampling was first introduced in 1953 in an article by Nicholas C. Metropolis and other collaborators [127] and extended by Wilfred K. Hastings [128]. Broadly speaking, a Monte Carlo method is an algorithm that aims to obtain a numerical result through repeated random sampling. The most paradigmatic example is obtaining the area of a circle by randomly sampling points in the circumscribed square, and then multiplying the fraction of samples inside the circle by the area of the square (see Fig. 2.2). This family of methods was first developed by Metropolis and his collaborator Stanislaw Ulam in 1949 [129]. Metropolis decided to name this method after the Monte Carlo casino in Monaco, where Ulam's uncle used to go to gamble [130].

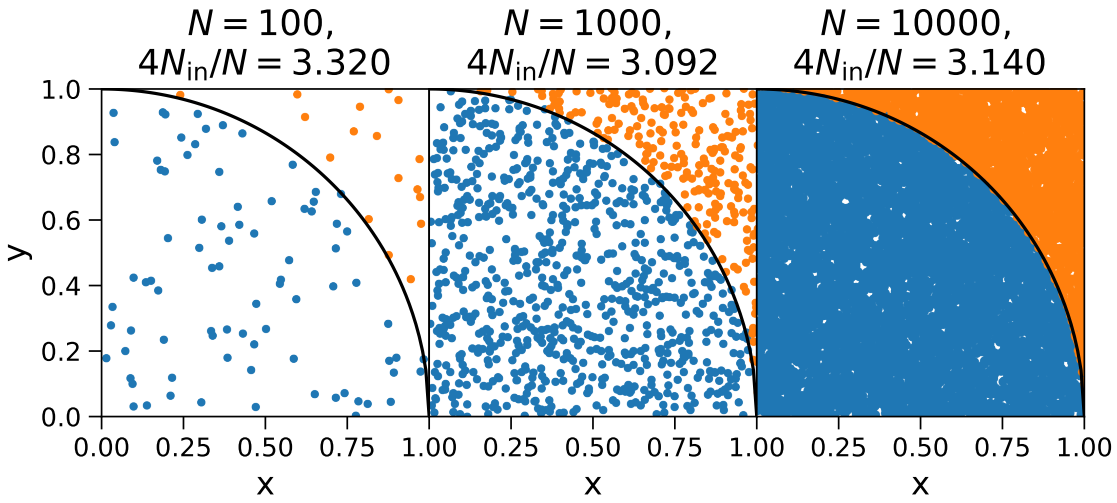

Figure 2.2: Example of a Monte Carlo method for the computation of π. N denotes the number of points, while $N_{\rm in}$ is the number of them inside the radius $x^2 + y^2 = 1$ (black line). The exact value of π is given by $4A_{\rm circle}/A_{\rm square}$, so an approximation is given by $4N_{\rm in}/N$. For each realization, we can see the number of used points and their approximation of π, which statistically gets better as N increases.

There are many implementations of MCMCs in different programming languages. Here, I will focus on Python, for which some of the most popular ones are EMCEE [131] or PyMC [132].

The idea of MCMC sampling is to have a certain number of *walkers*, which can be thought of as particles occupying a different position at each iteration. Each walker starts at a random position at the parameter space and moves randomly through it according to some rules, evaluating the likelihood and prior at each new point. Because, at each iteration, the following point is selecting only based on the present state, disregarding the previous ones, the final set of points for each walker is said to be a *Markov chain*, completing the other half of the method's name.

The term MCMC is, subsequently, naming a family of different methods based on the same concept. I will describe here the rules for the original Metropolis algorithm, but there are many more possibilities. If we have a function $f(x)$ proportional to the desired PDF, such as the numerator

of Eq. (2.67), the rules can be summarized in the following steps:

- First, each walker is initialized by choosing a random position x_1 within the parameter space. Additionally, some proposal function $g(x|y)$ must be chosen from which to draw subsequent points. In the original article by Metropolis et al. [127], this function was a uniform distribution over a circular shape centered on y, but one can also choose a Gaussian distribution centered on this point. In general, the formalism attributed to Metropolis used a symmetric (in x, y) proposal function, and Hastings extended the formalism to more generic proposal functions [128].

- For each iteration at position x_i, a candidate x' is proposed by randomly sampling the proposal distribution $g(x'|x_i)$. Then, the acceptance ratio is defined as

$$\alpha = \frac{f(x')}{f(x_i)}, \tag{2.75}$$

  where we notice here the irrelevance of a possible normalization constant in $f(x)$. Then, a random number u is generated uniformly in the interval [0,1], so that

  + If $u \leq \alpha$, the candidate is accepted, so that $x_{i+1} = x_i$. In particular, this is always satisfied if $f(x') > f(x_i)$.
  - If $u > \alpha$, the candidate is rejected, so that $x_{i+1} = x_i$.

With these rules, the algorithm will tend to find the points of maximum probability, but still sampling the nearby area with a certain probability, dropping more as f decreases. After a sufficient time of iterations, the sampled points should reach an equilibrium distribution which coincides with the distribution of $f(x)$.

This algorithm has some drawbacks, of which we mention three of them. First, the points of nearby iterations of a certain chain are correlated, so, to correct for this behavior, it is necessary to take the points of a chain only every N_{thin} iterations. For this purpose, a useful quantity is the autocorrelation time τ_i [133], which measures how many iterations have to pass until a point "forgets" where it started. This quantity is chain-dependent, so it is usually good to set a common autocorrelation time as $\tau = \max_i \tau_i$. Then, we can *thin* our distribution by this quantity, $N_{\text{thin}} = \tau$ (even half of it is enough, $N_{\text{thin}} = \tau/2$), which means taking only the iterations every N_{thin} steps.

Another problem of this method is that the first iterations do not follow the final distribution so, once sampled, it is necessary to get rid of them, in a procedure called *burn-in*, which consists on removing the first N_{burn} iterations. A good number is usually around 2 or 3 times τ. Finally, the MCMC does not have a natural stopping criterion, so the user has to impose one. The usual practice is to stop the MCMC after $50 - 100$ autocorrelation times.

We will apply this method in Chapter 10. For now, let us see the other main family of samplers.

Nested sampling

Nested sampling is an alternative to MCMC which was proposed in 2004 by John Skilling [134]. This method is designed to compute the evidence and generates posterior samples as a byproduct.

The idea of nested sampling is populating the parameter space by drawing a certain number of so-called *live points* from the prior distribution. Then, at each iteration i, the point with the lowest likelihood L_i is removed and saved as a sample point with a certain assigned prior volume w_i, adding its contribution $L_i w_i$ to the evidence. The point is then substituted by a new one with a higher likelihood, possibly found with some MCMC steps.

The algorithm is continuously moving towards higher likelihood areas. At each iteration, if we assume that all the remaining prior volume has a likelihood equal to the maximum likelihood live point, we get an upper bound for the evidence. This quantity can then be used to impose a termination condition, so that the algorithm stops when the current computed evidence reaches a certain fraction of the upper bound. In practice, this is given by the quantity $(\Delta \ln Z)_i = \ln Z_{i,\max} - \ln Z_i$, where $Z_{i,\max}$ denotes the evidence upper bound at iteration i and Z_i, the actual computed number. What this is saying is that, at most, $\ln Z$ will be able to increase by $(\Delta \ln Z)_i$, so at some small value, which is usually around 0.1, it is pointless to continue the sampling since the evidence is already very precisely characterized: it is usually several orders of magnitude higher.

A variation of these methods is given by the *dynamic nested sampling*, in which the number of samples in different regions is dynamically adjusted to maximize accuracy. Examples of implementation of nested sampling in Python include PyMultinest [135] and PolyChord [136, 137], while for dynamic nested sampling there is the dynesty package [138], which is the state-of-the-art sampler in areas like gravitational-wave physics and other branches of Astrophysics and Cosmology.

In the next sections, we will see some applications of these techniques to real gravitational-wave data.

2.3.3 Post-processing techniques

Contours, credible regions and upper bounds

In these analyses based on parameter estimation, the output is an n-dimensional posterior distribution. If we want to give an estimate for a certain parameter, the usual procedure is to marginalize over the rest of the parameters and provide some central value and estimated uncertainty. The central value can be the mean, the median or the value that maximizes the likelihood, which is called *maximum likelihood estimate* (MLE).

For the uncertainty, one takes the marginalized posterior distribution to determine the central interval that encloses some fraction of the total probability, which is called *credible interval*, as opposed as in frequentist analysis, where they are called *confidence intervals*. Here, "central" means there is exactly half of the remaining probability below it, and half above it. For a Gaussian distribution of mean μ and width σ, the total probability enclosed between $\mu - \sigma$ and $\mu + \sigma$ is 0.68, so, by analogy, any central interval enclosing 68% of the total probability is called *1-sigma region*, and its half-width is called *1-sigma uncertainty*, or 1-sigma error. Similarly, the 2-sigma region encloses 95% of the total probability, while the 3-sigma region covers 99.7%. These regions are illustrated in Fig. 2.3. It is thus common to provide the 1-sigma (or n-sigma) error as an uncertainty estimation.

However, there might be cases in which we do not aim to provide a final value of a parameter. In the case of a SGWB analysis, this background has not yet been detected, so it is still soon to derive

its value, which is dominated by uncertainties. Instead, it is better to provide an upper bound, indicating that the SGWB amplitude is very likely to be under that value. In this case, one can take the corresponding posterior distribution and find the point below which the probability is 95%, thus labeled 95% *credible-level* (CL) *upper bound* (see Fig. 2.3). One can also provide upper bounds with different credible levels, but 95% is a standard widely used in the literature [139, 28, 97, 140].

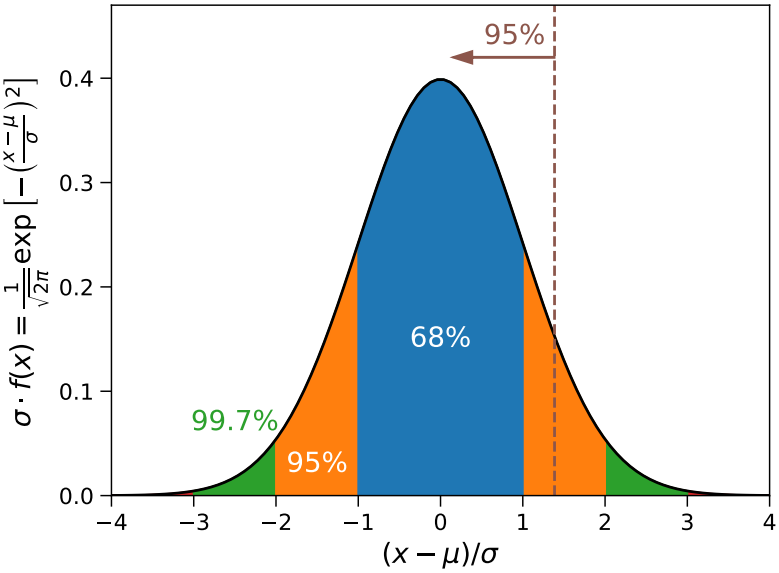

Figure 2.3: Gaussian PDF illustrating the 1-sigma (blue), 2-sigma (orange+blue) and 3-sigma (green+orange+blue) regions, covering the 68%, 95% and 99.7% of the total central probability, respectively. The dashed, vertical line also marks the 95% credible-level upper bound.

In addition, it is often useful to look at 2D posteriors, marginalized over all the parameters except for two of them. In this case, one can also define credible regions, which, in analogy with the 1D case, are usually plotted at 68% and 95% credible levels. Some authors refer to them as 1-sigma and 2-sigma regions, which is somewhat confusing: in 2D, a multivariate Gaussian with covariance matrix $\sigma\mathbb{I}$, with $\mathbb{I}$ the identity matrix, encloses 39% probability inside the radius $|\vec{x}| = \sigma$ and 0.86% inside $|\vec{x}| = 2\sigma$. Thus, it is preferable to simply call them 68% and 95% CL regions, to avoid the ambiguity. See the CORNER Python package documentation [141] for a more detailed discussion.

These credible level regions are marked by a closed curve enclosing, called *contour*. Some examples of 2D contours, which are usually plotted together with the marginalized 1D posteriors in a joint figure called *corner plot*, can be seen in Figs. 2.4, 2.6, 3.1 and D.1-D.3.

In Section 2.5 and Chapter 10, we will use these concepts to set upper bounds to some SGWB-related quantities. Before that, let us see one more useful post-processing technique for MCMC.

Evidence estimate for Gaussian posteriors

Even if both MCMC and nested sampling are used for parameter estimation, there are some differences between them that make either one or the other better suited for each problem. Nested sampling has the advantage that it computes the evidence of the model, while MCMC, in general, does not.

When the algorithm only provides the posterior samples, and does not give any estimate of the model evidence, it can be difficult to compute it in a precise way. As defined in Eq. (2.68), the evidence computation involves an integral in an n-dimensional space, which can be computationally expensive to estimate accurately.

Nevertheless, under some hypotheses, it is possible to obtain analytic estimates. This is the case if the posterior distribution approximately follows a multivariate Gaussian distribution, which is usually the case for large datasets due to the Central Limit Theorem [113]. In particular, this assumption holds in our article [4], explained in detail in Chapter 10. If this is the case, we only need the posterior covariance matrix Σ and the maximum likelihood $\mathcal{L}$ to compute the evidence, using the approach described in [142].

With the notations introduced at the beginning of the section, the multivariate Gaussian posterior hypothesis implies that

$$\mathcal{L}(\vec{\theta})\pi(\vec{\theta}) \approx C \exp\left(-\frac{1}{2}(\vec{\theta}-\vec{\mu})^T\Sigma^{-1}(\vec{\theta}-\vec{\mu})\right) \tag{2.76}$$

where μ is the mean of the distribution, Σ its covariance matrix and C a certain unknown constant. We should keep in mind that this is not a proper distribution because it is not normalized (the normalization comes from dividing by the evidence in Eq. (2.67)), so C is not a normalization constant. In order to compute it, we realize that $\mathcal{L}(\vec{\mu})\pi(\vec{\mu}) = C$. Here, we introduce the additional assumption that the priors are uniform, so that $\pi(\vec{\theta}) = 1/V$ for any $\vec{\theta} \in V$, where V is the prior volume. Therefore,

$$\mathcal{L}(\vec{\theta})\pi(\theta) \approx \frac{\mathcal{L}(\vec{\mu})}{V} \exp\left(-\frac{1}{2}(\vec{\theta}-\vec{\mu})^T\Sigma^{-1}(\vec{\theta}-\vec{\mu})\right) \tag{2.77}$$

As a result, the evidence is just its integral,

$$Z = \int_V \mathcal{L}(\vec{\theta})\pi(\vec{\theta})d\vec{\theta} \approx \frac{\mathcal{L}(\vec{\mu})}{V} \int_V \exp\left(-\frac{1}{2}(\vec{\theta}-\vec{\mu})^T\Sigma^{-1}(\vec{\theta}-\vec{\mu})\right) d\vec{\theta}. \tag{2.78}$$

In order to make this integral simpler, we now make a third assumption, which that the distribution of our posteriors has a low value at the edge of the prior volume. This way, the probability outside V can be approximated by zero, so that the previous integral can be computed in the full $\mathbb{R}^n$, with n the dimension of the parameter space. Knowing that the result of this integral is

$$\int_{\mathbb{R}^n} \exp\left(-\frac{1}{2}(\vec{\theta}-\vec{\mu})^T\Sigma^{-1}(\vec{\theta}-\vec{\mu})\right) d\vec{\theta} = (2\pi)^{n/2}\det(\Sigma)^{1/2}, \tag{2.79}$$

we finally have

$$Z = \int_{\mathbb{R}^n} \mathcal{L}(\vec{\theta})\pi(\vec{\theta})d\vec{\theta} \approx \frac{\mathcal{L}(\vec{\mu})}{V}(2\pi)^{n/2}\det(\Sigma)^{1/2}. \tag{2.80}$$

Finally, if we compare two different models M_1 and M_2 with equal prior probabilities, their Bayes factor in Eq. (2.70) will be given by

$$\mathcal{B}^{M_1}_{M_2} \approx \frac{\mathcal{L}_1(\vec{\mu}_1)}{\mathcal{L}_2(\vec{\mu}_2)} \frac{V_2}{V_1} (2\pi)^{(n_1-n_2)/2} \left(\frac{\det(\Sigma_1)}{\det(\Sigma_2)} \right)^{1/2} . \tag{2.81}$$

2.3.4 Parameter estimation of isotropic SGWB

Applying the theory from Sec. 2.2, we can now compare the data to a given model for $\Omega_{\rm gw}(f)$. For this purpose, we take a Gaussian likelihood and use the estimators $\hat{\Omega}^{IJ}_{\rm gw}(f)$ in Eq. (2.61) with its variance $\hat{\sigma}^2_{IJ}(f)$ in Eq. (2.62), so that

$$\ln \mathcal{L} = -\frac{1}{2} \sum_{IJ} \sum_{f} \left(\frac{\hat{\Omega}^{IJ}_{\rm gw}(f) - \lambda_{IJ} \Omega^{M}_{\rm gw}(f)}{\sigma_{IJ}} \right)^2 , \tag{2.82}$$

where the factor λ_{IJ} accounts for the calibration uncertainty in each baseline. Following the approach in [143], this factor is modeled as a Gaussian distribution with mean 1 and variance ϵ^2_{IJ}, and then marginalized analytically before running the parameter estimation [110]. If we denote the calibration uncertainty of each detector I by ϵ_I, then the variance for λ_{IJ} can be estimated as the quadratic sum, $\epsilon^2_{IJ} = \epsilon^2_I + \epsilon^2_J$. See [5, 28, 122, 139] for the exact numbers used in each work.

Additionally, the frequency range we consider for parameter estimation is usually from 20 to 1726 Hz. Outside this range, the detectors still take data, but their sensitivity starts being too low to be useful for any analysis.

2.4 Constraints from LVK

The LVK collaboration analyzes the data from their detectors (LIGO, Virgo, KAGRA) and produces estimates and upper bounds for the stochastic gravitational wave background after every observing run. These works which look for the SGWB are usually called *searches*. We are currently immersed in the fourth observing run of GW detectors (O4), so the most results are those from O3 [28], produced in 2021. During this third observing run, the KAGRA detector sensitivity was not enough to produce these estimates, similar to what happened with Virgo for O1 [139] and O2 [122]. Therefore, there are three baselines used for the analysis: HL, HV and HV, where H stands for LIGO Hanford, L for LIGO Livingstone and V for Virgo.

The estimates provided in [28] can be classified in two types: broadband estimates like the ones defined in Eqs. (2.65) and (2.66) and others derived from the posteriors of a Bayesian analysis using the formalism of Sec. 2.3. In any of the cases, when a power-law $\Omega_{\rm gw}(f)$ (Eq. (2.63)) is considered, they work with three scenarios:

- $\alpha = 0$. This corresponds to a flat $\Omega_{\rm gw}(f)$ spectrum, which arises for cosmic strings [78, 79]. R^2 inflation [76] or slow-roll inflation [144], as can be seen in Fig. 2.1.
- $\alpha = 2/3$. This corresponds to the frequency dependence of the inspiral of CBCs, as can be seen in Eq. (1.196) and is computed more in detail in Chapter 5.

α	$\hat{\Omega}_\alpha/10^{-9}$					
	O1	O2	O3			O1+O2+O3
			HL	HV	LV	
0	44 ± 59	22 ± 22	-2.1 ± 8.2	229 ± 98	-134 ± 63	1.1 ± 7.5
2/3	35 ± 44	20 ± 16	-3.4 ± 6.1	145 ± 60	-82 ± 40	-0.2 ± 5.6
3	3.7 ± 6.5	3.5 ± 2.8	-1.3 ± 0.9	9.1 ± 4.1	-4.9 ± 3.1	-0.6 ± 0.8

Table 2.1: Broadband estimates $\hat{\Omega}_\alpha$ given by Eq. (2.65), for a power-law $\Omega_{\rm gw}$ of exponent α and reference frequency $f_{\rm ref} = 25$ Hz. A separate estimate is provided for O1 [139], O2 [122] and O3 [28] LVK data, in this last case separated by baseline, together with the joint O1+O2+O3 estimates.

- $\alpha = 3$. This corresponds to a flat strain spectrum $S_h(f)$, as seen in the relation between $\Omega_{\rm gw}$ and $S_h(f)$ in Eq. (2.15). It approximately describes some astrophysical sources such as supernovae [70, 71, 72, 73].

For each of these power-law indices, they obtain the broadband estimates as in Eq. (2.65) for a reference frequency of $f_{\rm ref} = 25$ Hz. They do this separately for each baseline, and also provide a combined estimate with the three of them for O3 together with the HL baseline for O1 and O2, which was the only one available in those observing runs. The results are summarized in Table 2.1, together with the O1 and O2 results for reference. We can see how the combined estimates get lower with each observing run.

In addition, the LVK collaboration uses the narrowband estimates in Eqs. (2.61) and (2.62) to do parameter estimation with the likelihood in Eq. (2.82). For this purpose, they consider a power-law $\Omega_{\rm gw}(f)$ with the three fixed indices $\alpha = 0, 2/3, 3$ mentioned above, but also one with free α. They do two runs for each case: in one of them, the prior for Ω_α is uniform, where the lower and upper ends are large enough so the posterior does not have any support there. In the other case, a log-uniform prior is taken (meaning a uniform prior in $\log \Omega_\alpha$), where the upper end satisfies the same criterion as for the uniform case and the lower end is taken to be $\Omega_\alpha = 10^{-13}$. For the cases of free α, a Gaussian prior is chosen for this exponent, with zero mean and standard deviation 3.5.

For each of these runs, upper bounds are provided in Table 2.2. Additionally, the corner plot for the case of variable α and log-uniform prior for Ω_α is shown in Fig. 2.4. We can see how the upper bounds progressively get reduced with each observing run.

In the article [28], there are also other models considered, but the goal of this section was just to give a brief overview of the state of the art in LVK, so the power-law models are enough for this purpose.

In addition to the formalism that has been explained here, the LVK collaboration does some data quality checks and additional modifications to the data: high-pass filtering, glitch removing through a technique called gating [145], removing time segments for which σ estimates are too different from its neighbours (delta-sigma cut [146]), etc. I will not cover them in this thesis, so one can refer to [28, 110] for more details. They are also integrated in standard tools like PYGWB [147, 110]. In the next subsection, we will see a similar parameter estimation work which we did in a recent article using this Python package, where the model is more complicated than the power laws considered here.

α	$\hat{\Omega}_\alpha^{\rm up}$ (95%) $/10^{-9}$					
	Uniform prior			Log-uniform prior		
	O1	O2	O3	O1	O2	O3
0	170	60	17	64	35	5.8
2/3	130	48	12	51	30	3.4
3	17	7.9	1.3	6.7	5.1	0.39
Free	250	110	27	55	34	6.6

Table 2.2: 95% credible-level upper bounds for the amplitude Ω_α of a power-law $\Omega_{\rm gw}(f)$ of exponent α and reference frequency $f_{\rm ref} = 25$ Hz. A separate estimate is provided for uniform and log-uniform priors and for the different datasets, consisting on O1 [139], O1+O2 [122] and O1+O2+O3 [28] LVK data. Three fixed-α cases are provided, as well as one with free α.

2.5 Constraints to non-Gaussianities from O3 data

In this section, I summarize the content of our article [5], in which we set constraints to a non-Gaussian, scalar-induced gravitational wave background. My main contribution to this work was the data analysis part, so this section will be focused on this aspect of the article.

2.5.1 Introduction

As we have seen at the beginning of this chapter, particularly in Fig. 2.1, there are a lot of sources, both astrophysical and cosmological, which can generate a stochastic gravitational wave background through different mechanisms. In particular, large curvature fluctuations generated during inflation produce one of these contributions, at the second perturbative order. This is called the *scalar-induced gravitational wave* (SIGW) *background*.

This is a very interesting source due to two reasons: first, it allows to test and characterize existing inflation models through gravitational waves at LVK frequencies [91, 92, 93, 94, 95, 96, 97], which correspond to much smaller scales than those probed by CMB observations. The second reason is that it relates to the formation of primordial black holes (PBHs), a topic which will be explained in more detail in Chapter 4. If these PBHs exist and constitute a relevant fraction of dark matter, the primordial curvature perturbations must be large enough to produce them, causing a strong contribution for the SIGW background. Thus, from the constraints of this contribution, one can better characterize the PBH scenario, which is getting increasing attention by the scientific community as more GW signals are detected.

Previous works have set constraints to this background from LVK O2 [96] and O3 [97] data. However, these articles assumed a Gaussian distribution for the primordial curvature perturbations, while other works argue that such a shape cannot be assumed, and the so-called *non-Gaussianities* are important [148, 149, 150, 151, 81, 85]. We elaborate more on the topic of non-Gaussianities in Subsec. 4.2.2. In our work [5], we set constraints to a non-Gaussian SIGW background, assuming a simple $F_{\rm NL}$ parametrization [152, 153, 154].

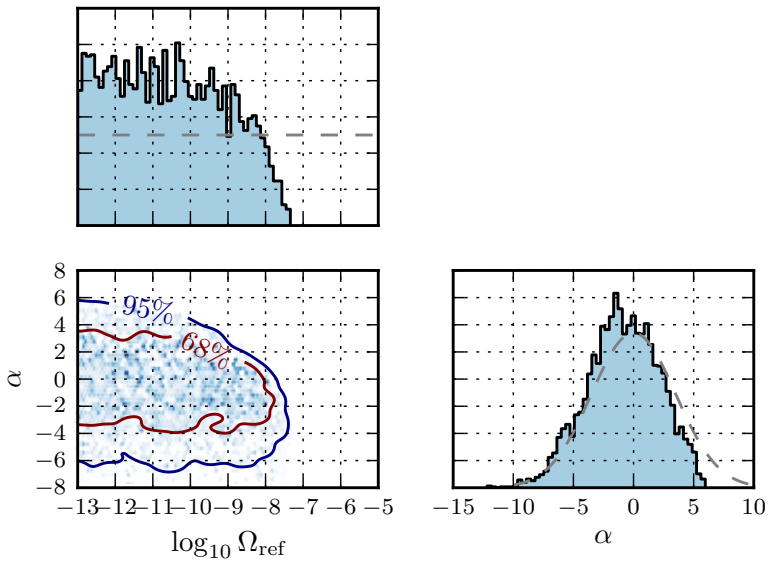

Figure 2.4: Corner plot for the parameter estimation run by LVK with a Gaussian prior for α and log-uniform prior for Ω_α, denoted here by $\Omega_{\rm ref}$. Figure taken from [28].

2.5.2 The model

The formalism to model a scalar-induced gravitational wave and, moreover, with non-Gaussianities, is not very related to the topic of this thesis and, therefore, it is only explained in detailed in App. A. What I will explain here are the strictly necessary elements to understand the data analysis component of the article.

We denote by ζ the primordial curvature perturbation in uniform energy density slices on super-horizon scales, which is a standard quantity in inflation theory. Its Gaussian component will be denoted by ζ_g. Following references like [155, 156, 154], we study the simplest and well-studied type of non-Gaussianity, which is local and quadratic,

$$\zeta(\vec{x}) = \zeta_g(\vec{x}) + F_{\rm NL}\zeta_g^2(\vec{x}), \tag{2.83}$$

where $F_{\rm NL}$ is called *non-linearity parameter*. One of its key properties is its power spectrum, which, for the Gaussian part, we denote by $P_g(k)$, so that

$$\langle \zeta_g(\vec{k})\zeta_g(\vec{k}')\rangle = (2\pi)^3\delta^3(\vec{k}+\vec{k}')P_g(k). \tag{2.84}$$

We consider a monochromatic power spectrum, which is expressed as

$$P_g(k) = \frac{2\pi^2}{k^3}A_g\delta(\ln k - \ln k_*), \tag{2.85}$$

where A_g is its amplitude and k_* is a scale parameter. This scale in k will determine another scale

in frequency through the relation

$$f = \frac{k}{2\pi} = 25 \left(\frac{k}{1.67 \times 10^{16}\ \mathrm{Mpc}^{-1}} \right) \mathrm{Hz}. \tag{2.86}$$

The frequency scale f_* corresponding to by k_* will determine the position of a peak in the $\Omega_{\rm gw}(f)$ spectrum, as we can see in Fig. 2.5.

As we can see in App. A, our model for SIGW will be proportional to f^2 times seven terms with different dependence on the A_g and $F_{\rm NL}$ parameters:

- The first contribution is the Gaussian part, which is proportional to A_g^2. We will denote this contribution as $A_g^2 \Omega_g(f/f_*)$.
- The next three terms correspond to the leading-order non-Gaussian correction. They are proportional to $F_{\rm NL}^2 A_g^3$, and we will denote the sum of these three terms as $F_{\rm NL}^2 A_g^3 \Omega_{\rm NG,1}(f/f_*)$.
- The final three terms are the next-order correction, proportional to $F_{\rm NL}^4 A_g^4$. We will denote their sum by $F_{\rm NL}^4 A_g^4 \Omega_{\rm NG,2}(f/f_*)$.

In order to have an intuition for the effect of the $F_{\rm NL}$ parameter, we can have a look at Fig. 2.5, where we plot the SIGW contribution to $\Omega_{\rm GW}(f)$ for a fixed value of A_g.

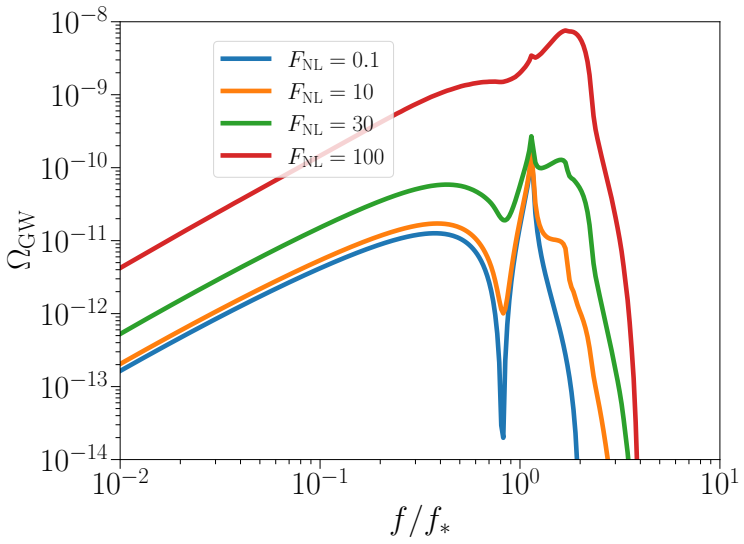

Figure 2.5: $\Omega_{\rm GW}(f)$ spectrum for different $F_{\rm NL}$ values, with $A_g = 0.001$.

Finally, we also consider the contribution from CBCs. The reason is that they are expected to be the dominant contribution in LVK frequencies [28, 29], so ignoring it will provide biased results. At the point we are now, with no detection of a SGWB, accounting for this effect may

not be crucial, but it will become more relevant with subsequent observing runs, as data gets a progressively stricter constraining power. Similar to other works [28, 97], we just model the inspiral part with a power-law of exponent 2/3 and reference frequency $f_{\rm ref} = 25$ Hz.

Therefore, our model can be expressed as

$$\Omega_{\rm gw}(f) = A_g^2 \Omega_g \left(\frac{f}{f_*}\right) \left(+ F_{\rm NL}^2 A_g^3 \Omega_{\rm NG,1} \left(\frac{f}{f_*}\right) \left(+ F_{\rm NL}^4 A_g^4 \Omega_{\rm NG,2} \left(\frac{f}{f_*}\right) + \Omega_{\rm CBC} \left(\frac{f}{f_{\rm ref}}\right)^{2/3} . \quad (2.87)$$

Note that, while $f_{\rm ref}$ is degenerate with $\Omega_{\rm CBC}$ and thus can be fixed without loss of generality, f_* is not degenerate with the other parameters, due to the more complicated frequency dependence of Ω_g, $\Omega_{\rm NG,1}$ and $\Omega_{\rm NG,2}$. Therefore, it will also be a free parameter. As a result, our model has four free parameters: A_g, f_*, $F_{\rm NL}$ and $\Omega_{\rm CBC}$, where we use k_* for the parameter estimation instead of f_*.

2.5.3 Data analysis

We run a similar parameter estimation as in the previous section, using the likelihood in Eq. (2.82). These runs are done through the PYGWB [147, 110] Python package, which relies on BILBY [124] for parameter estimation, using data from the first three observing runs of LVK [139, 122, 28, 157, 158]. To sample the parameter space, we use the DYNESTY [138] sampler, with the default `dlogz=0.1` convergence criterion and a large number of live points (of order 100,000) to get smoother posteriors. This `dlogz` parameter corresponds to the $\Delta \ln Z$ for nested sampling explained in Subsec. 2.3.2. Additionally, the priors for each parameter are indicated in Table 2.3.

Parameters	Prior
$\Omega_{\rm CBC}$	Log-uniform$[10^{-10},\ 10^{-7}]$
A_g	Log-uniform$[10^{-3.5},\ 10^{1}]$
$F_{\rm NL}$	Log-uniform$[10^{-1},\ 10^{4}]$
$k_*/{\rm Mpc}^{-1}$	Log-uniform$[10^{15.5},\ 10^{18.5}]$

Table 2.3: Prior distributions used for the parameter estimation.

First, we run the parameter estimation for the four free parameters with the priors in Tab. 2.3, showing the posterior distributions in the corner plot of Fig. 2.6. We add two lines to the $F_{\rm NL} - A_g$ subplot: the orange one marks the asymptotic behavior of the 95% CL contour, where the third term in Eq. (2.87), proportional to $F_{\rm NL}^4 A_g^4$, dominates. This line follows the equation $F_{\rm NL} A_g \approx 0.380$. The second, red line, roughly corresponds to the boundary where non-Gaussianities start to be comparable to the Gaussian contribution. For this line, we assumed Ω_g and $\Omega_{\rm NG,1}$ are similar in magnitude, so that the first and second terms in Eq. (2.87) are comparable when $A_g^2 \approx F_{\rm NL}^2 A_g^3$, or $F_{\rm NL}^2 A_g \approx 1$. Thus, the transition between Gaussian and non-Gaussian for the 95% CL contour occurs at its intersection with the red line, which is at $F_{\rm NL} \simeq 3.55$. We quote this transition value as one of our results, but one should keep in mind that this number not only depends on the data, but it is also prior and credible-level dependent.

From the $A_g - k_*$ subplot, we can also derive that, at 95% credible level, $A_g \lesssim 0.015$ for the best-constrained scale, $k_* \simeq 2.04 \times 10^{16}$ Mpc. However, this constraint marginalizes over $F_{\rm NL}$

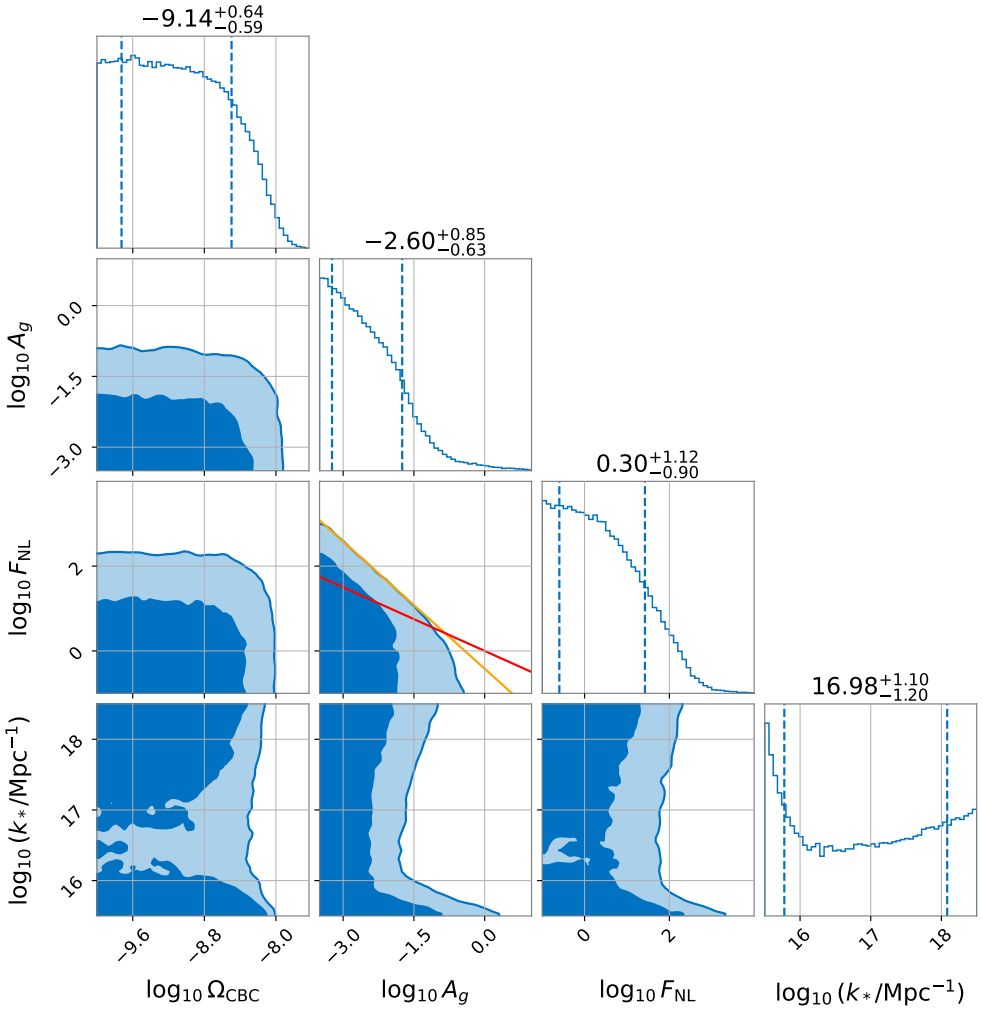

Figure 2.6: Posterior distributions for the combined SIGW and CBC search, where the blue and light blue contours correspond to the 68 and 95% CL regions, respectively. For reference, we plot the red line corresponding to $F_{\rm NL}^2 A_g = 1$, which is the boundary where the non-Gaussian terms start to dominate over the Gaussian contribution in the $\Omega_{\rm gw}(f)$ power spectrum (Eq. (2.87)). The orange line corresponds to the asymptotic behavior at large $F_{\rm NL}$ values, following $F_{\rm NL} A_g = 0.380$.

and A_g, which mixes all contributions of different $F_{\rm NL}$ and it is thus complicated to understand its effect. For this purpose, we did some 3-parameter runs with fixed $F_{\rm NL}$, while the rest of the parameters keep their priors from Table 2.3. From their posteriors, we take the 95% CL curves in the $A_g - k_*$ plane and show all of them together in Fig. 2.7. We can see that the constraints on A_g become tighter as $F_{\rm NL}$ increases, given that a larger $F_{\rm NL}$ enhances the overall SGWB amplitude. It is also worth noting that the shape of these curves varies with $F_{\rm NL}$, but in any case, similar k_* produce a minimum in all of them, corresponding to the best constrained frequencies in LVK data. Additionally, our curve for $F_{\rm NL} = 0$ should recover the Gaussian case studied in [97], which we find to be the case, except for some small differences due to our choice of priors and narrower primordial power spectrum $P_g(k)$ (2.85). Hence, both of our works are consistent.

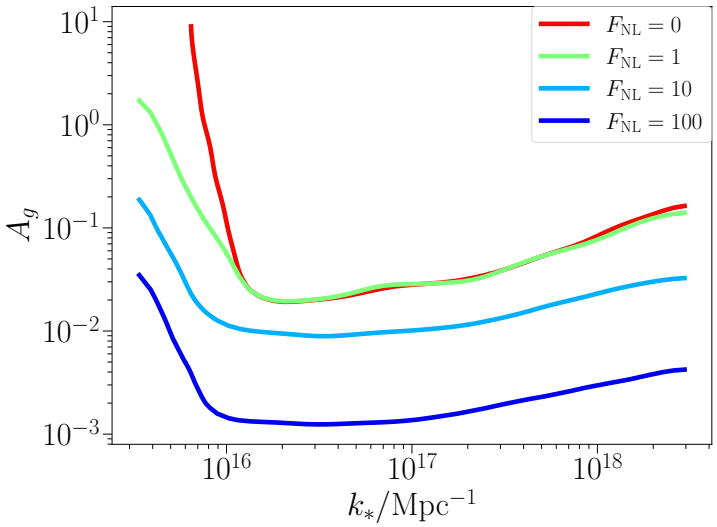

Figure 2.7: Posterior 95% CL contours for $A_g - k_*$, obtained from the fixed $F_{\rm NL}$ runs. The 95% CL region corresponds to the area under these curves.

Finally, we also examined the effect of the scale k_* on the $F_{\rm NL} - A_g$ constraints. Similarly to the previous case, we now fixed the scale parameter k_* and did 3-parameter runs with the rest of the priors corresponding to the ones in Table 2.3. In Fig. 2.8, we show the 95% CL contours for $F_{\rm NL} - A_g$ for $k_* = 10^{16}$, $10^{16.5}$ and 10^{17} Mpc. One of the main changes with respect to the 4-parameter case is that the asymptotic behavior for large $F_{\rm NL}$ keeps the same trend $F_{\rm NL}A_g$ =const., but the constant gets tighter. This is expected, since a parameter estimation run with less free parameters is usually more constraining. There is also small variability between different scales and, in particular, the constraint at $k_* = 10^{16.5}$ Mpc is slightly stronger, given that it corresponds to the case where the peak in $\Omega_{\rm gw}(f)$ is located at the most sensitive range of the LVK detectors:

$$F_{\rm NL}A_g \approx \begin{cases} 0.115 & (k_*/\mathrm{Mpc}^{-1} = 10^{16}) \\ 0.100 & (k_*/\mathrm{Mpc}^{-1} = 10^{16.5}) \\ 0.112 & (k_*/\mathrm{Mpc}^{-1} = 10^{17}). \end{cases} \tag{2.88}$$

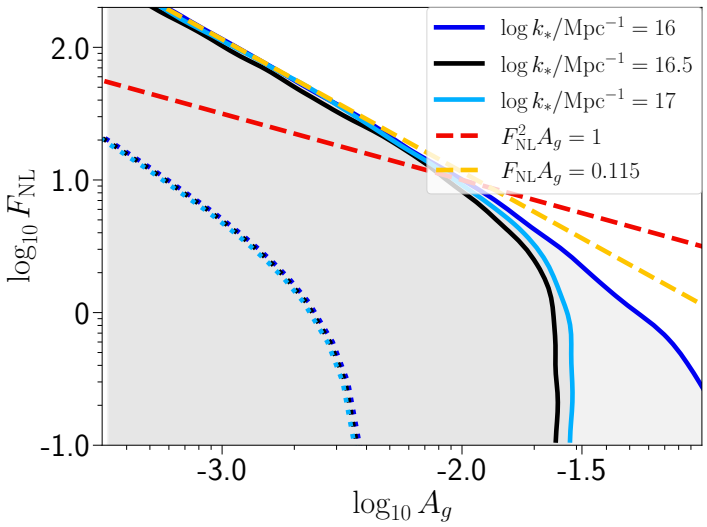

Figure 2.8: Posterior 95% CL contours for $A_g - F_{\rm NL}$ plane (solid lines), obtained from the fixed k_* runs. The dashed lines represent the asymptotic behavior for large non-Gaussianity (orange) and the red one marks the boundary where non-Gaussian term start to dominate over the Gaussian contribution in $\Omega_{\rm gw}(f)$, similar to the lines in Fig. 2.6. Dotted lines correspond to analytically derived relations between $F_{\rm NL}$ and A_g which show the limit at which PBHs make up 100% of the dark matter, showing small differences between different values of k_*.

We can see another, more obvious difference in Fig. 2.8 for low values of $F_{\rm NL}$ and high A_g, in which the contour for A_g is almost independent of $F_{\rm NL}$ for $k_* = 10^{-16.5}$ and 10^{-17} Mpc, while there is a clear correlation with $F_{\rm NL}$ for $k_* = 10^{-16}$ Mpc. The reason is that, below the dashed, red line, the non-Gaussian contributions are subdominant with respect to the Gaussian one. Also, as we can see in Fig. 2.5, the non-Gaussian contributions are more relevant for $f > f_*$. In this case, given the subdominance of the non-Gaussian contributions, only $k_* = 10^{-16}$ Mpc manages to make some difference by generating a relevant non-Gaussian contributions on LVK sensitive frequencies, which explains the difference of behavior with the other scales. Finally, the dotted lines represent the limit at which PBHs would constitute all the dark matter ($f_{\rm PBH} = 1$, see Chapter 4). They were computed using peak theory [159, 160] to estimate PBH abundance, while for generalizations for non-Gaussianity, we refer to [161, 162]. We can see that, for now, the constraints coming from gravitational waves are less stringent than those imposed by overproduction of PBHs.

2.5.4 Conclusions

In this work, we derived constraints for non-Gaussian primordial curvature perturbations using the most recent gravitational-wave data from LVK (O1-O3). This was done via the SIGW induced by second-order cosmological perturbations, which constitutes a unique probe for inflation at much smaller scales than those constrained by CMB measurements. Our model takes into account both

this SIGW contribution and the standard background coming from CBC inspirals.

From our 4-parameter run shown in Fig. 2.6, we derived an upper bound $A_g < 0.015$ for $k_* = 2.04 \times 10^{16}$ Mpc at 95% credible level. In addition, we observed that the influence of non-Gaussianities on $\Omega_{\rm gw}(f)$ becomes non-negligible when $F_{\rm NL} \simeq 3.55$. Given that marginalized constraints inevitably depend on the range of priors, we have also run similar analyses with either the $F_{\rm NL}$ parameter or the peak scale k_* fixed (Figs. 2.7 and 2.8). Although the current constraints are weaker than those imposed by overproduction of PBHs, Fig. 2.8 shows that, by refining these constraints with new measurements, gravitational waves will eventually be able to place meaningful constraints on the PBH production. In particular, it is expected that much stronger constraints are imposed by third-generation GW detectors such as the Einstein Telescope [17] and Cosmic Explorer [18].

Finally, we have assumed a quadratic, local non-Gaussianity, which represents the simplest parametrization. However, it is known that non-Gaussian tails can vary significantly depending on the mechanisms which generate these large curvature perturbations [85, 81, 163, 164, 149, 165, 166, 167, 168, 150, 169]. One of the main theoretical challenges is developing a computing method for the SIGW spectrum which is able to handle arbitrary shapes of non-Gaussianity. Once such a robust framework is developed, we will be able to provide more valuable observational constraints for primordial curvature perturbations. This task is becoming increasingly important due to the anticipated increase in observational opportunities with gravitational waves.

Chapter 3

SGWB anisotropies

In the previous chapter, we have worked under three assumptions for the SGWB: that it is stationary, unpolarized and isotropic. In the absence of a detection, the assumption of isotropy is the most reasonable approach: similar to the CMB, we expect that this assumption is satisfied to first order. However, we also know from the CMB that anisotropies carry a tremendous amount of information which is inaccessible via the isotropic component. Hence, once we detect the isotropic component of the SGWB, the next goal will be to characterize its anisotropies.

Simultaneous to the isotropic searches, there have also been *directional searches* looking for these anisotropies, going as far back as to, at least, the analysis of the fifth science run (S5) of LIGO [170] in 2011, while the most recent results are those from O3 [171]. On the other hand, isotropic searches have been performed from LIGO's first science run (S1), with the first analysis being released in 2003 [172].

In this chapter, we will study the formalism for an anisotropic SGWB, based mainly on [111, 112], in Sec. 3.1. In Sec. 3.2, we will see a data analysis work on the SGWB anisotropies [3], to which I contributed mainly in the code optimization and model selection analysis.

3.1 Formalism for anisotropic SGWB

In Section 2.1, we saw the formalism for an isotropic SGWB. We will follow a similar approach, changing and introducing new notation where necessary. For this purpose, we start from the two-point estimator Eq. (2.3), for which we defined an angle-independent function called PSD, $S_h(f)$. Now, we aim to follow a similar procedure but introducing an angular dependence, so we define a function $\mathcal{P}(f,\vec{n})$ such that

$$\langle \tilde{h}^*_A(f,\vec{n})\tilde{h}_{A'}(f',\vec{n}')\rangle = \frac{1}{4}\delta(f-f')\delta^2(\vec{n},\vec{n}')\delta_{AA'}\mathcal{P}(f,\vec{n}). \tag{3.1}$$

Besides the introduction of an angular dependence, note the differences with respect to Eq. (2.3): the normalization factor 4π for the solid angle integration is missing, and the $1/2$ factor has been replaced by $1/4$. This is to match the notation of [111], which will be the main reference we will

follow for this chapter, as well as our article [3]. It is also common to denote the angular dependence by $\hat{\Omega}$ instead of $\vec{n}$, but we will stick to the latter to match our notation from previous sections.

We can then go forward in our isotropic formalism in Sec. 2.1 by substituting $S_h(f) \mapsto 2\pi\mathcal{P}(f,\vec{n})$, as long as an integration over the solid angle has not been made. Otherwise, one can substitute $S_h(f) \mapsto (1/2) \times \int d^2\Omega\, \mathcal{P}(f,\vec{n})$. Then, from Eq. (2.15), we get

$$\Omega_{\rm gw}(f) = \frac{2\pi^2}{3H_0^2} f^3 \int d^2\Omega\, \mathcal{P}(f,\vec{n}). \tag{3.2}$$

Similar to what was done for $\Omega_{\rm gw}$ in Eq. (2.8) and $\Omega_{\rm gw}(f)$ in Eq. (2.12), which have different definitions, it is common practice to define, in another slight abuse of notation,

$$\Omega_{\rm gw}(f,\vec{n}) \equiv \frac{1}{\rho_c} \frac{d\rho_{\rm gw}}{d(\ln f)\, d^2\Omega}, \tag{3.3}$$

so that, from Eq. (3.2), we have

$$\Omega_{\rm gw}(f,\vec{n}) = \frac{2\pi^2}{3H_0^2} f^3 \mathcal{P}(f,\vec{n}). \tag{3.4}$$

We must now go through the formalism for detected gravitational waves in Sec. 2.2. We first decompose the signal as in Eq. (2.29) with one key difference: in the isotropic case, the Earth's rotation was irrelevant, given that one can always do the analysis in the Earth's reference system and, even if the background rotates, the isotropic component will remain invariant. Now, we want to characterize the background anisotropies, so a rotation will make them change in time. Therefore, we consider a static reference frame in which it is the Earth what rotates, and not the background, so the detector's position will be time-dependent. In practice, the analyses in the literature account for the Earth rotation, which is the clearly dominant effect, but not for the Earth's motion around the Sun or the Solar System local motion. These subdominant effects can be modeled as time-dependent anisotropies inducing a dipole, similar to the case of the CMB [173, 174]. We will talk more about this in Subsec. 3.2.3.

In any case, for now, we will suppose that the background is time-independent, but the detector's position $x_I(t)$ is not. Whenever it is necessary, we will assume that our detector is ground-based, so that its position is periodic over time, with a period corresponding to an Earth's sidereal day (a standard day is measured with respect to the Sun, not the background). Thus, Eq. (2.29) can now be replaced by

$$h_I(t) = \sum_{A=+,\times} \int_{-\infty}^{\infty} df \int d^2\Omega\, \tilde{h}_A(f,\vec{n}) F_I^A(\vec{n},t) e^{-2\pi i f(t-\vec{n}\cdot\vec{x}_I(t)/c)}. \tag{3.5}$$

We can now correlate the signals of different detectors and get the equivalent equation to Eq. (2.32),

$$\langle s_I(t) s_J(t)\rangle = \frac{1}{2} \sum_{A=+,\times} \int_0^{\infty} df \int d^2\Omega\, F_I^A(\vec{n},t) F_J^A(\vec{n},t) \mathcal{P}(f,\vec{n}) e^{2\pi i f \vec{n}\cdot(\vec{x}_I(t)-\vec{x}_J(t))/c)}. \tag{3.6}$$

If we now short-Fourier transform the left-hand side, similar to what was done in Sec. 2.2 but without yet relating these quantities to $\Omega_{\rm gw}(f)$, we get

$$2\langle s_I^*(f,t) s_J(f,t)\rangle = \frac{T}{2} \sum_{A=+,\times} \int d^2\Omega\, F_I^A(\vec{n},t) F_J^A(\vec{n},t) \mathcal{P}(f,\vec{n}) e^{2\pi i f \vec{n}\cdot(\vec{x}_I(t)-\vec{x}_J(t))/c)}, \tag{3.7}$$

where, as usual, the factor 2 on the left-hand side comes from redefining the frequency integration range from the real to the positive numbers. Given that the right-hand side now depends on time, the expected value of the left-hand side must not be understood as a time average, but an average over many equivalent times, where the concept of "equivalent" is given by the Earth rotation. Therefore, two times are equivalent if their difference is an integer multiple of a sidereal day.

We now define the quantity

$$\gamma_{IJ}(\vec{n}, f, t) \equiv \frac{1}{2} \sum_{A=+,\times} F_I^A(\vec{n}, t) F_J^A(\vec{n}, t) e^{2\pi i f \vec{n} \cdot (\vec{x}_I(t) - \vec{x}_J(t))/c}, \tag{3.8}$$

which has the same role as the overlap reduction function in Eq. (2.33): accounting for the relative position of the two detectors and absorbing other factors which are not relevant in the analysis. In the isotropic case, and substituting the detector positions by their static versions, this function would be related to the ORF $\gamma_{IJ}(f)$ as

$$\gamma_{IJ}(f) = \frac{5}{4\pi} \int\!\!\int d^2\Omega\, \gamma_{IJ}(\vec{n}, f, t). \tag{3.9}$$

Using Eq. (3.8) and going back to the definition of the cross-spectral density $C_{IJ}(f,t)$, we can rewrite Eq. (3.7) as

$$\langle C_{IJ}(f,t) \rangle = \int\!\!\int d^2\Omega\, \gamma_{IJ}(\vec{n}, f, t) \mathcal{P}(f, \vec{n}), \tag{3.10}$$

In general, it is assumed that the angular and frequency dependences can be factorized,

$$\mathcal{P}(f, \vec{n}) = \mathcal{P}(\vec{n}) \bar{H}(f), \tag{3.11}$$

where $\bar{H}(f)$ is normalized so that, for a reference frequency $f_{\rm ref}$, $\bar{H}(f_{\rm ref}) = 1$. In particular, this means that, when considering a power-law model, there is no global amplitude in $\bar{H}(f)$,

$$\bar{H}(f) = (f/f_{\rm ref})^{\alpha - 3}, \tag{3.12}$$

where the exponent is usually set to $\alpha - 3$ so that, from Eq. (3.4), $\Omega_{\rm gw}(f, \vec{n})$ is proportional to f^α.

This factorization is standard in the literature and does not imply much loss of generality for small enough frequency bands [111, 112]. In any case, a similar formalism would apply if we considered a coupled dependence of the frequency and sky distribution, although some notations and simplifications would have to be modified. For simplicity and in order to follow the most standard approach, we will keep this assumption during this chapter. Thus, Eq. (3.10) can be rewritten as

$$\langle C_{IJ}(f,t) \rangle = \bar{H}(f) \int\!\!\int d^2\Omega\, \gamma_{IJ}(\vec{n}, f, t) \mathcal{P}(\vec{n}). \tag{3.13}$$

3.1.1 Basis decomposition

We now decompose the angular dependence in some basis, starting by the angular dependence of $\Omega_{\rm gw}(f, \vec{n})$, encoded in $\mathcal{P}(\vec{n})$. For this purpose, we need an orthonormal basis for the sphere $e_\mu(\vec{n})$, so that it should satisfy the property

$$\int\!\!\int d^2\Omega\, e_\mu^*(\vec{n}) e_\nu(\vec{n}) = \delta_{\mu\nu}. \tag{3.14}$$

Then, we can decompose $\mathcal{P}(\vec{n})$ as

$$\mathcal{P}(\vec{n}) = \mathcal{P}_\mu e_\mu(\vec{n}), \tag{3.15}$$

where, in this chapter, we also sum over repeated Greek indices, since they are related to an arbitrary spherical base, not to spacetime tensors in GR. Using the basis orthonormality property in Eq. (3.14), the coefficients can be obtained from $\mathcal{P}(\vec{n})$ as

$$\mathcal{P}_\mu = \iint d^2\Omega\, \mathcal{P}(\vec{n}) e^*_\mu(\vec{n}). \tag{3.16}$$

The two most standard basis choices are:

- A pixel basis, so that the index μ is the pixel position. The decomposition in Eq. (3.15) can then be expressed as
$$\mathcal{P}(\vec{n}) = \mathcal{P}_{\vec{n}'}\delta(\vec{n}, \vec{n}'). \tag{3.17}$$
This is the preferred choice to look for gravitational-wave point sources, in what is called *radiometer* analysis [175, 176, 177].

- A spherical harmonics basis, so that the index μ divides into the two multipole indices l, m. If we denote the spherical harmonics by $Y_{lm}(\vec{n})$, the decomposition in Eq. (3.15) can be expressed as
$$\mathcal{P}(\vec{n}) = \mathcal{P}_{lm} Y_{lm}(\vec{n}), \tag{3.18}$$
where we consider the dipole direction of this basis to be aligned with the Earth's rotation axis. This is the preferred choice to look for a diffuse background, dominated by low multipoles.

In this chapter, we will focus on the spherical harmonics basis. Since they will be extensively used in Chapters 8, 9 and 10, there is a detailed introduction to them in Sec. 8.7. For this chapter, we do not need to make use of any property aside from the orthonormality, so it is not necessary to introduce them in detail at this point.

If we decompose $\mathcal{P}(\vec{n})$ as in Eq. (3.15), we should express $\gamma_{IJ}(\vec{n}, f, t)$ in a similar basis. For this purpose, we decompose it as

$$\gamma_{IJ}(\vec{n}, f, t) = \gamma_{IJ,\mu}(f, t) e^*_\mu(\vec{n}), \tag{3.19}$$

where the coefficients can be obtained as

$$\gamma_{IJ,\mu}(f, t) = \iint d^2\Omega\, \gamma_{IJ}(\vec{n}, f, t) e_\mu(\vec{n}). \tag{3.20}$$

Note that these definitions differ from Eqs. (3.15) and (3.16) by a complex conjugation, following the notation in [178, 111, 3]. The reason to have opposite definitions becomes obvious when we substitute both $\gamma_{IJ}(\vec{n}, f, t)$ given by Eq. (3.19) and $\mathcal{P}(\vec{n})$ given by Eq. (3.15) into Eq. (3.13):

$$\begin{aligned}
\langle C_{IJ}(f,t)\rangle &= \bar{H}(f) \iint d^2\Omega \left(\gamma_{IJ,\mu}(f,t) e^*_\mu(\vec{n})\right) \left(\mathcal{P}_\nu e_\nu(\vec{n})\right) \\
&= \bar{H}(f)\gamma_{IJ,\mu}(f,t)\mathcal{P}_\nu \iint d^2\Omega\, e^*_\mu(\vec{n}) e_\nu(\vec{n}) \\
&= \bar{H}(f)\gamma_{IJ,\mu}(f,t)\mathcal{P}_\nu \delta_{\mu\nu} \\
&= \bar{H}(f)\gamma_{IJ,\mu}(f,t)\mathcal{P}_\mu,
\end{aligned} \tag{3.21}$$

so that the basis will not appear in the subsequent analysis.

The spherical harmonics basis has several advantages with respect to the pixel basis. In particular, for an isotropic background, using that $Y_{00} = 1/\sqrt{4\pi}$, Eq. (3.2) for $\Omega_{\rm gw}(f)$ in terms of $\mathcal{P}(f,\vec{n})$, Eq. (3.11) for the factorization of $\mathcal{P}(f,\vec{n})$ in terms of $\bar{H}(f)$ and $\mathcal{P}(\vec{n})$, and the spherical harmonics decomposition of $\mathcal{P}(\vec{n})$ in Eq. (3.15) imply

$$\Omega_{\rm gw}(f) = \frac{2\pi^2}{3H_0^2} f^3 \bar{H}(f)\sqrt{4\pi}\mathcal{P}_{00}, \tag{3.22}$$

from which we can derive the isotropic component from the anisotropic analysis. In addition, Eq. (3.9) for the relation of the ORF $\gamma_{IJ}(f)$ with the anisotropic $\gamma_{IJ}(f,\vec{n})$, together with its decomposition in Eq. (3.19), implies

$$\gamma_{IJ}(f) = \frac{5}{\sqrt{4\pi}}\gamma_{IJ,00}(f,t) \tag{3.23}$$

for any t. Furthermore, in the anisotropic case, the time dependence of $\gamma_{IJ,\mu}(f,t)$ in the spherical harmonics basis is especially simple. The spherical harmonics with multipole coefficient m show an angular periodicity $2\pi/m$ in ϕ so, in the context of a rotation $\phi = 2\pi t/T$, they have a temporal periodicity of T/m. Therefore, we can write

$$\gamma_{IJ,lm}(f,t) = \gamma_{IJ,lm}(f,0)\exp\left(2\pi i m \frac{t}{1\text{ sidereal day}}\right)\Bigg(\tag{3.24}$$

3.1.2 Anisotropic SGWB data analysis

In the isotropic analysis in Subsec. 2.2.2, we defined our likelihood from the $\hat{\Omega}_{\rm gw}(f,t)$ estimators in Eq. (2.61) and its variance in Eq. (2.62). In the anisotropic analysis, instead of using this estimator, the common practice is to use the cross-correlated spectra $C_{IJ}(f,t)$ and make use of the identity in Eq. (3.21). Going through a similar procedure as the one in Subsec. 2.2.2, one can show that its variance is [111, 112, 3]

$$\hat{\sigma}^2_{C,IJ}(f,t) = \frac{P_I(f,t)P_J(f,t)}{T\Delta f}. \tag{3.25}$$

Then, using Eq. (3.21), the equivalent likelihood to the one in Eq. (2.82), is

$$\ln\mathcal{L} = -\frac{1}{2}\sum_{IJ}\sum_{t,f}\frac{T\Delta f|C_{IJ}(f,t) - \bar{H}(f)\gamma_{IJ,\mu}(f,t)\mathcal{P}_\mu|^2}{P_I(f,t)P_J(f,t)}, \tag{3.26}$$

Expanding the square of this equation, we get

$$2\ln\mathcal{L} = -\sum_{IJ}\sum_{t,f}\frac{T\Delta f|C_{IJ}(f,t)|^2}{P_I(f,t)P_J(f,t)} + 2{\rm Re}[\mathcal{P}^*_\mu X_\mu] - \mathcal{P}^*_\mu\Gamma_{\mu\nu}\mathcal{P}_\nu, \tag{3.27}$$

where we defined

$$X_\mu = \sum_{IJ}\sum_{t,f}\Bigg(\gamma^*_{IJ,\mu}(f,t)\frac{T\Delta f\,\bar{H}(f)}{P_I(f,t)P_J(f,t)}C_{IJ}(f,t), \tag{3.28}$$

$$\Gamma_{\mu\nu} = \sum_{IJ} \sum_{t,f} \left(\gamma^*_{IJ,\mu}(f,t) \frac{T \Delta f \, \bar{H}^2(f)}{P_I(f,t) P_J(f,t)} \gamma_{IJ,\nu}(f,t) \right). \tag{3.29}$$

If $\bar{H}(f)$ is given by a power law with a fixed exponent, meaning we do not consider it as a free parameter, then the likelihood in Eq. (3.27) is quadratic in the coefficients. This makes it straightforward to derive the maximum likelihood estimate: one can find the local extrema by taking the partial derivatives with respect to $\mathcal{P}_\mu$ and making them equal to zero. In this case, the maximum likelihood estimates for the $\mathcal{P}_\mu$ are given by

$$\hat{\mathcal{P}}_\mu = (\Gamma^{-1})_{\mu\nu} X_\nu. \tag{3.30}$$

Due to this equation, X_μ is usually called *"dirty" map*, as it represents the sky distribution of the gravitational wave background as seen through the beam matrix of the two detectors, $\Gamma_{\mu\nu}$. Then, the estimator $\hat{\mathcal{P}}_\mu$ in Eq. (3.30) is named *"clean" map*, showing the real sky distribution of the gravitational waves. In addition, in the weak-signal approximation, the dirty map variance is given by [111]

$$\langle X_\mu X^*_\nu \rangle - \langle X_\mu \rangle \langle X^*_\nu \rangle \approx \Gamma_{\mu\nu}, \tag{3.31}$$

so that, for the clean map, we have

$$\langle \hat{\mathcal{P}}_\mu \hat{\mathcal{P}}^*_\nu \rangle - \langle \hat{\mathcal{P}}_\mu \rangle \langle \hat{\mathcal{P}}^*_\nu \rangle \approx \left(\Gamma^{-1} \right)_{\mu\nu}. \tag{3.32}$$

Given that this is a matrix whose inverse is the covariance matrix of the parameters, $\Gamma_{\mu\nu}$ is called *Fisher information matrix*.

Aside from requiring fixing the power-law exponent, the estimate $\hat{\mathcal{P}}_\mu$ has another, more important problem: the invertibility of $\Gamma_{\mu\nu}$. Similar to how we saw that the detector is blind to certain directions in Subsec. 2.2.1, the Fisher matrix has some eigenvalues close to zero, which make it close to singular and thus difficult to invert numerically. One possible solution is regularizing it by manually imposing a minimum eigenvalue. A reasonable criterion used in the literature [111, 112] is to keep the 2/3 largest eigenvalues, denoting the smallest one of them by $\lambda_{\min}$, and then set the smallest 1/3 eigenvalues to this $\lambda_{\min}$. This, however, introduces some bias in the results.

On the contrary, doing Bayesian inference over the likelihood defined in Eq. (3.27) does not present this problem, while it also allows to have a variable exponent in the power law or more generic models for $\bar{H}(f)$. In our article [3], explained in the next section, we follow this statistical approach.

3.2 Bayesian PE for targeted anisotropic GWB

3.2.1 Introduction

From the introduction of Chapter 2, we know there are many theoretical models which predict stochastic gravitational wave background contributions, spreading over a wide range of frequencies. Some of the main features we can use to distinguish between them are their amplitude and spectral shape, as studied previously. However, some of these sources also predict anisotropic angular

distributions [179, 180, 181, 182, 183, 184, 185, 186, 187, 188, 189, 190], so we can use these signatures to further characterize these signals and differentiate them better.

Most articles on the SGWB focus on its isotropic component [191, 139, 122, 28, 2]. However, there are also directional searches which look for anisotropies [170, 192, 193, 194, 171], mostly by computing the maximum likelihood estimates described in the previous sections. Finally, there a few which do *targeted* (assuming an a priori model) searches [195, 196], either by following a Bayesian approach or other statistical methods, but they are not so numerous as the previous ones.

In our article [3], we introduced a parameter estimation formalism based on the Bayesian framework. In addition to parameter estimation, we describe how to easily inject signals on the data and do different tests over them. In this thesis, I will focus on the formalism and model selection aspects of the article, the latter being the main part I contributed to.

3.2.2 The formalism

We start from the formalism explained in Sec. 3.1 with the choice of a spherical harmonics basis. In our article, we work with $\mathcal{P}_{lm}$ coefficients normalized by $\mathcal{P}_{00}$, such that

$$\bar{\mathcal{P}}_{lm} \equiv \frac{\mathcal{P}_{lm}}{\mathcal{P}_0}. \tag{3.33}$$

Therefore, we need an additional parameter which is able to change the global amplitude of the background. We denote this parameter by ϵ, so that the decomposition in Eq. (3.11) is now

$$\mathcal{P}_{lm}(f) = \epsilon \bar{H}(f) \bar{\mathcal{P}}_{lm}. \tag{3.34}$$

Therefore, for the isotropic case, Eq. (3.22) is now

$$\Omega_{\rm gw}(f) = \frac{2\pi^2}{3H_0^2} f^3 \bar{H}(f) \sqrt{4\pi}\epsilon. \tag{3.35}$$

In order to explain the data analysis formalism, we will use ϵ with this normalization. However, for the real data analysis, we normalize ϵ by $1/(\frac{2\pi^2}{3H_0^2} f_{\rm ref}^3)$ so that it coincides with the isotropic energy density parameter $\Omega_{\rm gw}(f_{\rm ref})$, given that it is much more natural to interpret the results with this normalization.

With these changes, the likelihood in Eq. (3.27) now takes the form

$$2\ln\mathcal{L} = -\sum_{IJ}\sum_{t,f} \frac{T\Delta f |C_{IJ}(f,t)|^2}{P_I(f,t)P_J(f,t)} + 2\epsilon \mathrm{Re}[\bar{\mathcal{P}}_\mu^* X_\mu] - \epsilon^2 \bar{\mathcal{P}}_\mu^* \Gamma_{\mu\nu} \bar{\mathcal{P}}_\nu, \tag{3.36}$$

where X_μ and $\Gamma_{\mu\nu}$ have the same definitions as in Eqs. (3.28) and (3.29), which we copy here again for better clarity in the next subsection:

$$X_\mu = \sum_{IJ}\sum_{t,f} \gamma^*_{IJ,\mu}(f,t) \frac{T\Delta f\, \bar{H}(f)}{P_I(f,t)P_J(f,t)} C_{IJ}(f,t), \tag{3.37}$$

$$\Gamma_{\mu\nu} = \sum_{IJ}\sum_{t,f} \gamma^*_{IJ,\mu}(f,t) \frac{T\Delta f\, \bar{H}^2(f)}{P_I(f,t)P_J(f,t)} \gamma_{IJ,\nu}(f,t). \tag{3.38}$$

Likelihood evaluation optimization

In general, the likelihood evaluation in Eq. (3.36) involves some products and multipole index contractions followed by a sum in frequency, another one in time and finally, in baseline, with the consequent computational cost. If we want our implementation to be generic, all these steps are unavoidable, but in practice, there are many cases in which we can skip some of these steps.

First of all, the first term in Eq. (3.36) can be computed in advance, so that, in practice, it behaves as a constant in each likelihood evaluation. In addition, if neither $\bar{H}(f)$ nor $\bar{\mathcal{P}}_\mu$ depend on time, the sum in this variable can be done beforehand. Moreover, whenever we have a known anisotropy distribution for which we do not want to estimate any parameter, then the $\bar{\mathcal{P}}_{lm}$ appearing in the second and third terms in Eq. (3.36) can be contracted with the corresponding $\gamma_{IJ,\mu}(f,t)$ in advance.

Thus, in this last ideal case, in each likelihood evaluation and for each baseline, it is only necessary to evaluate $\bar{H}(f)$, which may be parameter-dependent, multiply by precomputed quantities and by the global amplitude ϵ, integrate in frequency and sum the three contributions. Assuming that the frequencies are the same for all the baselines, we can also do the sum in baselines in advance. However, in general, the analyses in our article have only used one baseline, so this additional modification would not have made any difference.

This precomputation formalism can also be extended for parameter-dependent $\bar{\mathcal{P}}_{lm}$, as long as they can be decomposed as a sum of a few terms with parameter-dependent coefficients. This will be the case for the dipole artifact caused by Doppler effect introduced in the next subsection.

Signal injection

If we want a signal to be added to our data, from Eq. (3.21), we know that the cross-spectra $C_{IJ}(f,t)$ have to be modified like

$$C'_{IJ}(f,t) = C_{IJ}(f,t) + \epsilon^{\mathrm{inj}} \bar{H}^{\mathrm{inj}}(f) \gamma_{IJ,\mu}(f,t) \bar{P}^{\mathrm{inj}}_\mu. \tag{3.39}$$

If we substitute the extra term in the likelihood in Eq. (3.36), we get three additional terms,

$$-2\epsilon^{\mathrm{inj}} \mathrm{Re}\left[(\bar{\mathcal{P}}^{\mathrm{inj}}_\mu)^* X^{\mathrm{inj}}_\mu\right] - \left(\epsilon^{\mathrm{inj}}\right)^2 (\bar{\mathcal{P}}^{\mathrm{inj}}_\mu)^* \Gamma^{\mathrm{inj}}_{\mu\nu} \bar{\mathcal{P}}^{\mathrm{inj}}_\nu + 2\epsilon\epsilon^{\mathrm{inj}} \mathrm{Re}\left[\bar{\mathcal{P}}^*_\mu \Gamma^{(c)}_{\mu\nu} \bar{\mathcal{P}}^{\mathrm{inj}}_\nu\right], \tag{3.40}$$

where X^{inj}_μ and $\Gamma^{\mathrm{inj}}_{\mu\nu}$ follow the same definition as Eqs. (3.37) and (3.38), except that $\bar{H}(f)$ is replaced by its injected quantity $\bar{H}^{\mathrm{inj}}(f)$ and $\Gamma^{(c)}_{\mu\nu}$ is the coupled Fisher matrix, defined as

$$\Gamma^{(c)}_{\mu\nu} = \sum_{IJ} \sum_{t,f} \left(\gamma^*_{IJ,\mu}(f,t) \frac{T\Delta f\, \bar{H}(f) \bar{H}^{\mathrm{inj}}(f)}{P_I(f,t) P_J(f,t)} \gamma_{IJ,\nu}(f,t). \right. \tag{3.41}$$

In the article [3], some statistical consistency tests are done, so one can refer there to see the validity of this injection method. In the next subsection, instead, we will focus on the model selection aspects of this work, which involve injecting a signal and trying to recover it with different models.

3.2.3 Model selection

Given some observational data, it may be challenging to correctly derive its underlying model. For instance, a broken power-law $H(f)$ with similar exponents can easily be mistaken by a simple power-law model, especially if the noise is relevant. In this section of the article, we use our Bayesian formalism, particularly the Bayes factor explained in Sec. 2.3, to quantitatively compare between several models for a given injected signal.

In order to do these tests, we first took the noise from the CSD in the LIGO detectors with the projected O4 sensitivity. Then, we injected a signal from a certain model M_1 following the approach in the previous section. Subsequently, we run parameter estimation over the resulting $C_{IJ}(f,t)$ using the same model M_1 and, in a different run, we do the same for a different model M_2, with the same injected signal from M_1. Finally, we compute the Bayes factor between both models, and repeat the procedure for different values of injected parameters. We then plot the value of the Bayes factor over a 2-dimensional parameter space by coloring each tile, with each color representing a different value according to a color scale. This is what we will call a *heatmap*, which is one of the best ways to visualize the distribution of the Bayes factor over the parameter space.

Broken power-law versus power-law $\bar{H}(f)$ model

The first case we studied was under which conditions our pipeline was able to distinguish a broken power-law (BPL) $\bar{H}(f)$ from a simple power law (PL). The simple power law is modeled as in Eq. (3.12), while the broken power law is defined as

$$H_{\mathrm{BPL}}(f) \propto \begin{cases} (f/f_0)^{\alpha_1 - 3} & \text{if } f < f_0 \\ (f/f_0)^{\alpha_2 - 3} & \text{if } f \geq f_0 \end{cases}, \tag{3.42}$$

which must then be normalized so that $\bar{H}_{\mathrm{BPL}}(f_{\mathrm{ref}}) = 1$. This model has four free parameters: the two exponents α_1 and α_2, the middle frequency f_0 and the global amplitude ϵ. We can see an example posterior for this model in Fig. 3.1. In order to do this analysis, we injected a BPL model with fixed $\alpha_1 = 2/3$ and $f_0 = 100$ Hz, thus exploring the injected (ϵ, α_2) parameter space. For ϵ, we took a log-uniform prior distribution from 10^{-12} to $10^{0} = 1$, while for α_1, α_2, a Gaussian prior with zero mean and 3.5 standard deviation was chosen. Finally, for f_0, we took a uniform distribution between 20 and 500 Hz. For $\mathcal{P}_{lm}$, we took a model which follows the sky distribution of the Galactic plane, with maximum l of 7.

In Fig. 3.2, we show the heatmap produced from the Bayes factors, for different values of the injected parameter space. We can see that higher values of ϵ make it easier to identify the correct model with significant evidence, where the transition occurs around $\epsilon \sim 10^{-7} - 10^{-6}$ the correct identification. Additionally, the Bayes factor tends to increase for higher values of α_2, corresponding to a higher overall amplitude signal. Finally, we observe a gap in $\alpha_2 = 2/3$, which is due to it coinciding with the fixed value of α_1. In this case, both models become completely degenerated and none of them are preferred, $\mathcal{B}^{\mathrm{BPL}}_{\mathrm{PL}} \sim 1$.

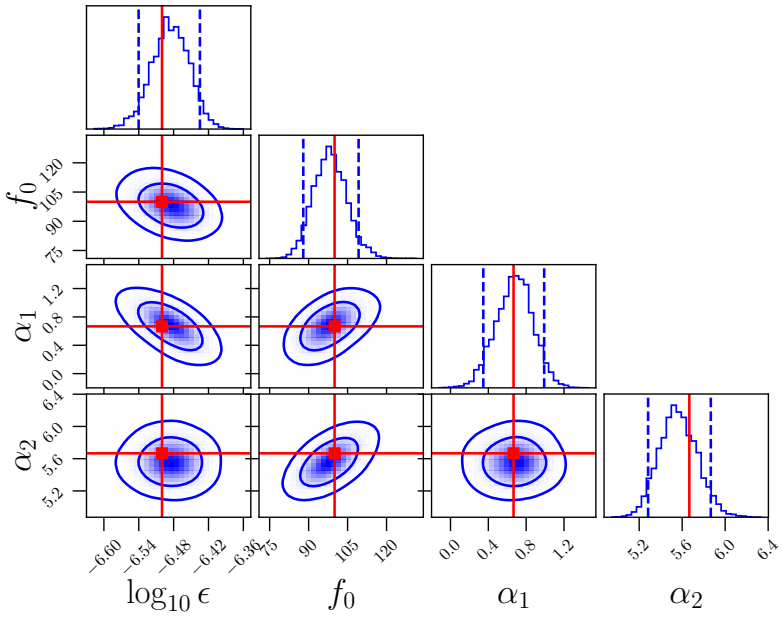

Figure 3.1: Example posterior for an injected and recovered broken power-law model, with $\ln \mathcal{B}^{\mathrm{BPL}}_{\mathrm{PL}} = 417$. The recovery is consistent with the injection, indicated by the red markers and lines.

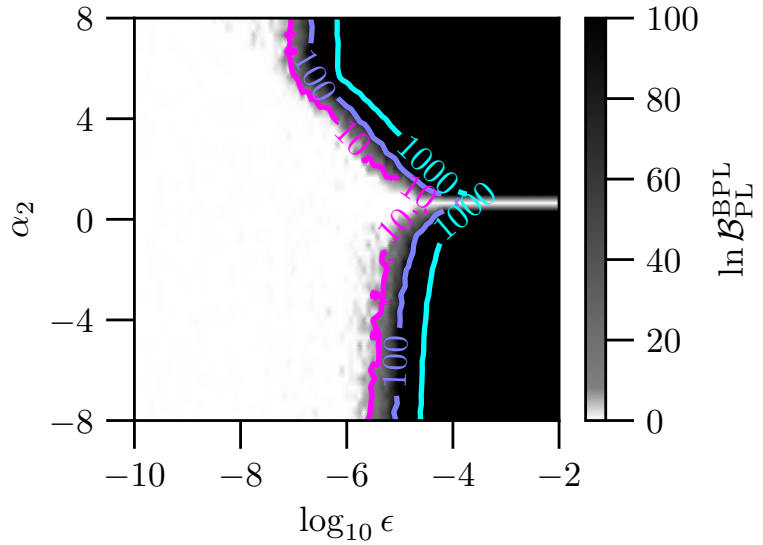

Figure 3.2: Heatmap showing the Bayes factor for the broken power-law versus power-law $\bar{H}(f)$ recovery models, for different injected values of ϵ and α_2 with $f_0 = 100$ Hz and $\alpha_1 = 2/3$.

Galactic plane versus isotropic $\mathcal{P}_{lm}$

Similar to the previous subsection, we did a similar study by comparing different $\mathcal{P}_{lm}$ models, fixing $\bar{H}(f)$ to a power law. We did not introduce any new free parameter in $\mathcal{P}_{lm}$, thus exploring the (ϵ, α) parameter space.

We started by injecting a Galactic plane $\mathcal{P}_{lm}$ with maximum $l = 7$, just as in the previous subsection. Then, we tried to recover the parameters with both this model and a purely isotropic model, that is, $\mathcal{P}_{lm} = 0$ if $l \neq 0$ or $m \neq 0$. We obtained the heatmap shown in Fig. 3.3, which indicates that the Galactic plane model is correctly recovered at around $\epsilon = 10^{-6}$ in the most conservative case, similar to the previous case. This threshold decreases as α increases, given that it enhances the signal for high frequencies. For most of the explored parameter space, the pipeline is then able to detect the signature of higher-order spatial modes and distinguish it from an isotropic background.

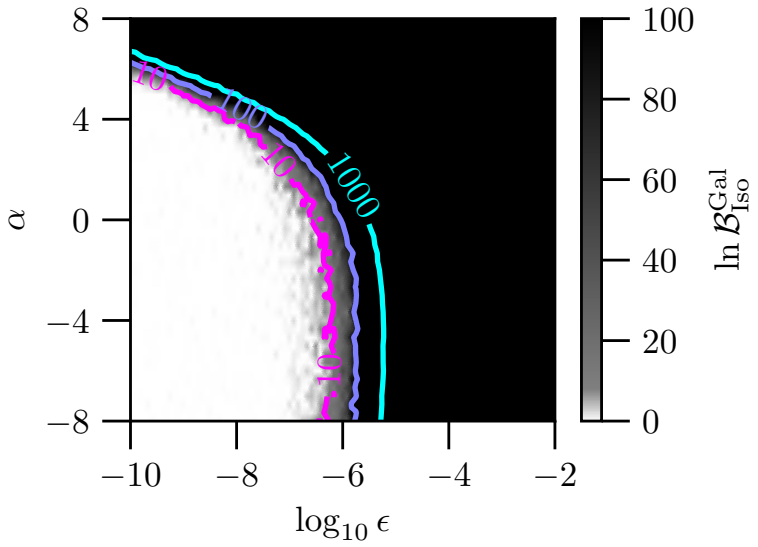

Figure 3.3: Heatmap showing the Bayes factor for the Galactic plane versus isotropic $\mathcal{P}_{lm}$ recovery models, for different injected values of ϵ and α and an injected Galactic plane $\mathcal{P}_{lm}$ model.

Dipole artifact versus isotropic $\mathcal{P}_{lm}$

As it is well-known from the CMB, the SGWB is expected to show a dipole anisotropy induced by the Doppler shift produced by the observer's motion with respect to the background rest frame. Based on the CMB literature [197, 198], we derived the expression for this anisotropy model in the SGWB. The derivation is included in App. B. This subsection was originally part of our preprint corresponding to the article [3], but was removed before publication in order to release a second article focused on dipole artifacts, accounting also for the time dependence, as it is done in [195].

As a toy model in our article, we consider that the values for the observer's speed and direction are the ones measured by Planck in 2018 [173], that is, $v = 369.82 \pm 0.11$ km/s, $l = 264.021 \pm 0.011$ deg, $b = 48.253 \pm 0.005$ deg. An example sky map of the dipole artifact produced by these values is shown in Fig. 3.4.

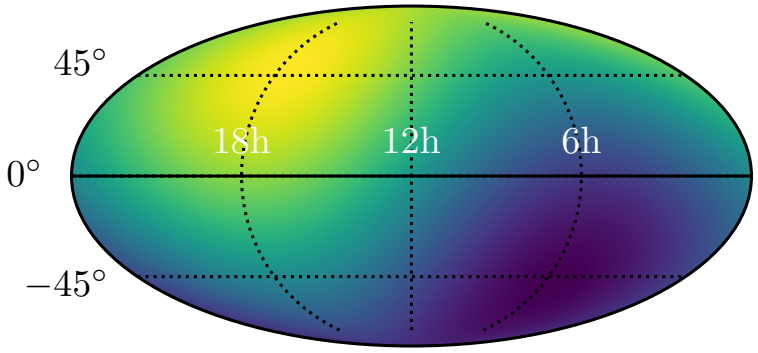

Figure 3.4: Sky map of the dipole artifact for $\alpha = 2/3$ and Planck values for the relative speed and direction, plotted in a Mollweide projection. The color map represents an arbitrary scale.

However, this model is not physically realistic for several reasons. First, the velocity derived by Planck corresponds to the relative motion of the Solar system with respect to the CMB rest frame (solar dipole), while we should also account for the Earth's orbital motion around the Sun (orbital dipole). However, the orbital dipole is time-dependent, so it is more difficult to incorporate to our formalism (see [195] for a more detailed analysis) and it is left for future work. Furthermore, the main dipole anisotropy for the SGWB may not come from this dipole artifact: the main contribution to the SGWB is expected to come from unresolved CBCs, so the effect of their anisotropic distribution in the sky might be dominant over the Doppler shift correction.

In any case, we injected this signal with a maximum $l = 2$ and recover with both this model and, again, an isotropic model. The recovery with the dipole artifact model assumes fixed Planck values, instead of trying to fit them, so the only free parameters are ϵ and α. Hence, we explore this parameter space, obtaining Fig. 3.5.

In Fig. 3.5, we can see that, for $\alpha < 4$, the threshold at which both models are distinguished is higher than in previous cases, being around $\epsilon \sim 10^{-4}$. This is consistent with the dipole anisotropy being weaker than the isotropic component by a factor 10^3, as we can see in the expressions of App. B for $\beta = v/c \sim \mathcal{O}(10^{-3})$. Additionally, we observe a gap in $\alpha = 4$, which corresponds to the value for which the dipole anisotropy vanishes due to the Lorentz invariance of $\Omega_{\rm gw}/f^4$. This is further discussed in App. B.

3.2.4 Conclusions

In the summarized article [3], we developed a parameter estimation formalism for a targeted anisotropic stochastic gravitational wave background. Using Bayesian inference, the algorithm

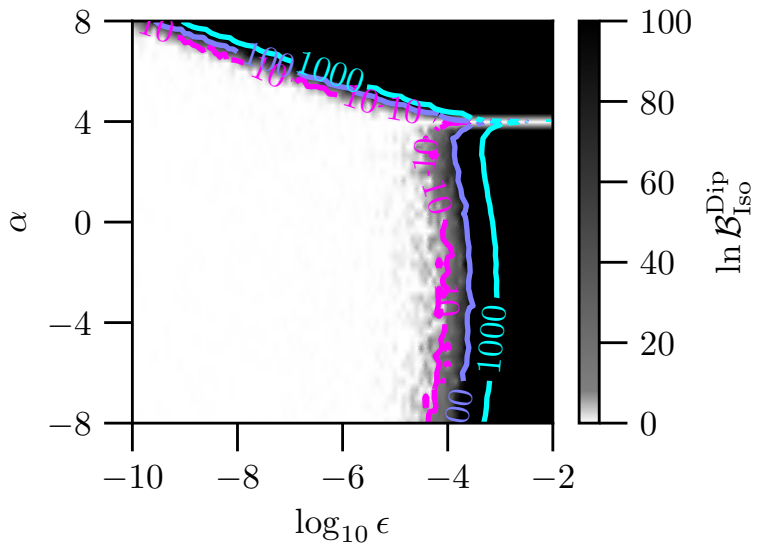

Figure 3.5: Heatmap showing the Bayes factor for the dipole artifact $\mathcal{P}_{lm}$ model versus the isotropic one.

provides the posterior distribution for a given model of anisotropies, which generalizes the work done for isotropic searches. Furthermore, we developed signal injection tools which enhance the capabilities of our pipeline.

We also illustrated the capabilities of the formalism for model selection, with the difference between models being in either $\bar{H}(f)$ or $\mathcal{P}_{lm}$. We explored the parameter region where our algorithm can distinguish two different models, obtaining a structure consistent with our expectations. We also computed the general equations for the dipole artifact caused by Doppler shift, detailed in App. B, and used them for model selection assuming only a solar dipole, thus neglecting the orbital dipole contribution, which we leave for future work.

Moreover, the article also does some other studies: statistically checking the injection formalism, optimizing the maximum l which is needed to correctly recover given $\bar{P}_{lm}$ models, running a search for millisecond pulsars and using simulated data to address the prospects with future detectors. These topics have been left out of this thesis and we refer to our article [3] for further details.

We conclude this section by remarking that, in the absence of a detection of a SGWB in the LVK frequency band, current efforts in the GW community are focused on the isotropic analysis. However, as sensitivity from the detectors increases and we add KAGRA, LIGO-India and next-generation detectors such as Einstein Telescope and Cosmic Explorer, these works on the SGWB anisotropies will become increasingly important.

With this, we finish the topic of SGWB anisotropies. In the next chapters, we will delve into the topic of primordial black holes (Chapter 4) and compute the SGWB they produce (Chapter 5) from their hyperbolic encounters, whose formalism was detailed in Sec. 1.4.

Chapter 4

Primordial black holes

4.1 Introduction

Standard, astrophysical black holes (ABH) are generated as remnants of core-collapse supernovae, which are produced from massive stars during their last evolutionary stages. On the other hand, primordial black holes are theorized to have formed in the early Universe from the collapse of overdense regions, thus having a very different origin to ABHs, not involving a star precursor. This idea was introduced by Yakov Zel'dovich and Igor Novikov [24] in 1967 and was further pursued by Stephen Hawking [25] and his student Bernard Carr [26, 27] during the 1970s. During this decade, they were already proposed as candidates for dark matter [25, 26, 199], either accounting for all or at least part of it, and have not yet been confirmed or ruled out to this day.

In this chapter, these astronomical objects will be introduced, explaining the mechanisms that can generate them and how we can compute the overdensity thresholds they need to be produced. Furthermore, different clustering and population scenarios will be presented, as well as the merger rates we can expect from them. In particular, these rates will be used later in Chapter 5 to explain one of our works [2], in which we estimate the SGWB produced by PBHs within both CBCs and hyperbolic encounters.

For Sections 4.2 and 4.4, one of the main references will be the recent review by the LISA Cosmology Working group [200], which constitutes a very complete introduction to PBHs and their GW signatures. For Section 4.3, we will instead focus on own work based on Ilia Musco's [201, 202, 203] and Albert Escrivà's [204, 205].

4.2 PBH generation mechanisms

Primordial black holes are generated from the collapse of overdensities δ above a certain critical threshold δ_c. If we denote the spectrum of overdensities by $P(\delta)$, then the fraction of PBHs at

formation is given by

$$\beta_f = \int_{\delta_c}^{\infty} P(\delta) d\delta. \tag{4.1}$$

Another useful parameter to characterize the abundance of PBHs is $f_{\rm PBH}$, defined as the fraction of dark matter which is in the form of PBHs. Thus, in order to produce a relevant amount of PBHs, it is then necessary to have a large probability to generate such overdense regions.

There are various mechanisms to produce these overdensities, the most standard of which is enhancing the primordial curvature power spectrum during inflation. This can be achieved either from single-field inflationary models [206, 207, 208, 209, 210], such as critical Higgs inflation [211, 212], or from multi-field inflationary models, such as hybrid inflation [213, 214, 215]. Another possibility is to enhance just the tail of the spectrum distribution, leaving behind the Gaussianity hypothesis and entering into non-Gaussianities [150, 216, 217]. Finally, other possible mechanisms for PBH generation include phase transitions [218], scalar field instabilities [219] or the collapse of cosmic strings [220].

In this section, we will review the single-field inflation scenario, which is one of the most accepted, and briefly comment on non-Gaussianities and one of the scenarios in which they arise, which is called quantum diffusion.

4.2.1 Single-field inflation

From the CMB temperature anisotropies measured by Planck, inflation models are very well constrained at large scales. However, small scales remain mostly unconstrained, so there is still a wide variety of inflationary models compatible with observations. The behavior at small scales is also of great physical importance, because sufficiently large overdensities could have induced a gravitational collapse leading to the formation of primordial black holes.

A relevant production of PBHs requires a considerably large growth of the power spectrum on small scales. Therefore, the simplest single-field slow-roll inflationary models do not produce them, given that they predict a nearly scale-invariant primordial power spectrum. There are several solutions to this problem, including a large positive running of the primordial curvature power spectrum [208] or violation of the usual slow-roll conditions [209, 221, 95, 222]. In these models, the amount of produced PBHs depends on the model parameters, so generating the correct amount of PBHs usually involves some degree of fine-tuning.

One of the most natural possibilities to produce PBHs is that the inflationary potential has an inflection point, generating a plateau that slows down the inflaton. We will next see one of the single-field inflation models that can produce one of these points.

Critical Higgs inflation

Critical Higgs inflation [211, 212] is one of the best physically-motivated single-field models of inflation which the capability to produce a quasi-inflection point. The non-minimally coupled Higgs action is given by

$$S = \int d^4x\sqrt{g}\left[\left(\frac{M_{\rm Pl}^2}{2} + \frac{\xi(\phi)}{2}\phi^2\right)R - \frac{1}{2}(\partial\phi)^2 - \frac{1}{4}\lambda(\phi)\phi^4\right] \tag{4.2}$$

where $M_{\rm Pl} = 1/\sqrt{8\pi G}$ is the Planck mass and, around the critical point $\phi = \mu$,

$$\lambda(\phi) \approx \lambda_0 + b_\lambda \ln^2(\phi/\mu), \tag{4.3}$$
$$\xi(\phi) \approx \xi_0 + b_\xi \ln(\phi/\mu). \tag{4.4}$$

It is now necessary to do some redefinitions, so that the new metric is

$$\overline{g}_{\mu\nu} = (1 - M_{\rm Pl}^{-2}\xi(\phi)\phi^2) g_{\mu\nu}, \tag{4.5}$$

and the new scalar field is

$$\varphi = \int d\phi \frac{\sqrt{1 + M_{\rm Pl}^{-2}\xi(\phi)\phi^2 \left(1 + 6\left(\xi(\phi) + \frac{1}{2}\phi\xi'(\phi)\right)^2\right)}}{1 + M_{\rm Pl}^{-2}\xi(\phi)\phi^2}. \tag{4.6}$$

With these redefinitions, one can show [211, 212, 200] that the effective inflationary potential is

$$V(x) = \frac{V_0(1 + a\ln^2 x)x^4}{(1 + c(1 + b\ln x)x^2)^2}, \tag{4.7}$$

with

$$x = \frac{\phi}{\mu}, \quad V_0 = \frac{\lambda_0\mu^4}{4}, \quad a = \frac{b_\lambda}{\lambda_0}, \quad b = \frac{b_\xi}{\xi_0}, \quad c = \frac{\xi_0\mu^2}{M_{\rm Pl}^2}. \tag{4.8}$$

This potential is approximately constant for large values of x,

$$V(x) \underset{x\to\infty}{\longrightarrow} V_0 \frac{a}{(bc)^2} = \frac{M_{\rm Pl}^4}{4}\frac{b_\lambda}{b_\xi^2} \ll M_{\rm Pl}^4. \tag{4.9}$$

In addition, for some volume of the parameter space (see [211] for details), there is a critical point with a secondary plateau, which induces a large peak in the primordial curvature power spectrum. This can be seen in Fig. 4.1, which was generated with the parameters indicated in [211],

$$\lambda_0 = 2.23\times10^{-7}, \quad \xi_0 = 7.55, \quad \left(\frac{\mu}{M_{\rm Pl}}\right)^2 = 0.102, \quad b_\lambda = 1.2\times10^{-6}, \quad b_\xi = 11.5, \tag{4.10}$$

which correspond to

$$a = 5.38, \quad b = 1.52, \quad c = 0.770. \tag{4.11}$$

Within this framework, it is possible to get a large production of PBH while respecting CMB constraints for the parameter ranges

$$10^{-9} \lesssim \lambda_0 \lesssim 8\times10^{-7}, \quad 0.5 \lesssim \xi_0 \lesssim 15, \quad 0.05 \lesssim x^2\mu^2 \lesssim 1.2,$$
$$8\times10^{-9} \lesssim b_\lambda \lesssim 4\times10^{-6}, \quad 1 \lesssim b_\xi \lesssim 18. \tag{4.12}$$

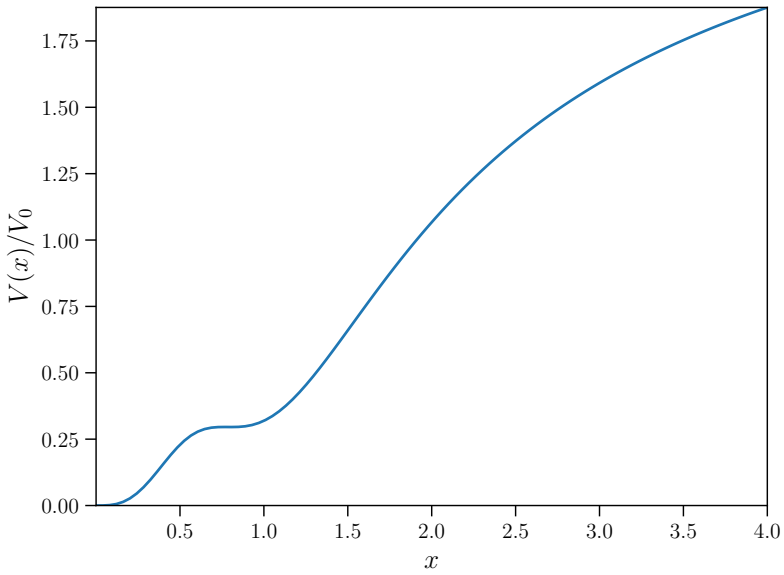

Figure 4.1: Higgs potential $V(x)$ defined in Eq. (4.9), with the parameters from Eq. (4.11), as indicated in [211].

4.2.2 Non-Gaussianities

As we just discussed, one of the possibilities to generate PBHs is to enhance the primordial curvature power spectrum. However, as we saw in the introduction, what determines the PBH formation and abundance is the probability that primordial curvature perturbations exceed a certain threshold, which is determined by their full PDF, computed from the primordial curvature spectrum. Therefore, if this distribution is not Gaussian, the particular shape of its tail can also play an important role for PBH generation.

These non-Gaussianities, which were previously mentioned in Sec. 2.5, can arise due to several reasons, including quantum diffusion [150] and the presence of a stochastic spectator field [217]. We will now briefly comment on the quantum diffusion scenario.

It is expected that small primordial curvature perturbations are well-described by an approximately Gaussian distribution, close to the peak of their PDF. However, PBHs are formed from large density perturbations, which involve the tail of the distribution and can thus be far from the Gaussian regime. In order to characterize the different behaviors, the stochastic inflation formalism divides the inflaton field into two components: quantum fluctuations at small scales and an effectively classical field at large scales, where the coarse-graining scale separating both behaviors is given by the Hubble horizon. In slow-roll, when the quantum fluctuations cross this horizon, they become overdamped, leading to a squeezed state which can be treated as classical noise [216]. The large-scale classical field is then constantly receiving this stochastic noise, which enters the field equations of motion with an amplitude $H/2\pi$. This is what is called *quantum diffusion*.

As a result of quantum diffusion, exponential tails arise in the primordial curvature spec-

trum [150, 216], which then significantly deviates from Gaussianity. The shape of such non-Gaussianities is not properly captured by perturbative parametrizations involving the $f_{\rm NL}$ parameter, such as the one described in Sec. 2.5. We can see this in Fig. 4.2, obtained from [150], where the power spectrum of overdensities is presented for a Gaussian primordial curvature spectrum, as well as for two models involving exponential tails (labelled as "Elliptic2" and "Elliptic4"), effective descriptions based on $f_{\rm NL}$ and a lognormal power spectrum. From this figure, it is clear that the different descriptions may coincide around the peak, for which a Gaussian description suffices, but drastically differ in their tails. This failure to capture the quantum diffusion effect with an effective $f_{\rm NL}$ description is one of the reasons why, at the end of our conclusions in this Sec. 2.5, we argued that a robust formalism to characterize non-Gaussianity is needed to set constraints from GWs in a more systematic way. Thus, our work has to be understood under the limitations of our description.

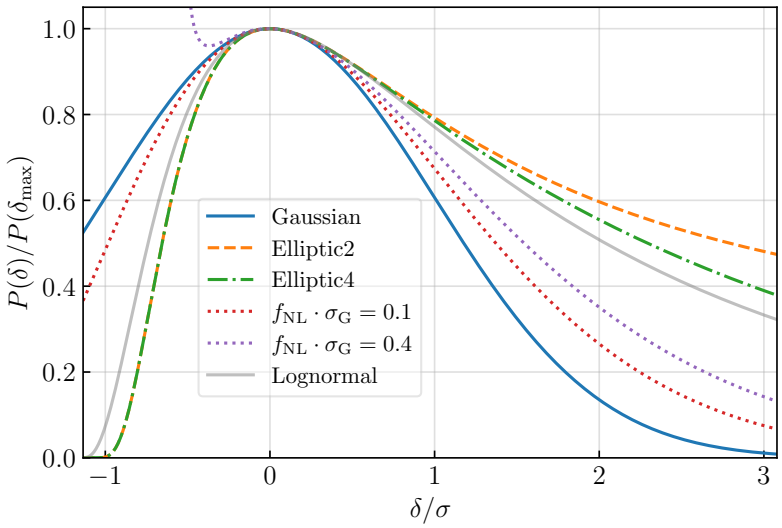

Figure 4.2: Normalized power spectrum of overdensity perturbations for a Gaussian primordial curvature power spectrum, as well as other distributions from quantum diffusion models (Elliptic2 and Elliptic4), effective descriptions using $f_{\rm NL}$ parameters and a lognormal power spectrum. The free parameters of the distributions are set so that the behavior around the peak is similar. Figure taken from [150], where we refer to for additional details on these shapes.

In the next section, we will study the formation mechanism of PBHs, deriving it from basic General-Relativistic equations.

4.3 Collapse of density perturbations

The problem of when and how overdensities collapse to form black holes has been extensively studied since the works by Carr in the 1970s [26, 27], in which he already computed the first threshold for

PBH formation. Using arguments based on Jeans length, he obtained a critical overdensity threshold δ_c so that

$$\delta_c \sim c_s^2 \sim \frac{1}{3}, \tag{4.13}$$

where c_s is the sound speed of the radiation fluid. There were some other articles at that time, mainly by Novikov and Polnarev [223, 224, 225]. Decades later, Choptuik discovered critical collapse in 1992 [226], to which a series of articles followed by different authors, mainly focused on numerical simulations [227, 228, 229, 230].

In this section, we will see how to run these numerical simulations, mainly aiming to compute the overdensity threshold δ_c for a Gaussian-profile overdensity in an ideal fluid, assuming spherical symmetry. We will do so by referring to the recent works by Ilia Musco [230, 203, 231, 232, 201] for the first subsections, and then refer to the articles by Albert Escrivà [204, 205] for further computational details, complementing them with additional equations and figures obtained from own simulations. This will be the first approach to Numerical Relativity in this thesis, which will be covered with more detail for binary black holes in Chapter 6. Finally, we will conclude with some remarks on how these thresholds evolve with the thermal history of the Universe.

During this section, we will work in geometrized units, $G = c = 1$, which is the most natural unit system for numerical simulations.

4.3.1 The Misner-Sharp formalism

The main formalism to numerically approach the collapse of overdensities is the Misner-Sharp formalism, introduced by Charles Misner and David Sharp in 1964 [233]. We will follow this framework starting from the basic equations of GR. First, we take a spherically symmetric metric,

$$ds^2 = -A^2(t,r)dt^2 + B^2(t,r)dr^2 + R^2(t,r)d\Omega^2. \tag{4.14}$$

On the matter side, we assume an ideal fluid with equation of state

$$P(t,r) = \omega\rho(t,r), \tag{4.15}$$

with $P(t,r)$ being the pressure fluid and $\rho(t,r)$ its density. Its energy-momentum tensor in a comoving reference system $u^\mu = (A^{-1}, 0, 0, 0)$ is then

$$T^{\mu\nu} = (P+\rho)u^\mu u^\nu + Pg^{\mu\nu} = \text{diag}\left(\frac{\rho}{A^2}, \frac{P}{B^2}, \frac{P}{R^2}, \frac{P}{R^2\sin^2\theta}\right)\Bigg(\tag{4.16}$$

Nevertheless, we will keep the equations generic without explicitly substituting Eq. (4.15), and then particularize for this case.

From the metric in Eq. (4.14) and the energy-momentum tensor in Eq. (4.16), we can compute the Einstein equations (1.46), which take the form

$$-\frac{2\dot{B}\dot{R}R}{A^2B} - \frac{\dot{R}^2}{A^2} - \frac{2B'R'R}{B^3} + \frac{2R''R}{B^2} + \frac{R'^2}{B^2} - \frac{1}{R^2} = -8\pi G\rho R^2, \tag{4.17}$$

$$\frac{\dot{R}A'}{A} + \frac{\dot{B}R'}{B} - \dot{R}' = 0, \tag{4.18}$$

$$\frac{2A'R'R}{AB^2} - \frac{\dot{R}^2}{A^2} + \frac{2\dot{A}\dot{R}R}{A^3} - \frac{2\ddot{R}R}{A^2} + \frac{R'^2}{B^2} - 1 = 8\pi G P R^2, \tag{4.19}$$

$$\frac{A''}{AB^2} - \frac{A'B'}{AB^3} + \frac{A'R'}{AB^2R} - \frac{\dot{B}\dot{R}}{A^2BR} + \frac{\dot{A}\dot{B}}{A^3B} - \frac{\ddot{B}}{A^2B} + \frac{\dot{A}\dot{R}}{A^3R} - \frac{\ddot{R}}{A^2R} - \frac{B'R'}{B^3R} + \frac{R''}{B^2R} = 8\pi G P, \tag{4.20}$$

corresponding to the (0,0), (0,1), (1,1) and (2,2) components of the Einstein equations, respectively. In these expressions, we have defined

$$\dot{f} \equiv \frac{\partial f}{\partial t}, \quad f' \equiv \frac{\partial f}{\partial r}. \tag{4.21}$$

Eqs. (4.17), (4.18), (4.19) and (4.20) constitute four equations of motion, where a fifth one is obtained from the equation of state (4.15). These expressions completely determine the temporal evolution, given that we have five variables A, B, R, P and ρ.

In addition, we can obtain two extra equations from the energy-momentum conservation $\nabla_\mu T^{\mu\nu}$,

$$\frac{A'}{A} + \frac{P'}{\rho + P} = 0, \tag{4.22}$$

$$\frac{\dot{B}}{B} + 2\frac{\dot{R}}{R} + \frac{\dot{\rho}}{\rho + P} = 0. \tag{4.23}$$

Note that these constraints come from the contracted Bianchi identities, and thus do not introduce any independent information to the four Einstein equations. However, they are simpler and thus more suitable to work with. Additionally, in numerical simulations, it is also useful to have at least one constraint equation for consistency checks in the code.

In their current form, however, the previous equations are difficult to work with. The only exception is Eq. (4.22), which will be the first equation we are interested in for our simulations. In order to get more equations in a suitable form, the Misner-Sharp formalism introduces three new variables, U, Γ and M, adding up to a total of eight. We then want to have eight independent equations, to which we will add another one, redundant with the other eight, which will serve as a check for the accuracy in the computations.

The new variables U and Γ are the temporal and spatial comoving derivatives of R,

$$U = \frac{\dot{R}}{A}, \tag{4.24}$$

$$\Gamma = \frac{R'}{B}, \tag{4.25}$$

where U represents the velocity of the fluid and Γ is a generalized Lorentz factor. These two equations will be used for the simulations, which, together with Eq. (4.22) and the equation of state (4.15), adds up to a total of four. With these definitions, Eq. (4.18) becomes

$$\dot{R}' = A'U + \dot{B}\Gamma, \tag{4.26}$$

which will be used later. The final variable we introduce is the mass,

$$M = \frac{R}{2}(1 + U^2 - \Gamma^2). \tag{4.27}$$

This is the fifth equation we will use. Using now Eq. (4.26) to simplify Eqs. (4.17) and (4.19), they become

$$M' = 4\pi G\rho R^2 R', \tag{4.28}$$

$$\dot{M} = -4\pi G P R^2 \dot{R}, \tag{4.29}$$

respectively. Equation (4.28) is called the *Hamiltonian constraint* and it is the one used to check numerical accuracy, as well as it shows why the variable M represents a mass. Eq. (4.29), on the other hand, is the sixth equation we will use.

The seventh equation will come from Eq. (4.23), for which we can substitute $\dot{R}'$ in Eq. (4.26) and U' from the radial derivative of Eq. (4.24). With this, we get a time evolution equation for ρ,

$$\dot{\rho} = -A(\rho + P)\left(\frac{U'}{R'} + 2\frac{U}{R}\right). \tag{4.30}$$

We get the eighth and final equation by taking the time derivative of U from Eq. (4.24), comparing it to Eq. (4.19) and using Eqs. (4.22), (4.25) and (4.27):

$$\dot{U} = -A\left(\frac{\Gamma P'}{B(\rho + P)} + \frac{M}{R^2} + 4\pi G P R\right). \tag{4.31}$$

In fact, we can use Eq. (4.25) in this equation to get rid of B, allowing us to work with seven variables. The complete set of these equations is called the Misner-Sharp-Hernandez equations [233, 234, 235].

Simplifications for an ideal fluid

If we use the equation of state given by Eq. (4.15), we can substitute all instances of P and work with six variables instead of seven. In addition, Eq. (4.22) can be integrated analytically:

$$\frac{A'}{A} + \frac{\omega}{1+\omega}\frac{\rho'}{\rho} = 0 \quad \Rightarrow \quad A(t,r) = \left(\frac{\rho_b(t)}{\rho(t,r)}\right)^{\frac{\omega}{1+\omega}}, \tag{4.32}$$

where $\rho_b(t) = \lim_{r\to\infty}\rho(t,r)$, since $\lim_{r\to\infty} A(t,r) = 1$ for all t.

To summarize and for clarity, we review and rewrite the simplified equations that will ultimately be used. These can be divided in:

- Four equations explicitly providing time derivatives, which are Eqs. (4.24), (4.29), (4.30) and (4.31). These will be used for the time evolution in the code. Rewritten in a suitable way, they are

$$\dot{R} = AU, \qquad \dot{\rho} = -A(1+\omega)\rho\left(\frac{U'}{R'} + 2\frac{U}{R}\right), \tag{4.33}$$

$$\dot{M} = -4\pi G\omega A U \rho R^2, \qquad \dot{U} = -A\left(\frac{\omega}{1+\omega}\frac{\Gamma^2}{\rho}\frac{\rho'}{R'} + \frac{M}{R^2} + 4\pi G\omega\rho R\right)\Bigg(\tag{4.34}$$

- Two equations from which one can get A and Γ, which are Eqs. (4.32) and (4.27), respectively. These will be used inside each iteration of the time evolution method, in order to compute the right-hand sides of the previous equations:

$$A = \left(\frac{\rho_b(t)}{\rho(t,r)}\right)^{\frac{\omega}{1+\omega}}, \quad \Gamma^2 = 1 + U^2 - \frac{2M}{R}, \tag{4.35}$$

- The Hamiltonian constraint equation, Eq. (4.28),

$$M' = 4\pi G\rho R^2 R'. \tag{4.36}$$

We now have the evolution equations for spherically-symmetrical collapse of overdensity perturbations. We thus need the other main element of numerical simulations: the initial conditions.

4.3.2 Initial conditions

In order to obtain the initial conditions, we first consider a background metric similar to the FLRW metric but with a curvature profile $K(r)$,

$$ds^2 = -dt^2 + \frac{(R')^2}{1 - K(r)r^2}dr^2 + a^2(t)r^2 d\Omega^2, \tag{4.37}$$

where $a(t)$ is the scale factor without considering perturbations. We will also denote by $\rho_b(t), P_b(t)$ the background density and pressure. In particular, note that none of these quantities is space-dependent. The curvature profile we consider is Gaussian,

$$K(r) = \mathcal{A}\exp\left(-\left(\frac{r^2}{2L^2}\right)^{\beta}\right) \tag{4.38}$$

for a certain length scale L. There are generalizations for arbitrary shape profiles, for which one can refer to [201]. In this article, the author proves that the threshold for gravitational collapse strongly depends on the overdensity profile, so it is important to account for this aspect of the initial conditions. Nevertheless, here we focus on Gaussian perturbations as a paradigmatic model.

The variables we work with are inter-related by the Einstein equations seen in the previous subsection, so we need to generate valid initial conditions in order to guarantee a physical scenario and a stable simulation. For this purpose, the usual approach is to perturb the metric and hydrodynamical variables so that the perturbed quantities satisfy the Einstein equations. The intensity of this perturbation will be characterized by the ϵ parameter, defined as the ratio between the comoving Hubble length $(aH)^{-1}$ and the perturbation length scale r_k,

$$\epsilon(t) = \frac{1}{a(t)H(t)r_k} = \frac{1}{\dot{a}(t)r_k}, \tag{4.39}$$

One could think that a natural choice for the length scale r_k is simply the L parameter in Eq. (4.38). However, we will later see there are more suitable options. In order to generate the initial conditions, we will work in the long-wavelength regime, where $r_k \gg (aH)^{-1}$ and thus $\epsilon \ll 1$.

According to [236, 203, 201], the order $O(\epsilon)$ of the metric quantities corresponds to a decaying mode that can be neglected. Therefore, following these references, we assume that the leading order of the perturbation is $O(\epsilon^2)$, so the metric and hydrodynamical variables will be perturbed as

$$A(t,r) = 1 + \epsilon^2 \tilde{A}, \qquad \rho(t,r) = \rho_b(t)(1+\epsilon^2\tilde{\rho}) \tag{4.40}$$

$$B(t,r) = \frac{R'}{\sqrt{1-K(r)r^2}}(1+\epsilon^2\tilde{B}), \qquad U(t,r) = H(t)R(t)(1+\epsilon^2\tilde{U}), \tag{4.41}$$

$$R(t,r) = a(t)r(1+\epsilon^2\tilde{R}), \qquad M(t,r) = \frac{4\pi}{3}\rho_b(t)R^3(1+\epsilon^2\tilde{M}), \tag{4.42}$$

where the perturbed variables will depend on the position, while $\epsilon(t)$ provides the time dependence. We can obtain equations for these variables by perturbing the equations of motion, and they can be solved analytically within this regime. The results have already been computed in [203, 201], so here we just reproduce them:

$$\tilde{A} = -\frac{\omega}{5+3\omega}\frac{1}{r^2}[r^3K(r)]'r_k^2, \qquad \tilde{\rho} = \frac{1+\omega}{5+3\omega}\frac{1}{r^2}[r^3K(r)]'r_k^2, \tag{4.43}$$

$$\tilde{B} = \frac{3\omega}{(1+3\omega)(5+3\omega)}r\left[\frac{1}{3r^3}(r^3K(r))'\right]'r_k^2, \qquad \tilde{U} = -\frac{1}{5+3\omega}K(r)r_k^2, \tag{4.44}$$

$$\tilde{R} = -\frac{1}{(1+3\omega)(5+3\omega)}\left\{\frac{\omega}{r^2}[r^3K(r)]' + K(r)\right\}r_k^2, \qquad \tilde{M} = \frac{3(1+\omega)}{5+3\omega}K(r)r_k^2. \tag{4.45}$$

Compaction function, length scales and collapse thresholds

Before finishing this section and based on the previous equations, it is convenient to define a few more quantities which will be useful to analyze the output. In particular, it is necessary to properly define when we consider that a black hole has been formed. First, we define the averaged mass excess in a certain volume as

$$\delta(t,r) \equiv \frac{1}{V}\int_0^R 4\pi R^2 \frac{\rho-\rho_b}{\rho_b}\,dR, \tag{4.46}$$

where $V = \frac{4}{3}\pi R^3$. In the long wavelength approximation, substituting the expressions for ρ in Eqs. (4.40), (4.43) and R in Eq. (4.42), (4.45), we have, at $O(\epsilon^2)$,

$$\delta(t,r) = \frac{3}{r^3}\int_0 dr'\epsilon^2 r'^2\tilde{\rho}(t,r) = \frac{3(1+\omega)}{5+3\omega}\epsilon^2(t)K(r)r_k^2. \tag{4.47}$$

From this equation, we can see that the curvature profile $K(r)$ characterizes the initial shape of the overdensity, so we will sometimes refer to it as the overdensity profile.

Now, we define the formation of a black hole by the condition $R = 2(M - M_b)$, that is, when the radius R coincides with the Schwarzschild radius of the excess mass $M - M_b$ contained within the spherical volume determined by R. In order to characterize this behavior, it is useful to define the *compaction function* as

$$C(t,r) = \frac{2[M(t,r) - M_b(t,r)]}{R(t,r)}. \tag{4.48}$$

Therefore, if this function reaches 1 at any instant and radius, then a black hole has been formed inside that radius. From the expressions for M and R in Eqs. (4.42), we can write, at $O(\epsilon^2)$,

$$C(t,r) = \frac{8\pi}{3}\rho_b(t)a(t)^2r^2\epsilon^2(t)\tilde{M}(t,r) = H(t)^2a(t)^2r^2\epsilon^2(t)\tilde{M}(t,r) = \tilde{M}(t,r)\frac{r^2}{r_k^2}, \tag{4.49}$$

where we have used the Friedmann equation for a flat Universe in the second step and the relation between ϵ and H in Eq. (4.39). Substituting the expression for $\tilde{M}$ in Eq. (4.45), we get

$$C(t,r) = \frac{3(1+\omega)}{5+3\omega}K(r)r^2. \tag{4.50}$$

Aside from characterizing the black hole formation, this function naturally imposes a length scale r_m, which is given by the position of its local maximum in the long-wavelength regime. Imposing the condition $C'(t,r_m) = 0$ in Eq. (4.50), we get the expression

$$K(r_m) + \frac{r_m}{2}K'(r_m) = 0, \tag{4.51}$$

This is arguably the most suitable length scale to work with, given that the interesting behavior of our simulation will be around the compaction function peak, as we can later see in Fig. 4.3. However, traditionally, another length scale choice r_0 has been used, which is imposed by the condition $\tilde{\rho}(t,r_0) = 0$ in the long-wavelenth regime. Using Eq. (4.43) for the expression of $\tilde{\rho}$, one then has

$$K(r_0) + \frac{r_0}{3}K'(r_0) = 0, \tag{4.52}$$

For the Gaussian profile given by Eq. (4.38), these definitions imply

$$r_m = \sqrt{2}L, \quad r_0 = \sqrt{3}L. \tag{4.53}$$

Finally, in order to define the thresholds for collapse, one needs a magnitude representing the amplitude of the overdensity. The usual criterion is to use δ in Eq. (4.47) in either of these scales without its temporal dependence given by $\epsilon(t)$. The convention is then to set $\epsilon(t) = 1$, which, to linear order, corresponds to the time of horizon crossing: from Eq. (4.39), we have $r_k = [a(t_H)H(t_H)]^{-1}$. Note that the different choices of length scale correspond to different times of horizon crossing. Then, the collapse thresholds are usually computed in terms of δ for either of these scales at horizon crossing, that is,

$$\delta_m \equiv \delta(t_{H,m}, r_m), \quad \delta_0 \equiv \delta(t_{H,0}, r_0), \tag{4.54}$$

where the second choice has traditionally been more common. We denote the thresholds on these quantities as δ_c and $\delta_{0,c}$, respectively. For a Gaussian perturbation (4.38), using Eq. (4.47) for δ, we get the expressions

$$\delta_m = \frac{3(1+\omega)}{5+3\omega}\mathcal{A}e^{-1}r_m^2, \quad \delta_0 = \frac{3(1+\omega)}{5+3\omega}\mathcal{A}e^{-3/2}r_0^2. \tag{4.55}$$

4.3.3 Numerical simulations

With the initial conditions defined in the previous subsection, we are now ready to run our simulations, for which we define a certain radial interval $[0, r_{\max}]$ in which our variables will be defined. In order to guarantee stable simulations, we choose $r_{\max}$ sufficiently large and, for each iteration, we impose on this point the boundary conditions given by the asymptotic $r \to \infty$ quantities, which are taken from the analytical solution to the unperturbed FLRW metric.

For the time integration, we can take any robust method such as a fourth-order Runge-Kutta, although higher-order methods provided by SCIPY [237] are more stable and easy to use. However, contrary to standard differential equations, Eqs. (4.33) and (4.34) are partial differential equations (PDEs) which involve another layer of complexity: spatial derivatives, which are also related to the grid we take in $[0, r_{\max}]$. Depending on the problem, one can use a uniform grid with a simple differentiation algorithm such as finite differences, which locally approximate the grid functions by small-order polynomials, for which the derivative can easily be computed. In this case, however, differentiating using this technique on a uniform grid leads to numerical instabilities and the eventual crash of the simulation.

In order to overcome this issue, one option is to use a special grid with adaptive mesh refinement (AMR), which is the approach taken in [201], aside from a logarithmic grid. Adaptive mesh refinement is a technique consisting on dynamically (at each iteration) increasing the grid resolution in those regions of the space where more accuracy is needed, while keeping a lower resolution for less demanding areas. In our case, for instance, at radii close to $r_{\max}$, the variable derivatives will be close to zero, so there is no need to have a high resolution. On the opposite side, closer to $r = 0$, the variables are more subject to change and present higher derivatives, so more grid points will be needed to accurately compute them, with the precise areas that demand them changing at each iteration (see Fig. 4.3. This idea of adaptive mesh refinement will be further detailed in Chapter 6 for 3-dimensional and heavier simulations of binary black holes.

Nevertheless, adaptive mesh refinement is not the only solution to get stable gradients. In the next subsection, we focus on another technique which was used in [204, 205]: the Chebyshev spectral method.

Chebyshev spectral method

The Chebyshev spectral method belongs to one class of numerical algorithms called *spectral*, or sometimes *pseudo-spectral* methods, which are based on decomposing grid fields using a set of basis functions. One of the best references for these algorithms which is focused on Chebyshev spectral methods is [238]. The mathematical reason why spectral methods are useful is their convergence properties: on the one hand, a finite differences method of order n with a uniform grid of N points introduces numerical errors of order $O((1/N)^n)$, where the order of the method is given by the number of neighbour points taken into account to compute the derivatives. On the other hand, spectral methods use global basis functions accounting for all the points in their domain, so the information from all these points is accounted for when taking a derivative. Thus, spectral methods have order N, so their error reduces as $O((1/N)^N)$, which implies an exponential reduction.

The Chebyshev spectral method is based on the Chebyshev polynomials of the first kind, defined

in the domain $[-1, 1]$ as

$$T_n(\cos\theta) = \cos(n\theta) \tag{4.56}$$

These polynomials naturally impose a set of grid points that one should follow. Given a total number of points $N_{\rm Cheb} + 1$, *Chebyshev collocation points* are

$$x_k = \cos\left(\frac{k\pi}{N_{\rm Cheb}}\right) \tag{4.57}$$

The advantage of these points is that the Chebyshev polynomials can then be easily evaluated,

$$T_n(x_k) = \cos\left(\frac{nk\pi}{N_{\rm Cheb}}\right) \tag{4.58}$$

This procedure is called *Chebyshev collocation method*.

The goal is to approximate a general function $f(x)$, defined, for now, in the domain $[-1, 1]$, by a polynomial $P_{N_{\rm Cheb}}(x)$ of order $N_{\rm Cheb}$ which satisfies

$$P_{N_{\rm Cheb}}(x_k) = f(x_k) \quad \forall k = 0, \ldots, N_{\rm Cheb}. \tag{4.59}$$

Using as a basis the Chebyshev polynomials, so that

$$P_{N_{\rm Cheb}}(x) = \sum_{n=0}^{N} a_n T_n(x), \tag{4.60}$$

the coefficients can be computed as [238]

$$a_n = \frac{2/c_n}{N_{\rm Cheb}} \sum_{k=0}^{N} \frac{f(x_k)}{c_k} T_n(x_k), \tag{4.61}$$

with $c_k = 2$ if $k = 0$ or $k = N_{\rm Cheb}$ and $c_k = 1$ otherwise.

The previous equations then imply that, given a function $f : [-1, 1] \to \mathbb{R}$ and a number of points $N_{\rm Cheb} + 1$, we can approximate f by

$$P_{N_{\rm Cheb}}(x) = \sum_{k=0}^{N} L_k(x) f(x_k), \tag{4.62}$$

with

$$L_k(x) = \frac{2/c_k}{N_{\rm Cheb}} \sum_{n=0}^{N} \frac{T_n(x_k)}{c_n} T_n(x). \tag{4.63}$$

Following [204], these functions can also be expressed as

$$L_k(x) = \frac{(-1)^{k+1}(1 - x^2)T'_N(x)}{c_k N^2 (x - x_k)}. \tag{4.64}$$

We will now see how differentiation and integration can both be done in a very efficient way with this formalism.

Differentiation

Given the expression (4.62), we can see that obtaining the derivatives of $P_N(x)$ is as easy as differentiating the $L_k(x)$ functions. Furthermore, we will only be interested in the derivatives on the grid points. We then define the *Chebyshev differentiation matrix* as

$$D_{ij} \equiv L'_j(x_i). \tag{4.65}$$

From Eq. (4.62), we then have an expression for the derivatives at the grid points,

$$P'_N(x_i) = \sum_{j=0}^{N} D_{ij} P_N(x_i). \tag{4.66}$$

This equation implies that, given an array of data, we can obtain its derivative with a simple matrix multiplication, where the matrix is independent of the time or the grid function and can be computed beforehand. This makes differentiation at each iteration very fast. Computed explicitly, the matrix coefficients are [239]

$$D_{ij} = \frac{c_i}{c_j} \frac{(-1)^{i+j}}{(x_i - x_j)}, \quad i \neq j, \tag{4.67}$$

$$D_{ii} = \frac{-x_j}{2(1-x_j^2)}, \quad i \neq 0, N_{\rm Cheb}, \tag{4.68}$$

$$D_{00} = -D_{N_{\rm Cheb} N_{\rm Cheb}} = \frac{2N_{\rm Cheb}^2 + 1}{6}. \tag{4.69}$$

In fact, only the non-diagonal terms are relevant, since the ones in the diagonal can be computed by using the property

$$D_{ii} = -\sum_{\substack{j=0 \\ j\neq i}}^{N_{\rm Cheb}} D_{ij}, \tag{4.70}$$

which is actually numerically more stable. This property is immediately derived from Eq. (4.66) by using that a polynomial $P_N(x_i) = 1$ for all i identically maps to a zero derivative.

Finally, we must conclude how to apply this theory, specific for functions defined in the $[-1, 1]$ interval, to a real interval $[a, b]$. In order to do this, if we have a certain function $f : [a, b] \to \mathbb{R}$, we can map it to a new function defined in $[-1, 1]$ with the transformation

$$g : [a, b] \to [-1, 1], \quad x \mapsto g(x) \equiv -1 + 2\frac{x-a}{b-a}. \tag{4.71}$$

Then, we can compute the derivative using Eq. (4.66) and transform back to the original interval. In practice, this means that the differentiation matrix has to be multiplied by the derivative of the transformation function g, which is $2/(b-a)$. Therefore, the only difference is a slight redefinition of the differentiation matrix.

Using this method and the formalism from previous subsections, we are now able to run numerical simulations for isotropic gravitational collapse. In the next subsection, we will see some interesting results from the point of view of primordial black holes.

4.3.4 Numerical results

At the early Universe, the dominating fluid was radiation, which is characterized by an equation of state with parameter $\omega = 1/3$. It is then natural to start applying this formalism to simulations in a radiation fluid.

If we use a Gaussian profile for the initial overdensity, as given by Eq. (4.38), we have two free parameters a priori: the amplitude $\mathcal{A}$ and length scale L. The length scale can preferably be replaced by either r_m or r_0, where we will use r_m for the discussion. We also observe that, from a simulation with fixed $r_m = 1$, we can recover the behavior of any equivalent (same parameters) simulation with a different r_m, just by doing a simple rescaling. In order to do it, we should realize that any function $f(r)$ we obtain from a simulation with $r_m = 1$ is actually representing the quantity $f(r/r_m)$. The time should also be rescaled, but it will in general be indicated as the ratio with the initial time (which is non-zero so that $H(t)$ is well-behaved).

Then, the only effective parameter is the amplitude $\mathcal{A}$. As we saw in the Subsection 4.3.2, we can replace this parameter with either δ_m or δ_0. In any case, we can see two different qualitative behaviors which are shown in Fig. 4.3: when the initial amplitude is large enough, the compaction function tends to increase its peak and ends up producing a black hole when it reaches 1. On the other hand, if the overdensity does not exceed a certain threshold, the compaction function maximum eventually decays away and does not lead to the formation of a black hole.

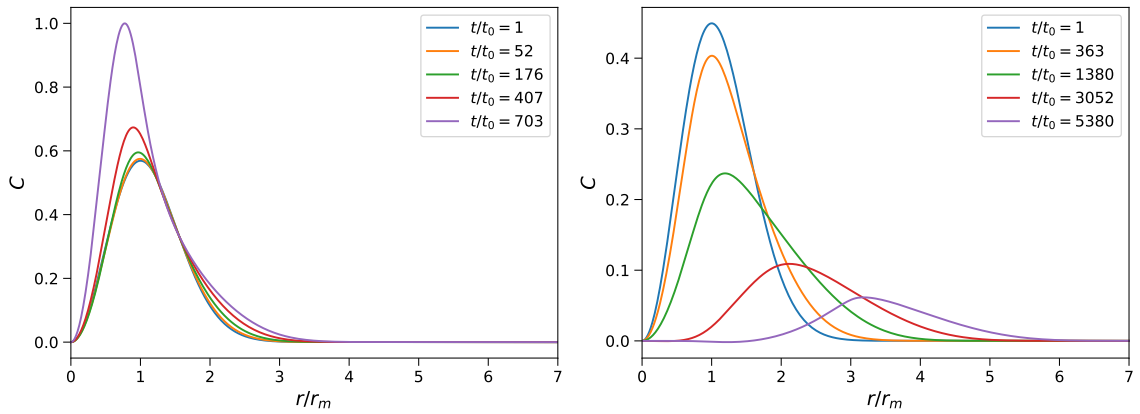

Figure 4.3: Time evolution of the compaction function $C(r)$ for an initial overdensity of $\delta_m = 0.57$, leading to the formation of a black hole (left), and $\delta_m = 0.45$, for which the pertubation decays away (right). In both cases, a radiation fluid is considered, $\omega = 1/3$.

We can then numerically compute the threshold in either δ_m or δ_0 by looking for it between a minimum and maximum value so that the maximum produces collapse and the minimum does not. Then, we can run a simulation with their mean value and, if it produces collapse, it becomes the new maximum and, otherwise it becomes the new minimum, in a simple bisection algorithm. For a Gaussian overdensity profile in radiation, the thresholds are

$$\delta_c \approx 0.498, \quad \delta_c = 0.453, \tag{4.72}$$

matching existing literature [230, 231, 232, 201, 204, 202]. The mass of the final black hole depends on the initial overdensity, but it obeys a very simple power law in the regime $\delta_m - \delta_c \lesssim 10^{-2}$, which is called *critical collapse* [226]. In this case, the mass can be computed as

$$m_{\mathrm{PBH}} = \mathcal{K}(\delta_m - \delta_c)^{\gamma} M_H, \tag{4.73}$$

with $M_H = 1/(2H(t_H))$ [204, 240] the mass of the cosmological horizon at t_H, and where $\mathcal{K}$ and γ are parameters whose values depend on the equation of state and overdensity profile. In the case of a Gaussian perturbation in a radiation fluid, they are approximately [204, 202]

$$\mathcal{K} \approx 6, \quad \gamma \approx 0.36. \tag{4.74}$$

For details of how these parameters, as well as the threshold, change with different overdensity profiles, see [201, 202]. Here, instead, we will focus on the changes with the equation of state parameter ω and comment on their consequences for PBH formation.

4.3.5 Threshold dependence of equation of state

By varying ω, one can see how the threshold varies. In Fig. 4.4, which reproduces a figure in [232] with own code based on [204], we notice how it starts at zero for $\omega = 0$ and increases as ω grows. This has a very clear physical interpretation: as ω increases, by definition (4.15), the pressure also does, which tends to prevent the collapse. Therefore, a more intense gravitational force produced by a larger overdensity is required for the collapse to succeed.

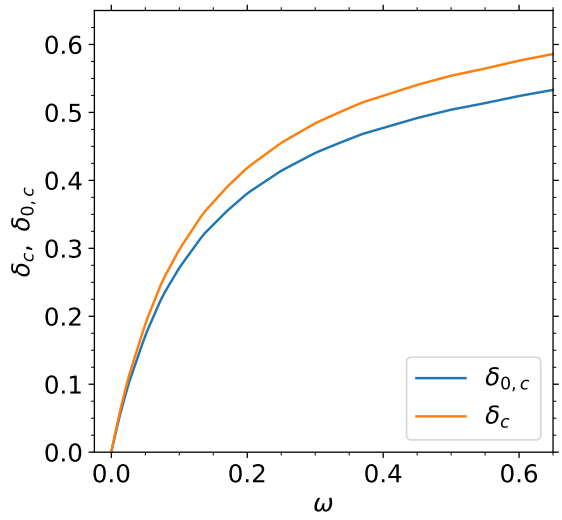

Figure 4.4: Thresholds δ_c and $\delta_{0,c}$ for δ_m and δ_0, respectively, as functions of the equation of state parameter ω.

From this behavior, we can derive some interesting consequences for primordial black holes which have to do with the thermal history of the Universe.

Thermal history of the Universe

At the early Universe, right after the inflation period, the Universe was constituted by a pure radiation fluid ($\omega = 1/3$). Up to the present day, eventually, matter ($\omega = 0$) started to dominate and, finally, dark energy ($\omega = -1$) became the main contribution to the energy density content of the Universe. However, as we know from the thermal history of the Universe, even within radiation domination, the equation of state parameter was not always close to $1/3$. As the Universe cooled down, the different particles progressively became non-relativistic, producing abrupt changes in the relativistic degrees of freedom, as we can see in the left panel of Fig. 4.5, which should be chronologically read from right to left. These changes caused the equation of state parameter to drop from $1/3$, as we can see in the right panel of the same figure.

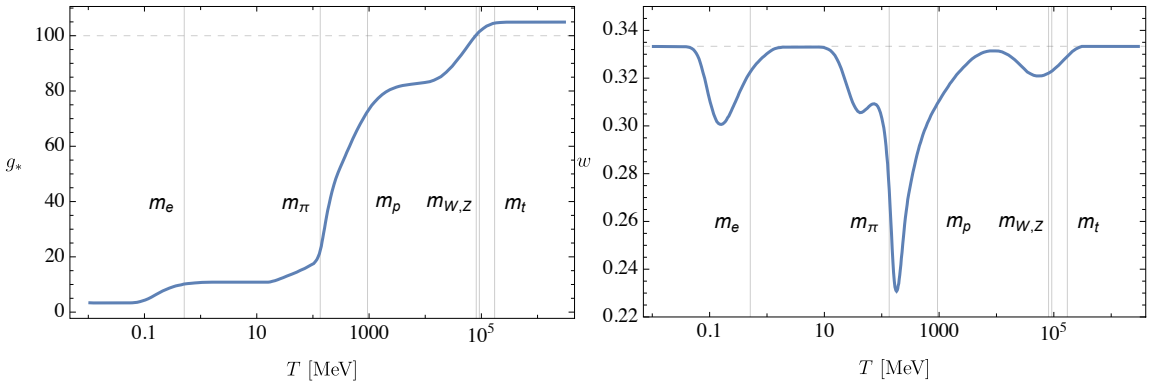

Figure 4.5: Relativistic degrees of freedom g_* (left) and equation of state parameter ω (right) evolution with temperature, showing the particles whose decoupling caused the changes. Figures taken from [168] and [200].

For primordial black holes, these changes in ω directly relate to a higher production of PBH, as inferred from the lower overdensity thresholds seen in Fig. 4.4. Additionally, as the Universe cooled down, the Hubble parameter $H(t)$ decreased, which translates into larger horizon masses $1/2H(t)$ and, via Eq. (4.73), larger PBH masses. Therefore, each of the bumps in ω observed in the left panel of Fig. 4.5translates into a larger amount of PBHs being produced with a mass roughly corresponding to the Hubble horizon at that time. In practice, these higher productions are seen as peaks in the mass spectrum of PBHs, as we can see in both panels of Fig. 4.6.

With this, we conclude this section, in which we have studied how PBHs are formed more in detail and explore the consequences of the change of threshold with the equation of state parameter, leading to their peculiar distribution in masses. In the next section, we will briefly review how these PBHs are distributed in space, as well as their interactions.

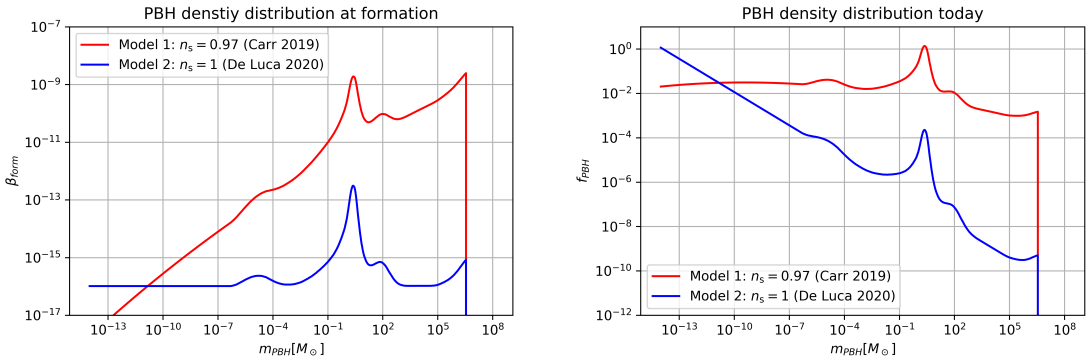

Figure 4.6: Left panel: density fraction of PBHs at formation (β_f defined in Eq. (4.1)) for the different PBH masses. Right panel: dark matter fraction of PBHs today. In both cases, two models are considered, where the first one comes from Refs. [241, 242] and the second one corresponds to Refs. [243, 244]. Figures taken from [168] and [200].

4.4 Merger rates of primordial black holes

Up to now, we have focused on the formation of isolated primordial black holes. Assuming that the density fluctuations are homogeneous, these black holes would be formed randomly, following a Poisson-like distribution. In this case, some of them would be generated so close to each other so as to decouple from the Universe expansion. Then, the gravitational attraction would dominate and drive their dynamics, constituting PBH clusters.

In particular, PBHs which form very close to another one can either directly merge or form PBH binaries, depending on the gravitational influence of other nearby objects. Black hole binaries which are formed shortly after PBHs are formed, before matter-radiation equality, are called *early binaries*, constituting one of the possible channels through which PBHs can form binary black holes [245, 246, 247, 248].

The other main mechanism for binary formation is that, at late times, PBHs within dense clusters dynamically capture another black hole, forming a *late binary* [249, 250]. These dynamical captures are produced when the two black holes interact in a hyperbolic-like encounter and, after the energy loss due to their interaction, their remaining kinetic energy is not enough to overcome their mutual gravitational pull, ending up being bound to each other.

There are many works focusing on either of these channels, or both, studying their merger rates. It is still not clear which of them should dominate, given that it depends on the mass distribution and clustering properties of PBHs [251]. In this thesis, we will focus on the late binary channel, which will be used to explain in detail our article on the SGWB produced by hyperbolic encounters of PBHs [2] in Chapter 5. For the early binaries, one can instead refer to [200, 246, 247, 252, 253, 254, 255].

4.4.1 Merger rates of PBH late binaries

We consider a hyperbolic-like interaction between two black holes with masses m_1 and m_2, with the orbital elements described in Sec. 1.4. The condition that a BBH forms from a close hyperbolic encounter is that the energy loss due to GW emission exceeds the kinetic energy $E_\infty = 1/2\,\mu v_\infty^2$. The energy loss by the GW emission is given by Eq. (1.217), with a function of the eccentricity $f(e)$ given by Eq. (1.218). Using Eq. (1.205) for the expression of v_∞, we can express the distance of closest approach r_p given by Eq. (1.202) as

$$r_p = \frac{GM}{v_\infty^2}(e-1), \tag{4.75}$$

so that the condition $E_\infty \leq |\Delta E|$ can be rewritten as [249, 250]

$$G(e) \geq \frac{15}{16}\frac{M^2}{m_1\,m_2}\frac{c^5}{v_\infty^5}\,, \tag{4.76}$$

with

$$G(e) \equiv \frac{f(e)}{(e-1)^{7/2}} = \begin{cases} \dfrac{425\pi}{4}\,(e^2-1)^{-7/2} & \text{for } e \approx 1\,, \\ \dfrac{37\pi}{8}\,(e^2-1)^{-3/2} & \text{for } e \gg 1\,. \end{cases} \tag{4.77}$$

If this condition is satisfied, the two black holes can become bound to each other and form a BBH. As explained in Sec. 1.3, they then describe a quasi-elliptic motion in which the energy loss makes them progressively closer to each other until, eventually, they merge. However, if this binary is located in a dense cluster, it has been shown that a third BH is likely to interact with the BBH during its evolution, breaking the binary system and preventing the merger [256, 248, 257]. One of the possibilities to get stable binaries in such dense environments is that they are formed at the cluster center and, later, they are ejected to the outskirt of the cluster. Such binaries are thus not disrupted, so that they eventually merge and emit GWs. We then want to estimate the merger rate of these binaries.

In order to compute the merger rate, we first write its cross-section σ. From scattering theory, we know that

$$\sigma = \pi b^2 = \pi\left(\frac{GM}{v_\infty^2}\right)^2 (e^2-1), \tag{4.78}$$

where b is the impact parameter defined in Sec. 1.4 that, in the last step, we have substituted in terms of v_∞ using Eqs. (1.198) and (1.205). We now assume that, in order for the dynamical capture to be effective, $e \approx 1$, which is the first case for the definition of $G(e)$ in Eq. (4.77). Substituting (e^2-1) in Eq. (4.78) using the condition (4.76) under this hypothesis, we obtain the cross-section for BBH formation,

$$\sigma^{\rm BBH} = \pi\left(\frac{340\pi}{3}\right)^{2/7}\frac{G^2 M^{10/7}(m_1\,m_2)^{2/7}}{c^{10/7}v_\infty^{18/7}}\,. \tag{4.79}$$

Thus, the formation rate of BBHs per individual event is given by

$$\tau_{\rm ind} = n(m) v_{\rm PBH}\sigma^{\rm BBH}, \tag{4.80}$$

where $n(m)$ is the number density of PBHs and $v_{\rm PBH} = v_\infty/\sqrt{2}$ is the PBH velocity. We assume a simplified clustering scenario in which PBHs are clustered in overdense regions, parametrized by a local density contrast $\delta_{\rm loc}$. If we assume that PBHs constitute all of the dark matter, $f_{\rm PBH} = 1$, we can write the number density as

$$n(m) \equiv \delta_{\rm loc} \frac{\overline{\rho}_{\rm DM}}{m}, \tag{4.81}$$

with the mean dark matter energy density $\overline{\rho}_{\rm DM} = \Omega_{\rm DM}\rho_c$, where $\Omega_{\rm DM} \simeq 0.25$ is the density parameter for dark matter.

However, it is more useful to work with the total merger rate per comoving volume. We can obtain this rate by multiplying $\tau_{\rm ind}$ by the number of PBHs in the comoving volume. This is similar to the previous step but, in this case, we multiply the averaged number density in the Universe, $n(m)/\delta_{\rm loc} = \overline{\rho}_{\rm DM}/m$, instead of the clustered one $n(m)$. Otherwise, we would obtain the merger rate in a given cluster volume, which is not what we are interested on. By taking into account a given mass distribution for the PBHs, the total merger rate is then given by [251]

$$\begin{aligned} \frac{d^2\tau^{\rm BBH}}{d\ln m_1\, d\ln m_2} &= \frac{1}{\delta_{\rm loc}}\, \sigma^{\rm BBH}\, v_{\rm PBH}\, n(m_1)\, n(m_2) \\ &\approx 14.8\ {\rm yr}^{-1}{\rm Gpc}^{-3} h_{70}^4 \left(\frac{\Omega_{\rm DM}}{0.25}\right)^2 \left(\frac{\delta_{\rm loc}}{10^8}\right) \left(\frac{v_\infty}{10\ {\rm km/s}}\right)^{-11/7} f(m_1)\, f(m_2) \frac{M^{10/7}}{(m_1\, m_2)^{5/7}}\,, \end{aligned} \tag{4.82}$$

where $f(m)$ is the logarithmic mass function of PBH. To be more conservative, we normalize it such that $\int d(\ln m)\, f(m) = f_{\rm PBH} \leq 1$, thus allowing for PBHs to constitute only a fraction of dark matter. Typical values for v_∞ are a few tens of km/s and $\delta_{\rm loc}$ can be taken of order 10^8, as in Ref. [251].

We conclude here our review of primordial black holes, which covered their main properties, some formation mechanisms, the numerical computation of their overdensity thresholds, as well as how they would impact their mass distribution over the thermal history of the Universe and, finally, their merger rates in the late binary scenario. These areas are enough for the objectives of this thesis, but there are many more aspects of these objects which can be covered, such as the formation mechanisms we have left unexplained, the behavior of early binaries, the constraints to PBH abundance from different methods and their detectability prospects. For them, one can refer to the review by the LISA Cosmology working group [200] and references therein.

In the next chapter, we will study an additional aspect of PBHs: how the late binaries contribute to the stochastic gravitational wave background, as well as address their detectability. Furthermore, we will discuss how the picture changes for hyperbolic encounters, as was studied in our article [2]. Additionally, in Chapter 7, we will use the PBH theory introduced in this chapter to derive some consequences of the spin induction effect produced during close hyperbolic encounters, as we studied in our article [1].

Chapter 5

SGWBs from close hyperbolic encounters of PBHs

5.1 Introduction

As we saw in Chapter 4, primordial black holes may have formed in the early Universe from the gravitational collapse of overdense regions. These objects have been studied for decades, as they may account for all or part of the dark matter in the Universe.

There is not yet definite proof of the existence of PBHs, but recently, GW observations of BBH mergers are providing rich information on the black hole population [258]. In fact, some analyses based on the mass and rate distributions [241, 259, 260, 242, 261, 252, 262] or spin properties [263, 264] suggest that the observed BBHs could be of primordial origin.

Another approach to probing PBHs is to look for a SGWB, which can be formed both at the PBH formation via scalar-induced GWs [93, 265, 266], as seen in Sec. 2.5, and by the superposition of GWs from BBHs [267, 251, 268, 269, 270], as we will study in this chapter. Until now, the LIGO and Virgo detectors have been improving the upper limit on the amplitude of SGWBs [28], and constraints on PBHs through SGWBs have been discussed [271, 96, 272]. In the future, the upgraded version of the LIGO-Virgo-KAGRA detector network [19] (and later with LIGO-India [273]) and next-generation GW experiments such as Einstein Telescope (ET) [17], Cosmic Explorer (CE) [18], LISA [20], TianQin [21], Taiji [22], DECIGO [23], will allow us to detect SGWBs with greater sensitivities for a wide range of frequencies, as we commented during the discussion of Fig. 2.1.

In this chapter, we will review one of our works [2] in which we propose an important additional source for SGWBs, which is the one formed by overlapped GW bursts from close hyperbolic encounters. Gravitational waves from these unbound interacting systems can be observed by GW experiments and have been studied in the literature [274, 275, 67, 68, 54, 53, 276, 55]. In fact, the dense environment at the center of PBH clusters can enhance the rate of these events, with an eccentricity close to unity [277], leading to strong GW bursts. Furthermore, if the interaction is strong enough, they can produce nontrivial dynamics, such as spin induction [1, 278] and subsequent mergers [279].

In this work, we made the first estimation of the SGWB amplitude from CHEs, discussing its detectability in future GW experiments and comparing it to the one from BBHs.

5.2 Stochastic background of GWs

For SGWBs of point source origin, the GW spectrum can be computed by

$$\Omega_{\rm GW}(f) = \frac{1}{\rho_c}\int_0^\infty dz\,\frac{N(z)}{1+z}\,\frac{dE_{\rm GW}}{d\ln f_r}\,, \tag{5.1}$$

where $f_r = (1+z)f$ is the emitted GW frequency, which is redshifted with respect to the one we measure, and $N(z)$ is the number density of GW events at redshift z, given by

$$N(z) = \frac{\tau(z)}{(1+z)H(z)}\,. \tag{5.2}$$

Here, $H(z)$ is the Hubble parameter and $\tau(z)$ is the merger rate per unit time per comoving volume. For a broad mass distribution of black holes, the merging rate should be replaced by

$$\tau(z) = \int\!\!\int d(\ln m_1)\,d(\ln m_2)\,\frac{d^2\tau}{d\ln m_1\,d\ln m_2}\,. \tag{5.3}$$

5.2.1 Binary BHs

We first compute the stochastic gravitational wave background from BBHs. As in Sec. 4.4, we assume the late binary scenario which is the one closely related to CHE. Thus, we can directly use the merger rate derived in Eq. (4.82).

For the energy emission, we could take the energy spectrum from Eq. (1.196). However, we followed a slightly different formalism in [280, 281], which includes the contributions of the inspiral, merger, and ringdown parts of the BBH waveform. In the absence of spin and eccentricity, the GW energy spectrum takes the form

$$\frac{dE^{\rm BBH}}{d\ln f_r} = \frac{(\pi G)^{2/3} m_1\,m_2}{3c^2 M^{1/3}}\,f_r^{2/3}\,\mathcal{F}(f_r)\,, \tag{5.4}$$

where $\mathcal{F}(f_r)$ describes the deviation from the frequency dependence of the inspiral phase $f_r^{2/3}$. It is explicitly given by

$$\mathcal{F}(f_r) = \begin{cases} (1+\alpha_2 u^2)^2 & \text{for} \quad f_r < f_1, \\ w_1 f_r (1+\epsilon_1 u + \epsilon_2 u^2)^2 & \text{for} \quad f_1 \le f_r < f_2, \\ w_2 f_r^{7/3}\left(1+4\left(\frac{f_r-f_2}{\sigma}\right)^2\right)^{-2} & \text{for} \quad f_2 \le f_r < f_3, \end{cases} \tag{5.5}$$

where $u \equiv (\pi M G f_r/c^3)^{1/3}$, $\alpha_2 = -323/224 + 451\eta/168$, $\eta \equiv m_1 m_2/M^2$, $\epsilon_1 = -1.8897$, $\epsilon_2 = 1.6557$.

The transition frequencies and the width are given by $\{f_1, f_2, f_3, \sigma\} \equiv c^3/(\pi MG)\beta_i$ with

$$\begin{aligned}\beta_1 &= 0.066 + 0.6437\eta - 0.05822\eta^2 - 7.092\eta^3,\\ \beta_2 &= 0.185 + 0.1469\eta - 0.0249\eta^2 + 2.325\eta^3,\\ \beta_3 &= 0.3236 - 0.1331\eta - 0.2714\eta^2 + 4.922\eta^3,\\ \beta_4 &= 0.0925 - 0.4098\eta + 1.829\eta^2 - 2.87\eta^3.\end{aligned} \tag{5.6}$$

The normalization constants w_1 and w_2 are

$$\begin{aligned}w_1 &= f_1^{-1}\frac{[1+\alpha_2 u_1^2]^2}{[1+\epsilon_1 u_1 + \epsilon_2 u_1^2]^2},\\ w_2 &= w_1 f_2^{-4/3}[1+\epsilon_1 u_2 + \epsilon_2 u_2^2]^2,\end{aligned} \tag{5.7}$$

where $u_i \equiv (\pi MG f_i/c^3)^{1/3} = \beta_i^{1/3}$.

We can see that, for low frequencies, $\mathcal{F}(f_r) \approx 1$, so that Eq. (5.4) reduces to Eq. (1.196).

Assuming a time-independent merger rate, we can numerically integrate the redshift dependence of Eq. (5.1). In particular, the low-frequency tail is characterized by $\mathcal{F}(f_r) = 1$, so the redshift dependence is integrated as

$$\int_0^\infty \frac{dz}{(1+z)^{4/3}H(z)} = 0.76\, H_0^{-1}\,, \tag{5.8}$$

where $H(z)$ is the Hubble parameter as a function of redshift. In the previous equation, we substituted the value of the matter energy density parameter $\Omega_{\rm M} = 0.31$. The low-frequency limit of the SGWB from BBH is then

$$\begin{aligned}\Omega_{\rm GW}^{\rm BBH}(f) \approx{}& 2.39\times 10^{-13}\, h_{70}\left(\frac{\Omega_{\rm DM}}{0.25}\right)^2\left(\frac{\delta_{\rm loc}}{10^8}\right)\left(\frac{v_\infty}{10\ {\rm km/s}}\right)^{-11/7}\left(\frac{f}{\rm Hz}\right)^{2/3}\\ &\times\int\!\!\int dm_1\, dm_2 \frac{f(m_1)\, f(m_2)\, (m_1+m_2)^{23/21}}{(m_1\, m_2)^{5/7}}\,,\end{aligned} \tag{5.9}$$

with m_i in solar mass units.

Furthermore, we can refine the analysis by assuming a redshift-dependent merger rate, $\tau^{\rm BBH} \propto (1+z)^\beta$, with exponent $0 < \beta < 1.28$ [272, 248]. In this case, the low-frequency part of the spectrum gets enhanced by at most a constant factor 3.9, slightly modifying the shape of the spectrum near the peak. However, the slope at low frequencies stays at $f^{2/3}$ and the cutoff at high frequencies remains invariant. We will visualize this effect in the next section.

5.2.2 Close hyperbolic encounters

In the dense environment at the center of a cluster, a large fraction of BH encounters does not end up producing bound systems, instead producing a single scattering event. These encounters have been studied much less than BBHs but, in fact, CHEs should be more common at the inner part of BH clusters [277]. In addition, they also emit GWs, which should be considered both for individual events [54, 53] and for their contributions to the SGWB.

If a pair of BHs does not satisfy the condition Eq. (4.76), then the two BHs eventually get further away in a close hyperbolic encounter. The cross-section σ is again given by Eq. (4.78), this time without the condition in Eq. (4.76) imposed on the eccentricity. Thus, aside from the BH masses, we have two free parameters: v_∞ and e. Multiplying by the averaged number density (see Subsec. 4.4.1 for the discussion on $\delta_{\rm loc}$), we obtain the total event rate,

$$\begin{aligned}\frac{d^2\tau^{\rm CHE}}{dm_1\,dm_2} &= \frac{1}{\delta_{\rm loc}}\sigma v_{\rm PBH}\, n(m_1)\, n(m_2)\\ &\approx 25.4\times 10^{-8}\ {\rm yr}^{-1}{\rm Gpc}^{-3}\, h_{70}^4 \left(\frac{\Omega_{\rm DM}}{0.25}\right)^2 \left(\frac{\delta_{\rm loc}}{10^8}\right) \frac{f(m_1)}{m_1}\frac{f(m_2)}{m_2}\frac{M^2}{m_1\,m_2}\frac{e^2-1}{(v_\infty/c)^3}\,. \end{aligned} \tag{5.10}$$

Using Eq. (1.205) for v_∞, from now on, we substitute this velocity by its expression in terms of the semi-major axis a. As for BBHs, we also include the factor $(1+z)^\beta$ in order to parametrize the event rate time dependence.

The energy spectrum of hyperbolic encounters was shown in Eq. (1.219) using Refs. [68, 53]. We also include it here for convenience,

$$\frac{dE_{\rm GW}^{\rm CHE}}{d\ln f_r} = \nu\frac{dE_{\rm GW}}{d\nu} = \frac{4\pi}{45}\frac{G^3 m_1^2 m_2^2}{a^2 c^5 \nu_0}\,\nu^5 F_e(\nu)\,, \tag{5.11}$$

where $\nu \equiv 2\pi\nu_0\, f_r$, with $\nu_0^2 \equiv a^3/GM$, is the dimensionless frequency, and $F_e(\nu)$ is such that [54]

$$\begin{aligned}\nu^5 F_e(\nu) &\simeq \frac{12F(\nu)}{\pi\, y\,(1+y^2)^2}\, e^{-2\nu\,\xi(y)}\,,\\ F(\nu) &= \nu^2\left(1-y^2-3\,\nu\, y^3+4\,y^4+9\,\nu\, y^5+6\,\nu^2 y^6\right)\,,\\ \xi(y) &= y-\tan^{-1}y\,,\\ y &= \sqrt{e^2-1}\,. \end{aligned} \tag{5.12}$$

In order to integrate the redshift dependence of Eq. (5.1), we define the following function

$$\begin{aligned} I[y,\,x_0] \equiv& \frac{\pi}{12}\int_0^\infty dz\,\frac{\nu^5\,F_e(\nu)\,H_0\sqrt{\Omega_{\rm M}}}{(1+z)^2 H(z)}(1+z)^\beta \simeq \frac{\pi x_0^{5/2-\beta}}{12}\int_{x_0}^\infty d\nu\,\nu^{3/2+\beta}F_e(\nu)\\ =&\frac{2x_0^{5/2-\beta}}{(2\xi)^{3/2+\beta}}\frac{1}{y(1+y^2)^2}\left[2(1-y^2+4y^4)\,\xi^2\,\Gamma\left(-\frac{1}{2}+\beta,\,2x_0\xi\right)\right.\\ &\left.+\,3y^3(-1+3y^2)\,\xi\,\Gamma\left(\frac{1}{2}+\beta,\,2x_0\xi\right)+3y^6\Gamma\left(\frac{3}{2}+\beta,\,2x_0\xi\right)\right] \end{aligned} \tag{5.13}$$

where Γ is the upper incomplete gamma function and we define

$$x_0 \equiv 2\pi\nu_0 f, \quad \text{so that} \quad \nu = x_0(1+z). \tag{5.14}$$

At low frequencies, we find that the function follows

$$x_0^\alpha \propto f^\alpha, \quad \alpha = \min\{2,\,5/2-\beta\}. \tag{5.15}$$

This is one of the key features of the CHE contribution to the SGWB: a measurement of the slope of the low-frequency tail would provide information about the redshift dependence of the event rate. For BBH, however, this event rate dependence of redshift only shifts the amplitude without changing the slope. Since the merger rates of astrophysical and primordial black holes evolve very differently with redshift, this feature of CHEs could help distinguish between them.

For the subsequent discussion, we focus on the constant event rate case $\beta = 0$, so that the previous integral simplifies to

$$I[y,\, x_0] \simeq 2\, x_0^2\, e^{-2x_0\xi(y)} \left(\frac{1 - y^2 + 4y^4 + \frac{3}{2}\frac{x_0 y^6}{\xi(y)}}{y\,(1+y^2)^2} \right) \Bigg(\tag{5.16}$$

This function peaks at around $x_0^{\rm peak} \simeq 1/\xi(y)$ and decays as $\exp(-2x_0\xi(y))$ at higher frequencies. For $y \ll 1$, we can use the first order of the Taylor expansion of $\xi(y)$, which is $\xi(y) \approx y^3/3$, to estimate the peak frequency as

$$f_{\rm peak} \simeq 43\,{\rm Hz} \left(\frac{y}{0.01}\right)^{-3} \left(\frac{M}{200 M_\odot}\right)^{1/2} \left(\frac{a}{0.1\ {\rm AU}}\right)^{-3/2} , \tag{5.17}$$

which depends on the intrinsic properties of the CHE (M, a, e). Putting all of this together and redefining

$$I[y, x_0] = \frac{2x_0^2}{y} e^{-2x_0\xi(y)} \tilde{I}[y, x_0], \tag{5.18}$$

so that $\tilde{I}[y, x_0]$ is of order unity at low frequencies, we find

$$\begin{aligned} \Omega_{\rm GW}^{\rm CHE}(f) \approx & 9.81 \times 10^{-13}\, h_{70} \left(\frac{\Omega_{\rm M}}{0.3}\right)^{-1/2} \left(\frac{\Omega_{\rm DM}}{0.25}\right)^{2} \left(\frac{\delta_{\rm loc}}{10^8}\right) \left(\frac{a}{0.1\ {\rm AU}}\right) \left(\frac{f}{10{\rm Hz}}\right)^{2} \left(\frac{y}{0.01}\right) \Bigg(\\ & \times \int \Bigg(\frac{dm_1}{100 M_\odot} \frac{dm_2}{100 M_\odot} f(m_1)\, f(m_2)\, e^{-2x_0\xi(y)}\, \tilde{I}[y, x_0] \,. \end{aligned} \tag{5.19}$$

In addition, for the peak frequency in Eq. (5.17), we can approximate

$$\begin{aligned} \Omega_{\rm GW}^{\rm CHE}(f_{\rm peak}) \approx & 3.6 \times 10^{-13}\, h_{70} \left(\frac{\Omega_{\rm M}}{0.3}\right)^{-1/2} \left(\frac{\Omega_{\rm DM}}{0.25}\right)^{2} \left(\frac{\delta_{\rm loc}}{10^8}\right) \left(\frac{a}{0.1\ {\rm AU}}\right)^{-2} \\ & \times \left(\frac{y}{0.01}\right)^{-5} \frac{m_1}{100 M_\odot} \frac{m_2}{100 M_\odot} \frac{m_1 + m_2}{200 M_\odot} \,. \end{aligned} \tag{5.20}$$

For instance, by taking $m_1 = m_2 = 300 M_\odot$, $a = 5$AU and $y = 2 \times 10^{-3}$, we find $\Omega_{\rm GW}(f_{\rm peak}) \approx 1.2 \times 10^{-11}$ at the LIGO frequency band, $f_{\rm peak} \approx 26$ Hz. On the other hand, $m_1 = m_2 = 300 M_\odot$, $a = 5 \times 10^7$AU and $y = 10^{-5}$ yields $\Omega_{\rm GW}(f_{\rm peak}) \approx 3.9 \times 10^{-14}$ at the LISA frequency band, $f_{\rm peak} \approx 6.7$ mHz.

Eq. (5.20) shows the intuitively expected behavior that we get larger SGWB amplitudes for larger masses, smaller semi-major axes, and smaller y (eccentricity close to unity). These parameter values would be distributed on a wide range and, in principle, we should obtain the SGWB spectrum by marginalizing over them. Given that we do not know the distributions of the involved parameters, for simplicity, we assume log-normal distributions of median $m_0/a_0/y_0$ and its variance $\sigma_m/\sigma_a/\sigma_y$.

5.2.3 Comparison between BBHs and CHEs

In Fig. 5.1, we plot some example GW spectra for BBHs and CHEs. In order to get reasonable contributions for both the LISA and LIGO frequency bands, we marginalized over mass distributions centered at $100 - 300 M_\odot$. However, a more detailed analysis should consider more physically motivated mass distributions. As illustrated by Eqs. (5.17) and (5.20), higher masses produce greater backgrounds peaking at higher frequencies, while the opposite is true for lower masses. For reference, in Fig. 5.1, we also plot the *power-law integrated* (PI) *sensitivity curves* of the detectors, which show their sensitivity to detect a power-law background after integrating this power law over frequency. These PI sensitivity curves are thus very helpful to address the detection of power-law like SGWBs, given that they account for the increase of sensitivity obtained from the integration.

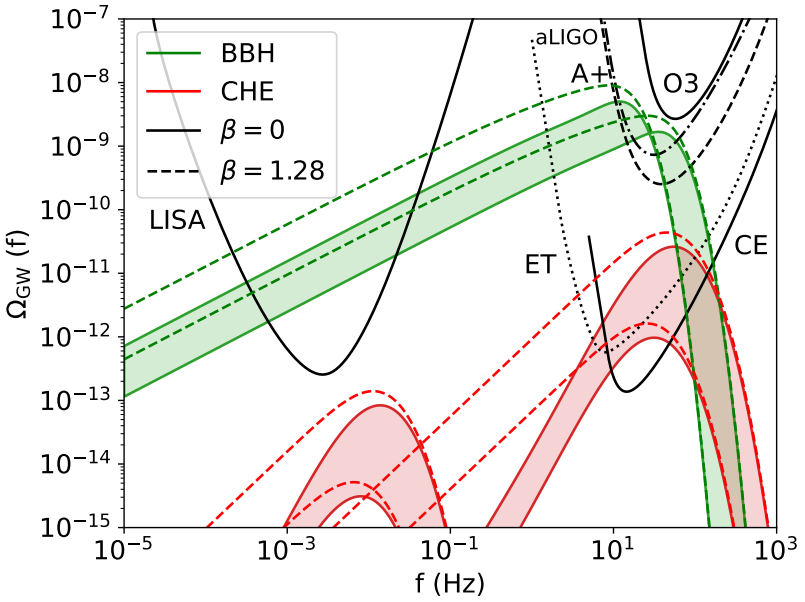

Figure 5.1: Comparison of the SGWB spectrum originating from BBHs and CHEs, both for $\beta = 0$ (solid lines) and 1.28 (dashed lines). The power-law integrated sensitivity curves of several GW detectors are also plotted for a signal-to-noise ratio of 10 and an observation time of 1 year, following the formalism in [282]. For the BBH curves, we take $m_1 = m_2 = 100 - 300\ M_\odot$ and $v_\infty = 30$km/s. The CHE curves correspond to the same range of masses with $a_0 = 5$AU, $y_0 = 2 \times 10^{-3}$ for ~ 10Hz, and $a_0 = 5 \cdot 10^7$AU, $y_0 = 10^{-5}$ for the mHz range. For all cases, we take $\sigma_a, \sigma_y = 0.1$, $\sigma_m = 0.5$, and $f_{\rm PBH} = 1$. For a smaller fraction of PBHs, the GW spectral amplitude simply scales as $\Omega_{\rm GW} \propto f_{\rm PBH}^2$.

Another thing we can observe in Fig. 5.1 is that the SGWB spectrum from CHEs is steeper than the one from BBHs, which is expected from the frequency dependence of Eqs. (5.19) and (5.13). In the case of the constant merger rate $\beta = 0$, the SGWB spectrum inherits the f^2 dependence of the spectrum of the individual event at low frequencies, while the individual BBH spectrum does the same for the $f^{2/3}$ dependence. A possible physical interpretation is that a CHE emits a single burst of GWs, whereas the ones from a BBH are essentially periodic with increasing frequency. It

is, therefore, natural that the BBH case has a broader spectrum in frequency.

In addition, we can see the different behavior of the BBH and CHE tails as the merger rate dependence with redshift increases its exponent β. As mentioned before, the change of the BBH curves with β is just an overall enhancement up to a factor 3.9, whereas the CHE curves notably modify their slopes. This sensitivity of the CHE background to β is very relevant, since the rate dependence on redshift is one of the features that distinguish astrophysical from primordial black holes [280]. Therefore, a measurement of the tail of the CHE background could provide useful information about the relative abundance of both populations.

For the LIGO frequency range, with modest values of the parameters, we can see in Fig. 5.1 that the CHE spectrum can reach ET and CE sensitivities. Although the CHE contribution is below the BBH curves, we note that the disruption of the binary system in a dense environment, which could lower the GW amplitude, is not taken into account. We should also take into account that some BBH events with a large signal can be detected individually and subtracted from the data [283].

More restrictive parameters are needed in order to produce a relevant CHE background in the LISA frequency band, although the joint observation with TianQin or Taiji could improve the sensitivity in these frequencies [284, 285, 286]. This difficulty can easily be understood if we rewrite Eq. (5.20) in terms of the peak frequency,

$$\Omega_{\rm GW}^{\rm CHE}(f_{\rm peak}) \approx 4.4\times10^{-13}\, h_{70} \left(\frac{\Omega_{\rm M}}{0.3}\right)^{-1/2} \left(\frac{\Omega_{\rm DM}}{0.25}\right)^{2} \left(\frac{\delta_{\rm loc}}{10^{8}}\right) \left(\frac{f_{\rm peak}}{50\ {\rm Hz}}\right)^{4/3} \times \left(\frac{y}{0.01}\right)^{-1} \frac{m_1}{100M_\odot}\frac{m_2}{100M_\odot} \left(\frac{m_1+m_2}{200M_\odot}\right)^{1/3}. \tag{5.21}$$

From this expression, we can see that, for fixed masses and eccentricity, the maximum amplitude $\Omega_{\rm GW}^{\rm CHE}(f_{\rm peak})$ grows with $f_{\rm peak}^{4/3}$. Therefore, with modest parameters as the CHE curves in the LIGO range, the amplitude of the background decays significantly if we try to translate the curve to the LISA range. On the other hand, however, this is a hint that the SGWB from CHE may play an important role in higher frequency ranges, such as the ultra-high frequency (MHz-GHz) band for which there are good prospects of detection in the future [287] (see Chapter 8 for a more detailed discussion on GW detection in different frequency bands).

5.3 Conclusions

In our article [2], we proposed a new source for stochastic gravitational wave backgrounds, which comes from CHEs. We computed the SGWB spectrum from a superposition of GWs from CHE events and compared the amplitude with the one from BBHs. We have seen that they have different frequency dependencies, which would help to distinguish the two different origins when detection of SGWB is made. Furthermore, as shown in Fig. 5.1, we have found that there exist combinations of parameter values that can make the CHE contribution detectable by future GW interferometers, especially with ET, CE or ultra-high frequency experiments, and with more difficulty in the LISA range.

In addition, we discovered that a change on the event rate dependence on redshift translates

into a change of slope for the CHE contribution of the low-frequency tail. This is something that does not happen for BBH and opens the possibility to probing the time evolution of the event rate.

As we have discussed, formations of BBHs and CHEs strongly depend on the clustering nature of the PBHs. Current cosmological observations have not yet provided a clear picture of BH distribution in the Universe. Detection of SGWB would provide new implications on the BH evolution. In addition, we have focused on SGWB from PBHs, but GWs from astrophysical black holes would also contribute to the SGWB. Given the fact that the event rate evolves differently with time for ABHs and PBHs, the slope of the tail of the CHE background could serve to disentangle both contributions and derive their relative abundance. The combination of other information from further investigations, such as spectral shapes [288, 289, 272], anisotropy [290, 291, 194] or popcorn features [292, 293], can also help to obtain implications on the origin of BHs.

As a final remark, we assumed a simplified scenario in which the overdense regions are uniform and parametrized by $\delta_{\rm loc}$ (see Subsec. 4.4.1). However, our work can be extended to incorporate a more detailed clustering profile of PBHs. Besides, we could consider more realistic distributions of the CHE parameters, such as semi-major axis and eccentricity. In fact, we have observed that when we make the log-normal distribution of the parameters wider, the spectral shape changes dramatically, and the peak amplitude tends to get enhanced. We leave the detailed analysis for future work.

Chapter 6

Numerical Relativity

The first gravitational-wave detection in 2015 [7] opened up a new window of observations to the Universe. We have seen in previous chapters that compact binary coalescences are the dominant events we can observe with current detectors, so it is of key importance to interpret these signals correctly. In Section 1.3, we studied the gravitational waves produced by the inspiral of CBCs assuming quasi-circular orbits. However, the merger dynamics is highly non-linear and cannot be modelled with analytical approximations, so it is necessary to solve Einstein's equations with more precision, resorting to Numerical Relativity. Furthermore, if we relax the assumption of quasi-circular orbits, there is a huge parameter space which CBCs can occupy, with different masses, eccentricities and spins (intrinsic parameters), as well as varying orientations and distances to the source (extrinsic parameters, which can easily be treated analytically).

In general, NR simulations are very computationally expensive to run, so they are not useful to do parameter estimation of CBCs, for which a lot of GW templates, or *waveforms*, are required. As a result, many approximate models to generate them, or *gravitational-wave approximants*, have been developed in recent years. They can be classified into several types:

- Effective one body (EOB) models [294] combine perturbative results, such as the mentioned post-Newtonian and post-Minkowskian, together with physically motivated shapes for the merger, as well as ringdown models coming from BH perturbation theory. Some state-of-the-art examples include SEOBNRv5PHM [36] and TEOBResumS [37].

- Phenomenological models [295, 296] fit the inspiral, merger and ringdown from EOB models, PN approximations and NR, getting a fast waveform generation. Some examples include IMRPhenomTPHM [30], IMRPhenomXPHM [31] and IPhenomXO4a [32].

- NR surrogates interpolate between waveforms from NR simulations, being the most reliable option within their parameter space, but of limited applicability. Some examples include NRSur7dq4 [297] and NRHybSur3dq8_CCE [298].

These models have a lot of parameters which are calibrated to numerical simulations, so that they can reproduce NR accuracy within the parameter space they were calibrated for, while taking just

a fraction of a second to generate a GW template, or *waveform*. However, recent works [299, 300] have pointed out that these templates are still insufficient to get an accurate estimation for the parameters of the GW signals we receive. Furthermore, the problem will only get worse as the sensitivity of GW detectors increases. Therefore, a lot NR simulations are still required to have a good, accurate coverage of the full parameter space.

In this chapter, we will cover some of the basic concepts of Numerical Relativity, as well as use an NR software, the Einstein Toolkit [301, 302], to run some simulations and analyze their outputs. We will do this both for standard BBHs and for the less studied hyperbolic encounters.

During this chapter and the next one, related to NR, we will work in geometrized units, $G = c = 1$, as we did in Sec. 4.3. In this case, the unit mass will provide the unit length and time. Furthermore, the numerical simulations we will see are invariant under a change of total mass, so we will set $M = m_1 + m_2 = 1$. Therefore, when interpreting the output, the time and length have to be rescaled by M. Thus, the figures will be plotted in terms of t/M or x/M.

6.1 Introduction to NR

The first attempt to solve Einstein's equations numerically dates back to an article by Susan Hahn and Richard Lindquist in 1964 [303]. In this work, the authors evolve initial data generated by Charles Misner [304] to simulate a BBH head-on collision. However, it was not until 2005 when the first BBH with angular momentum was successfully simulated by Pretorius [33], followed soon after by the groups at Brownsville [34] and NASA Goddard [35]. The success of these simulations was essential to the field of gravitational waves, given that it was only 10 years later, the LIGO detectors received the first ever detected gravitational wave, GW150914 [7]. The detection and analysis of this signal would not have been possible if templates from numerical simulations had not yet been ready.

During this section, we will cover some of the formalisms used in NR and briefly comment on some of the issues related to numerical simulations, such as the generation of initial conditions or technical details as the AMR, already mentioned in Sec. 4.3. This section will be based on several references, such as [305, 306, 301].

6.1.1 The 3+1 ADM formalism

As we saw in Sec. 4.3, within Numerical Relativity, it is important to choose a suitable formalism in which the problem can be treated well. In this section, we will not get to the full equations and initial conditions as we did in Sec. 4.3, but only give a brief overview of the formalisms which are more common in Numerical Relativity and, in particular, for BBH simulations.

In order to work with the Einstein equations, their covariant four-dimensional form is not suitable to describe a temporal evolution. It is then more convenient to split the four-dimensional manifold into a time succession of three-dimensional manifolds (*slices*), which is called *foliation*. This clear separation between the time and spatial components is called *3+1 decomposition*, and it is a very general framework in which one can define multiple formalisms.

The most extended application of the 3+1 decomposition is the ADM (Arnowitt-Deser-Misner) formalism [307], which expresses the spacetime metric as

$$ds^2 = g_{\mu\nu}dx^\mu dx^\nu = -\alpha^2 dt^2 + \gamma_{ij}(dx^i + \beta^i dt)(dx^j + \beta^j dt), \tag{6.1}$$

where α is called *lapse*, β^i is the *shift* and γ_{ij} is the spatial metric. Another important quantity is the *extrinsic curvature*, defined as

$$K_{ij} \equiv -\frac{1}{2\alpha}(\partial_t - \mathcal{L}_{\vec{\beta}})\gamma_{ij}, \tag{6.2}$$

where $\mathcal{L}_{\vec{\beta}}$ is the Lie derivative with respect to the shift vector. With these definitions, the Einstein equations form a hyperbolic-elliptic system of PDEs which are suitable to work with. Their exact form is given in [305, 308, 309], involving some additional definitions and subtleties which are not relevant for the goals of this thesis.

Another formalism which is commonly used is the BSSN (Baumgarte-Shapiro-Shibata-Nakamura) [310, 311], which is a variation of ADM. The most relevant modification is a conformal transformation so that the new metric $\tilde{\gamma}_{ij}$ has unit determinant and the new extrinsic curvature $\tilde{A}_{ij}$ is traceless. One can then define these quantities from γ_{ij} and K_{ij} as

$$\tilde{\gamma}_{ij} = (\det\gamma)^{-1}\gamma_{ij}, \quad \tilde{A}_{ij} = (\det\gamma)^{-1}\left(K_{ij} - \frac{1}{3}\gamma_{ij}\gamma^{kl}K_{kl}\right)\left(\tag{6.3}$$

This formalism has been widely used to simulate BBHs and, in particular, it is the one used in all the simulations shown in this chapter and the next one. For the exact equations, one can refer to [305, 312].

Any of these formalisms provides the Einstein equations in a suitable form. Then, the next step is to generate valid initial conditions that can be numerically evolved.

6.1.2 Initial conditions

From the classic Keplerian point of view, the initial conditions of a BBH simulation would consist on two black holes of certain masses m_1 and m_2, separated a certain distance d, with certain initial momenta $\vec{p_1}$ and $\vec{p_2}$ and spins $\vec{\chi}_1$ and $\vec{\chi}_2$, where $\vec{\chi}$ is each black hole rotation angular momentum divided by its mass squared, so that it is dimensionless. The situation is depicted in Fig. 6.1. In general, since NR simulations are independent of the total mass $M = m_1 + m_2$, only one mass parameter is necessary to fully describe these masses: the mass ratio q. In our simulations, we use the convention $m_1 \geq m_2$, so, in order for q to adapt to the convention $0 < q \leq 1$, we define it as

$$q \equiv \frac{m_2}{m_1}. \tag{6.4}$$

Other references, however, use the convention $q \geq 1$, so one has to be careful when using concepts such as "high" or "low" mass ratios. In addition, in order for the center of mass to stay fixed, it is convenient to take symmetric initial momenta, $\vec{p_1} = -\vec{p_2}$.

However, in the context of General Relativity, setting initial conditions means to fill the simulation volume with all the needed variables in GR. In the ADM formalism, this involves setting the metric elements in Eq. (6.1), which is not trivial just from the mentioned physical quantities.

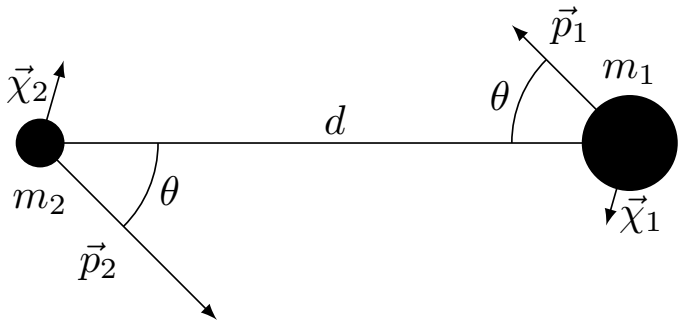

Figure 6.1: Initial conditions for numerical BBH simulations, where we take $m_1 \geq m_2$ and $\vec{p}_1 = -\vec{p}_2$.

Different methods to generate initial conditions have been developed over the last decades. The first BBH head-on collision by Hahn and Lindquist [303] used initial data generated by Misner [304]. Around the same years, the Brill-Lindquist initial data [313] was also developed, which has been used for decades to simulate head-on collisions [314]. The reason that these two types of initial value data were used for this purpose is that they represent two initially static black holes without spin, so its applicability is very limited.

One of the most used methods to generate initial data is based on the Bowen-York prescription [315], usually referred to as *puncture* initial data, which extends the Brill-Lindquist solution to arbitrary angular momentum and allows for initial spins. This method was further simplified by Brandt and Brügmann [316] and a particularly extended algorithm was proposed in [317], which is used in NR softwares such as the Einstein Toolkit [301, 302] or GRChombo [318, 319, 320]. The introduction of angular momentum allowed to develop more general BBH simulations, moving on from head-on collisions.

Junk radiation

The mentioned methods represent physical solutions to the Einstein's equations which are useful to start the numerical evolution. However, these initial conditions do not correspond to the exact state of two black holes having evolved from their previous, natural dynamics. The mentioned initial solutions are constructed from the hypothesis of conformal flatness, which does not correspond to a relaxed state of black holes with certain angular momentum. They are thus unphysically perturbed and, after some evolution time, they relax to an equilibrium configuration in which they evolve normally. During this relaxation, however, they emit a spurious gravitational-wave burst, which is usually referred to as *junk radiation* [321, 322, 323]. We can see this initial burst in Fig. 6.2, which shows the Weyl scalar Ψ_4 (directly related to the GWs, as we will see in Subsec. 6.2.3), for the BBH simulation described in Sec. 6.2. In the next section, this initial burst can also be seen in Fig. 6.6. Therefore, when running an NR simulation, one has to be aware that the initial instants are not physical, so they have to be interpreted with caution.

In order to run our numerical simulations, we need two additional elements: the boundary conditions and the grid. For the boundary conditions, one of the options is to impose Sommerfeld radiative conditions [324]. These assume that, near the boundary, all the fields behave as outgoing

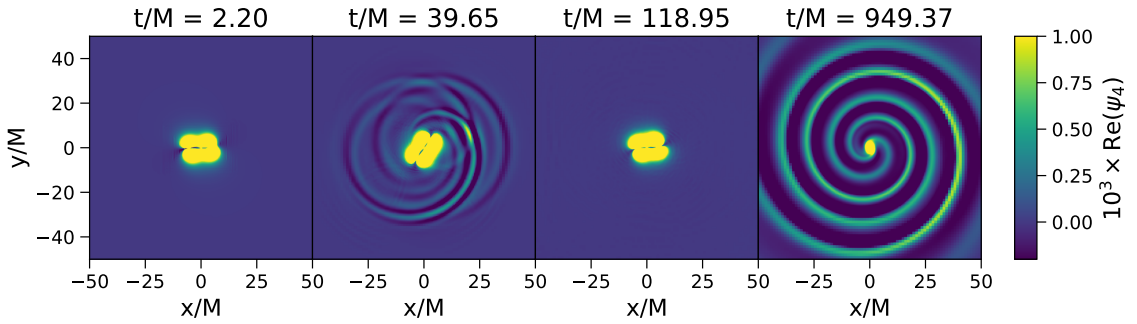

Figure 6.2: Real part of the Weyl scalar Ψ_4 defined in Eq. (6.14) in the xy plane for four different instants of the BBH simulation described in Sec. 6.2. It illustrates the junk radiation (second panel) generated when the initial conditions (first panel) relax to an equilibrium configuration (third panel). For reference, the fourth panel shows the physical gravitational waves generated at the merger.

spherical waves. Thus, this completely removes any mode propagating inwards to the center of the simulation. For more details on the implementation, see [325].

For the grid, BBH numerical simulations have the same accuracy problem as the one discussed for the collapse problem in Sec. 4.3: a uniform grid is too computationally expensive for the resolution that certain areas require. We comment on this in the next subsection.

6.1.3 Adaptive mesh refinement

In a BBH simulation, we usually have a simulation volume whose length is several tens or even hundreds times the black holes Schwarzschild radii. This is necessary so that the boundary conditions do not significantly impact the main area of interest in the simulation, which is only possible if the boundary is sufficiently far away.

On the other hand, the black hole horizons need to be modelled with a high resolution both in space and time, so as to accurately capture their dynamics. This resolution should be of order a hundredth of the Schwarzschild radii, or better. If this resolution is uniformly kept for the full grid, this would imply of order 10^4 points per side, which would be around 10^{12} in total. In addition, in each of these points, different fields are defined, so this would imply of order 10^{13-14} grid variables stored in memory at each time iteration. This is clearly computationally prohibitive.

In addition, there is no need to have such a resolution in all the simulation volume. At large distances from the black holes, there are only gravitational waves which do not need such an accuracy to be modelled. Therefore, the usual practice is to implement some adaptive mesh refinement structure, which was a term already discussed in Sec. 4.3. These schemes usually consist on several grid *levels* on top of each other. The coarsest level covers the full simulation volume with a moderate resolution, both in space and time. The next level covers just a fraction of this volume, where the side ratio is sometimes taken to be $1/2$ for simplicity and convenience, and the resolution increases in a certain factor for which 2 is also a convenient choice. Usually, for the first refinement levels,

it is only necessary to increase the spatial resolution, not the time step, and they are centered on the center of the simulation. However, as the refinement levels progress, two grids are required per level, each of them centered on one black hole, and they need to be refined both in space and time. An AMR scheme for 7 refinement levels is depicted in Fig. 6.3, where we can see how the grid centers follow the motion of the black holes, as well as the reduction of covered volume with each refinement level. The improvement of spatial resolution can also be seen from the inset plots, and the time resolution, which cannot be inferred from the plot, also improves by a factor of 2 per refinement level, except for the transition from the basic (blue) to the first refinement level (orange), which have identical time steps.

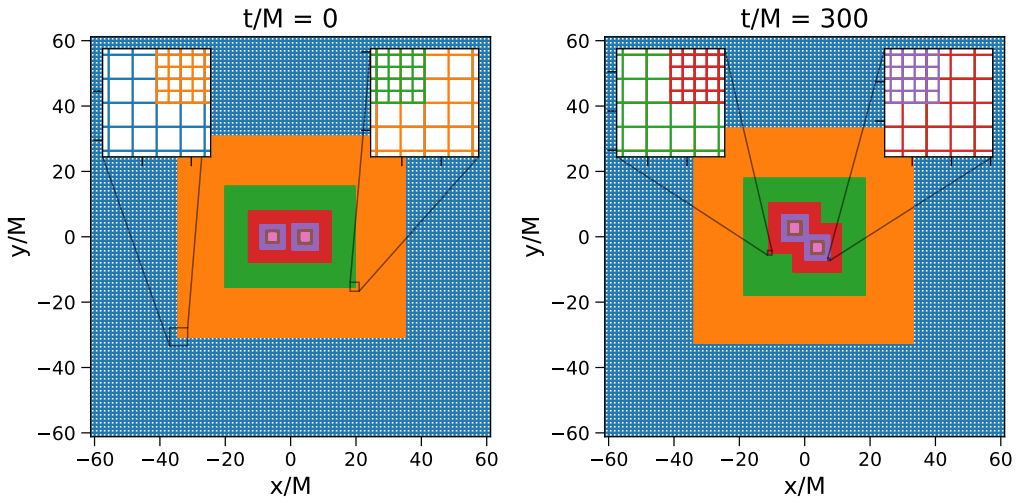

Figure 6.3: Adaptive mesh refinement scheme in the xy plane for different instants of the BBH simulation described in Sec. 6.2. Each color represents a different refinement level, for a total of seven in both panels. The inset plots show the transition from one refinement level to the following one.

This concludes the introduction to the required elements involved in the successful generation of a Numerical-Relativity simulation. There are other important concepts which will be explained, but they are more related to the output, and are more clearly understood using a example BBH simulation. This is what we will see in the next section.

6.2 Numerical simulations with the Einstein Toolkit

Since the first successful BBH simulation by Pretorius [33], several softwares for Numerical Relativity have been developed. Some examples include the mentioned Einstein Toolkit [301, 302] and GRChombo [318, 319, 320], but also NRPy+ [326, 327], SpEC [328, 329], LaZev [34] or BAM [330], among many others.

In this thesis, we will focus on the Einstein Toolkit, given that it is the software that was used in our article [1], which will be explained in Chapter 7.

6.2.1 The Einstein Toolkit

The Einstein Toolkit [301, 302] is a collection of state-of-the-art software components and tools devoted to simulate General-Relativistic astrophysical systems. It is open source, with more than 210 components written in different programming languages (C, C++, Fortran, OpenCL, CUDA, etc.). The Einstein Toolkit provides regular, tested releases around twice per year, the last of which was the "Lisa Meitner" release in December 2023[1]. In addition, its growing community (>350 members from >43 countries) provides user support through different channels. There are also a few articles providing a comprehensive introduction to the toolkit [306, 301, 331].

Most of the Einstein Toolkit components use the Cactus Computational Toolkit [332, 333], which is the framework providing the modular infrastructure so that all the separate components work together correctly. Due to the *Cactus* name, these components, similar to the packages in other programming languages, are named *thorns*. There are many of these thorns, most of which are documented in the Einstein Toolkit website [302], which can be classified according to their different roles. We now name a few just to give a general idea, but more comprehensive and detailed descriptions are given in [306, 301, 302, 331].

- The Carpet thorn [334, 335] provides the AMR grid infrastructure, separating the technical part of the simulation from other thorns more related to the simulation physics. This thorn is also in charge of splitting the grid functions and arrays among the parallel processes, as well as coordinating their communication; modifying the AMR grid when requested (regridding) and performing input/output operations in parallel. A newer, more flexible thorn called CarpetX, which also aims to provide support for GPUs, is also in development.

  In addition, the Llama [336] code allows for a simulation domain consisting of different overlapping patches.

- The PunctureTracker thorn tracks the black hole positions, so that the periodic AMR regridding can be done according to their motion.

- The ADMBase thorn defines grid functions related to the AMR formalism, while TmunuBase does the same for the stress-energy tensor and HydroBase for the hydrodynamical evolution.

- The TwoPunctures thorn [317] provides initial puncture data, using optimized spectral interpolation [337]. It is the main thorn used for BBH initial conditions, but there are other options, as well as a variety of thorns developed for initial value data generation for different types of simulation.

- The McLachlan code [338, 339, 340] evolves the grid variables in time using the BSSN formalism described in Subsec. 6.1.1. It generates the corresponding thorns a using Kranc [341, 342], a Mathematica application for code generation of PDEs.

- The NewRad thorn implements the Sommerfeld radiative boundary conditions described in Subsec. 6.1.2 [325].

Finally, the Simulation Factory, or `SimFactory` [343], allows to configure, build, submit and manage the simulations in a user-friendly way. It is the tool which connects the user with the capabilities of the Einstein Toolkit.

[1] https://einsteintoolkit.org/about/releases/ET_2023_11_announcement.html

Some other relevant thorns, more related to the output, have not yet been named on purpose. They will be introduced in the next subsections with an example BBH simulation.

Processing and post-processing

In order for a simulation to run successfully, it mainly needs to store in memory the grid variables, as well as the AMR structure and other technical information. From the point of view of a physicist, however, nearly all of this raw information is useless as it is. The black hole positions can be obtained as direct output due to their relationship with the AMR structure, but their masses, spins or the gravitational waves they produce are not relevant for the evolution of the grid variables.

It is then necessary to process some of this raw information. In the Einstein Toolkit, some of this *processing* is done by the software, simultaneously to the time evolution. Some other, however, must be derived from the simulation output by the user, which is what we will call *post-processing*. In the next subsections, we will see how either the NR simulation software or the user can produce some physically relevant quantities from the raw simulation output.

The GW150914 simulation

During this section, we will explain some of the concepts involved in Numerical Relativity using an example BBH simulation. In particular, it is the one provided in the gallery of the Einstein Toolkit[2] [344], which uses most of the thorns and tools already described [301, 336, 334, 345, 317, 346, 332, 338, 341, 343].

This simulation computes the last orbits of a BBH with parameters similar to the BBH responsible for the first ever detected gravitational-wave signal: GW150914 [7]. The mass ratio is 0.806, while the initial separation is set to $d = 10M$, the symmetric momentum is $p = 0.0953M$ with angle $\theta = 89.49°$, and the dimensionless spins are $\chi_{1,z} = 0.31$, $\chi_{2,z} = -0.46$, with their x and y components set to zero. In addition, as it could be seen in Fig. 6.3, the main simulation volume has a half-side around 61M, but the Llama multiblock infrastructure allows for GW extraction (see Subsec. 6.2.3) at radii as high as 500M.

The GW150914 simulation has already been used to illustrate the junk radiation in Fig. 6.2 and the AMR scheme in Fig. 6.3, as well as in Fig. 1.3 in Chapter 1 to illustrate the components of a merger. In the next subsections, we will use it to explain other relevant concepts in NR concepts and show some of the Einstein Toolkit capabilities.

6.2.2 Apparent horizons

In General Relativity, there are several definition of masses and angular momenta which are useful in different contexts. Some of them, like the ADM mass and momentum, use global properties of the spacetime. In these subsection, however, we will use some local properties near the black holes to characterize their masses and spins.

[2] https://einsteintoolkit.org/gallery/bbh/index.html

First, it is necessary to have a notion of the black hole horizons. In stationary spacetimes, such as Schwarzschild's and Kerr's, the *event horizon* is a very useful concept. An event horizon is defined as a co-dimension 1 null hypersurface from which neither time-like nor light-like geodesics can reach future null infinity [347]. This is a gauge-independent and global property of spacetime which is, however, not very practical in a dynamic spacetime. Instead, a useful concept used in numerical simulations is the *apparent horizon*. At each spacetime slice, (the spatial hypersurfaces at each time instant, defined in Subsec. 6.1.1), one defines the apparent horizon of a black hole as the outermost trapped surface around its center [348]. Simply speaking, a trapped surface is a closed surface formed by a set of points where every light ray points to the interior of the surface. Therefore, the outermost of these surfaces marks the boundary between the regions where light can escape and where it cannot, that is, a horizon. Apparent horizons are thus a local concept, defined at each iteration, which is more useful in practice than the global notion of event horizon. On the other hand, apparent horizons are gauge-dependent, since they depend on the spacetime slicing. For a more formal discussion on trapped surfaces, see [349], while for the notion of apparent horizon, see [350].

In the Einstein Toolkit, one of the thorns that looks for these apparent horizons is AHFinderDirect [345, 351], while their surface shapes and centroids are stored by SphericalSurface. We can see examples of these apparent horizons in Fig. 6.4, both for the GW150914 simulation and the second hyperbolic simulation described in the next section. In this figure, we can see how their shapes vary over time, but also how their sizes tend to reduce as they get closer to the other black hole.

Apparent horizons are particularly useful to obtain local measurements of the black holes. In particular, from the area A of this surface, the thorn AHFinderDirect provides a measurement of the black hole mass as

$$m_H = \sqrt{\frac{A}{16\pi}}. \tag{6.5}$$

In Chapter 7, we will be interested in the black hole spins, so let us see more in detail how this measurement can be derived.

Spin measurements

Similarly to the mass, one can easily derive a local measurement of black hole spins by using the shape of their apparent horizons. We denote the spin by $\vec{J}$, Particularly, we denote by C_p and C_e the polar and equatorial horizon circumferences, respectively. Then, the Kerr metric satisfies [278, 352, 353]

$$\frac{C_p}{C_e} = \frac{1+\sqrt{1-(a/m)^2}}{\pi} E \left(-\frac{(a/m)^2}{(1+\sqrt{1-(a/m)^2})^2} \right) \tag{6.6}$$

where m is the black hole mass, $a/m = |\vec{\chi}|$ is its dimensionless spin parameter, and $E(x)$ is the complete elliptic integral of the second kind,

$$E(x) = \int_0^{\pi/2} d\theta \sqrt{1 - x \sin^2\theta}. \tag{6.7}$$

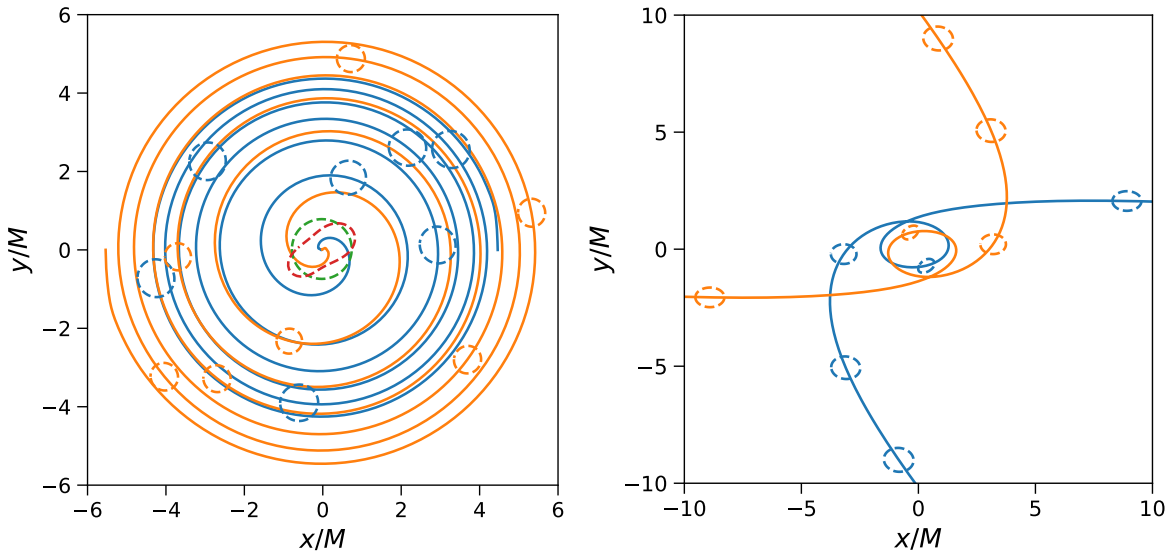

Figure 6.4: Apparent horizons (dashed lines) for some iterations of the GW150914 simulation (left panel) and for the hyperbolic simulation with $\theta_2 = 3.12°$ described in Sec. 6.3 (right panel), with their positions (solid lines) plotted for reference. The blue lines denote the heaviest initial black hole, while the orange one denotes the lightest one. In the case of GW150914, the red dotted line marks the joint apparent horizon around its formation time, and the green line is also the joint horizon, after some relaxation time.

Thus, one can simply get C_p and C_e for each black hole from the simulation output, and derive their spins using Eq. (6.6).

With the Einstein Toolkit, there is, however, no need to make these computations. The thorn QuasiLocalMeasures [346] directly provides measurements for the masses and spins, as well as other local quantities. It uses the so-called isolated and dynamic horizon formalisms, which we will not cover here and for which one can refer to [346, 354, 355]. Instead, we remark that, due to the nature of apparent horizons, these quantities are gauge-dependent. However, at $t \to \pm\infty$, in the absence of gravitational interaction, the asymptotic quantities provide gauge-independent information. In particular, the Christodoulou spin in Eq. (6.6) and the ones obtained from the isolated and dynamic horizon formalisms coincide. Therefore, in the next sections, even if we plot the spin evolution with time during all the simulation, the only relevant quantities are the initial and final ones.

In Fig. 6.5, we can see how the parent black holes produce a final black hole with a larger spin that the sum of the initial spins. This indicates a transfer of the orbital angular momentum. Note how the spins remain practically constant during all the evolution, unlike what we will see for hyperbolic encounters in Sec. 6.3.

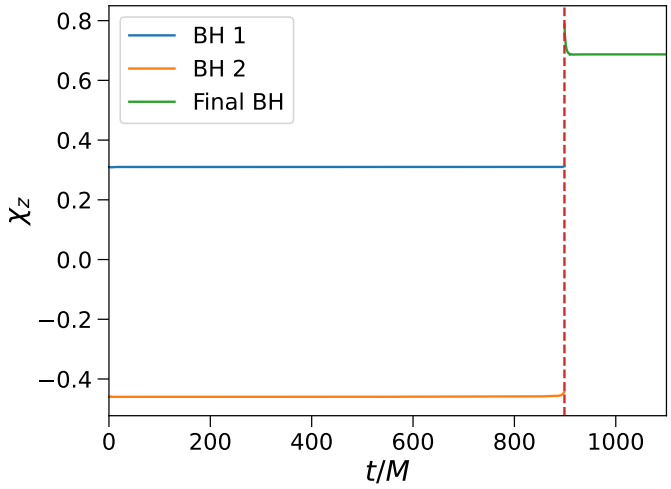

Figure 6.5: Spin component on the z axis of the two parent black holes of GW150914 before their merger, which is indicated by the dashed vertical line, and of the final black hole after the fusion.

6.2.3 Gravitational-wave extraction

One of the main reasons to run numerical simulations for BBH is to obtain the gravitational waves they produce, in order to use their waveforms for parameter estimation of signals in GW detectors. However, the strain amplitude h seen in Chapter 1 is not directly obtainable from the output of numerical simulations. Instead, numerical simulations usually provide Weyl scalars, which are directly related to them.

The Weyl scalar

The Weyl tensor is defined as the trace-free part of the Riemann tensor, [40]

$$C_{\mu\nu\rho\sigma} = R_{\mu\nu\rho\sigma} - \frac{1}{2}(g_{\mu\rho}R_{\nu\sigma} - g_{\mu\sigma}R_{\nu\rho} - g_{\nu\rho}R_{\mu\sigma} + g_{\nu\sigma}R_{\mu\rho}) + \frac{1}{6}R(g_{\mu\rho}g_{\nu\sigma} - g_{\mu\sigma}g_{\nu\rho}). \tag{6.8}$$

On the other hand, in the Newman-Penrose formalism [356], one defines a null tetrad l^μ, n^ν, m^ρ, $\bar{m}^\sigma$ such that

$$-l^\mu n_\mu = m^\mu \bar{m}_\mu = 1, \quad l^\mu m_\mu = l^\mu \bar{m}_\mu = n^\mu m_\mu = n^\mu \bar{m}_\mu = 0, \tag{6.9}$$

while their norms vanish due to them being null vectors. Based on this tetrad, the following

quantities are defined:

$$\Psi_0 = C_{\mu\nu\rho\sigma} l^\mu m^\nu l^\rho m^\sigma, \tag{6.10}$$
$$\Psi_1 = C_{\mu\nu\rho\sigma} l^\mu n^\nu l^\rho m^\sigma, \tag{6.11}$$
$$\Psi_2 = C_{\mu\nu\rho\sigma} l^\mu m^\nu \bar{m}^\rho n^\sigma, \tag{6.12}$$
$$\Psi_3 = C_{\mu\nu\rho\sigma} n^\mu l^\nu n^\rho \bar{m}^\sigma, \tag{6.13}$$
$$\Psi_4 = C_{\mu\nu\rho\sigma} n^\mu \bar{m}^\nu n^\rho \bar{m}^\sigma, \tag{6.14}$$

which are called the *Weyl scalars*.

The last one of these scalars, Ψ_4, is used in Numerical Relativity to compute the gravitational waves h_+ and $h_\times$. In order to see the relation between Ψ_4 and the gravitational waves, we first assume that the GW is far away from the source, at a certain distance r, and propagating in Minkowski spacetime. For simplicity, we first analyze the situation in which the GW propagates in direction z and we use Cartesian coordinates. In addition, in the TT gauge (1.31), we have we have $h_{11} = -h_{22} = h_+$ and $h_{12} = h_\times$, with all $h_{i3} = 0$. Therefore, the non-vanishing components of the Riemann tensor in linearized theory, given by Eq. (1.5), are

$$R_{txtx} = R_{txxz} = -R_{tyty} = -R_{tyyz} = -\frac{1}{2}\ddot{h}_+, \quad R_{txty} = R_{txyz} = -\frac{1}{2}\ddot{h}_\times. \tag{6.15}$$

Furthermore, in vacuum, the Ricci tensor $R_{\mu\nu}$ vanishes, so that the Weyl tensor equals the Riemann tensor, $C_{\mu\nu\rho\sigma} = R_{\mu\nu\rho\sigma}$.

In Numerical Relativity, a convenient choice of null tetrad is

$$l^\mu = \frac{1}{\sqrt{2}}(1,0,0,1), \qquad m^\mu = \frac{1}{\sqrt{2}}(0,-i,1,0), \tag{6.16}$$
$$n^\mu = \frac{1}{\sqrt{2}}(1,0,0,-1), \qquad \bar{m}^\mu = \frac{1}{\sqrt{2}}(0,i,1,0), \tag{6.17}$$

which satisfy the conditions in Eq. (6.9). Using this tetrad and the non-vanishing components of the Riemann tensor in Eq. (6.15), the Ψ_4 defined in Eq. (6.14) becomes

$$\Psi_4 = \ddot{h}_+ - i\ddot{h}_\times. \tag{6.18}$$

In general, for an arbitrary direction, we can use spherical coordinates and define the null tetrad

$$l^\mu = \frac{1}{\sqrt{2}}(\hat{t} + \hat{r}), \qquad m^\mu = \frac{1}{\sqrt{2}}(\hat{\phi} - i\hat{\theta}), \tag{6.19}$$
$$n^\mu = \frac{1}{\sqrt{2}}(\hat{t} + \hat{r}), \qquad \bar{m}^\mu = \frac{1}{\sqrt{2}}(\hat{\phi} + i\hat{\theta}), \tag{6.20}$$

where the hat denotes the 4-vector in the corresponding direction. This extends the result in Eq. (6.18) for the transversal polarizations of a GW propagating in arbitrary radial direction $\hat{r}$.

As a result, from the Ψ_4 in a simulation, we can obtain the GW strain by integrating twice,

$$h_+(t,r) - ih_\times(t,r) = \int_{-\infty}^{t} dt' \int_{-\infty}^{t'} dt''\, \Psi_4(t'',r). \tag{6.21}$$

In a numerical simulation, this integration cannot be done from $t \to -\infty$, so one has to define a starting point which does not get too affected by the initial junk radiation described in Subsec. 6.1.2. The usual practice is to do this integral in Fourier space, via a technique called *fixed frequency integration* [357], for which one has to set a minimum allowed frequency, thus getting rid of unphysical low frequencies. However, any integration method introduces some degree of numerical artifacts, which could impact the parameter estimation based on these waveforms. Thus, there have recently been some works [358] arguing that parameter estimation should be done directly on Ψ_4, rather than the strain. In this case, the detector strain would have to be differentiated twice, which introduces less numerical error than integration on the Weyl scalar.

In any case, in order to obtain the strain amplitude of the GWs in a numerical simulation, it is not necessary to do this integration in each grid point. We are interested in measuring the GWs at a certain distance r, which is sufficiently large so that the distant source limit holds. Then, since h_+ and $h_\times$ decay like $1/r$ (see Eqs. (1.99), (1.100)), we can extrapolate them to an arbitrary distance. Furthermore, in the sphere of radius r, we can decompose [359]

$$h_+(t,\vec{r}) - ih_\times(t,\vec{r}) = \sum_{l=2}^{\infty}\sum_{m=-l}^{l} h_{lm}(t,r)\,{}_{-2}Y_{lm}(\theta,\phi), \tag{6.22}$$

where ${}_{-2}Y_{lm}(\theta,\phi)$ are the spin-weighted spherical harmonics of spin weight -2. These are a generalization of standard spherical harmonics (explained in more detail in Subsec. 8.7.1), but with axial rotation symmetry for the corresponding spin. In our case, the spin is -2 to reflect the quadrupolar nature of gravitational waves. For more detailed explanations on spin-weighted spherical harmonics, see [360, 361], or [359, 362] for specific references in the context of GWs.

Given that gravitational waves are quadrupolar at the leading order, in general, the $l = 2$ modes will clearly dominate. We can see this in Fig. 6.6, where the $(2, 2)$ mode dominates the Weyl scalar Ψ_4 and, in the case of the strain, this dominance becomes moer obvious. Thus, the Weyl scalar is usually obtained only for the first few multipoles measured at certain specified radii, which must be high enough for the distant source limit to hold, but not so high to be very close to the boundaries.

In the Einstein Toolkit, the WeylScal4 thorn [306] provides this Weyl scalar Ψ_4, whose 2D information was used to generate Fig. 6.2. The multipole decomposition at the desired radii is handled by the Multipole thorn, thus leaving the Weyl scalar Ψ_4 in a more suitable form to work with. Furthermore, the kuibit Python package [363] has a lot of utilities to help with the post-processing, allowing to easily load any of the simulation output from the Einstein Toolkit, including the Weyl scalar multipoles, and integrating them to obtain the GW strain.

In Fig. 6.6, we can also observe the different regimes of a BBH (inspiral, merger and ringdown), both in the Weyl scalar and the strain. For the strain, we can see how the $h_\times$ is dephased $\pi/2$ with respect to h_+ at the inspiral, as we computed explicitly in Subsec. 1.3.3. In addition, we can see the initial junk radiation in both plots: as an initial burst in Ψ_4 and as an irregular behaviour at the beginning of the strain time series.

6.2.4 Challenges: mass ratios, eccentricity, precession

These BBH numerical simulations need a large amount of RAM memory to run, so that it is only possible to do so in a high-performance-computing (HPC) cluster. In addition, the one for

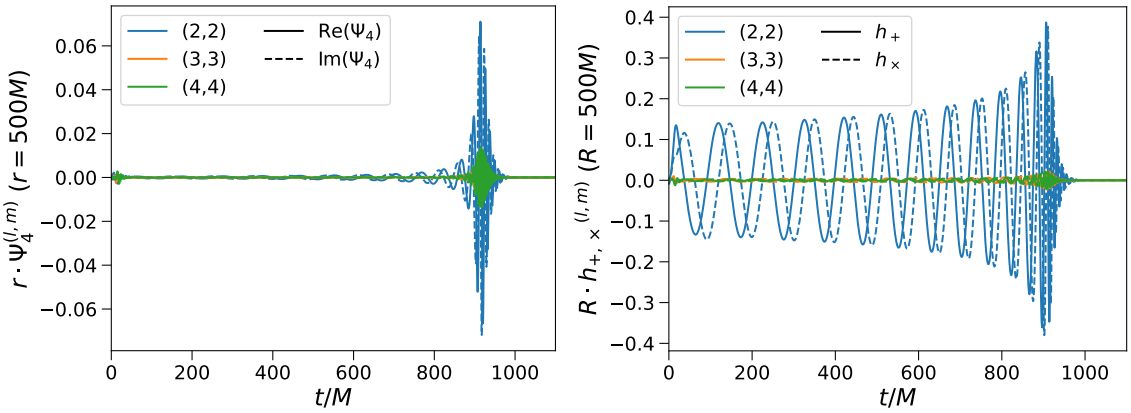

Figure 6.6: Weyl scalar Ψ_4 (left) and strain amplitudes for each polarization, h_+, $h_\times$ (right), for the GW150914 simulation. These quantities are provided for the multipoles (l, l), $2 \leq l \leq 4$.

GW150914, which is not particularly demanding, takes some days to complete, although that depends on the cluster specificities.

In order to do finer parameter estimation for the real GW signals, it is desirable to run many of these simulations, covering the largest possible volume of the parameter space. This includes lower mass ratios, considering eccentric BBHs and exploring spins in arbitrary directions.

Going to lower mass ratios is conceptually very simple, but becomes numerically problematic. A lower mass ratio implies that one of the black holes becomes smaller, so it needs higher spatial and temporal resolution to correctly capture its behavior with an NR simulation. To achieve such resolutions, it is necessary to introduce additional layers to the AMR scheme, which increases the computational cost in both RAM memory and simulation time. For very asymmetric systems, one can resort to perturbation theory, but NR simulations are still needed until that point. Up to now, the mass ratios that have been achieved arrive until $q = 0.0078$ $(1/128)$ [364]. These simulations were done by the group at the Center for Computational Relativity and Gravitation (CCRG) at Rochester Institute of Technology (RIT) and are publicly available through their BBH waveform catalogs[3] [365].

On the other hand, eccentric simulations do not pose a numerical challenge, but they are conceptually harder to model. Knowing the initial momenta for an NR simulation to result in a quasi-circular trajectory is already complicated [366, 367], so computing the initial conditions for a given eccentricity is even more challenging. In addition, in General Relativity, eccentricity varies over time, so it is more difficult to measure. Nevertheless, there are different expressions to compute the eccentricity from a BBH trajectory [366, 368], so what one can do is trying different initial configurations for the NR simulations and measuring the resulting eccentricity with these formulae. There are some groups which are already populating the eccentricity parameter space [365, 369], as well as some attempts to model these waveforms [370, 371, 372]. Until recently, however, these efforts had focused more on quasi-circular orbits, which is reasonable due to the BBH circularization

[3] https://ccrg.rit.edu/~RITCatalog

phenomenon mentioned in Chapter 1.

Something similar happens for spins. Due to the orbital dynamics, it is expected that the highest spin component for the BHs involved in a BBH comes from the direction parallel to the orbital angular momentum. Therefore, many simulations and models focused on correctly capturing the behavior of BBHs with spins orthogonal to the orbital plane (z direction), but not so many with x and y components. Furthermore, non-zero x and y spin components make the orbital plane precess. While this does not add much more complexity to NR simulations, precessing BBH systems are more challenging to model analytically. Some references for studies on precessing BBH systems include [365, 373, 374].

Additionally, in this thesis we have focused on BBHs, but as we saw in Chapter 1, neutron stars can also form binary systems with other neutron stars or BHs and generate CBCs. The signals that these events produce are very similar to CBCs from BBHs, but the tidal deformability of NSs generates some differences, which are more notorious after the merger (see [375] for a detailed study). In addition, neutron stars are more complex to model due to their internal structure, unlike BHs. Moreover, aside from CBCs, a pair of compact objects can generate another type of interactions, as we saw in previous chapters: hyperbolic encounters. These events also generate gravitational waves and can be simulated with NR, as we will see in the next section for a pair of black holes.

6.3 Hyperbolic encounters

Black hole simulations of hyperbolic encounters are conceptually similar to run to the standard simulations of BBH. However, there are certain differences.

Hyperbolic encounters do not produce periodic orbits, so the junk radiation must be somehow removed before the main part of the interaction. In order to achieve this, the black holes must start much more separated than for a BBH. If a typical distance for a BBH was $d = 10M$, for a hyperbolic encounter it should be of order $d = 100M$. This means that the simulation volume must be much larger, in order for the boundaries not to interfere with the simulation. In practice, this implies more refinement levels, which make the hyperbolic run more computationally expensive in terms of RAM memory.

On the other hand, hyperbolic interactions are much faster, due to the lack of periodic orbits. While a BBH stays for some time in the inspiral phase, the hyperbolic interaction is produced with the subsequent separation of the black holes, thus stopping the GW production at a significant level. Therefore, a hyperbolic simulation is much shorter to run, which saves computation time.

In order to see some of the differences, three simulations have been run with slightly different parameters. Following the set-up of Fig. 6.1, the initial distance is $d = 100M$, the masses are equal ($q = 1$) and the initial spins are zero in the three cases. The symmetric momenta are $p = 0.0953M$ and the angles are $\theta_1 = 4.01°$, $\theta_2 = 3.12°$ and $\theta_3 = 3.1°$.

In Fig. 6.7, the trajectories for these simulations are plotted. In the first panel, corresponding to the more open encounter, we can see how the Keplerian hyperbolic trajectory is now "bent" due to the stronger gravitational interaction given by GR. In the second one, this effect is even stronger, producing a full orbit before the objects separate again. For this second case, in particular, we can

see the BH apparent horizons in Fig. 6.4, right. Finally, the third panel shows a dynamical capture, in which the seemingly hyperbolic encounter produced an energy loss as high as to bind the system, producing a subsequent merger shortly after.

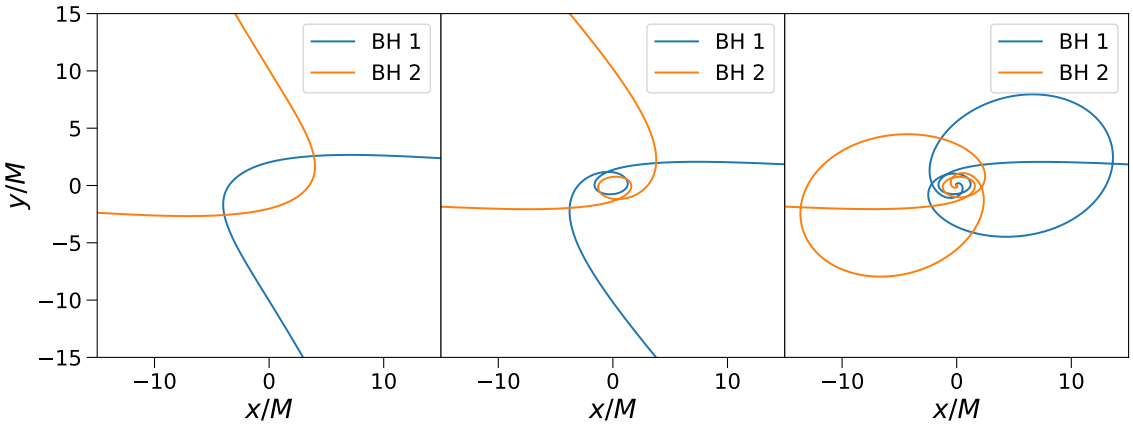

Figure 6.7: Black hole positions for the three hyperbolic simulations described in Sec. 6.3, from the most open to the closest one.

The corresponding GW strains are shown in Fig. 6.8. In the first panel, we can see the GW burst produced by the first encounter, which consists on essentially one oscillation. The second panel shows around three, due to the longer interaction seen in Fig. 6.7, from which we can also see the more notorious change of phase. Finally, the third panel shows two bursts, the first of which is very similar to the previous panel, as expected due to the similarity of initial conditions (the only difference is the angle, $\theta_2 = 3.12°$ versus $\theta_3 = 3.1°$), and the second one corresponding to the final merger. It is worth noting that, unlike the CBC from Sec. 6.2, this merger occurs without any long inspiral phase, given that all the energy and angular momentum that would be needed to maintain the quasi-circular motion has already been radiated away in the first, hyperbolic-like interaction.

The gravitational waves produced by hyperbolic encounters can be of similar order to the ones produced by CBCs, as we could see in Fig. 6.8. However, their narrower localization in time makes them much more challenging to detect, given that one cannot get the sensitivity increase obtained in CBCs by integrating over their inspiral for longer periods of time. This is one of the reasons why these signals have not been detected yet. Another reason is that, due to their burst-like nature, their shapes may be confused with glitches from the detectors [57]. Nevertheless, there are growing efforts from different groups devoted to the study and detection of these signals [57, 61, 62, 59], so it is expected that they will eventually be detected as the sensitivity of the detectors keeps getting better.

Finally, aside from their gravitational waves, hyperbolic encounters show another interesting effect. If we plot the black hole spins, similar to Fig. 6.5, we find out that close hyperbolic encounters induce non-negligible spins on initially non-spinning black holes. We can see this in Fig. 6.9, corresponding to the simulation with $\theta_2 = 3.12°$.

This spin induction effect was first reported in [278] and subsequently studied for a broader

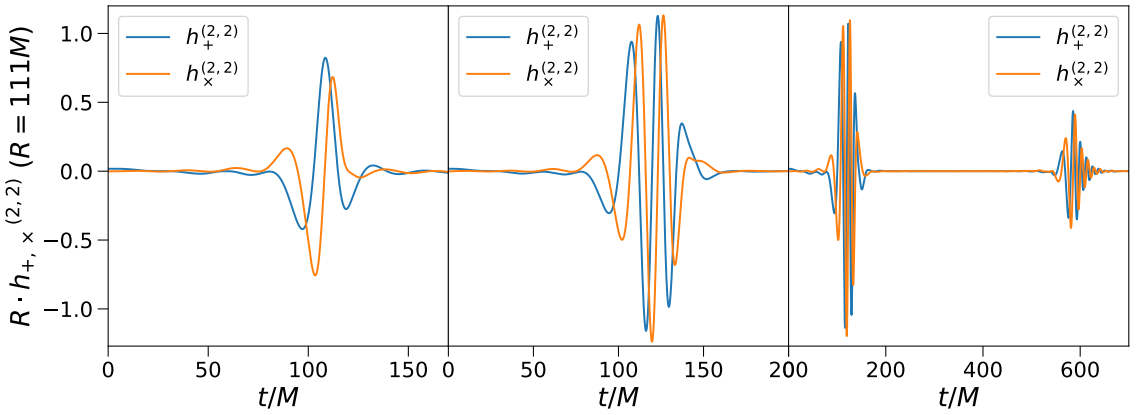

Figure 6.8: Gravitational-wave strains for the three hyperbolic simulations described in Sec. 6.3, from the most open to the closest one.

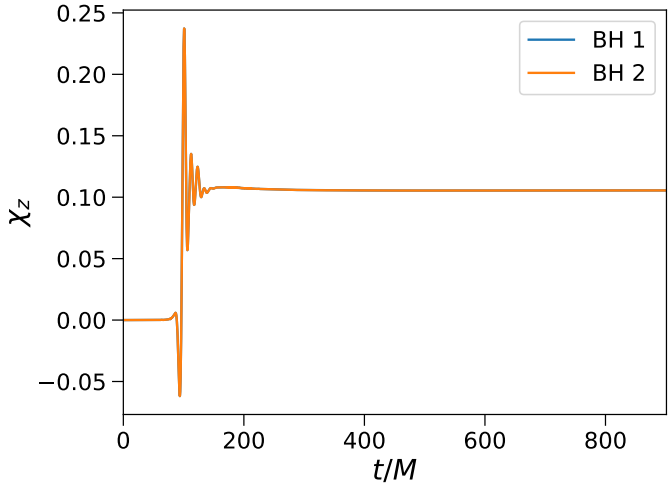

Figure 6.9: Spin component on the z axis for both black holes of the hyperbolic simulation described in Sec. 6.3 with $\theta_2 = 3.12°$. The two curves overlap due to the symmetry of the simulation.

parameter space, including different masses, in our article [1]. In our paper, we also discussed the implications this effect has for primordial black holes. In the next chapter, we will see this work in detail.

Chapter 7

Spin induction on BHs from CHEs

7.1 Introduction

In the third observing run of Advanced LIGO [6] and Advanced Virgo [12], a particular event, labeled GW190521, was detected. The estimated progenitor black hole masses were 91 $M_\odot$ and 67 $M_\odot$ [16], with the probability that at least one of them was in the range $65 - 120$ $M_\odot$ was 99.0% [376]. This is precisely where there should be a gap in the black hole mass distribution, due to pair-instability supernovae [377], so this event attracted a lot of attention when it was made public. Several explanations were proposed [376], such as a hierarchical merger scenario, or that a star with an over-sized hydrogen envelope could give rise to such massive black holes. Other possibilities included eccentric mergers, high-mass black hole-disk systems [378] or primordial origin for the progenitor black holes [210, 379, 242], which is the scenario we consider in our article.

The main problem of the primordial explanation is that PBHs are initially generated with low spin [380], due to the spherical nature of their collapse, as seen in Sec. 4.3. This motivates the study of spin induction mechanisms for PBHs, which would provide a satisfactory explanation for these intermediate mass black holes. For instance, in [381], the authors argue that PBHs could explain the GW190521 signal if they accrete efficiently before the reionization epoch.

As we saw in Sec. 6.3, one of the options for a non-spinning black hole to acquire spin is to interact with another one in a close hyperbolic encounter. A numerical exploration of this effect was done in [278], proving that the induced spin could be significant and reach at least $\chi \approx 0.2$ for equal masses.

In this chapter, we explain the article [1] in which we explored this spin induction effect for different-mass black holes, including a numerical simulation with mass ratio $q = 0.1$. In addition, we studied the trends for varying impact parameter and eccentricity, and also for the change of mass ratio. We finally compare these trends to some analytical expressions, coming from simple approaches to this effect based on frame-dragging.

7.2 Grid structure and initial conditions

In order to simulate black hole hyperbolic encounters in full GR, we used the, at the time, latest version of the Einstein Toolkit software [301, 302], which was the "DeWitt-Morette" release (November 2020). Nearly all the thorns and tools mentioned in Sec. 6.2 were used: the Cactus Computational Toolkit [332, 333], the AMR grid infrastructure provided by Carpet [334, 335], the initial data generation from TwoPunctures [317, 337], McLachlan [338, 342, 340] for the time evolution from BSSN formalism, the AHFinderDirect thorn [345, 351] to track the horizons, QuasiLocalMeasures [346] for spin measurements and WeylScal4 [306] to obtain the complex Weyl scalar Ψ_4.

7.2.1 Equal mass case

The parameter files we used, similar to the ones which generated the simulations in Sec. 6.3, were based on the ones used in [278]. They are similar to the one given by the BBH example [344] studied in Sec. 6.2, but with some key modifications that allow increasing the initial separation up to 100 GM/c^2. For equal masses ($m_1 = m_2 = M/2 \equiv m$), this is a separation of 100 Schwarzschild radii.

The initial conditions follow the set-up in Fig. 6.1. For the equal-mass cases, the initial separation of $d = 100M$ implies that the black holes are initially located at $x = \pm 50M$, $y = z = 0$. The symmetric momenta then guarantee that the center of mass will always lie at the coordinate origin.

The parameters p/M and θ are related to the impact parameter b and eccentricity e. If the initial momenta were instantaneously translated into initial velocities, we could compute the initial relative speed measured from the rest frame of one of the black holes V, as well as the distance d' and angle θ', where we should account for the Lorentz contraction and time dilation. In this case, from the equations in Sec. 1.4, we have

$$b/M = \frac{(d'/M)V}{\sqrt{V^2 - \frac{2}{d'/M}}} \sin\theta'. \tag{7.1}$$

$$\sqrt{e^2 - 1} = (d'/M)V\sqrt{V^2 - \frac{2}{d'/M}}\sin\theta'. \tag{7.2}$$

However, the initial momenta take some time to propagate to the metric quantities and, consequently, to the black hole speeds. Therefore, we cannot establish such a direct correspondence between the orbital parameters and initial momenta. Nevertheless, we can interpret an increase in θ as an enhancement of both the eccentricity and impact parameter, as the previous equations show.

In order to accommodate these initial conditions, the spatial region is increased to the cube $x, y, z \in [-768M, 768M]$. For the AMR structure, each grid uses half-lengths of 0.75×2^n, for $n = 0, 1, \ldots, 6, 8, 9, 10$. The corresponding steps are $2^n \times \Delta x_{mr}$, for $n = 0, 1, \ldots, 9$, where Δx_{mr} is the size of the most refined grid. Adopting the notation in [278], we refer to $\Delta x_{mr} = (1/56)M$ as *low*, $(3/200)M \approx (1/66.7)M$ as *medium* and $(3/256)M \approx (1/85.3)M$ as *high* resolutions.

The time step is initially determined as the spatial step of the bigger grid times a factor `dtfac`, which we set to 0.05625. Then, this value is divided by a different number on each refinement level, which is controlled via the `time_refinement_factors` array, which we set as `[1, 1, 1, 1, 2, 4, 8, 16, 32, 64]`. Thus, the coarsest four grids are updated at the same rate and, from then on, any finer grid is updated twice as fast as the previous one.

Finally, we use two symmetries to speed up the code. First, we use the reflection symmetry across the z-plane, which is the orbital plane. In addition, for the equal-mass case, the rotating symmetry of 180° in the z plane with respect to the origin is also present. Both symmetries reduce the spatial domain by a factor of 4.

7.2.2 Changing the mass ratio

Throughout this work, we mainly used mass ratios in the range $0.7 \leq q \leq 1$. This range was chosen to test how the spin induction varies for different mass black holes, but keeping the ratio close to 1 not to significantly alter the grid structure and the analysis of the problem. Some of the issues arising for smaller mass ratios will be addressed in Sec. 7.4, while they were also mentioned at the end of Sec. 6.2.

Generalizing the previous set-up for mass ratios of $0.7 \leq q \leq 1$ implies some changes with respect to the equal mass case. First, for a mass ratio of 1, each black hole has half the total mass, which is 0.5 in code units. The previous resolutions mean that, per Schwarzschild radius (1 in code units), we have $1/\Delta x_{mr}$ (56, 66.7, 85.3) divisions. However, if we keep the structure for a mass ratio of 0.7, for instance (Schwarzschild radii of 1.18 and 0.82), the number of divisions per Schwarzschild radius is reduced by a factor $1/0.82 \approx 1.22$ for the smaller black hole.

Therefore, what we did was adding an extra refinement level for the smallest black hole, in order for its resolution to be better than for the equal mass case. This makes sure that our results are, at least, as good as the equivalent resolution for the $q = 1$ case. In addition, in order to check that this asymmetry in the extra refinement levels does not introduce errors in the simulation, we ran a few examples with the extra refinement for the $q = 1$ case. For the low resolution, the discrepancies between both spins and with respect to the non-refined case are less than 1%, which is the typical error involved in simulations of this resolution. Another difference from the symmetric case is that we must disable the 180° rotating symmetry, which essentially doubles the needed computational resources.

Finally, the initial positions are also set to $y = z = 0$, with the x so that the initial center of mass is the coordinate origin. We also set $\vec{p}_1 = -\vec{p}_2$, as we did for symmetric masses, to try to keep the center of mass constant. However, due to the mass difference and the fact that the momentum takes some time to stabilize, it is not always satisfied that $m_1\vec{v}_1 + m_2\vec{v}_2 = 0$, which implies that the center of mass $\frac{1}{M}(m_1\vec{r}_1 + m_2\vec{r}_2)$ is not completely fixed and moves a bit from the origin. This offset is found to be more relevant for lower values of q and greater values of the initial momentum, as one would expect. In our case, the center of mass is displaced from the origin, at most, around $5.5M$ during the strong interaction. This does not compromise the final spin measurements, but could have an impact on Weyl scalar-related quantities, such as the gravitational wave strain or the radiated energy. It is, in any case, another reason to choose being modest with the value of the mass ratio.

7.3 Numerical results

We ran some simulations with equal masses, consisting in different initial incidence angles θ for the four initial momenta ($p/M = 0.245, 0.3675, 0.49, 0.75$ per black hole) considered in [278]. For each case, the smallest angle we considered, $\theta_{\rm min}$, was the one producing the maximum spin-up according to [278], which is the boundary between hyperbolic events and dynamical captures ($e \approx 1$), as shown in Sec. 6.3.

In addition, for these four momenta and their corresponding maximum spin-up incidence angles θ, we ran a series of simulations for $0.7 \leq q \leq 1$, which is the only parameter we varied in this case. In particular, due to the change in mass while fixing the momenta, the smallest black hole is faster for $q \neq 1$ than in the equal-mass case, with respect to both the center of mass and the other black hole.

The dimensionless spin $\chi = a/m$ was computed from the QuasiLocalMeasures thorn, but we also double-checked it by comparing it to the Christodoulou spin in Eq. (6.6), to test the consistency. We found that both measurements coincide for late times in all cases.

Before explaining the results, we first addressed their precision.

7.3.1 Error analysis

The differences between the low, medium and high resolutions for the equal mass case were already treated in [278]. We double-checked them for some of the highest values of the incidence angle θ, which they do not cover. In particular, the differences between low and medium resolution up to $\theta = 4^\circ$ are $< 0.5\%$ for $p/M = 0.49$, but for $\theta = 5.7^\circ$ they rise to $\sim 6\%$. This is probably due to the low induced spin, which begins to be too close to zero (~ 0.0004) and, therefore, the absolute errors involved start to become higher in relative terms. Therefore, the low resolution is enough as long as we take the very low spin values with this caution.

The $q < 1$ cases are a bit more complex for the error analysis. From running simulations of low and medium resolution and both with and without extra refinement level, we saw that the spin measurement of the most massive black hole is very robust ($< 2\%$ differences for all cases), but the smallest black hole needs, at least, either medium resolution or the extra refinement level not to present relevant errors (up to $\sim 9\%$ discrepancies). Therefore, we opted to generate all the results both with medium resolution and the extra refinement level.

In addition, in order to have an idea of the error of these simulations, we ran the $q = 0.7$, $p/M = 0.245, 0.75$ with high resolution, for which we found maximum differences of order 0.2%. This fact, together with the $q = 1$ error analysis done in Ref. [278], tells us that the differences are smaller than 0.6%. Therefore, these are the typical errors involved in our simulations with varying q.

Furthermore, we also monitored accuracy test variables such as the Hamiltonian constraint. Due to the enormous storage weight of all the 3D values, we only monitored the average and norms. The results for the Hamiltonian constraint were values of order 10^{-6} at most for the 2-norm [1], 10^{-8}

[1] The n-norm is defined by $||A||_n = (\sum |A(i,j,k)|^n/N)^{1/n}$, with i, j, k the spatial grid indices and N the total number of points.

for the 1-norm and 10^{-10} for the average. This is coherent with what was obtained for the cases in [278] and better than the results for the BBH gallery example [344], which further reinforces the idea that the computations are accurate enough.

7.3.2 General behavior of the simulations

Taking a look at the time evolution of the spin in any of the simulations, we can see three separate regions. In the first one, we can observe a spin value of approximately zero for both black holes. This is the region where the initial conditions progressively propagate to the metric quantities (the shift is initially zero) as the black hole speeds grow and stabilize, while both black holes progressively get closer.

When both black holes are close enough, they begin to strongly interact and we can see a drastic change on the spins, as well as some oscillations. During this second period, some of the energy and angular momentum are radiated away as gravitational waves. We can see that in Fig. 7.1. The strain amplitude was derived from the Weyl scalar on the sphere of radius $R = 67.88M$ and shifted to compensate for the propagation time to the detector, $\Delta t = -R$. For this purpose, we used the PostCactus post-processing software [382], which was the precursor of kuibit [363]. Both of these codes compute the strain from Eq. (6.21) using fixed-frequency integration.

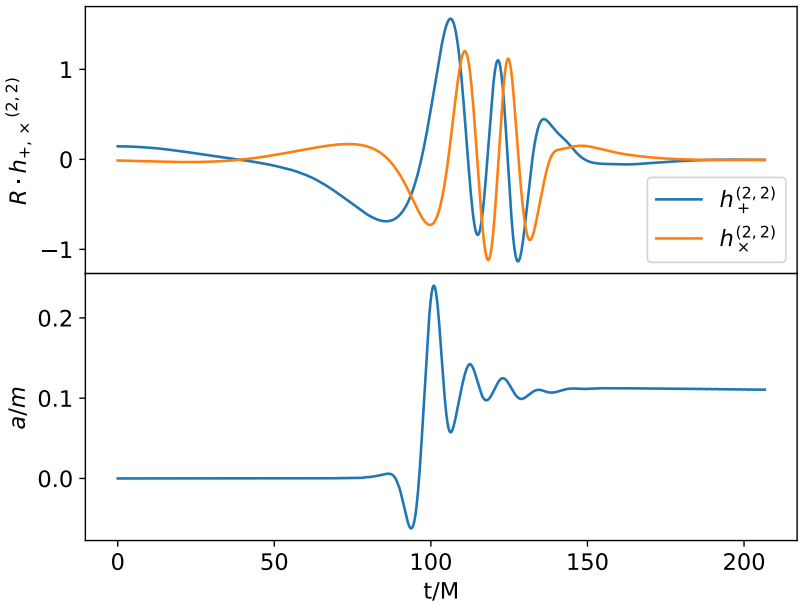

Figure 7.1: Strain of the emitted gravitational wave from the $l = k = 2$ multipole (upper panel) and spin evolution (lower) during a hyperbolic encounter with $p/M = 0.49$, $q = 1$ and $\theta = 3.12°$.

On the third and final region, we can see that there is a constant, non-zero spin: the initially non-spinning black holes are now rotating. We measure the final spin at $t = 250M$, which is enough for it to have stabilized for all the simulations considered.

7.3.3 Equal masses, varying incidence angle

First, we present the four cases $p/M = 0.245$, 0.3675, 0.49, 0.75 for $q = 1$ and different values of θ, between the maximum spin-up incidence angle and an upper bound $\theta \leq 5.73°$. In order to give an idea of these parameters, we fitted an initial part of the trajectory (from $t/M = 30$ to $t/M = 80$) to a hyperbola. In Table 7.1, we provided the ranges of impact parameters b and eccentricities e for the considered cases, as well as the distances of closest approach r_p. Note that the latter can reach values below $2M$, which would correspond to the sum of the Schwarzschild radii of both black holes, since the apparent horizons of two interacting, rotating black holes are typically smaller, especially when they get close to each other. For these simulations, we get apparent horizon radii of order $R_S/2$ before the strong interaction and $R_S/3$ during it, similarly to what can be seen in other numerical simulations like the one in Fig. 13 in Ref. [301]. We can also observe this behavior of the apparent horizons in Fig. 6.4.

p/M	θ (deg)	r_p/M	b/M	e
0.245	3.47 – 4.58	1.98 – 4.63	6.28 – 8.30	2.15 – 2.71
0.3675	3.13 – 4.58	1.62 – 4.90	5.72 – 8.37	1.84 – 2.48
0.490	3.12 – 5.73	1.48 – 6.79	5.78 – 10.6	1.64 – 2.63
0.750	3.42 – 5.73	1.50 – 6.36	6.61 – 11.0	1.38 – 1.94

Table 7.1: Ranges of θ considered for each initial momentum, as well as the equivalent minimum distances and fitted impact parameters and eccentricities.

Before comparing the final spins in all the cases, we first show the spin evolution versus the time for $p/M = 0.49$ in Fig. 7.2. We note that the induced spin decreases with growing θ. This is expected, since the closest distance between the black holes increases with the incidence angle, which makes the encounter weaker.

For the four considered initial momenta, Fig. 7.3 shows the final spins versus θ. In particular, one thing we noted is that they are reasonably well fitted by a power law. For the $p/M = 0.49$ case, the power law also fits well the other points that are shown in Fig. 4a in [278], where this spin variation with the incidence angle was already described.

The results of the power law fits are given in Table 7.2. These were done by linearly fitting the log-log plot, in order to give each point the same importance in terms of relative weight. By doing a least square error fitting to a power law, the smaller values of the spin would have had little impact on the fit.

p/M	n	θ_0 (deg)	$\theta_{\rm min}$ (deg)	r^2
0.245	-14.8	2.62	3.47	0.9936
0.3675	-11.0	2.40	3.13	0.9982
0.490	-9.0	2.42	3.12	0.9997
0.750	-7.7	2.79	3.42	0.9989

Table 7.2: Fitted parameters for Fig. 7.3 to a power law $\chi = (\theta/\theta_0)^n$, as well as $\theta_{\rm min}$ for reference and the linear correlation coefficient r^2 for the $(\log(\theta), \log(\chi))$ data to the corresponding linear function.

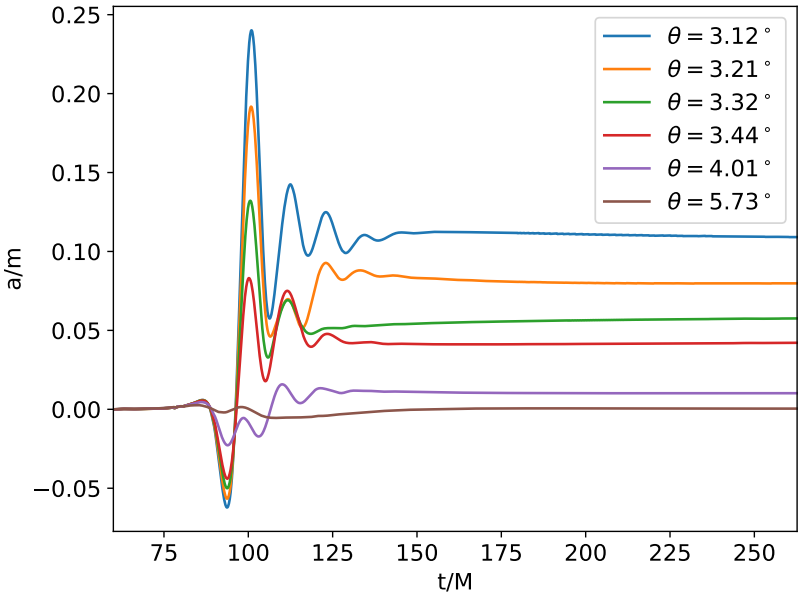

Figure 7.2: Spin evolution during a hyperbolic encounter with $p/M = 0.49$, $q = 1$ and different values of θ.

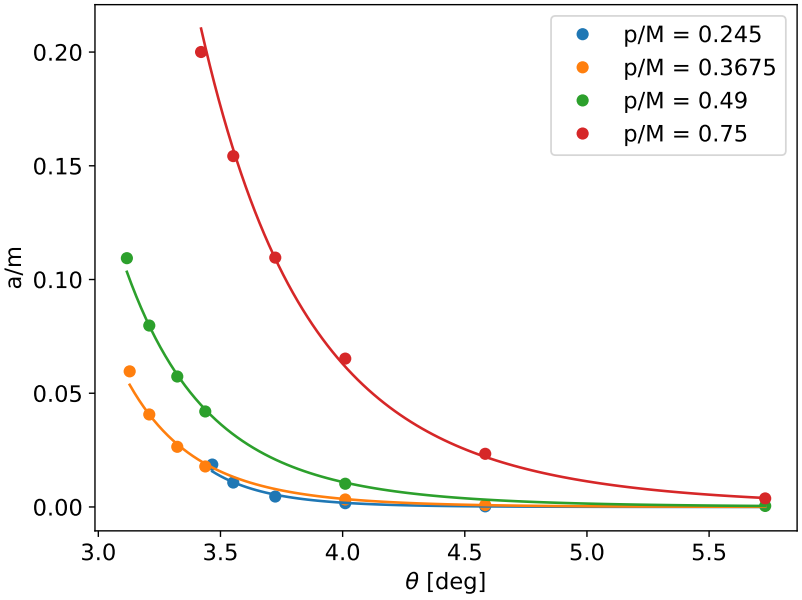

Figure 7.3: Final spin for hyperbolic encounters with different momenta and $q = 1$ versus θ, as well as their fit to a power law.

Finally, in order to better compare these trends, we show the same results in Fig. 7.4, but now with all the curves normalized by the maximum spin-up value and subtracting $\theta_{\min}$ to the incidence angles so that all the curves start from the same point.

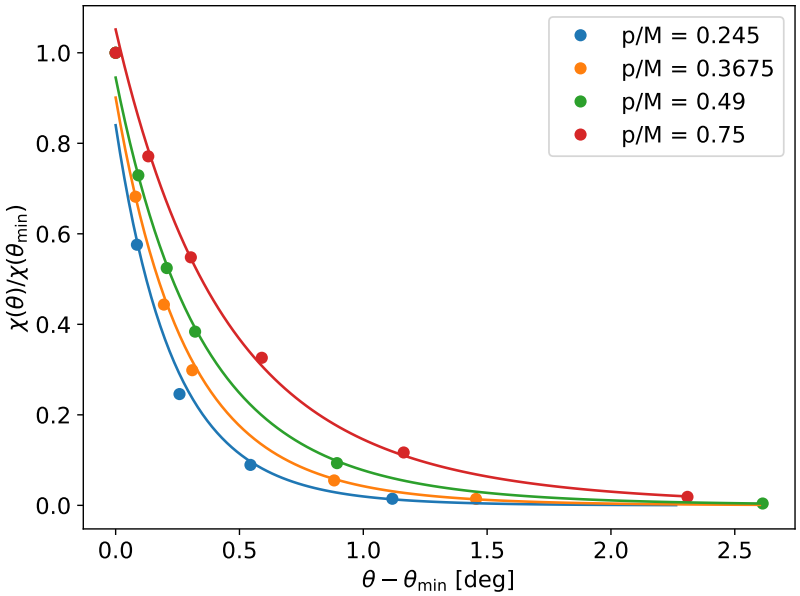

Figure 7.4: Same as Fig. 7.3, with the curves normalized by the maximum spin-up value and subtracting $\theta_{\min}$ to θ.

7.3.4 Varying the mass ratio

We will now see the results for the $0.7 \leq q < 1$ simulations. In Fig. 7.5, we plot the time evolution of the spin in simulations of different mass ratio, with $p/M = 0.49$. Note how each black hole now gets a different spin, where *the highest value is obtained for the most massive black hole*. It is also notorious how the difference between both spins is increased as q gets smaller, as well as the increase of the highest spin and decrease of the smallest one with decreasing q.

A similar behavior is observed for the other values of the initial momentum. The final spins are shown in Fig. 7.6. They are plotted with respect to the masses to avoid having two points per value of the x magnitude, as we would have if we plotted with respect to the mass ratio. Note that the pairs of masses that add up to one come from the same simulation. We can see that they adapt reasonably well to linear fits.

In order to better check and visualize how different the trend is for the different initial momenta, we can divide the results by the central value, getting Fig. 7.7. In this case, since the point $m/M = 0.5$, $\chi(q)/\chi(q = 1) = 1$ is common for all the cases, we impose that the linear fits must go through this point and just fit the slope.

We can see that the relative increase between the different values of q is bigger for the smallest

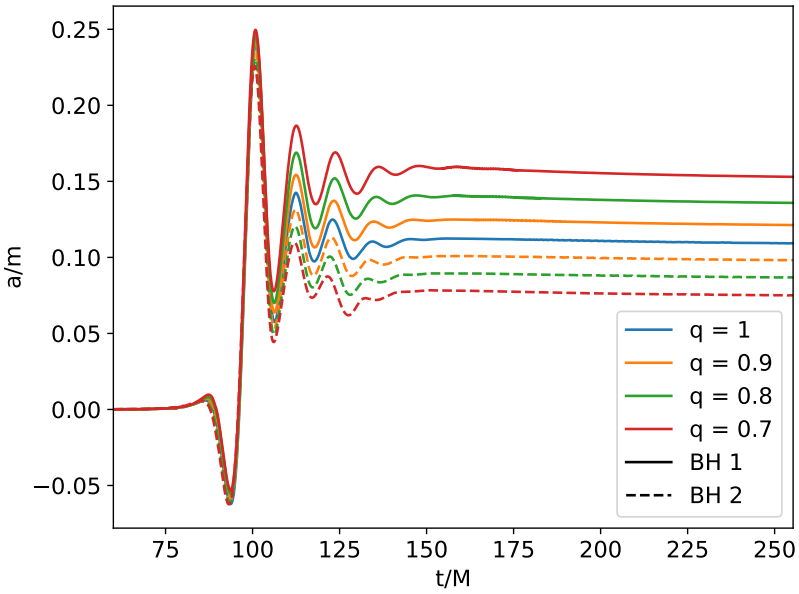

Figure 7.5: Spin evolution during a hyperbolic encounter with $p/M = 0.49$, $\theta = 3.12°$ and different values of q.

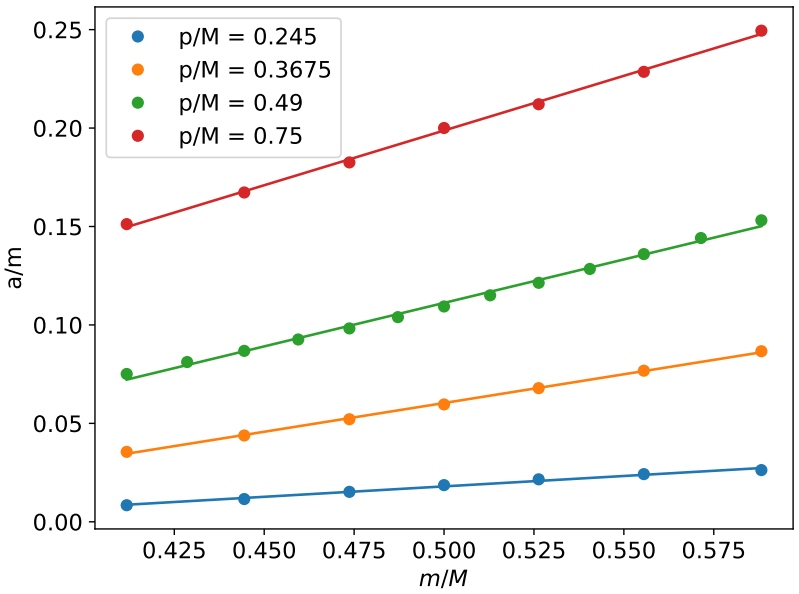

Figure 7.6: Final spin for hyperbolic encounters with different initial momenta and θ corresponding to the $q = 1$ highest spin-up versus the black hole mass, as well as their linear fits.

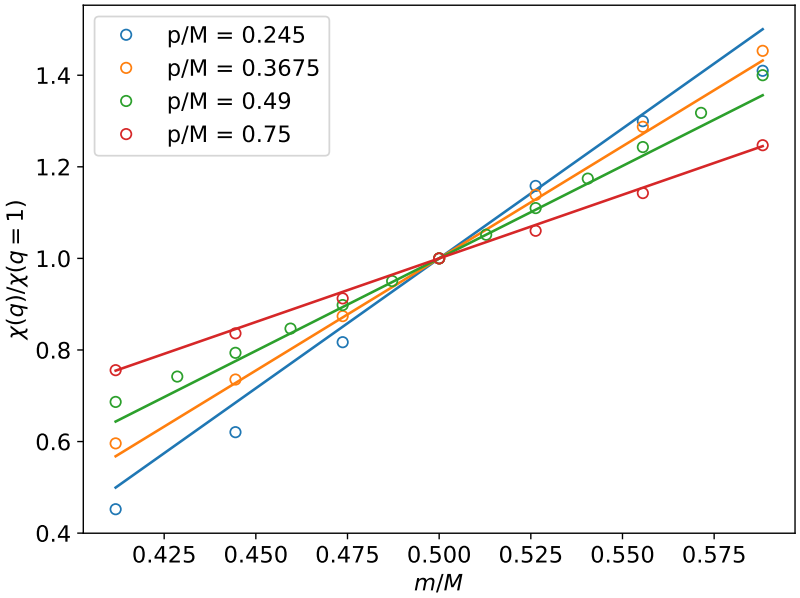

Figure 7.7: Same as Fig. 7.6, where we divided each value of χ by the one corresponding to the same initial momentum and $q = 1$. The points are now open in order to better see the overlapping values, and the linear fits now have the restriction to pass through the central, common point.

values of p/M. In addition, the linear fit is generally good, but for the $p/M = 0.245$ case is worse than for the other cases. The information about the fits in Fig. 7.7 is provided in Table 7.3, as well as the spin of the $q = 1$ cases, which can be used to derive the equivalent slope for the χ vs m/M fit. Here, we can see how the slope decreases with increasing p/M.

p/M	θ (deg)	slope	r^2	$\chi(q = 1)$
0.245	3.46	5.7	0.979	0.0186
0.3675	3.13	4.9	0.997	0.0596
0.490	3.12	4.0	0.989	0.109
0.750	3.42	2.8	0.997	0.200

Table 7.3: Fitted parameters for Fig. 7.7, with their linear correlation coefficient r^2 and values of the central spin.

7.4 Towards lower mass ratios: the case of q=0.1

Finally, we ran a simulation with $q = 0.1$, $p/M = 0.49$ and $\theta = \theta_{\rm min} \approx 3.12°$. In order to compensate for the loss of (relative) resolution for the smallest black hole, we added four extra refinement levels to its grid. We also decided to fix medium resolution. As a result of this configuration, the simulation is much slower than the previous ones.

Unlike the other simulations with $p/M = 0.49$ and $\theta = 3.12°$, which are hyperbolic, this one ended up producing a merger. One of the possible explanations is that the small black hole starts from a high initial speed, since it has the same momentum as the black holes in other simulations but much smaller mass ($m \approx 0.091$), which would imply more energy loss until its encounter with the heavier black hole. Another possible explanation is a stronger dynamics for $q < 1$.

7.4.1 Issues with the Weyl scalar

One of the issues that arise in this simulation is the fact that the center of mass is displaced with respect to the origin. We already saw that the maximum deviation for $0.7 \leq q < 1$ was found to be around $5.5M$, but, in this case, it is around $24M$. This is a problem for the measurements of the Weyl scalar, which are taken at spheres centered at the coordinate origin and, in our case, with radius $r = 67.88M$. As a result, computing the strain amplitude of the emitted gravitational wave or its radiated power is also complicated.

This effect has been corrected via a transformation of the Weyl scalar from the sphere centered at the origin (S_0) to the sphere centered at $\vec{r}_{\rm CM}(t - R/c)$ ($S_{\rm CM}$) for each time t. In order to do this transformation, one has to:

- Convert the available Ψ_4 multipoles (in our case, up to $l = 4$) to a scalar field defined at S_0.
- For each $(t, \vec{p}(t))$, with $\vec{p}(t) \in S_{\rm CM}$, get the light ray that originated at $(t - R/c, \vec{r}_{\rm CM}(t - R/c))$ and passes through $\vec{p}$ and take the value $r\Psi_4$ when it passes through S_0. Then, divide by R to get the value of Ψ_4 at the desired point.
- Convert the resulting scalar field at $S_{\rm CM}$ back into multipoles.

In practice, we have a grid (t, θ, φ) for $S_{\rm CM}$ and need the equivalent points (θ', φ') at S_0, its radius r' with respect to $S_{\rm CM}$ and the time at which the light ray passes through it, $t - (r' - R)/c$. The situation is depicted in Fig. 7.8.

We should note, however, that this correction is far from perfect. First, this assumes that a light ray exactly propagates through the coordinate system at speed $c = 1$, while the space-time curvature can slow down this speed. In addition, we have only produced up to the $l = 4$ multipole, which is enough for a sphere centered at the origin but, in this case, the contribution of the multipoles $l \geq 5$ measured at S_0 could be non-negligible even for multipoles $l \leq 4$ at $S_{\rm CM}$.

Correctly measuring the Weyl scalar is important to determine some gravitational wave-related quantities, such as its strain amplitude. We show the amplitudes for the modes $l = k \leq 4$ in Fig. 7.9, with the corresponding time shift of $-R$, together with the spin evolution.

7.4.2 The spins

Even if this simulation ended up in a merger, we can observe the spin evolutions and draw some conclusions. First, we see how the spin-induction phenomenon works in the same way as in other cases: higher spin is induced on the heaviest black hole. This can be observed in the lower panel of Fig. 7.9, which represents the temporal spin evolution.

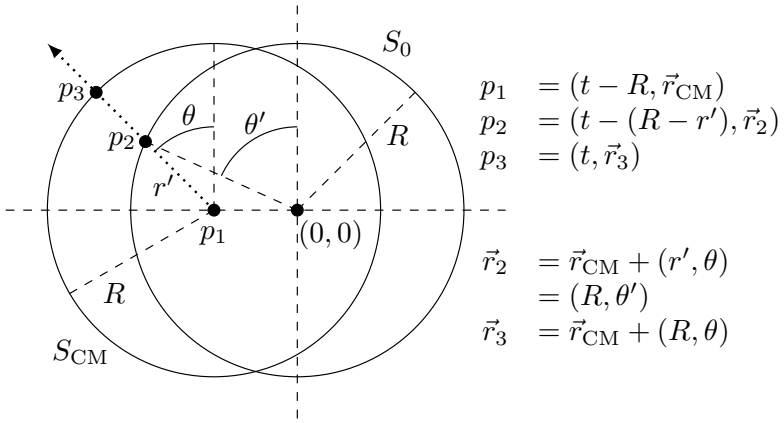

Figure 7.8: All the relevant points and quantities involved in the transformation of the Weyl scalar from the sphere S_0 to the sphere $S_{\rm CM}$, for an arbitrary space-time point $p_3 = (t, \vec{r}_3)$, $r_3 \in S_{\rm CM}(t-R)$. The dotted line represents the light ray which passes through the three relevant points p_i, $i = 1, 2, 3$.

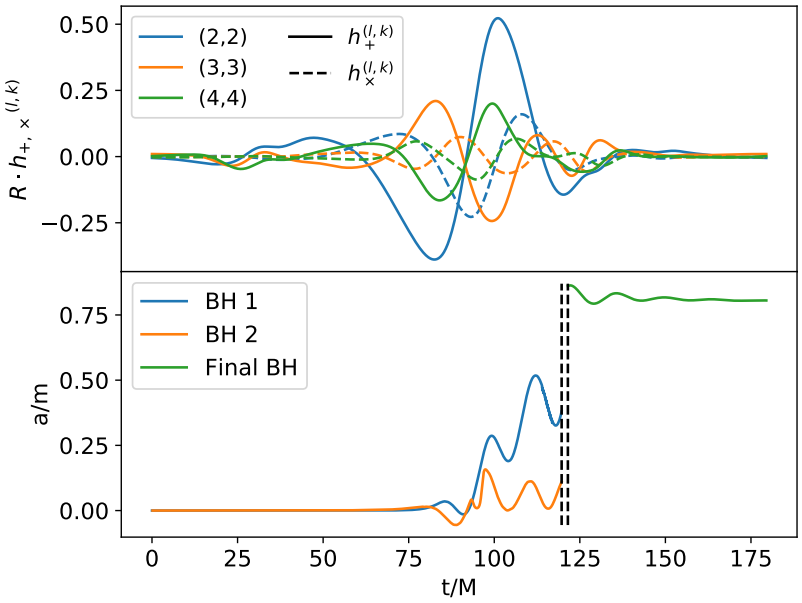

Figure 7.9: Strain amplitudes of the $q = 0.1$ simulation for the modes $l = k \leq 4$ (upper panel), together with the spin evolution (lower), where the first black hole is the most massive one. The dashed, vertical lines separate the periods before and after the merger.

In Fig. 7.9, we drew two dashed, vertical lines. The first of them marks the moment when the centroids of both apparent horizons are at a distance equal to the sum of their mean radii. This means that both black holes are already too close to continue tracking each of them separately. The second vertical line marks the moment from which the joint horizon can be followed.

One of the main conclusions that should be drawn from this simulation is that two initially non-spinning black holes involved in a hyperbolic encounter that ends in merger can naturally acquire a relevant spin while they approach each other. In practice, this means that, if we observe only the last oscillations of a merger through its emitted gravitational waves, and estimate their initial spins from an inspiral waveform template, we cannot assume that they had this large spin asymptotically away from the merger. If they started as a hyperbolic event, they could have acquired their spin as they scattered off each other, emitting gravitational waves and becoming a bounded system that finally merged in a few oscillations.

7.5 Comparison with analytic expressions

The problem of analytically deriving the induced spins in a close hyperbolic encounter is not trivial. In fact, in order to accurately predict the results of our simulations, one would have to get to, at least, PPN(4) order [278, 383]. This strong field interaction cannot definitely be modelled with weak field approximations, as the minimum separations of order 1–7M in Table 7.1 show.

Nevertheless, one can take some naive approaches to this question in order to, at least, see whether we can qualitatively predict the trends or not. This is what we tried to do in this section with the different expressions derived in the App. C, namely (C.6) and (C.24), (C.25).

7.5.1 Trend for varying incidence angle

First, we study the behavior for varying θ. If we substitute v_0 in terms of v_∞ using Eq. (1.205), we can write

$$\chi = f \times \frac{(e+1)^{1/2}}{(e-1)^{5/2}} v_\infty^5, \tag{7.3}$$

with f given by

$$f_{\rm ring} = \frac{16}{5}\eta \tag{7.4}$$

for the ring expression (Eq. (C.6)) and by

$$f_{\rm 1.5PN,1} = \left[\frac{4}{5}\eta + \frac{6}{5}(1-\sqrt{1-4\eta})\right]\frac{m_1}{M}, \tag{7.5}$$

$$f_{\rm 1.5PN,2} = \left[\frac{4}{5}\eta + \frac{6}{5}(1+\sqrt{1-4\eta})\right]\frac{m_2}{M} \tag{7.6}$$

for the PPN(1.5) approximation (Eqs. (C.24) and (C.25).

In order to relate the previous expressions to θ, we can use the expression (7.2). By neglecting the Lorentz contraction and since the constants involved are the same for all the cases with fixed

initial momentum, we conclude that $\sin\theta \propto \sqrt{e^2-1}$. Therefore, for low values of θ, we can use $\theta \propto \sqrt{e^2-1}$.

By neglecting the missing factors, we can assume that $\theta \ll 1$ implies $e \gtrsim 1$, which implies treating the $e+1$ factors as constants. By doing this, we find that our equations can explain a trend $\chi \sim \theta^{-5}$. This is not enough to predict the exponents that we observe in the results (Table 7.2), but the difference could be easily explained as the missing strong field interaction that we do not take into account, which underestimates the spin for lower θ (lower impact parameter and eccentricity).

7.5.2 Trend for varying mass ratio

According to the ring expression (C.6), we would not expect different final spins for both black holes of a given simulation. However, the PPN(1.5) expressions (C.24), (C.25) do predict different spins. In fact, they accurately predict the fact that the greater spin is induced in the most massive black hole.

Another success of the PPN(1.5) approximation is that it predicts that the induced spin on a given black hole is directly proportional to its mass. This is what we see in the results, particularly in Figs. 7.6 and 7.7. By dividing by the central spin, as in this second figure, and assuming that the relative speed is the same in all the cases, we can cancel out some constants and get a straight line with slopes

$$\frac{4}{7}\left[2\eta+3\left(1-\sqrt{1-4\eta}\right)\right]m_1, \tag{7.7}$$

$$\frac{4}{7}\left[2\eta+3\left(1+\sqrt{1-4\eta}\right)\right]m_2, \tag{7.8}$$

for the most and least massive black holes, respectively. For $q \sim 1$, both slopes are 1, which at least reproduces the order of magnitude of the slopes in Table 7.3, but the difference is clear. Again, this can be explained because our approximation does not tackle strong-field interactions.

Also, this time, there is another source of error, which is that the numerical constants that we pretend to get rid of by dividing by the central spin do not disappear. Since they involve speeds, they are different for each value of q, which could impact the trends.

7.6 Conclusions

Following the work in [278], we showed that it is possible to induce spins in two initially non-spinning, equal-mass black holes. They are larger for higher initial velocities and smaller values of the impact parameter.

In addition, we studied hyperbolic encounters where the two black holes have different masses and found that, for a given impact parameter and initial relative velocity, the highest spin is induced on the most massive black hole. In particular, we found that the spin induction effect can be significantly enhanced for the most massive black hole when the mass ratio becomes large. This result suggests a viable mechanism for significant spin induction in PBHs, contrary to the case of gas accretion, where the induced spins cannot acquire large values.

Furthermore, we were able to qualitatively predict the trends of the spin with varying impact angle and mass-ratio with simple weak-field approximations. However, in order to get more accurate predictions of the induced spins, one would have to resort to higher orders of the PPN formalism. This is left for future work.

With our expressions for the induced spins, we might expect more accurate predictions for more modest values of the involved parameters (weaker interaction). However, they are difficult to generate with the Einstein Toolkit, since the errors involved in low spin measurements are higher in relative terms. Also, the interaction times could get significantly bigger and we would need larger separations, which might be problematic from a technical point of view. Nevertheless, with enough computing power and time, these simulations are possible and should be explored in the future.

Finally, we found that two initially non-spinning black holes involved in a dynamical capture with intermediate mass ratio ($q \sim 0.1$) can naturally acquire a relevant spin, $\chi \simeq 0.8$, for the more massive black hole. This result is relevant for the interpretation of some of the events like GW190521 found by LIGO/Virgo, since the progenitors could have started being very massive but spinless primordial black holes.

We note that most of the hyperbolic encounters in dense PBH clusters occur at large impact parameters (many times their Schwarzschild radius) and small relative velocities ($v_0 \ll c$), and therefore the induced spin will be negligible for the majority of the black holes in the cluster. However, from time to time, a hyperbolic encounter between a large-mass-ratio pair will spin-up the more massive PBH to values of χ significantly different from zero, up to $\chi \leq 0.2$. This could explain why we observe in LVK GW events [264] a distribution of spins peaked around zero with dispersion $\Delta\chi \sim 0.2$. A more refined study taking into account the distribution of eccentricities, impact parameters and relative velocities in dense PBH clusters [277] should give us a prediction for the expected spin distribution depending on the mass and compactness of the cluster. We leave this for future work.

Chapter 8

Gravitational wave constraints from astrometry

8.1 The stochastic gravitational wave background in different frequencies

Standard gravitational-wave detectors are able to probe frequencies in the Hz-kHz range (LVK [6, 12, 13], Einstein Telescope [17], Cosmic Explorer [18]). In the future, we will have the space-based detector LISA [20] measuring gravitational waves in the mHz range. However, the SGWB spreads through all the frequency spectrum, with interesting sources at lower and higher frequencies, as we saw in Chapter 2 and particularly in Fig. 2.1.

One of the most popular methods to constrain the SGWB at low frequencies are pulsar timing arrays (PTAs). This method is based on monitoring a series of pulsars and measuring their time delays, which are attributed to a stochastic gravitational wave background. Last year, there were a series of publications by all the PTA collaborations: the North American Nanohertz Observatory for Gravitational Waves (NANOGrav) [8], the Indian Pulsar Timing Array (InPTA) and European Pulsar Timing Array (EPTA) [9], and the Parkes Pulsar Timing Array (PPTA) [10], as well as a joint analysis by the International Pulsar Timing Array Collaboration (IPTA) [11] some months later. In these publications, they claimed evidence of a SGWB, but not yet a detection.

The SGWB can also be constrained at even lower frequencies, from 10^{-20} Hz to around 10^{-16} Hz, by using polarization measurements from the CMB [109]. In this case, the latest data are provided by Planck [384], where one can use the measurements of the B modes to generate the PI sensitivity curve for a SGWB [385, 386].

Additionally, there is a lot of work being done for high-frequency gravitational waves, where sources such as cosmic strings or phase transitions would still be relevant, as well as mergers from light primordial black holes. There are different experiments being proposed, such as mechanical resonators (resonant spheres in the kHz [387, 388], bulk acoustic wave devices in the MHz-GHz [389]) or devices based on the inverse Gertsenshtein effect [390], by which photons turn into gravitational

waves in the presence of a magnetic field [391, 392] (also up to the GHz), only to name a few. A comprehensive review of this field, sometimes called *Ultra-High Frequency Gravitational Waves* (UHFGW), is provided in [287].

In this chapter, we will focus on the SGWB constraints one can derive from astrometric surveys, such as Gaia, which bridge the gap from CMB polarization measurements to PTAs.

8.2 Introduction to gravitational wave constraints from astrometry

The formalism relating gravitational waves to astrometry was already studied over the past century [393, 394, 395, 396, 397, 398, 399, 400] and at the beginning of this one [401, 402, 403]. In particular, Gwinn et al. [404] used proper motions from quasars obtained from Very Long Baseline Interferometry (VLBI) to set an upper bound $\Omega_{\rm GW} \lesssim 10^{-1}$ for 10^{-17} Hz $\lesssim f \lesssim 10^{-9}$ Hz. Later, Titov et al. [405] updated this limit to $\Omega_{\rm GW} \lesssim 10^{-2}$.

Furthermore, since the review by Book and Flanagan [403] in 2010 and the launch of the Gaia mission [406] in 2013, the field was revitalized with more articles, such as the constraints from Darling et al. [140] and Aoyama et al. [407], which will be commented extensively and reanalyzed in Chapters 9 and 10; as well as more theoretical or mock data-based works [408, 409, 410, 411].

The formalism is detailed in the following sections, leading to the expressions we needed for our work on astrometric constraints from Gaia DR3 [4]. The main idea is to compute the change in the observed sky position $\vec{n}$ of a star in the presence of a gravitational wave through the trajectory of the light it produces, from its emission at the source (S) to its observation from Earth (O). We will denote this shifted position $\vec{n}'$, with the difference being the *angular deflection* $\delta\vec{n} \equiv \vec{n}' - \vec{n}$. The situation is depicted in Fig. 8.1.

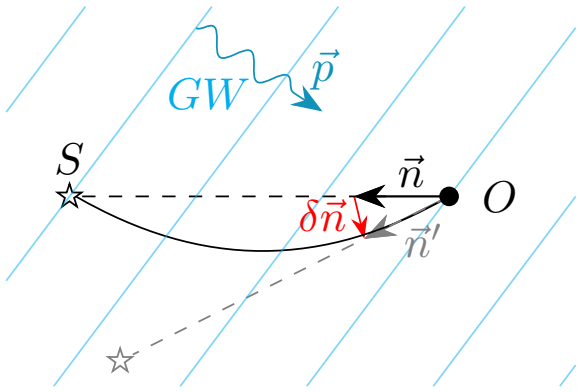

Figure 8.1: Illustration of the concept of angular deflection. In the absence of a GW, the star at source S is observed in the direction of the unitary vector $\vec{n}$. With the passage of a gravitational wave, this position is deflected to $\vec{n}'$ (gray), with the angular deflection being $\delta\vec{n} = \vec{n}' - \vec{n}$ (red). The gravitational wave is represented by its propagation direction $\vec{p}$ and plane wavefronts (cyan).

The main reference for this part will be Book and Flanagan's review [403]. Most of the results in this reference will be explained, generally with more detail, and some of them will be expanded with own results or other references, especially in the final sections.

Following this article, I will first start by computing the angular deflection of a star due to the passage of a gravitational wave within a Minkowski background spacetime, which is simpler. Then, it can be extended to FLRW spacetimes by means of a conformal transformation. We will particularize for the case of distant sources and plane waves and, finally, compute the relevant equations for a SGWB context. These equations will then be decomposed into spherical harmonics, which is needed for the data analysis in Chap. 10.

Throughout these chapters, we will work in geometrized units $G = c = 1$.

8.3 Minkowski spacetime

8.3.1 Unperturbed case

We consider Minkowski spacetime perturbed by a gravitational wave, which is given by

$$ds^2 = g_{\mu\nu}dx^\mu dx^\nu = -dt^2 + (\delta_{ij} + h_{ij})dx^i dx^j, \tag{8.1}$$

with their non-zero Christoffel symbols given by

$$\Gamma^k_{0i} = \frac{1}{2}\partial_0 h_{ki}, \quad \Gamma^0_{ij} = \frac{1}{2}\partial_0 h_{ij}, \quad \Gamma^k_{ij} = \frac{1}{2}[\partial_j h_{ki} + \partial_i h_{kj} - \partial_k h_{ij}]. \tag{8.2}$$

Within this spacetime, we study the evolution of a light ray of unperturbed frequency ω_0 emitted from a source at position $\vec{x}_S$ and observed at the Earth $\vec{x} = 0$ at a certain time t_0. In absence of a gravitational wave, the worldline of the light ray is given by a straight line with direction of propagation $-\vec{n}$, with $\vec{n} \equiv \vec{x}/|\vec{x}|$. The photon 4-momentum will therefore be

$$k^\mu_0 = \omega_0(1, -\vec{n}). \tag{8.3}$$

Throughout this chapter, we will work with the 4-momentum k^μ as the tangent vector to the corresponding photon worldline. Therefore,

$$k^\mu(\lambda) = \frac{dx^\mu(\lambda)}{d\lambda}, \tag{8.4}$$

with λ being the affine parameter of the geodesic $x^\mu(\lambda)$. This means we can parametrize the worldline as

$$x^\mu_0(\lambda) = (t_0, \vec{0}) + \omega_0(\lambda, -\lambda\vec{n}), \tag{8.5}$$

where $\lambda_O = 0$ corresponds to the detection on Earth and $\lambda_S = -|\vec{x}_S|/\omega_0$, to the emission at the source.

In addition, we will use u^μ to denote the 4-velocity,

$$u^\mu \equiv \frac{dx^\mu}{dt}, \tag{8.6}$$

thus matching the notation in [403].

8.3.2 Perturbed case

We consider the perturbed trajectory and photon 4-momentum as the sum of two contributions:

$$x^\mu(\lambda) = x_0^\mu(\lambda) + x_1^\mu(\lambda), \quad k^\mu(\lambda) = k_0^\mu(\lambda) + k_1^\mu(\lambda) \tag{8.7}$$

From the geodesic equation,

$$\frac{d^2x^\mu}{d\lambda^2} + \Gamma^\mu_{\beta\gamma} k^\beta k^\gamma = 0, \tag{8.8}$$

and the fact that $\Gamma^i_{00} = 0$ (the non-zero Christoffel symbols are given by Eq. (8.2)), we realize that stationary observers follow geodesics. Therefore, we can consider the source and observer's spatial coordinates to be fixed.

Given that all the Christoffel symbols are first order in h, in order to stay at first order in the geodesic equation (8.8), we only need the zero-th order of the 4-momentum, which gives

$$\frac{d^2x_1^0}{d\lambda^2} = -\frac{\omega_0^2}{2} n^i n^j \partial_0 h_{ij}, \quad \frac{d^2x_1^k}{d\lambda^2} = -\frac{\omega_0^2}{2}[-2n^i \partial h_{ki} + n^i n^j (\partial_j h_{ki} + \partial_i h_{kj} - \partial_k h_{ij})], \tag{8.9}$$

In order to obtain the full trajectory, we have to integrate these equations from $\lambda = 0$ to an arbitrary λ. Doing it just once, we get the perturbed 4-momentum,

$$k_1^0(\lambda) = -\frac{\omega_0^2}{2} n^i n^j \mathcal{I}_{ij}(\lambda) + I_0, \quad k_1^j(\lambda) = -\frac{\omega_0^2}{2} n^i R_{ij}(\lambda) + J_0^j, \tag{8.10}$$

while integrating twice recovers the trajectory:

$$x_1^0(\lambda) = -\frac{\omega_0^2}{2} n^i n^j \mathcal{K}_{ij}(\lambda) + I_0\lambda, \quad x_1^j(\lambda) = -\frac{\omega_0^2}{2} n^i S_{ij}(\lambda) + J_0^j\lambda, \tag{8.11}$$

with

$$\mathcal{I}_{ij}(\lambda) = \int_0^\lambda d\lambda' \partial_0 h_{ij}(\lambda'), \quad \mathcal{J}_{ijk}(\lambda) = \int_0^\lambda d\lambda' \partial_k h_{ij}(\lambda'), \tag{8.12}$$

$$\mathcal{K}_{ij}(\lambda) = \int_0^\lambda d\lambda' \mathcal{I}_{ij}(\lambda'), \quad \mathcal{L}_{ijk}(\lambda) = \int_0^\lambda d\lambda' \mathcal{J}_{ijk}(\lambda'), \tag{8.13}$$

$$R_{ij}(\lambda) = -2\mathcal{I}_{ij}(\lambda) + n^k(\mathcal{J}_{ijk}(\lambda) + \mathcal{J}_{jki}(\lambda) - \mathcal{J}_{ikj}(\lambda)), \tag{8.14}$$

$$S_{ij}(\lambda) = -2\mathcal{K}_{ij}(\lambda) + n^k(\mathcal{L}_{ijk}(\lambda) + \mathcal{L}_{jki}(\lambda) - \mathcal{L}_{ikj}(\lambda)), \tag{8.15}$$

and I_0 and J_0^j being integration constants.

There are no extra integration constants when integrating k^μ to get x^μ, given that $x_1(0) = 0$. This is because the perturbed photon trajectory must include the detection event $(t_0, \vec{0})$, which is already given by the unperturbed trajectory. Therefore, the perturbation at this instant must be zero. This is the most straightforward simplification we can make to the equations due to boundary conditions, but there are more, as will be detailed next.

Boundary conditions

We impose several boundary conditions to further simplify the previous equations:

- The perturbed photon trajectory must intersect the source worldline, i.e. there must be a $\tilde{\lambda}_S$, which at zero-th order is just λ_S, such that $x_0^j(\tilde{\lambda}_S) + x_1^j(\tilde{\lambda}_S) = x_S^j$. Using Eq. (8.11),

$$x_S^j = -\omega_0 \tilde{\lambda}_S n^j - \frac{\omega_0^2}{2} n^i S_{ij}(\tilde{\lambda}_S) + J_0^j \tilde{\lambda}_S. \tag{8.16}$$

  We can project this equation perpendicular to $\vec{n}$ to get the perpendicular component of J_0^i:

$$J_{0\perp}^i = \frac{\omega_0^2}{2\lambda_S}(\delta^{ik} - n^i n^k) n^j S_{jk}(\lambda_S), \tag{8.17}$$

  where, to first order, the zero-th order $\tilde{\lambda}_S = \lambda_S$ can be used due to the S_{jk} dependence on h.

- The photon is emitted with unperturbed frequency ω_0. This frequency can be computed as

$$\omega_0 = -g_{\mu\nu} k^\mu u_s^\nu, \tag{8.18}$$

  with u_s^μ the 4-velocity of the source. Given that, in the previous subsection, we assumed that the source had constant position, its 4-velocity is $u_s^\mu = (1, \vec{0})$, so we have the equality $-g_{\mu 0} k^\mu = \omega_0$. Again, we can approximate that, at the source, $\lambda = \lambda_S$ to get

$$I_0 = \frac{\omega_0^2}{2} n^i n^j \mathcal{I}_{ij}(\lambda_S). \tag{8.19}$$

- The photon geodesic must be null, which gives the constraint $g_{\mu\nu} k^\mu k^\nu = 0$. Expanding the metric and $k^\mu = k_0^\mu + k_1^\mu$, this gives

$$h_{\mu\nu} k_0^\mu k_0^\nu + 2\eta_{\mu\nu} k_1^\mu k_0^\nu = 0. \tag{8.20}$$

  We now substitute k_0^μ and k_1^μ by their expressions in Eqs. (8.3) and (8.10) to get

$$h_{ij}(\lambda)\omega_0^2 n^i n^j + 2\omega_0 \left[\frac{\omega_0^2}{2} n^i n^j \mathcal{I}_{ij}(\lambda) - I_0 \right] + 2\omega_0 n^j \left[\frac{\omega_0^2}{2} n^i R_{ij}(\lambda) - J_0^j \right] = 0 \tag{8.21}$$

  If we now use the expression

$$\frac{dh_{ij}}{d\lambda} = \omega_0 \partial_0 h_{ij} - \omega_0 n^k \partial_k h_{ij}, \tag{8.22}$$

  one can show that, from the definition of $\mathcal{I}_{ij}$ and R_{ij} in Eqs. (8.12) and (8.14),

$$\begin{aligned} \omega_0 n^i n^j (\mathcal{I}_{ij}(\lambda) + R_{ij}(\lambda)) &= \omega_0 n^i n^j (-\mathcal{I}_{ij}(\lambda) + n^k \mathcal{J}_{ijk}(\lambda)) \\ &= n^i n^j \iint_0^\lambda d\lambda' \omega_0 (-\partial_0 h_{ij}(\lambda') + n^k \partial_k h_{ij}(\lambda')) \\ &= n^i n^j [h_{ij}(0) - h_{ij}(\lambda)]. \end{aligned} \tag{8.23}$$

Substituting this in Eq. (8.21), the terms of $\mathcal{I}_{ij}$ and R_{ij} cancel the one with $h_{ij}(\lambda)$, so that

$$I_0 + n_i J_0^i = \frac{1}{2}\omega_0 n^i n^j h_{ij}(0). \tag{8.24}$$

Subtracting from this expression the previous Eq. (8.19), we get the parallel component of J_0:

$$n_i J_0^i = \frac{1}{2}\omega_0 n^i n^j h_{ij}(0) - \frac{\omega_0^2}{2} n^i n^j \mathcal{I}_{ij}(\lambda_S), \tag{8.25}$$

so, together with Eq. (8.17), we have the full expression for J_0^i:

$$J_0^i = \frac{\omega_0^2}{2\lambda_S}(\delta^{ik} - n^i n^k) n^j S_{jk}(\lambda_S) - \frac{\omega_0^2}{2} n^i n^j n^k \mathcal{I}_{jk}(\lambda_S) + \frac{1}{2}\omega_0 n^i n^j n^k h_{jk}(0) \tag{8.26}$$

8.3.3 Observed angular deflection

In order to get the angular deflection observed from Earth, we must account for two extra perturbed quantities. First, we will see how the observed frequency varies and then, how the local frame does.

Observed frequency and local reference frame

On the one hand, the observed frequency is given by the same expression as in Eq. (8.18), but now at the observer,

$$\omega_{\text{obs}} = -g_{\mu\nu} k^\mu u^\nu_{\text{obs}}. \tag{8.27}$$

Again, since the observer coordinates are constant, $u^\nu_{\text{obs}} = (1, \vec{0})$. Therefore, substituting the value of k^μ in Eqs. (8.3) and (8.10) and using Eq. (8.19) for the value of I_0,

$$\omega_{\text{obs}} = k^0(0) = \omega_0 + I_0 = \omega_0 + \frac{\omega_0^2}{2} n^i n^j \mathcal{I}_{ij}(\lambda_S). \tag{8.28}$$

On the other hand, even if the observer's coordinates remain constant, a local vector basis defining its proper reference frame may vary in time due to a GW. We account for this effect by defining a set of orthonormal basis vectors $\vec{e}_{\hat{j}}$ which, unperturbed, coincide with the coordinate basis, but are otherwise parallel-transported along the observer's worldline. Therefore, they satisfy $e^i_{\hat{j}} = \delta^i_{\hat{j}} + \delta e^i_{\hat{j}}$. In order to extend this basis to the dimension 4 of the spacetime, we define the 4-vectors $e^\mu_{\hat{j}} \equiv (0, \vec{e}_{\hat{j}})$ and complete the orthonormal set with an additional 4-vector $e^\mu_{\hat{0}} \equiv u^\mu = (1, \vec{0})$. To summarize,

$$e^\mu_{\hat{0}} = u^\mu = (1, \vec{0}), \quad e^i_{\hat{j}} = \delta^i_{\hat{j}} + \delta e^i_{\hat{j}}, \quad e^0_{\hat{j}} = 0. \tag{8.29}$$

We could have also defined a $\delta e^0_{\hat{j}}$ but, as we will see, it can be set to zero with no loss of generality.

From the parallel transport equation,

$$u^\mu \nabla_\mu e^\nu_{\hat{\sigma}} = 0, \tag{8.30}$$

we get the equations for the 4-vectors. For $e^{\nu}_{\hat{0}} = u^{\nu}$, the parallel transport equation is automatically satisfied. For the spatial 4-vectors,

$$u^{\alpha}[\partial_{\alpha} e^{\beta}_{\hat{j}} + \Gamma^{\beta}_{\alpha\gamma} e^{\gamma}_{\hat{j}}] = 0 \quad \Rightarrow \quad \partial_0 \delta e^{\beta}_{\hat{j}} + \Gamma^{\beta}_{0\gamma} e^{\gamma}_{\hat{j}} = 0, \tag{8.31}$$

where we have used that $u^{\mu} = (1, \vec{0})$. We now recall that, for the Christoffel symbols, given in Eq. (8.2), the only non-zero ones of the form $\Gamma^{\beta}_{0\gamma}$ are those in which both β and γ are spatial. Therefore, to first order,

$$\partial_0 \delta e^{i}_{\hat{j}} + \frac{1}{2} h^{i}_{\hat{j}} = 0 \quad \Rightarrow \quad \delta e^{i}_{\hat{j}}(t) = -\frac{1}{2} h^{i}_{\hat{j}}(t, \vec{0}) + \omega^{i}_{\hat{j}}, \tag{8.32}$$

with $\omega^{i}_{\hat{j}}$ a constant matrix. In addition, the fact that $\Gamma^{0}_{0\gamma} = 0$ implies that, if there were a $\delta e^{0}_{\hat{j}}$, its time derivative would be zero. Since we want to recover the canonical basis in the absence of a gravitational wave, we can safely set the integration constants to zero without loss of generality.

Therefore, at the detection event,

$$e^{\mu}_{\hat{\nu}} = \delta^{\mu}_{\hat{\nu}} - \frac{1}{2} h^{\mu}_{\hat{\nu}}(0), \tag{8.33}$$

where the expression also works for either $\mu = 0$ or $\nu = 0$ due to the definitions we made, and knowing that $h_{0\nu} = 0$ for all ν.

Angular deflection

Finally, we can compute the observed angular deflection. To do that, we take the two different expressions we have for the 4-momentum of the incoming photon and compute their i-th component evaluated at the observation event, $\lambda = 0$. On the one hand, we have, from Eqs. (8.3), (8.10), (8.26) and the fact that $R_{ij}(0) = 0$ from its definition in Eq. (8.14),

$$k^{i}(0) = -\omega_0 n^{i} + \frac{\omega_0^2}{2\lambda_S}(\delta^{ik} - n^{i}n^{k}) n^{j} S_{jk}(\lambda_S) - \frac{\omega_0^2}{2} n^{i}n^{j}n^{k} \mathcal{I}_{jk}(\lambda_S) + \frac{1}{2}\omega_0 n^{i}n^{j}n^{k} h_{jk}(0). \tag{8.34}$$

On the other hand, we can express the 4-momentum at the observer in terms of the local reference frame basis as

$$k^{\mu}(0) = k^{\hat{\beta}} e^{\alpha}_{\hat{\beta}} = \omega_{\rm obs} u^{\mu} - \omega_{\rm obs} n^{\hat{j}} e^{\mu}_{\hat{j}}, \tag{8.35}$$

which is just the local version of the unperturbed photon 4-momentum $k^{\mu}_0 = \omega_0(1, -\vec{n})$, with $\vec{n}$ being a unitary vector also in this reference frame, $\delta_{\hat{i}\hat{j}} n^{\hat{i}} n^{\hat{j}} = 1$.

From the previous equation, we can compute an expression for n^{i} which will be useful in the next section. We define $n^{\hat{0}} \equiv -1$ to unify both terms, and substitute $\omega_{\rm obs}$ by its expression in Eq. (8.27). We also assume the $\lambda = 0$ dependence to be implicit. Contracting with $g_{\alpha\delta} e^{\delta}_{\hat{\gamma}}$, we get

$$k^{\alpha} = (g_{\mu\nu} k^{\mu} u^{\nu}_{\rm obs}) n^{\hat{\beta}} e^{\alpha}_{\hat{\beta}} \quad \Rightarrow \quad g_{\alpha\delta} e^{\delta}_{\hat{\gamma}} k^{\alpha} = (g_{\mu\nu} k^{\mu} u^{\nu}_{\rm obs}) n^{\hat{\beta}} \delta_{\hat{\beta}\hat{\gamma}} \quad \Rightarrow \quad n^{\hat{\gamma}} = \frac{g_{\alpha\delta} k^{\alpha} e^{\delta}_{\hat{\gamma}}}{g_{\mu\nu} k^{\mu} u^{\nu}_{\rm obs}}. \tag{8.36}$$

Going back to Eq. (8.35) and substituting $\omega_{\rm obs}$ in Eq. (8.28) and $e^{\mu}_{\hat{j}}$ in Eq. (8.33), the spatial components are

$$k^i(0) = -\left(\omega_0 + \frac{\omega_0^2}{2} n^k n^l \mathcal{I}_{kl}(\lambda_S)\right) n^{\hat{j}} \left(\delta^i_{\hat{j}} - \frac{1}{2} h^i_{\hat{j}}(0)\right) \Bigg(\tag{8.37}$$

Again, we decompose $n^{\hat{j}} = n_0^{\hat{j}} + \delta n^{\hat{j}}$. At this point, we can drop the hats, since the reference frame is obvious in all the quantities involved. If we make Eqs. (8.34) and (8.37) equal, the zero-th order is simply

$$-\omega_0 n^i = -\omega_0 n_0^i, \tag{8.38}$$

so $n_0^i = n^i$, as expected. The first order then provides

$$k^i(0) = \frac{\omega_0^2}{2\lambda_S}(\delta^{ik} - n^i n^k) n^j S_{jk}(\lambda_S) + \frac{1}{2}\omega_0 n^i n^j n^k h_{jk}(0) = -\omega_0 \delta n^i + \frac{\omega_0}{2} n^j h^i_j(0). \tag{8.39}$$

We can then easily solve for δn^i and group the terms like

$$\delta n^i = \frac{1}{2}(\delta^{ik} - n^i n^k) n^j \left\{ h_{jk}(0) - \frac{\omega_0}{\lambda_S} S_{jk}(\lambda_S) \right\} \Bigg(\tag{8.40}$$

with S_{jk} given by Eq. (8.15).

8.4 FLRW metric

Given that the geometry of our Universe is best described by a Friedmann-Lemaître-Robertson-Walker metric, we would like to reproduce the previous results for this spacetime. Assuming a flat curvature parameter, the perturbed FLRW metric is given by

$$ds^2 = g_{\mu\nu} dx^\mu dx^\nu = a(\tau)^2 \{ -d\tau^2 + [\delta_{ij} + h_{ij}(\tau, \vec{x})] dx^i dx^j \}, \tag{8.41}$$

with its non-zero Christoffel symbols being

$$\Gamma^\mu_{0\nu} = \frac{\dot{a}}{a}\delta^\mu_\nu + \frac{1}{2}\delta^{\mu\sigma}\partial_0 h_{\sigma\nu}, \quad \Gamma^0_{ij} = \frac{\dot{a}}{a}(\delta_{ij} + h_{ij}) + \frac{1}{2}\partial_0 h_{ij}, \quad \Gamma^k_{ij} = \frac{1}{2}\delta^{kl}[\partial_j h_{li} + \partial_i h_{lj} - \partial_l h_{ij}]. \tag{8.42}$$

The metric in Eq. (8.41) can be re-expressed as

$$ds^2 = g_{\mu\nu} dx^\mu dx^\nu \equiv a(\tau)^2 \overline{g}_{\mu\nu} dx^\mu dx^\nu, \tag{8.43}$$

where $\overline{g}_{\mu\nu}$ is a conformally related, unphysical metric which is formally identical to our Minkowski spacetime (8.1) in the previous section,

$$\overline{g}_{\mu\nu} dx^\mu dx^\nu = -d\tau^2 + [\delta_{ij} + h_{ij}(\tau, \vec{x})] dx^i dx^j. \tag{8.44}$$

Therefore, we can establish a correspondence with the previous results, without the need to repeat the computations from scratch. We will denote with a bar all the quantities related to the metric $\overline{g}_{\mu\nu}$.

The main points we need to review, in light of the conformal relation to the Minkowskian case, are the following ones:

- Again, the observer and source can be assumed stationary, given that these trajectories are geodesics of the spacetime. This can be deduced from the fact that $\Gamma^i_{00} = 0$ (see Christoffel symbols in Eq. (8.42)).

- We consider a null geodesic $x^\mu(\lambda)$ of the spacetime given by $g_{\mu\nu}$, with λ its affine parameter. Then, it is known that it will also be a geodesic of the conformally related metric $\overline{g}_{\mu\nu}$ [412], with a different affine parameter ζ such that

$$\frac{d\zeta}{d\lambda} = \frac{1}{a(\tau(\lambda))^2}. \tag{8.45}$$

- Based on the previous point, the unperturbed photon trajectory is best parameterized using the affine parameter of $\overline{g}_{\mu\nu}$, like

$$\tau(\zeta) = \tau_0 + \omega_0\zeta, \quad x^i(\zeta) = -\zeta\omega_0 n^i. \tag{8.46}$$

- The 4-momentum and 4-velocity relations are given from the metric (8.41) and Eq. (8.45),

$$k^\mu = \frac{dx^\mu}{d\lambda} = \frac{1}{a^2}\frac{dx^\mu}{d\zeta} = \frac{1}{a^2}\overline{k}^\mu, \quad u^\mu = \frac{dx^\mu}{dt} = \frac{1}{a}\frac{dx^\mu}{d\tau} = \frac{1}{a}\overline{u}^\mu \tag{8.47}$$

- In order to remain normalized, the unperturbed basis vectors must be rescaled by a^{-1}. Therefore, the perturbed ones will be

$$e^i_{\hat{j}} = \frac{1}{a}\left(\delta^i_{\hat{j}} + \delta e^i_{\hat{j}}\right) \tag{8.48}$$

Again, since the observer is stationary, $u^\mu_{\text{obs}} = (1, \vec{0})$ and, similar to Eq. (8.31), the parallel transport equation is reduced to

$$\partial_0 e^\beta_{\hat{j}} + \Gamma^\beta_{0\gamma} e^\gamma_{\hat{j}} = 0. \tag{8.49}$$

Using the corresponding Christoffel symbol from Eq. (8.42) and Eq. (8.48),

$$-\frac{\dot{a}}{a^2}\left(\delta^\beta_{\hat{j}} + \delta e^\beta_{\hat{j}}\right) + \frac{1}{a}\partial_0\delta e^\beta_{\hat{j}} + \left(\frac{\dot{a}}{a}\delta^\beta_i + \frac{1}{2}\delta^{\beta k}\partial_0 h_{ki}\right)\frac{1}{a}\left(\delta^i_{\hat{j}} + \delta e^i_{\hat{j}}\right) = 0, \tag{8.50}$$

which leads, to first order, to

$$\partial_0\delta e^\beta_{\hat{j}} + \frac{1}{2}\delta^{\beta k}\partial_0 h_{k\hat{j}} = 0. \tag{8.51}$$

As in the Minkowskian case, this proves there is no need for a $\delta e^0_{\hat{j}}$, given that its null time derivative allows to set it to zero. Similarly, for the spatial indices, we get the same solution as in the Minkowskian case, so that

$$e^i_{\hat{j}} = \frac{1}{a}\left(\delta^i_{\hat{j}} - \frac{1}{2}h^i_{\hat{j}}\right) \tag{8.52}$$

or, in terms of the conformally related metric,

$$e^i_{\hat{j}} = \frac{1}{a}\overline{e}^i_{\hat{j}}. \tag{8.53}$$

Using these expressions, we can relate the observed position in local coordinates $n^{\hat{i}}$ with the equivalent one for $\overline{g}_{\mu\nu}$. From Eq. (8.36), we substitute the relations for the metrics in Eq. (8.43), the 4-momenta and 4-velocities in Eq. (8.47) and the basis vectors in Eq. (8.53). We realize all the $a(\tau)$ factors cancel out, so that

$$n^{\hat{\gamma}} = \frac{\overline{g}_{\alpha\delta}\overline{k}^{\alpha}\overline{e}^{\delta}_{\hat{\gamma}}}{\overline{g}_{\mu\nu}\overline{k}^{\mu}\overline{u}^{\nu}_{\rm obs}}. \tag{8.54}$$

Given that this expression is formally identical to the one for Minkowski spacetime (8.36), we can substitute the expression (8.40) but in terms of the quantities related to $\overline{g}_{\mu\nu}$, including its affine parameter ζ instead of λ. As a result, expanding the expression fully, we get

$$\delta n^i = \frac{1}{2}(\delta^{ik} - n^i n^k) n^j \left\{ h_{jk}(0) - \frac{\omega_0}{\zeta_S} \right. \\ \left. \times \left[-2\int_0^{\zeta_S} d\zeta' \int_0^{\zeta'} d\zeta'' \partial_0 h_{jk}(\zeta'') + n^l \int_0^{\zeta_S} d\zeta' \int_0^{\zeta'} d\zeta'' (\partial_l h_{jk}(\zeta'') + \partial_j h_{kl}(\zeta'') - \partial_k h_{jl}(\zeta'')) \right] \right\}. \tag{8.55}$$

8.5 Further simplifications

We can reduce the double integrals by applying some identities. First, we use Eq. (8.22) to transform the second term like

$$\frac{s^{ik}}{\zeta_S} n^j \int_0^{\zeta_S} d\zeta' \int_0^{\zeta'} d\zeta'' (\omega_0 \partial_0 h_{jk}(\zeta'')) = \frac{s^{ik}}{\zeta_S} n^j \int_0^{\zeta_S} d\zeta' \left[h_{jk}(\zeta'')|_0^{\zeta'} + \int_0^{\zeta'} d\zeta'' \omega_0 n^l \partial_l h_{jk}(\zeta'') \right], \tag{8.56}$$

where we denote $s^{ik} \equiv (\delta^{ik} - n^i n^k)$, common to the three terms. The second term we obtained in the previous expression exactly cancels the first and second terms of the third big term in Eq. (8.55), which are equal since the j and l indices are interchangeable. Therefore, and using the identity

$$\int_0^x dx' \int_0^{x'} dx'' f(x'') = \int_0^x dx' (x - x') f(x') \tag{8.57}$$

to get rid of the remaining double integral, we get

$$\delta n^i = \frac{s^{ik}}{2} n^j h_{jk}(0) + \frac{s^{ik}}{\zeta_S} n^j \int_0^{\zeta_S} d\zeta [h_{jk}(\zeta) - h_{jk}(0)] + \frac{\omega_0 s^{ik}}{2} \int_0^{\zeta_S} d\zeta \frac{\zeta_S - \zeta}{\zeta_S} n^j n^l \partial_k h_{jl}(\zeta). \tag{8.58}$$

8.5.1 Plane waves and the distant source limit

Later on, we will be interested in computing the effect of a stochastic gravitational wave background on the angular deflection spectrum. For this purpose, there are several simplifications that can be made to the previous expressions. First, we will consider a plane wave, given that, for very distant sources, we can consider the SGWB to be a superposition of plane waves. Then, we will assume that our sources are far enough that we can further simplify our equation.

Even if the more physically meaningful case of those studied is the FLRW metric, it is useful to first study the problem in the Minkowski spacetime. This simplifies the procedure and allows to get a better physical and mathematical intuition for what each term stands for.

Minkowski spacetime

In a Minkowski spacetime, the wave equation is simply given by

$$[\partial_t^2 - \nabla^2] h_{ij}(t, \vec{x}) = 0, \tag{8.59}$$

so that a plane wave with angular frequency Ω propagating in the direction $\vec{p}$ is given by

$$h_{ij}(t, \vec{x}) = \mathrm{Re}[\mathcal{H}_{ij} e^{-i\Omega(t - \vec{p}\cdot\vec{x})}] \quad \Rightarrow \quad h_{ij}(\lambda) = \mathrm{Re}[\mathcal{H}_{ij} e^{-i\Omega\{t_0 + \omega_0(1+\vec{p}\cdot\vec{n})\lambda}\}]. \tag{8.60}$$

Therefore, if we substitute in Eq. (8.58) (now with λ instead of ζ) since we are in Minkowski spacetime, we get, after some heavy simplification,

$$\begin{aligned}
\delta n^i = \mathrm{Re}\Bigg[\Bigg(\Bigg\{ 1 + \frac{i(2+\vec{p}\cdot\vec{n})}{\omega_0\lambda_S\Omega(1+\vec{p}\cdot\vec{n})} \Big[1 - e^{-i\Omega\omega_0(1+\vec{p}\cdot\vec{n})\lambda_S} \Big] \Bigg\} h^i \\
+ \Bigg\{ 1 + \frac{i}{\omega_0\lambda_S\Omega(1+\vec{p}\cdot\vec{n})} \Big[1 - e^{-i\Omega\omega_0(1+\vec{p}\cdot\vec{n})\lambda_S} \Big] \Bigg\} p^i \Bigg) \frac{n^j n^k \mathcal{H}_{jk} e^{-i\Omega t_0}}{2(1+\vec{p}\cdot\vec{n})} \\
- \Bigg\{ \frac{1}{2} + \frac{i}{\omega_0\lambda_S\Omega(1+\vec{p}\cdot\vec{n})} \Big[1 - e^{-i\Omega\omega_0(1+\vec{p}\cdot\vec{n})\lambda_S} \Big] \Bigg\} \Big(n^j \mathcal{H}^i_j e^{-i\Omega t_0} \Big] \Bigg(
\end{aligned} \tag{8.61}$$

In this expression, we can observe that the angular deflection depends on the value of the gravitational wave both on the source and the observer. This is similar to what happens for PTA [8, 9, 10]. In that case, the source terms cannot be neglected individually, but they are assumed to vanish when averaging over the different pulsars. In this case, however, we can get rid of the source terms at this point of the formalism.

For this purpose, we will assume that the source is far away enough, in what is called the *distant source limit*. Mathematically, we suppose that the distance to the source $|x_S| = \omega_0|\lambda_S|$ is much larger than the gravitational wave wavelength $c\Omega^{-1}$. In this case, those terms with denominator $\omega_0\lambda_S\Omega(1+\vec{p}\cdot\vec{n})$ in Eq. (8.61) become negligible and we get

$$\delta n^i = \mathrm{Re}\left[\left((n^i + p^i) \frac{\mathcal{H}_{jk} n^j n^k e^{-i\Omega t_0}}{2(1+\vec{p}\cdot\vec{n})} - \frac{1}{2} \mathcal{H}^i_j n^j e^{-i\Omega t_0} \right] \right(\tag{8.62}$$

where we observe no dependence of the gravitational wave at the source anymore, but just at the observer. With this approximation, we limit ourselves to a certain frequency range $\Omega \gg c/|x_S|$. However, the simplifications allow to completely neglect what happens at the source, which would otherwise complicate any analysis with real data. We will discuss this more for a work on real data in Chapter 10. As a double-check, it can be seen that $\delta\vec{n}$ in Eq. (8.62) is orthogonal to $\vec{n}$, which will also be used in Subsection 8.6.3.

FLRW spacetime

In the case of a FLRW metric, the wave equation is now given by

$$\left[\partial_\tau^2 + 2\frac{a'}{a}\partial_\tau - \nabla^2\right] h_{ij}(\tau, \vec{x}) = 0, \tag{8.63}$$

where the prime denotes derivative with respect to the proper time τ. The solution for a plane wave with angular frequency Ω propagating in the direction $\vec{p}$ is given by

$$h_{ij}(\tau, \vec{x}) = \mathrm{Re}\left[\mathcal{H}_{ij} e^{i\Omega \vec{p}\cdot\vec{x}} q_\Omega(\tau)\right] \quad \text{if} \quad q_\Omega'' + 2\frac{a'}{a}q_\Omega' + \Omega^2 q_\Omega = 0. \tag{8.64}$$

In this case, it is harder to simplify the equations before using the distance source limit. It is easier to apply both simplifications at once. Here, we must also assume that the wavelength a/Ω is much smaller than the horizon scale a^2/a', not just the distance to the source. Under this assumption, $\epsilon = a'/(\Omega a) \ll 1$, which makes the term $h_{jk}(\zeta)$ oscillate rapidly in the second term of Eq. (8.58), making it negligible with respect to the integral of $h_{jk}(0)$. For the third term in Eq. (8.58), the integrand oscillates rapidly, which makes the integral be dominated by the contributions near the integration limits or, in this case, just $\zeta = 0$ since the integrand vanishes at $\zeta = \zeta_S$. In this regime, we can also approximate

$$q_\Omega(\tau) \approx \frac{1}{a(\tau_0)} e^{-i\Omega\tau}, \tag{8.65}$$

which can easily be checked that solves Eq. (8.64) under these assumptions. In this case, we recover a standard plane wave. In addition, Eq. (8.58) has been left with only constant terms at the origin. Therefore, the terms that remain are exactly the same ones as in the Minkowskian case, which, operating, leads us to Eq. (8.62) again.

8.6 Angular deflection correlation

8.6.1 Autocorrelation spectrum

We now want an expression for the correlation, which is the quantity directly related to the stochastic gravitational wave background. We will start by analyzing the case in which the angular deflection in a given direction is correlated with itself, $\vec{n} = \vec{n}'$. This is later generalized for the case of different directions in Subsection 8.6.3. Again, for this section, the main reference is Book&Flanagan [403], but the computations will be more detailed and presented in a more convenient order for the purpose of this thesis.

We start by decomposing a generic wave into plane waves with different propagation directions $\vec{p}$ and polarizations $A = +, \times$, with amplitude $h_A(\vec{p})$, similar to Eq. (1.36). In this case, in order to match the notation in [403], we take the form in which we only have positive frequencies, so that we have to include the complex conjugate terms:

$$h_{ij}(\vec{x}, t) = \sum_{A=+,\times} \left(\int_0^\infty df \int d^2\Omega\, h_A(f, \vec{p}) e^{2\pi i f(\vec{p}\cdot\vec{x} - t)} e_{ij}^A(\vec{p}) + c.c. \right) \tag{8.66}$$

Substituting this expression into our Eq. (8.62) for the angular deflection, we get

$$\delta n^i(\vec{n},t) = \sum_{A=+,\times}\left(\int_0^\infty df \int d^2\Omega\, h_A(f,\vec{p}) e^{-2\pi i f t}\mathcal{R}^{ikl}(\vec{n},\vec{p}) e^A_{ij}(\vec{p}) + c.c., \tag{8.67}$$

with

$$\mathcal{R}^{ikl}(\vec{n},\vec{p}) = \frac{1}{2}\left[\frac{(n^i+p^i)n^k n^l}{1+\vec{p}\cdot\vec{n}} - n^k\delta^{il}\right]\left(\tag{8.68}$$

As we saw in Sec. 2.1, if h_{ij} is Gaussian, stationary and with zero mean, we have

$$\langle h_A(f,\vec{p}) h_B(f',\vec{p}')\rangle = 0, \tag{8.69}$$

$$\langle h_A(f,\vec{p}) h^*_B(f',\vec{p}')\rangle = \frac{3H_0^2\Omega_{\rm GW}(f)}{32\pi^3 f^3}\delta(f-f')\delta_{AB}\delta^2(\vec{p},\vec{p}'). \tag{8.70}$$

Taking the correlation between a pair of angular deflections $\delta\vec{n}(\vec{n},t)$ in Eq. (8.67) and using the previous Eq. (8.70), we get

$$\langle \delta n^i(\vec{n},t)\delta n^j(\vec{n}',t')\rangle = \int_0^\infty df \frac{3H_0^2}{32\pi^3 f^3}\Omega_{\rm GW}(f) e^{-2\pi i f(t-t')} H^{ij}(\vec{n},\vec{n}') + c.c., \tag{8.71}$$

with

$$H^{ij}(\vec{n},\vec{n}') = \sum_{A=+,\times}\left(\int d^2\Omega\, \mathcal{R}^{ikl}(\vec{n},\vec{p}) e^A_{kl}(\vec{p}) \mathcal{R}^{jrs}(\vec{n}',\vec{p}) \left(e^A_{rs}(\vec{p})\right)^* . \tag{8.72}$$

The previous expression is simplified by using the property

$$\sum_{A=+,\times}\left(e^A_{ij}(\vec{p})\left(e^A_{kl}(\vec{p})\right)^* = 2P_{ijkl}, \tag{8.73}$$

where P_{ijkl} is a projection tensor, onto the space of traceless symmetric tensors orthogonal to $\vec{p}$. It is given by

$$2P_{ijkl} = \delta_{ik}\delta_{jl} + \delta_{il}\delta_{jk} - \delta_{ij}\delta_{kl} + p_i p_j p_k p_l - \delta_{ik}p_j p_l - \delta_{jl}p_i p_k - \delta_{il}p_j p_k - \delta_{jk}p_i p_l + \delta_{ij}p_k p_l + \delta_{kl}p_i p_j. \tag{8.74}$$

Therefore, Eq. (8.72) can be simplified to

$$H^{ij}(\vec{n},\vec{n}') = 2\int\left(d^2\Omega\, \mathcal{R}^{ikl}(\vec{n},\vec{p})\mathcal{R}^{jrs}(\vec{n}',\vec{p}) P_{klrs}. \tag{8.75}$$

I now particularize for the case that both $\vec{n}$ and t coincide. As mentioned before, the case in which the directions are different will be studied in Subsection 8.6.3. In this case, one can use Eqs. (8.68), (8.74) to show

$$\begin{aligned} 2\mathcal{R}^{jrs}P_{klrs} = \frac{1}{2}\Bigg[\Bigg(&\frac{n^j+p^j}{1+\vec{p}\cdot\vec{n}}\Big\{2n_k n_l - \delta_{kl} + (\vec{p}\cdot\vec{n})^2(p_k p_l + \delta_{kl}) - 4(\vec{p}\cdot\vec{n})n_{(k}p_{l)} + p_k p_l \\ &- \Big\{2n_{(k}\delta^j_{l)} - n^j\delta_{kl} - 2n_{(k}p_{l)}p^j + p_k p_l n^j + (\vec{p}\cdot\vec{n})\left(p_k p_l p^j + \delta_{kl}p^j + 2p_{(k}\delta^j_{l)}\right)\Big\}\Bigg]\Bigg(\end{aligned} \tag{8.76}$$

where $T_{(\mu\nu)}$ denotes the symmetric part of the tensor $T_{\mu\nu}$.

Contracting with the remaining $\mathcal{R}^{ikl}$, we get

$$2\mathcal{R}^{ikl}\mathcal{R}^{jrs}P_{klrs} = \frac{1}{4}\left(1-(\vec{p}\cdot\vec{n})^2\right)\left[\frac{(n^i+p^i)(n^j+p^j)}{(1+\vec{p}\cdot\vec{n})^2}(1-(\vec{p}\cdot\vec{n})^2) - 2\frac{n^{(i}+p^{(i}}{1+\vec{p}\cdot\vec{n}}\left(n^{j)}-(\vec{p}\cdot\vec{n})p^{j)}\right) + (\delta^{ij}-p^ip^j)\right], \tag{8.77}$$

which, operating a bit, reduces the square bracket just to $\delta^{ij}-n^in^j$. Therefore, going back to Eq. (8.75),

$$H^{ij}(\vec{n},\vec{n}) = \frac{1}{4}\int d^2\Omega\,[1-(\vec{p}\cdot\vec{n})^2](\delta^{ij}-n^in^j). \tag{8.78}$$

This integral can easily be solved by defining θ as the angle between $\vec{p}$ and $\vec{n}$. In this case,

$$\int d^2\Omega\,[1-(\vec{p}\cdot\vec{n})^2] = 2\pi\int_0^\pi d\theta\sin\theta(1-\cos^2\theta) = 2\pi\left(2-\frac{2}{3}\right) = \frac{8\pi}{3}. \tag{8.79}$$

Therefore,

$$H^{ij}(\vec{n},\vec{n}) = \frac{2\pi}{3}(\delta^{ij}-n^in^j). \tag{8.80}$$

Substituting this expression into Eq. (8.71), we get

$$\langle\delta n^i(\vec{n},t)\delta n^j(\vec{n},t)\rangle = \frac{1}{8\pi^2}\int_0^\infty df\frac{H_0^2}{f^3}\Omega_{\rm GW}(f)(\delta^{ij}-n^in^j), \tag{8.81}$$

where, given that there were no imaginary numbers involved, the complex conjugate coincides with the first term, adding an extra factor 2. Taking the trace of the previous expression, we get our final expression for the spectrum of angular deflections:

$$\langle\delta\vec{n}^2\rangle = \theta_{rms}^2 = \frac{1}{4\pi^2}\int d\ln f\left(\frac{H_0}{f}\right)^2\Omega_{\rm GW}(f), \tag{8.82}$$

where it is explicitly indicated that this quantity can also be referred to as the root mean square angular fluctuation squared, θ_{rms}^2.

The main interest for this chapter is the obtention of the spectrum of proper motions so, differentiating $\delta\vec{n}$ in Eq. (8.67), a factor $4\pi^2f^2$ arises in the spectrum which produces the expression

$$\langle\delta\dot{\vec{n}}^2\rangle = \int d\ln f H_0^2\Omega_{\rm GW}(f). \tag{8.83}$$

Therefore, the quantity over which we are able to place constraints is the right-hand side of Eq. (8.83). However, to place constraints over the maximum amplitude of $\Omega_{\rm GW}(f)$ in our frequency range, it is usually assumed that $\Omega_{\rm GW}(f)$ has a simple functional form which is mostly relevant over one order of magnitude in f. To simplify things, one can assume that the amplitude of $\Omega_{\rm GW}(f)$ is constant in this frequency range, so that the following approximation holds:

$$\Omega_{\rm GW} \approx \frac{1}{H_0^2}\langle\delta\dot{\vec{n}}^2\rangle. \tag{8.84}$$

Under ideal conditions, one can get a rough estimate of the constraining power of a survey. If we consider that a certain mission will detect N sources, homogeneously distributed in the sky and all of them observed over a period T with a position resolution $\Delta\theta$, the correlated angular motion should be of order

$$\delta\dot{\vec{n}} \sim \frac{\Delta\theta}{\sqrt{N}T}. \tag{8.85}$$

Using Eq. (8.84), this leads to

$$\Omega_{\rm GW} \lesssim \frac{(\Delta\theta)^2}{NT^2H_0^2} \tag{8.86}$$

This expression has been used in the literature [403, 140, 411] to set constraints under idealized conditions. However, as we will see in Chapter 10, this does not always hold with real data.

8.6.2 Frequency validity range

To complete the previous subsection, the validity regime of the derived equations should also be addressed. In order to obtain our final expression in Eq. (8.62), we used the distant source limit, which is only able to constrain the frequency range to $f \gtrsim c/d$, with d the distance to the source. In the case of a set of sources, it should apply to all sources, so it should be the distance to the closest source. However, to provide a more stable lower frequency bound, the 25th percentile of the distance distribution is used, so that, for the lower constrained frequency, at least 75% of the sources fall under our assumptions. We denote this distance by d_{25}, which will be used in Chapter 9. In principle, one could be more conservative and take the 5th or 10th percentile, so that 95% or 90% of sources can be used in the lower constrained frequencies. However, 25% is more standard in the literature [140], so we will use this value.

For the lower end of the frequency range, we have the inverse of the observing period, $f \lesssim 1/T$. This is a bit counterintuitive, so it merits some discussion. If we were observing a source over a period T with a cadence Δt, in order to characterize a wave, its wavelength would need to fit inside the observing period, $\lambda < cT$. However, if it fits inside the cadence, the average over high frequencies will dilute the signal, so the wavelength should be higher, $\lambda > c\Delta t$. This would produce the interval $1/T \lesssim f \lesssim 1/\Delta t$, as it is used in references such as [413].

In our case, nevertheless, we will not be dealing with a time series, but rather, with the averaged proper motions over the full observing period. Therefore, we will only have a data point per source, so the cadence for the position measurements is all the observing time, $\delta t = T$. This provides the bound $f \lesssim 1/\delta t = 1/T$, as explained in the previous paragraph. The bound $f \gtrsim 1/T$ can however be relaxed if we do not need to track the wave oscillation within our observing time. In this case, what we will observe is the effect of higher wavelengths, which can locally be approximated to behave linearly. This linear time evolution in the tensor metric perturbation still induces spatially correlated fluctuations in the proper motions, producing an observational effect which can be used to constraint these frequencies.

As a result, our frequency validity range will be

$$\frac{c}{d_{25}} \lesssim f \lesssim \frac{1}{T}. \tag{8.87}$$

Going back to Eqs. (8.83) and (8.84), the integrals should also be evaluated in this frequency range. In the case of $f \gtrsim T^{-1}$, their effect can be neglected due to rapidly oscillating waves averaging out, and frequencies lower than c/d_{25} are neglected by hypothesis when we assume the distant source limit regime.

In the next subsection, the computation of the angular deflection correlation is generalized to arbitrary directions, which will be necessary in Sec. 8.7.

8.6.3 Generalization to different directions

We will now generalize the expression for the angular deflection correlation in Eq. (8.81) to arbitrary, non-coincident directions $\vec{n}$, $\vec{n}'$. The procedure is identical to the one in Subsection 8.6.1, but now $H^{ij}(\vec{n},\vec{n}')$ in Eq. (8.72) cannot be simplified assuming $\vec{n}' = \vec{n}$, which reduces the symmetry of the equations. Nevertheless, there are other symmetries we can take advantage of. First, given that $\delta\vec{n}$ is orthogonal to $\vec{n}$, as stated in Subsection 8.5.1, then $H^{ij}(\vec{n},\vec{n}')$ is orthogonal to $\vec{n}$ in the index i and to $\vec{n}'$ in j. Then, it can be decomposed into a tensor basis with the same property. First, we define the vectors

$$\vec{A} = \vec{n} \times \vec{n}', \quad \vec{B} = \vec{n} \times \vec{A}, \quad \vec{C} = -\vec{n}' \times \vec{A}, \tag{8.88}$$

where $\vec{A}$ and $\vec{B}$ are a basis for the orthogonal space to $\vec{n}$, and similarly with $\vec{A}$ and $\vec{C}$ for $\vec{n}'$, as long as $\vec{n} \neq \vec{n}'$. Then, the most general 2-tensor orthogonal to $\vec{n}$ in the first index and to $\vec{n}'$ in the second one is then

$$H^{ij}(\vec{n},\vec{n}') = \alpha(\vec{n},\vec{n}')A^iA^j + \beta(\vec{n},\vec{n}')A^iB^j + \gamma(\vec{n},\vec{n}')A^iC^j + \sigma(\vec{n},\vec{n}')B^iC^j. \tag{8.89}$$

Then, we notice that H^{ij} in Eq. (8.72) is invariant under rotations, so all the functions can only depend on the angle between $\vec{n}$ and $\vec{n}'$, which is denoted by Θ. Also, it is invariant under parity change $\vec{n} \mapsto -\vec{n}$, $\vec{n}' \mapsto -\vec{n}'$. This transformation leaves $\vec{A}$ invariant, but changes the sign of $\vec{B}$ and $\vec{C}$. Therefore, to preserve this symmetry, the terms depending on A^iB^j and A^iC^j must be null, so $\beta(\vec{n},\vec{n}') = \gamma(\vec{n},\vec{n}') = 0$. With these two symmetries, Eq. (8.89) can be simplified to

$$H^{ij}(\vec{n},\vec{n}') = \alpha(\Theta)A^iA^j + \beta(\Theta)B^iC^j. \tag{8.90}$$

The coefficients $\alpha(\Theta)$ and $\sigma(\Theta)$ can be evaluated by contracting H^{ij} with the basis tensors,

$$A_iA_jH^{ij} = \sin^4(\Theta)\alpha(\Theta), \quad B_iC_jH^{ij} = \sin^4(\Theta)\sigma(\Theta). \tag{8.91}$$

Using Eq. (8.75) for the case of different $\vec{n}$ and $\vec{n}'$, we can solve for $\alpha(\Theta)$ and $\sigma(\Theta)$:

$$\alpha(\Theta) = \frac{2}{\sin^4(\Theta)} \iint d^2\Omega\, A_i\mathcal{R}^{ikl}(\vec{n},\vec{p})A_j\mathcal{R}^{jrs}(\vec{n}',\vec{p})P_{klrs}, \tag{8.92}$$

$$\sigma(\Theta) = \frac{2}{\sin^4(\Theta)} \iint d^2\Omega\, B_i\mathcal{R}^{ikl}(\vec{n},\vec{p})C_j\mathcal{R}^{jrs}(\vec{n}',\vec{p})P_{klrs}, \tag{8.93}$$

Recalling the simplifications for the coincident directions case in Subsection 8.6.1, there was only a relevant scalar product, $\vec{n}\cdot\vec{p}$. Now, however, there are several of them, so it is convenient to name them. Following [403], we define $\kappa = \vec{n}\cdot\vec{p}$, $\kappa' = \vec{n}'\cdot\vec{p}$, $\lambda = \vec{n}\cdot\vec{n}'$ and $\mu = \vec{A}\cdot\vec{p}$, which satisfy

$$\mu^2 + \lambda^2 + \kappa^2 + \kappa'^2 = 1 + 2\lambda\kappa\kappa'. \tag{8.94}$$

This identity is easy to check for a simple parametrization like the following one:

$$\vec{n} = (0, 0, 1), \quad \vec{n}' = (0, \sin\Theta, \cos\Theta), \quad \vec{p} = (\sin\theta\cos\phi, \sin\theta\sin\phi, \cos\theta), \tag{8.95}$$

so that

$$\mu = \sin\Theta\sin\theta\cos\phi, \quad \kappa = \cos\theta, \quad \kappa' = \cos\theta\cos\Theta + \sin\theta\sin\phi\sin\Theta, \tag{8.96}$$

and with $\lambda = \cos\Theta$ by definition, for any parametrization. Then, the contractions with the $\mathcal{R}^{ijk}$ defined in Eq. (8.68) can be written as

$$A_i\mathcal{R}^{ikl}(\vec{n},\vec{p}) = \frac{1}{2}n^k\left(\frac{\mu n^l}{1+\kappa} - A^l\right), \qquad A_j\mathcal{R}^{jrs}(\vec{n}',\vec{p}) = \frac{1}{2}n'^r\left(\frac{\mu n'^s}{1+\kappa'} - A^s\right) \tag{8.97}$$

$$B_i\mathcal{R}^{ikl}(\vec{n},\vec{p}) = \frac{1}{2}n^k\left(-\frac{\kappa'+\lambda}{1+\kappa}n^l - n'^l\right), \qquad C_j\mathcal{R}^{jrs}(\vec{n}',\vec{p}) = \frac{1}{2}n'^r\left(-\frac{\kappa+\lambda}{1+\kappa'}n'^s + n^s\right) \tag{8.98}$$

In order to get $\alpha(\Theta)$ in Eq. (8.92), one has to contract the quantities in Eq. (8.97) with the projection tensor P_{klrs} defined in Eq. (8.74). For this purpose, the necessary contractions are

$$2P_{klrs}n^k n^l n'^r n'^s = \nu^2\nu'^2 - 2\mu^2, \qquad 2P_{klrs}n^k A^l n'^r n'^s = \mu(\kappa\kappa'^2 - 2\lambda\kappa' + \kappa), \tag{8.99}$$

$$2P_{klrs}n^k n^l n'^r A^s = \mu(\kappa'\kappa^2 - 2\lambda\kappa + \kappa'), \qquad 2P_{klrs}n^k A^l n'^r A^s = (\lambda - \kappa\kappa')(1 - \lambda^2 - \mu^2), \tag{8.100}$$

where $\nu^2 = (1-\kappa^2)$, $\nu'^2 = (1-\kappa'^2)$. For $\beta(\Theta)$, the necessary contractions are

$$2P_{klrs}n^k n^l n'^r n'^s = \nu^2\nu'^2 - 2\mu^2, \qquad 2P_{klrs}n^k n'^l n'^r n'^s = \nu'^2(\lambda - \kappa\kappa'), \tag{8.101}$$

$$2P_{klrs}n^k n^l n'^r n^s = \nu^2(\lambda - \kappa\kappa'), \qquad 2P_{klrs}n^k n'^l n'^r n^s = \nu^2\nu'^2. \tag{8.102}$$

The detailed computations to get the previous equations are very tedious to go through, and are therefore not provided step by step. Nevertheless, they are easy to check with standard algebra and using the identity given by Eq. (8.94). The same goes for the substitution of the previous equations into Eqs. (8.92) and (8.93), which leads to the following expression for $\alpha(\Theta)$ and $\sigma(\Theta)$:

$$\alpha(\Theta) = -\sigma(\Theta) = \frac{1}{4\sin^4\Theta}\int d^2\Omega\left[(\lambda - \kappa\kappa')(1-\lambda^2) - \mu^2(1+\lambda) + \frac{2\mu^2(\lambda+\kappa)(\lambda+\kappa')}{(1+\kappa)(1+\kappa')}\right] \tag{8.103}$$

Given that $\lambda = \cos\Theta$ does not depend on $\vec{p}$, we only need to compute the integrals of μ^2 and $\kappa\kappa'$. For this purpose, it is again convenient to take the simple parametrization given by Eqs. (8.95)and (8.96). In this case, the second term in κ' integrates to 0 over ϕ, so the first two relevant integrals in Eq. (8.103) are

$$\int d^2\Omega\,\mu^2 = \int_0^\pi d\theta\sin\theta\int_0^{2\pi} d\phi(\sin\Theta\sin\theta\cos\phi)^2 = \pi\sin^2\Theta\int_0^\pi d\theta\sin^3\theta = \frac{4\pi}{3}\sin^2\Theta, \tag{8.104}$$

$$\int d^2\Omega\,\kappa\kappa' = \int_0^\pi d\theta\sin\theta\int_0^{2\pi} d\phi\cos^2\theta\cos\Theta = 2\pi\cos\Theta\int_0^\pi d\theta\sin\theta\cos^2\theta = \frac{4\pi}{3}\cos\Theta. \tag{8.105}$$

As a result, the first two terms in Eq. (8.103) can be rewritten as

$$\frac{1}{4\sin^4(\Theta)}\left[\left(4\pi - \frac{4\pi}{3}\right)\cos\Theta\sin^2\Theta - \frac{4\pi}{3}\sin^2\Theta(1+\cos\Theta)\right] = \frac{\pi}{3}\frac{\cos\Theta - 1}{\sin^2\Theta}. \tag{8.106}$$

For the third term in Eq. (8.103), it is convenient to use a different parametrization for $\vec{n}$ and $\vec{n}'$, given by

$$\vec{n} = \left(0, \sin\frac{\Theta}{2}, \cos\frac{\Theta}{2}\right), \quad \vec{n}' = \left(0, -\sin\frac{\Theta}{2}, \cos\frac{\Theta}{2}\right), \quad \vec{p} = (\sin\theta\cos\phi, \sin\theta\sin\phi, \cos\theta) \tag{8.107}$$

so that

$$\mu = \sin\Theta\sin\theta\cos\phi, \quad \kappa = \cos\theta\cos\frac{\Theta}{2} + \sin\theta\sin\phi\sin\frac{\Theta}{2}, \quad \kappa' = \cos\theta\cos\frac{\Theta}{2} - \sin\theta\sin\phi\sin\frac{\Theta}{2}. \tag{8.108}$$

With these definitions, the third term in Eq. (8.103) becomes

$$\begin{aligned}
&\frac{1}{2\sin^2\Theta}\int d^2\Omega\, \sin^2\theta\cos^2\phi \frac{(\cos\Theta + \cos\theta\cos\frac{\Theta}{2})^2 - (\sin\theta\sin\frac{\Theta}{2}\sin\phi)^2}{(1+\cos\theta\cos\frac{\Theta}{2})^2 - (\sin\theta\sin\frac{\Theta}{2}\sin\phi)^2} \\
=&\frac{1}{2\sin^2\Theta}\int d^2\Omega\, \sin^2\theta\cos^2\phi \left[1 + \frac{\cos^2\Theta - 1 + 2\cos\theta\cos\frac{\Theta}{2}(\cos\Theta - 1)}{(1+\cos\theta\cos\frac{\Theta}{2})^2 - (\sin\theta\sin\frac{\Theta}{2}\sin\phi)^2}\right] \\
=&\frac{1}{2\sin^2\Theta}\int d^2\Omega\, \sin^2\theta\cos^2\phi \left[1 + 2\frac{(\cos\Theta - 1)\cos\frac{\Theta}{2}(\cos\frac{\Theta}{2} + \cos\theta)}{(1+\cos\theta\cos\frac{\Theta}{2})^2 - (\sin\theta\sin\frac{\Theta}{2}\sin\phi)^2}\right] \\
=&\frac{1}{2\sin^2\Theta}\int d^2\Omega\, \sin^2\theta\cos^2\phi \left[1 - 4\frac{\sin^2\frac{\Theta}{2}\cos\frac{\Theta}{2}(\cos\theta + \cos\frac{\Theta}{2})}{(1+\cos\theta\cos\frac{\Theta}{2})^2 - (\sin\theta\sin\frac{\Theta}{2}\sin\phi)^2}\right].
\end{aligned} \tag{8.109}$$

To simplify the previous equation, I first integrate in ϕ. For this purpose, I will omit the constant before the integral in the previous equation, as well as the integral in θ, getting

$$\begin{aligned}
&\int_0^{2\pi} d\phi \sin^2\theta\cos^2\phi \left[1 - 4\frac{\sin^2\frac{\Theta}{2}\cos\frac{\Theta}{2}(\cos\theta + \cos\frac{\Theta}{2})}{(1+\cos\theta\cos\frac{\Theta}{2})^2 - (\sin\theta\sin\frac{\Theta}{2}\sin\phi)^2}\right] \\
=&\pi\sin^2\theta - 4\cos\frac{\Theta}{2}\left(\cos\theta + \cos\frac{\Theta}{2}\right)\int_0^{2\pi} d\phi \frac{\sin^2\frac{\Theta}{2}\sin^2\theta(1-\sin^2\phi)}{(1+\cos\theta\cos\frac{\Theta}{2})^2 - (\sin\theta\sin\frac{\Theta}{2}\sin\phi)^2} \\
=&\pi\sin^2\theta - 4\cos\frac{\Theta}{2}\left(\cos\theta + \cos\frac{\Theta}{2}\right)\int_0^{2\pi} d\phi \left[1 + \frac{\sin^2\theta\sin^2\frac{\Theta}{2} - (1+\cos\theta\cos\frac{\Theta}{2})^2}{(1+\cos\theta\cos\frac{\Theta}{2})^2 - (\sin\theta\sin\frac{\Theta}{2}\sin\phi)^2}\right] \\
=&\pi\sin^2\theta - 4\cos\frac{\Theta}{2}\left(\cos\theta + \cos\frac{\Theta}{2}\right)\left[2\pi + \int_0^{2\pi} d\phi \frac{1 - k^2(\theta,\Theta)}{k^2(\theta,\Theta) - \sin^2\phi}\right],
\end{aligned} \tag{8.110}$$

with

$$k(\theta,\Theta) = \frac{1 + \cos\theta\cos\frac{\Theta}{2}}{\sin\theta\sin\frac{\Theta}{2}}. \tag{8.111}$$

Evaluating the last integral,

$$\int_0^{2\pi} d\phi \frac{1 - k^2(\theta,\Theta)}{k^2(\theta,\Theta) - \sin^2\phi} = -2\pi\frac{\sqrt{k^2-1}}{k} = -2\pi\frac{|\cos\theta + \cos\frac{\Theta}{2}|}{1 + \cos\theta\cos\frac{\Theta}{2}}. \tag{8.112}$$

Therefore, substituting this equation into Eq. (8.110) and recovering the integral in θ and the constant $1/(2\sin^2\Theta)$, we get that the third term in Eq. (8.103) is

$$\frac{\pi}{2\sin^2\Theta}\int_0^\pi d\theta\sin\theta\left\{\left(\sin^2\theta+8\cos\frac{\Theta}{2}\left(\cos\theta+\cos\frac{\Theta}{2}\right)\right)\left[\frac{\cos\theta+\cos\frac{\Theta}{2}}{1+\cos\theta\cos\frac{\Theta}{2}}-1\right]\right\}. \tag{8.113}$$

We can integrate Eq. (8.113) by separating the parts independent and dependent on the absolute value. For the first one, without the constant $\pi/(2\sin^2\Theta)$,

$$\int_0^\pi d\theta\sin\theta\left\{\left(\sin^2\theta-8\cos\frac{\Theta}{2}\left(\cos\theta+\cos\frac{\Theta}{2}\right)\right\}=\frac{4}{3}-16\cos^2\frac{\Theta}{2}=-\frac{20}{3}-8\cos\Theta. \tag{8.114}$$

For the second term in Eq. (8.113), we have to split the integration range into two, depending on the condition for the absolute value, $\cos\theta+\cos(\Theta/2)\geq 0$. Taking into account that θ is defined from 0 to π and defining Θ between 0 and 2π, the absolute value condition is equivalent to $\theta\leq\pi-\Theta/2$, range in which the absolute value symbols can simply be removed. On the other hand, in the range $\pi-\Theta/2<\theta(\leq\pi)$, a minus sign must be added when removing the absolute value. Given that the integral is identical except for a global minus sign, both ranges can be studied simultaneously. For this purpose, the notation $f(\theta)|_{c,d}^{a,b}=f(a)+f(b)-f(c)-f(d)$ will be introduced. It is also useful to note that, for the point separating both intervals, $\cos(\pi-\Theta/2)=-\cos(\Theta/2)$. Therefore, again without the constant $\pi/(2\sin^2\Theta)$, the second term in Eq. (8.113) can be computed as

$$\begin{aligned}
&8\cos\frac{\Theta}{2}\int_0^\pi d\theta\sin\theta\left(\cos\theta+\cos\frac{\Theta}{2}\right)\left(\frac{\cos\theta+\cos\frac{\Theta}{2}}{1+\cos\theta\cos\frac{\Theta}{2}}\right.\\
=&\frac{8}{\cos\frac{\Theta}{2}}\left[\int_0^{\pi-\frac{\Theta}{2}}-\int_{\pi-\frac{\Theta}{2}}^\pi\right]d\theta\sin\theta\frac{\left(\cos\frac{\Theta}{2}\cos\theta+\cos^2\frac{\Theta}{2}\right)^2}{1+\cos\theta\cos\frac{\Theta}{2}}\\
=&8\left[\int_0^{\pi-\frac{\Theta}{2}}+\int_\pi^{\pi-\frac{\Theta}{2}}\right]d\theta\sin\theta\left[\cos\theta+\frac{\cos\Theta}{\cos\frac{\Theta}{2}}+\frac{\sin^4\frac{\Theta}{2}}{\cos^2\frac{\Theta}{2}}\frac{\cos\frac{\Theta}{2}}{1+\cos\theta\cos\frac{\Theta}{2}}\right]\\
=&8\left[\frac{\cos^2\theta}{2}-\frac{\cos\Theta}{\cos\frac{\Theta}{2}}\cos\theta-4\frac{\sin^6\frac{\Theta}{2}}{\sin^2\Theta}\ln\left(1+\cos\frac{\Theta}{2}\cos\theta\right)\right]_{0,\pi}^{\pi-\frac{\Theta}{2},\pi-\frac{\Theta}{2}}\\
=&8\left[\left(\cos^2\frac{\Theta}{2}-1\right)+2\cos\Theta-4\frac{\sin^6\frac{\Theta}{2}}{\sin^2\Theta}\ln\frac{\left(1-\cos^2\frac{\Theta}{2}\right)^2}{1-\cos^2\frac{\Theta}{2}}\right]\\
=&8\frac{1+\cos\Theta}{2}+16\cos\Theta-32\frac{\sin^6\frac{\Theta}{2}}{\sin^2\Theta}\ln\left(\sin^2\frac{\Theta}{2}\right)\\
=&4+12\cos\Theta-64\frac{\sin^6\frac{\Theta}{2}}{\sin^2\Theta}\ln\left(\sin^2\frac{\Theta}{2}\right)
\end{aligned} \tag{8.115}$$

Summing this term with the one previously computed in Eq. (8.114) and recovering the constant $\pi/(2\sin^2\Theta)$, we get that the third term in Eq. (8.103) is

$$\frac{\pi}{\sin^2\Theta}\left(-\frac{4}{3}+2\cos^2\frac{\Theta}{2}\right)\left(-\frac{32\pi}{\sin^4\Theta}\ln(\sin\frac{\Theta}{2})\sin^6\frac{\Theta}{2}\right. \tag{8.116}$$

Finally, summing with the first two terms in Eq. (8.103) computed in Eq. (8.106), we get the final result

$$\alpha(\Theta) = -\sigma(\Theta) = \frac{\pi}{3\sin^2\Theta}(7\cos\Theta - 5) - \frac{32\pi}{\sin^4\Theta}\ln(\sin\frac{\Theta}{2})\sin^6\frac{\Theta}{2}, \tag{8.117}$$

where, given that $\alpha(\Theta) = -\beta(\Theta)$, H^{ij} in Eq. (8.90) can be expressed in a simpler way as

$$H^{ij}(\vec{n},\vec{n}') = \alpha(\Theta)(A^iA^j - B^iC^j), \tag{8.118}$$

which is the final result of this section.

In the next section, we will conclude the chapter by using this result to address the how different scales contribute to the SGWB effect on proper motions. We will achieve this via a multipole decomposition analysis.

8.7 Multipole decomposition

In order to set constraints using Eq. (8.84), it is convenient to know how the different scales in the sky contribute to $\langle\delta\dot{\vec{n}}^2\rangle$. For this purpose, we do a multipole decomposition analysis by decomposing the angular deflection using a vector spherical harmonics basis. Before introducing it, we will first review the standard spherical harmonics, which corresponds to the decomposition of a scalar field.

8.7.1 Scalar spherical harmonics

It is widely known that any square-integrable, complex-valued scalar field $f(\vec{n})$ defined in the unit sphere can be decomposed as an infinite sum of spherical harmonics,

$$f(\vec{n}) = \sum_{l=0}^{\infty}\sum_{m=-l}^{l} a_{lm}Y_{lm}(\vec{n}), \tag{8.119}$$

where a_{lm} are complex numbers, uniquely defined for each f, and $Y_{lm}(\vec{n})$ are the spherical harmonics, defined as

$$Y_{lm}(\vec{n}) = (-1)^m\sqrt{\frac{2l+1}{4\pi}\frac{(l-m)!}{(l+m)}}P_{lm}(\sin\delta)e^{im\alpha} \text{ for } m \geq 0, \tag{8.120}$$

$$Y_{lm}(\vec{n}) = (-1)^m Y^*_{lm}(\vec{n}) \text{ for } m < 0, \tag{8.121}$$

with P_{lm} being the associated Legendre polynomials, which can be obtained from the standard Legendre polynomials as

$$P_{lm}(x) = (1-x^2)^{m/2}\frac{d^mP_l(x)}{dx^m}. \tag{8.122}$$

For reference, the first spherical harmonics (up to $l = 2$) are provided in Table 8.1.

For future sections, it is also convenient to recall the Rodrigues formula for the Legendre polynomials [414], which makes them easily obtainable as

$$P_l(x) = \frac{1}{2^l l!}\frac{d^l}{dx^l}(x^2-1)^l. \tag{8.123}$$

Y_{00}	$\frac{1}{2}\sqrt{\frac{1}{\pi}}$
Y_{10}	$\frac{1}{2}\sqrt{\frac{3}{\pi}}\sin\delta$
Y_{11}	$-\frac{1}{2}\sqrt{\frac{3}{2\pi}}\cos\delta\, e^{i\alpha}$
Y_{20}	$\frac{1}{4}\sqrt{\frac{5}{\pi}}(3\sin^2\delta - 1)$
Y_{21}	$-\frac{1}{2}\sqrt{\frac{15}{2\pi}}\sin\delta\cos\delta\, e^{i\alpha}$
Y_{22}	$\frac{1}{4}\sqrt{\frac{15}{2\pi}}\cos^2\delta\, e^{2i\alpha}$

Table 8.1: Spherical harmonics up to $l = 2$ given by Eq. (8.120).

The factor $(-1)^m$ appearing in Eq. (8.120) is called Condon-Shortley phase [415] and, depending on the field, is either included in the spherical harmonics definition or in the Legendre polynomial definition (8.122). We use the first convention, which is the one mostly used in Quantum Mechanics and coincides with the main reference we will use for this section, which is Mignard and Klioner [416]. With this convention, these polynomials satisfy

$$P_{l,-m}(x) = (-1)^m \frac{(l-m)!}{(l+m)!} P_{lm}(x). \tag{8.124}$$

The spherical harmonics are an orthonormal basis for the space of complex-valued scalar fields defined in the unit sphere, so that

$$\int d^2\Omega\, Y_{lm}(\vec{n}) Y^*_{l'm'}(\vec{n}) = \delta_{ll'}\delta_{mm'}. \tag{8.125}$$

This is a result of the orthogonality of Legendre polynomials, together with the normalization of spherical harmonics,

$$\int_{-1}^{1} dx\, P_l(x) P_{l'}(x) = \frac{2}{2l+1}\delta_{ll'}. \tag{8.126}$$

Another property which will be used later is the addition theorem [415, p.53], which states the following identity:

$$P_l(\vec{n}\cdot\vec{n}') = \frac{4\pi}{2l+1}\sum_{m=-l}^{l} Y_{lm}(\vec{n}) Y^*_{lm}(\vec{n}'). \tag{8.127}$$

In the particular case that $\vec{n}' = \vec{n}$, the identity is known as Unsöld's theorem [417],

$$\sum_{m=-l}^{l} Y_{lm}(\vec{n}) Y^*_{lm}(\vec{n}) = \frac{2l+1}{4\pi}. \tag{8.128}$$

In addition, if the scalar field is real-valued, the symmetry of the spherical harmonics in m given by Eq. (8.120) can be used to reduce the sum to only non-negative values of m and real coefficients:

$$f(\vec{n}) = \sum_{l=0}^{\infty} \left[a_{l0} Y_{l0}(\vec{n}) + 2\sum_{m=1}^{l} \left[a^{\mathrm{Re}}_{lm} Y^{\mathrm{Re}}_{lm}(\vec{n}) - a^{\mathrm{Im}}_{lm} Y^{\mathrm{Im}}_{lm}(\vec{n}) \right] \right] \tag{8.129}$$

with $a_{lm}^{\mathrm{Re}} \equiv \mathrm{Re}(a_{lm})$, $a_{lm}^{\mathrm{Im}} \equiv \Im(a_{lm})$ and similarly for $Y_{lm}^{\mathrm{Re}}(\vec{n})$ and $Y_{lm}^{\mathrm{Im}}(\vec{n})$ with $Y_{lm}(\vec{n})$. The same notation will apply for different quantities later on. Additionally, $a_{l0} = \mathrm{Re}(a_{lm})$ under the hypothesis of $f(\vec{n})$ real, given that $Y_{lm}(\vec{n})$ are real by definition (Eq. (8.120)), so there is no need to distinguish real and imaginary parts.

This multipole decomposition is the starting point for all the CMB analysis [418], given that the main considered field is the temperature, which is a scalar. However, in our case, we want to deal with the vector field of proper motions. For this purpose, we need a different spherical harmonics basis.

8.7.2 Vector spherical harmonics

One of the options for our multipole decomposition is to take a spherical harmonics basis for each coordinate. However, while this gets the information contained in each multipole right, the separation in coordinates does not give a physical meaning to each basis. Instead, we can use the so-called *spheroidal* (or electric) and *toroidal* (or magnetic) spherical harmonics which are widely used in the literature [416, 140]. They are related to the standard spherical harmonics as:

$$\vec{S}_{lm} = \frac{1}{\sqrt{l(l+1)}} \nabla Y_{lm} = \frac{1}{\sqrt{l(l+1)}} \left[\frac{1}{\cos\delta} \frac{\partial Y_{lm}}{\partial \alpha} \vec{e}_\alpha + \frac{\partial Y_{lm}}{\partial \delta} \vec{e}_\delta \right] \tag{8.130}$$

$$\vec{T}_{lm} = -\vec{n} \times \vec{S}_{lm} = \frac{1}{\sqrt{l(l+1)}} \left[\frac{\partial Y_{lm}}{\partial \delta} \vec{e}_\alpha - \frac{1}{\cos\delta} \frac{\partial Y_{lm}}{\partial \alpha} \vec{e}_\delta \right] \tag{8.131}$$

where, in order to match the most common notation in the astronomical literature, we used the *right ascension* (RA) α and *declination* (DEC) δ instead of the usual spherical coordinates θ and ϕ. If both coordinate systems share the origin and coordinate axes, they are related as $\alpha = \phi$, $\delta = -\theta$. Another term we will use from the astronomical vocabulary is the word *epoch*, referring to an instant in time.

The spheroidal spherical harmonics come from a gradient, which means their curl will be zero, thus not getting any loop-like behavior. Their equilibrium points, whose number is related to the multipole values l and m, are either nodes or saddle points, but not centers. On the contrary, the toroidal spherical harmonics have zero divergence but non-zero curl, generating centers. This different behavior can be seen in Fig. 8.2, explaining the reason for their names. In addition, the first vector spherical harmonics (up to $l = 3$) are presented in Table 8.2.

It is immediate to notice that both of them are orthogonal to $\vec{r}$, thus being vector fields in the tangent space of the unit sphere. It is also obvious that $\vec{S}_{lm} \perp \vec{T}_{lm}$. Also, from their definition, they inherit some of the spherical harmonics properties, such as the orthonormality given by Eq. (8.125):

$$\int d^2\Omega\, \vec{S}_{lm} \vec{S}^*_{l'm'} = \int d^2\Omega\, \vec{T}_{lm} \vec{T}^*_{l'm'} = \delta_{ll'}\delta_{mm'}, \quad \int d^2\Omega\, \vec{S}_{lm} \vec{T}^*_{l'm'} = 0. \tag{8.132}$$

They are also a basis for the space of square-integrable, complex-valued vector fields $\vec{V}(\vec{n})$ defined in the tangent space of the unit sphere so, for each of these fields, there exist unique complex coefficients s_{lm}, t_{lm} such that

$$\vec{V}(\vec{n}) = \sum_{l=0}^{\infty} \sum_{m=-l}^{l} \left(s_{lm} \vec{S}_{lm}(\vec{n}) + t_{lm} \vec{T}_{lm}(\vec{n}) \right). \tag{8.133}$$

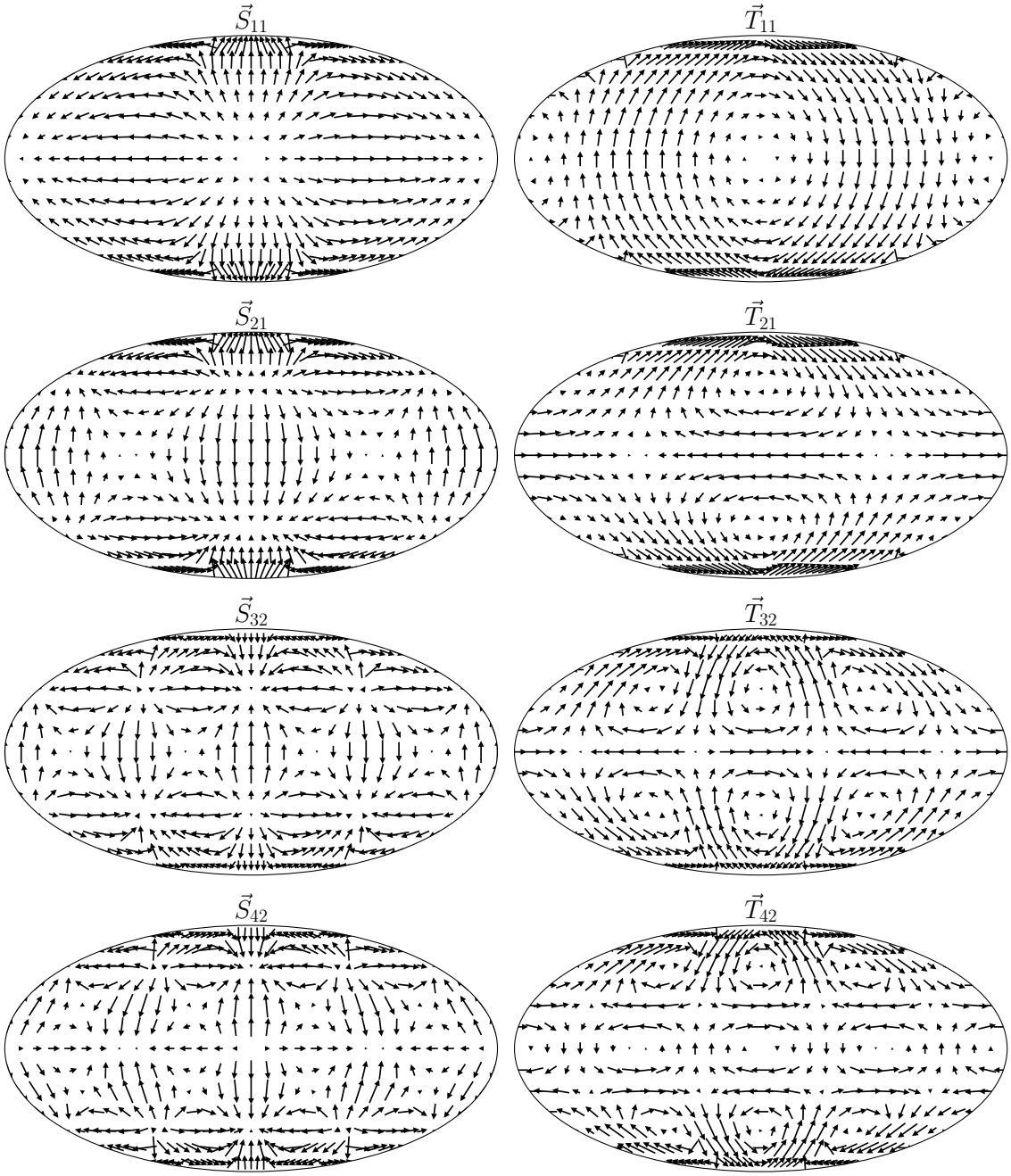

Figure 8.2: Several vector spherical harmonics. Each row presents the spheroidal (left) and toroidal (right) modes for the same multipole indices l and m.

Spherical harmonic	Amplitude	$\vec{e}_\alpha$	$\vec{e}_\delta$
$\vec{S}_{10}$	$\frac{1}{2}\sqrt{\frac{3}{2\pi}}$	0	$\cos\delta$
$\vec{S}_{11}$	$\frac{1}{4}\sqrt{\frac{3}{\pi}}$	$-i\,e^{i\alpha}$	$\sin\delta\,e^{i\alpha}$
$\vec{S}_{20}$	$\frac{1}{4}\sqrt{\frac{15}{2\pi}}$	0	$\sin 2\delta$
$\vec{S}_{21}$	$\frac{1}{4}\sqrt{\frac{5}{\pi}}$	$-i\sin\delta\,e^{i\alpha}$	$-\cos 2\delta\,e^{i\alpha}$
$\vec{S}_{22}$	$\frac{1}{8}\sqrt{\frac{5}{\pi}}$	$2i\cos\delta\,e^{2i\alpha}$	$-\sin 2\delta\,e^{2i\alpha}$
$\vec{S}_{30}$	$\frac{1}{8}\sqrt{\frac{21}{\pi}}$	0	$\cos\delta(5\sin^2\delta-1)$
$\vec{S}_{31}$	$\frac{1}{16}\sqrt{\frac{7}{\pi}}$	$-i(5\sin^2\delta-1)\,e^{i\alpha}$	$\sin\delta(15\sin^2\delta-11)\,e^{i\alpha}$
$\vec{S}_{32}$	$\frac{1}{8}\sqrt{\frac{35}{2\pi}}$	$i\sin 2\delta\,e^{2i\alpha}$	$-\cos\delta(3\sin^2\delta-1)\,e^{2i\alpha}$
$\vec{S}_{33}$	$\frac{1}{16}\sqrt{\frac{105}{\pi}}$	$-i\cos^2\delta\,e^{3i\alpha}$	$\cos^2\delta\sin\delta\,e^{3i\alpha}$
$\vec{T}_{10}$	$\frac{1}{2}\sqrt{\frac{3}{2\pi}}$	$\cos\delta$	0
$\vec{T}_{11}$	$\frac{1}{4}\sqrt{\frac{3}{\pi}}$	$\sin\delta\,e^{i\alpha}$	$i\,e^{i\alpha}$
$\vec{T}_{20}$	$\frac{1}{4}\sqrt{\frac{15}{2\pi}}$	$\sin 2\delta$	0
$\vec{T}_{21}$	$\frac{1}{4}\sqrt{\frac{5}{\pi}}$	$-\cos 2\delta\,e^{i\alpha}$	$i\sin\delta\,e^{i\alpha}$
$\vec{T}_{22}$	$\frac{1}{8}\sqrt{\frac{5}{\pi}}$	$-\sin 2\delta\,e^{2i\alpha}$	$-2i\cos\delta\,e^{2i\alpha}$
$\vec{T}_{30}$	$\frac{1}{8}\sqrt{\frac{21}{\pi}}$	$\cos\delta(5\sin^2\delta-1)$	0
$\vec{T}_{31}$	$\frac{1}{16}\sqrt{\frac{7}{\pi}}$	$\sin\delta(15\sin^2\delta-11)\,e^{i\alpha}$	$i(5\sin^2\delta-1)\,e^{i\alpha}$
$\vec{T}_{32}$	$\frac{1}{8}\sqrt{\frac{35}{2\pi}}$	$-\cos\delta(3\sin^2\delta-1)\,e^{2i\alpha}$	$-i\sin 2\delta\,e^{2i\alpha}$
$\vec{T}_{33}$	$\frac{1}{16}\sqrt{\frac{105}{\pi}}$	$\cos^2\delta\sin\delta\,e^{3i\alpha}$	$i\cos^2\delta\,e^{3i\alpha}$

Table 8.2: Vector spherical harmonics up to $l=3$ given by Eqs. (8.130), (8.131).

In addition, Unsöld's theorem in Eq. (8.128) also holds,

$$\sum_{m=-l}^{l}\vec{R}_{lm}(\vec{n})\cdot\vec{R}^*_{lm}(\vec{n})=\frac{2l+1}{4\pi}. \tag{8.134}$$

In the case of a real-valued vector field, the previous expression can be re-expressed similarly to Eq. (8.129):

$$\vec{V}(\vec{n})=\sum_{l=0}^{\infty}\;s_{l0}\vec{S}_{l0}+t_{l0}\vec{T}_{l0}+2\sum_{m=1}^{l}\left[s^{\rm Re}_{lm}\vec{S}^{\rm Re}_{lm}-s^{\rm Im}_{lm}\vec{S}^{\rm Im}_{lm}+t^{\rm Re}_{lm}\vec{T}^{\rm Re}_{lm}-t^{\rm Im}_{lm}\vec{T}^{\rm Im}_{lm}\right] \tag{8.135}$$

More generally, we will sometimes use the notation r_{lm} to refer to either s_{lm} or t_{lm} according to the index r, whose value can be either s or t. We then denote either $\vec{S}_{lm}$ or $\vec{T}_{lm}$ as $\vec{R}_{lm}$ depending

on the same index. In this case, Eq. (8.135) can be expressed as

$$\vec{V}(\vec{n}) = \sum_{r=s,t}\sum_{l=0}^{\infty} r_{l0}\vec{R}_{l0} + 2\sum_{m=1}^{l}\left[r_{lm}^{\mathrm{Re}}\vec{R}_{lm}^{\mathrm{Re}} - r_{lm}^{\mathrm{Im}}\vec{R}_{lm}^{\mathrm{Im}}\right] \tag{8.136}$$

8.7.3 Contributions per mode and multipole

We are now interested in computing how much the spheroidal and toroidal modes contribute to the angular deflection spectrum in Eq. (8.82), as well as how these contributions are spread over the different multipoles l. For this purpose, we can decompose

$$\langle \delta\vec{n}(\vec{n},t)^2\rangle = \int d(\ln f)\sum_{l=2}^{\infty}[\theta^s_{\mathrm{rms},l}(f)^2 + \theta^t_{\mathrm{rms},l}(f)^2]. \tag{8.137}$$

There might also mixed terms, coming from the correlations of the spheroidal and toroidal modes. However, we will later show that they vanish, so we do not define any $\theta_{\mathrm{rms},l}$ associated to them, and similarly for subsequent notation.

From Eq. (8.82), we know the frequency dependence of the integrand. We define a function $\sigma(f)$ (not to be confused with the one defined in Subsection 8.6.3) that accounts for this dependence, but is normalized to 1:

$$\sigma(f) = \frac{\Omega_{\mathrm{GW}}(f)/f^2}{\int d(\ln f')\,\Omega_{\mathrm{GW}}(f')/(f')^2}, \quad \text{so that} \quad \langle \delta\vec{n}(\vec{n},t)^2\rangle = \theta^2_{\mathrm{rms}}\int d(\ln f)\,\sigma(f). \tag{8.138}$$

At the same time, we define g_r as the fraction of power which is on the mode r (either spheroidal or toroidal), so that $g_s + g_t = 1$. Finally, for each mode, we define α_l^r as the fraction of power which is in multipole l, so that $\sum_{l=2}^{\infty}\alpha_l^r = 1$. With these definitions, we get that

$$\theta^r_{\mathrm{rms},l}(f)^2 = \theta^2_{\mathrm{rms}} g_r \sigma(f)\alpha_l^r, \tag{8.139}$$

so that

$$\langle \delta\vec{n}(\vec{n},t)^2\rangle = \sum_{r,l}\int d(\ln f)\,\theta^2_{\mathrm{rms}} g_r\sigma(f)\alpha_l^r. \tag{8.140}$$

During this subsection, we will then want to compute g_r and α_l^r, as well as prove that the mixed terms spheroidal-toroidal and vice versa do not contribute to the angular deflection spectrum.

Multipole decomposition

For the purposes of this subsections, we must now express the previous equation for $\langle \delta\vec{n}(\vec{n},t)^2\rangle$ given by Eq. (8.82) in terms of correlations of multipole coefficients $r_{lm}(t)$. In this subsection, the vector field we decompose is the angular fluctuation,

$$\delta\vec{n} = \sum_{rlm} r_{lm}\vec{R}_{lm}, \tag{8.141}$$

where, as explained in the previous section, $r = s,t$, $0 \leq l < \infty$, $-l \leq m \leq l$. Using the orthonormality of VSH in Eq. (8.132), the coefficients r_{lm} can be computed as

$$r_{lm}(t) = \int d^2\Omega \left(\delta\vec{n}(\vec{n},t)\cdot\vec{R}^*_{lm}(\vec{n})\right) \tag{8.142}$$

so that

$$\langle r_{lm}(t) r'_{l'm'}(t')^*\rangle = \int d^2\Omega \int d^2\Omega'\, R^*_{lm,i}(\vec{n}) R'_{l'm',j}(\vec{n}')\langle \delta n^i(\vec{n},t)\delta n^j(\vec{n}',t')\rangle. \tag{8.143}$$

Using the expression for $\langle \delta n^i(\vec{n},t)\delta n^j(\vec{n}',t')\rangle$ in Eq. (8.71),

$$\langle r_{lm}(t) r'_{l'm'}(t')^*\rangle = \frac{3H_0^2}{16\pi^3}\int_0^\infty df\, \cos[2\pi f(t-t')]\frac{\Omega_{\rm GW}(f)}{f^3} C_{rlmr'l'm'}, \tag{8.144}$$

where

$$C_{rlmr'l'm'} = \int d^2\Omega \int d^2\Omega'\, R^*_{lm,i}(\vec{n}) R'_{l'm',j}(\vec{n}') H^{ij}(\vec{n},\vec{n}'). \tag{8.145}$$

Using the definitions for $\sigma(f)$ in Eq. (8.138) and $\theta_{\rm rms}$ in Eq. (8.82), we can rewrite the correlation between multipole coefficients as

$$\langle r_{lm}(t) r'_{l'm'}(t')^*\rangle = \frac{3}{4\pi}\int_0^\infty df\, \cos[2\pi f(t-t')]\theta^2_{\rm rms}\frac{\sigma(f)}{f} C_{rlmr'l'm'}. \tag{8.146}$$

It is at this point where we can argue why the mixed modes st vanish. By definition (Eqs. (8.130), (8.131)), $\vec{S}_{lm}(\vec{n})$ is invariant under parity change $\vec{n} \mapsto -\vec{n}$, while $\vec{T}_{lm}$ changes sign. Given that $H^{ij}(\vec{n},\vec{n}')$ is invariant under both $\vec{n} \mapsto -\vec{n}$ and $\vec{n}' \mapsto -\vec{n}'$, as explained in Subsection 8.6.3, then the st terms will be symmetric in $\vec{n}$ and antisymmetric in $\vec{n}'$, which implies that the integral over $d^2\Omega'$ vanishes. A similar thing occurs for ts terms, so it is only necessary to take care of ss and tt correlations.

Spheroidal-spheroidal and toroidal-toroidal correlations

From the definition of the spheroidal VSHs, Eq. (8.130), the correlation coefficients in Eq. (8.145) are given by

$$C_{slmsl'm'} = \frac{1}{l(l+1)}\int d^2\Omega \int d^2\Omega'\, \nabla_i Y^*_{lm}(\vec{n})\nabla'_j Y_{l'm'}(\vec{n}') H^{ij}(\vec{n},\vec{n}'), \tag{8.147}$$

where $\nabla_i \equiv \partial/\partial(x_i)$, $\nabla'_j \equiv \partial/\partial(x'^j)$ are the usual 3D operators, with $\vec{n} = \vec{x}/|\vec{x}|$, $\vec{n}' = \vec{x}'/|\vec{x}'|$. These derivatives are related to the covariant derivative on the unit sphere ∇_A as

$$\nabla_i v^i = \partial_r v^r + \frac{2v^r}{r} + \nabla_A v^A. \tag{8.148}$$

Due to the fact that $H^{ij}(\vec{n},\vec{n}')$, given by Eq. (8.118), is orthogonal to $\vec{n}$ on the first index, it has no radial component for ∇_i, and the same thing happens for the one for ∇'_j in the second component.

Therefore, in both cases, the ∇ operators coincide with the covariant derivatives on the sphere, which implies they can be used for integration by parts. As a result, the previous equation can be transformed into

$$C_{slmsl'm'} = \frac{1}{l(l+1)} \int d^2\Omega \iint d^2\Omega' \, Y^*_{lm}(\vec{n}) Y_{l'm'}(\vec{n}') \beta^s(\Theta), \tag{8.149}$$

with

$$\beta^s(\Theta) = \nabla_i \nabla'_j [H^{ij}(\vec{n}, \vec{n}')] = \nabla_i \nabla'_j \{\alpha(\Theta)[A^i A^j - B^i C^j]\} \equiv \nabla_i \nabla'_j \{\alpha(\Theta) T^{ij}\}. \tag{8.150}$$

We can now decompose $\beta^s(\Theta)$ in Legendre polynomials. Using the addition theorem for spherical harmonics in Eq. (8.127), it can also be expressed in terms of spherical harmonics:

$$\beta^s(\Theta) = \sum_l \beta^s_l P_l(\cos\Theta) \tag{8.151}$$

$$= \sum_{lm} \frac{4\pi}{2l+1} \beta^s_l Y_{lm}(\vec{n}) Y^*_{lm}(\vec{n}'). \tag{8.152}$$

Substituting the latter expression into Eq. (8.149), we get

$$C_{slmsl'm'} = \delta_{ll'} \delta_{mm'} \frac{1}{l(l+1)} \frac{4\pi}{2l+1} \beta^s_l. \tag{8.153}$$

The toroidal-toroidal case reduces reduces to the *ss* case after several steps. For the *tt* correlations, from the toroidal VSHs definition in Eq. (8.131), the coefficients in Eq. (8.145) reduce to

$$C_{tlmtl'm'} = \frac{1}{l(l+1)} \int d^2\Omega \iint d^2\Omega' \, \left(\vec{n} \times \nabla_i Y^*_{lm}(\vec{n})\right) \left(\vec{n} \times \nabla'_j Y_{l'm'}(\vec{n}')\right) H^{ij}(\vec{n}, \vec{n}'), \tag{8.154}$$

Again, using integration by parts to transfer the derivatives from the spherical harmonics to the rest of the integral, the previous equation reduces to

$$C_{tlmtl'm'} = \frac{1}{l(l+1)} \int d^2\Omega \iint d^2\Omega' \, Y^*_{lm}(\vec{n}) Y_{l'm'}(\vec{n}') \beta^t(\Theta), \tag{8.155}$$

where, in this case,

$$\beta^t(\Theta) = \nabla_l \nabla'_p [\epsilon^{ikl} \epsilon^{jmp} n_k n'_m H_{ij}]. \tag{8.156}$$

Evaluating the cross products in this equation using $\vec{n} \times \vec{A} = \vec{B}$, $\vec{n}' \times \vec{A} = -\vec{C}$, $\vec{n} \times \vec{B} = -\vec{A}$, $\vec{n}' \times \vec{C} = A$, by definition in Eq. (8.88) we get

$$\epsilon^{ikl} \epsilon^{jmp} n_k n'_m H_{ij} = \epsilon^{ikl} \epsilon^{jmp} n_k n'_m \alpha(\Theta)(A_i A_j - B_i C_j) = \alpha(\Theta)(-B^l C^p + A^l A^p) = H^{lp}. \tag{8.157}$$

Therefore, β^t is identical to β^s, which means that both modes contribute equally. As a result,

$$g_s = g_t = \frac{1}{2}, \tag{8.158}$$

and the $C_{tlmt'l'm'}$ are identical to the ones $C_{slms'l'm'}$ in Eq. (8.153). If we substitute this equation into Eq. (8.146),

$$\langle r_{lm}(t) r'_{l'm'}(t')^* \rangle = \delta_{rr'}\delta_{ll'}\delta_{mm'} \iint_0^\infty df \cos[2\pi f(t-t')] \theta^2_{\rm rms} \frac{\sigma(f)}{f} \frac{3}{l(l+1)(2l+1)} \beta^r_l . \tag{8.159}$$

From this equation, we can relate β^r_l to α^r_l. First, we denote

$$\langle r_{lm}(t) r'_{l'm'}(t')^* \rangle = \delta_{rr'}\delta_{ll'}\delta_{mm'} \iint_0^\infty df \cos[2\pi f(t-t')] S_{rl}(f). \tag{8.160}$$

Then, using Eq. (8.140), we get the following identity:

$$\begin{aligned} \sum_{r,l} \iint d(\ln f) \theta^2_{\rm rms} g_r \sigma(f) \alpha^r_l &= \langle \delta\vec{n}(\vec{n},t)^2 \rangle \\ &= \sum_{rlm} \sum_{r'l'm'} \vec{R}_{lm}(\vec{n}) \vec{R}'_{l'm'}(\vec{n})^* \langle r_{lm}(t) r'_{l'm'}(t')^* \rangle \\ &= \sum_{rl} \iint_0^\infty df \sum_{m=-l}^{l} |\vec{R}_{lm}|^2 S_{rl}(f) \\ &= \sum_{rl} \int_0^\infty df \frac{2l+1}{4\pi} S_{rl}(f), \end{aligned} \tag{8.161}$$

where the last step uses Unsöld's theorem for VSH in Eq. (8.134). Therefore, on the one hand, we get an explicit expression for $S_{rl}(f)$ in terms of α^r_l,

$$S_{rl}(f) = \frac{4\pi}{2l+1} \theta^2_{rms} \frac{\sigma(f)}{f} g_r \alpha^r_l . \tag{8.162}$$

On the other hand, we get from Eq. (8.159) that

$$S_{rl}(f) = \frac{3}{l(l+1)(2l+1)} \theta^2_{\rm rms} \frac{\sigma(f)}{f} \beta^r_l . \tag{8.163}$$

Therefore, making both expressions for $S_{rl}(f)$ equal, we get that

$$g_r \alpha^r_l = \frac{3}{4\pi l(l+1)} \beta^r_l , \tag{8.164}$$

where $g_r = 1/2$ for $r = s, t$ as shown before. Thus, it only remains to compute the β^r_l to get the fraction of power at multipole l and mode r, α^r_l.

Computation of β^r

Before getting to the computation of β^r_l, we must first compute β^r (for either $r = s, t$, since they are equal, as we just showed) in Eq. (8.150) explicitly, which can be expanded as

$$\beta^r(\Theta) = [\nabla_i \nabla'_j \alpha(\Theta)] T^{ij} + [\nabla_i \alpha(\Theta)](\nabla'_j T^{ij}) + [\nabla'_j \alpha(\Theta)](\nabla_i T^{ij}) + \alpha(\Theta)(\nabla_i \nabla'_j T^{ij}). \tag{8.165}$$

To compute the divergences of T^{ij}, we can first rewrite it in a more manageable way. For this purpose, we can use the following expressions for A^i, B^i and C^i:

$$A^i = \epsilon^{ijk} n_j n'_k, \quad B^i = (\vec{n}\cdot\vec{n}')n^i - n'^i, \quad C^i = (\vec{n}\cdot\vec{n}')n'^i - n^i, \tag{8.166}$$

so that the tensor $T^{ij} = A^i A^j - B^i C^j$ is

$$T^{ij} = \epsilon^{ikl}\epsilon^{jrs} n_k n'_l n_r n'_s - ((\vec{n}\cdot\vec{n}')n^i - n'^i)((\vec{n}\cdot\vec{n}')n'^j - n^j) \tag{8.167}$$

We can now use the identities $\nabla_i n_j = \delta_{ij} - n_i n_j$, $\nabla'_i n'_j = \delta_{ij} - n'_i n'_j$ and $\nabla_i n'_j = \nabla_i n_j = 0$, which can easily be checked from the fact that $\vec{n} = \vec{r}/r$. With this, after some simplifications, we get

$$\begin{gathered}\nabla_i T^{ij} = (1 - 3(\vec{n}\cdot\vec{n}'))((\vec{n}\cdot\vec{n}')n'^j - n^j), \quad \nabla'_j T^{ij} = (1 - 3(\vec{n}\cdot\vec{n}'))((\vec{n}\cdot\vec{n}')n^i - n'^i), \\ \nabla_i\nabla'_j T^{ij} = -9(\vec{n}\cdot\vec{n}')^2 + 2(\vec{n}\cdot\vec{n}') + 3.\end{gathered} \tag{8.168}$$

The gradients of $\alpha(\Theta)$ can easily be computed by using that $\cos(\Theta) = \vec{n}\cdot\vec{n}'$, which implies $-\sin\Theta\nabla_i\Theta = n'_i - (\vec{n}\cdot\vec{n}')n_i$ and $-\sin\Theta\nabla'_j\Theta = n_j - (\vec{n}\cdot\vec{n}')n'_j$. Thus,

$$\begin{aligned}\nabla_i\alpha(\Theta) &= -\alpha'(\Theta)\frac{n'_i - (\vec{n}\cdot\vec{n}')n_i}{\sin\Theta}, \quad \nabla'_j\alpha(\Theta) = -\alpha'(\Theta)\frac{n_j - (\vec{n}\cdot\vec{n}')n'_j}{\sin\Theta}, \\ \nabla_i\nabla'_j\alpha(\Theta) &= -\alpha'(\Theta)\left\{\frac{\delta_{ij} - n_i n_j - n'_i n'_j + (\vec{n}\cdot\vec{n}')n_i n'_j}{\sin\Theta} + \frac{\cos\Theta[n'_i - (\vec{n}\cdot\vec{n}')n_i][n_j - (\vec{n}\cdot\vec{n}')n'_j]}{\sin^3\Theta}\right\}\Bigg(\\ &\quad + \alpha''(\Theta)\frac{[n'_i - (\vec{n}\cdot\vec{n}')n_i][n_j - (\vec{n}\cdot\vec{n}')n'_j]}{\sin^2\Theta}.\end{aligned} \tag{8.169}$$

Substituting Eqs. (8.168) and (8.169) into Eq. (8.165), contracting and using $\vec{n}\cdot\vec{n}' = \cos\Theta$, each of the terms of this equation is, respectively,

$$[\nabla_i\nabla'_j\alpha(\Theta)]T^{ij} = -\sin^2\Theta\alpha''(\Theta) - \sin\Theta\alpha'(\Theta) \tag{8.170}$$

$$[\nabla_i\alpha(\Theta)](\nabla'_j T^{ij}) = [\nabla'_j\alpha(\Theta)](\nabla_i T^{ij}) = [1 - 3\cos\Theta]\sin\Theta\alpha'(\Theta), \tag{8.171}$$

$$\alpha(\Theta)(\nabla_i\nabla'_j T^{ij}) = [-9(\vec{n}\cdot\vec{n}')^2 + 2(\vec{n}\cdot\vec{n}') + 3]\alpha(\Theta). \tag{8.172}$$

Summing the four of them, we get

$$\beta^s(\Theta) = [-9\cos^2\Theta + 2\cos\Theta + 3]\alpha(\Theta) + [1 - 6\cos\Theta]\sin\Theta\alpha'(\Theta) - \sin^2\Theta\alpha''(\Theta). \tag{8.173}$$

Using $\alpha(\Theta)$ defined in Eq. (8.117) and its derivatives, we get that the previous expression greatly simplifies to

$$\beta^r(\Theta) = \frac{4\pi}{3}\left(4 + (1 - \cos\Theta)\left\{12\ln\left(\sin\frac{\Theta}{2}\right) - 1\right\}\right)\Bigg(\tag{8.174}$$

8.7.4 Explicit computation of multipole power

From Eq. (8.174), we need to extract the coefficients of the decomposition in Legendre polynomials β^r_l, as in Eq. (8.151). For this, we can make use of the orthogonality of Legendre polynomials in

Eq. (8.126) to get

$$\iint_{-1}^{1} \beta^r(\Theta) P_l(\cos\Theta) d(\cos\Theta) = \frac{2}{2l+1}\beta_l^r. \tag{8.175}$$

This integral is computed numerically in Book&Flanagan [403], where they provide the numerical values for α_l^r. However, it is possible to solve it analytically and provide a general equation for these coefficients.

In order to solve this integral explicitly, it is convenient to express Eq. (8.174) in terms of $x \equiv \cos\theta$, and integrate in this variable. In addition, given that $P_0(x) = 1$, the orthogonality of Legendre polynomials implies that, for $l \geq 1$, the constant terms in Eq. (8.174) will not alter the result. Therefore, we can simply ignore them, since the vector spherical harmonics are only defined for $l \geq 1$.

We can actually do something similar for the terms proportional to $\cos\Theta$ for $l \geq 2$, given that $P_1(x) = x$. For $l = 1$, it is easy to check that the integral in Eq. (8.175) is zero, so this multipole does not contribute. There is a fundamental reason for this, which is the quadrupolar nature of gravitational waves. Therefore, applying these rules to Eq. (8.174), we can compute the coefficients as

$$\frac{1}{4\pi(2l+1)}\beta_l^r = \iint_{-1}^{1} (1-x)\ln(1-x) P_l(x) dx. \tag{8.176}$$

In order to solve this integral, we will write these polynomials using the Rodrigues formula in Eq. (8.123), and then integrate by parts. When doing so, it is easy to check that all the boundary terms vanish. For instance, for the first step,

$$\frac{2^l l!}{4\pi(2l+1)}\beta_l^r = \iint_{-1}^{1} dx(1-x)\ln(1-x)\frac{d^l}{dx^l}(x^2-1)^l \tag{8.177}$$

$$= \ln(1-x)\frac{d^{l-1}}{dx^{l-1}}(x^2-1)^l\Big|_{-1}^{1} + \iint_{-1}^{1} dx(1+\ln(1-x))\frac{d^{l-1}}{dx^{l-1}}(x^2-1)^l. \tag{8.178}$$

Given that $(x^2-1)^l$ is a $2l$-th degree polynomial with roots ± 1, each one with multiplicity l, then its $(l-1)$-th derivative will be an $(l+1)$-th polynomial with roots ± 1 with, at least multiplicity 1 each. Therefore, when multiplied by $(1-x)\ln(1-x)$, the limit in either of the bounds $x = \pm 1$ (although the only one that produces a possible indetermination is $x = -1$) is zero. In subsequent iterations of the integration by parts, a $\ln(1-x)$ will appear multiplying the $(l-2)$-th derivative of $(x^2-1)^l$ and, from there on, an $(x-1)^k$ multiplied by the $(l-k-2)$-th derivative of $(x^2-1)^l$. Therefore, the multiplicity of the roots ± 1 of the integrated $P_l(x)$ always dominates over the trend of the other factor, making all the boundary terms in the subsequent integrations by parts vanish.

As a result, we can solve the integral as

$$\begin{aligned}\frac{2^l l!}{4\pi(2l+1)}\beta_l^r &= \int_{-1}^{1} dx(1+\ln(1-x))\frac{d^{l-1}}{dx^{l-1}}(x^2-1)^l = \int_{-1}^{1} dx\frac{1}{1-x}\frac{d^{l-2}}{dx^{l-2}}(x^2-1)^l \\ &= \ldots = \int_{-1}^{1} dx\frac{(-1)^l(l-2)!}{(1-x)^{l-1}}(x^2-1)^l dx = (l-2)!\int_{-1}^{1} dx(1-x)(1+x)^l dx \\ &= (l-2)!\int_{-1}^{1} dx[2(1+x)^l-(1+x)^{l+1}]dx = (l-2)!\left[\frac{2^{l+1}}{l+1}-\frac{2^{l+2}}{l+2}\right] \\ &= \frac{(l-2)!}{(l+1)(l+2)}2^{l+2}. \end{aligned} \tag{8.179}$$

Thus, the final expression for β_l^r is

$$\beta_l^r = \frac{16\pi(2l+1)}{(l+2)(l+1)l(l-1)}, \quad \text{or} \quad \beta_l^r = 16\pi(2l+1)\frac{(l-2)!}{(l+2)!} \tag{8.180}$$

Going back to Eq. (8.164), relating α_l^r to β_l^r, and using $g_r = 1/2$, we get

$$\alpha_l^r = \frac{24(2l+1)}{l(l+1)}\frac{(l-2)!}{(l+2)!} \quad \text{or} \quad \alpha_l^r = \frac{2l+1}{l(l+1)}\binom{l+2}{4}^{-1}. \tag{8.181}$$

The latter expression is a very compact and exact way to express α_l^r for arbitrary $l \geq 2$ and, as far as I know, it is the first time it has been presented. This is a useful result to compute the power in the quadrupole, which, substituting $l = 2$ in the previous equation, is $5/6$, agreeing with [403, 404, 140], but it extends to any desired multipole without the need to do any heavy computation.

In fact, in Book&Flanagan [403], they provide a fit to their numerical data from multipoles $l = 2$ to $l = 11$, which is $\alpha_l^r = 32.34 l^{-4.921}$. With our expressions in Eq. (8.181), we can see why this trend is approximately proportional to l^{-5}: for $l \gg 1$, we can approximate

$$\alpha_l^r \approx 48 l^{-5}, \tag{8.182}$$

where the exact exponent for the power law is indeed -5, rather than -4.921, and the precise coefficient should be 48 rather than 32.34.

For convenience, I present the first values of α_l^r in Table 8.3, both the exact fraction and numerical evaluation, up to $l = 11$ for direct comparison with [403].

8.8 Data analysis

When we have real data, we will be interested in computing how much power we have in each multipole, to be able to relate it with the previous expressions. For this purpose, if we have a vector field with coefficients r_{lm}, we can define its power per multipole l and mode $r = s, t$ as

$$P_l^r = \sum_{m=-l}^{l} |r_{lm}|^2, \tag{8.183}$$

l	α_l^r	
	Exact	Num. value
2	5/6	0.833333333
3	7/60	0.116666667
4	3/100	0.3
5	11/1050	0.010476190
6	13/2940	0.004217687
7	5/2352	0.002125850
8	17/15120	0.001124339
9	19/29700	0.000639731
10	7/18150	0.000385675
11	23/94380	0.000243696

Table 8.3: Exact and numerical values for α_l^r in Eq. (8.181) for the first multipoles up to $l = 11$.

with the total power per multipole being

$$P_l = P_l^s + P_l^t. \tag{8.184}$$

These expressions would be related to the variables in the previous section as

$$\langle P_l^r \rangle = \theta_{\rm rms}^2 \alpha_l^r. \tag{8.185}$$

In the real-valued case, one can check that Eq. (8.184) turns into

$$P_l^r = r_{l0}^2 + 2\sum_{m=1}^{l} \left((r_{lm}^{\rm Re})^2 + (r_{lm}^{\rm Im})^2 \right). \tag{8.186}$$

This quantity is a measurement of how much every multipole and mode contributes to the second momentum of the vector. Because of the orthogonality properties of the vector spherical harmonics (Eq. (8.132)),

$$\int d^2\Omega\, \vec{V}(\vec{n})\vec{V}^*(\vec{n}) = \sum_{r=s,t}\sum_{l=0}^{\infty} P_l^r. \tag{8.187}$$

In an idealized case, with infinite resolution and perfect sky coverage, we should address the contributions coming from all the different scales in the sky. However, at the point our surveys are now, the data is still dominated by systematics and likely still far from a detection. Therefore, we cannot aim to extract any information from small scales, corresponding to high multipoles. Hence, it is best to aim to set constraints from the lowest possible multipole, which, in the case of gravitational waves and due to their quadrupolar nature, is the quadrupole.

Therefore, we will be interested in the total quadrupole power given by Eq. (8.184) with $l = 2$. As we computed in the previous section, Eq. (8.181) shows that the quadrupole power of a gravitational wave background is 5/6 of the total, as indicated in other references in the literature [403, 404, 140]. Therefore, if we decompose a proper motion field in vector spherical harmonics like in Eq. (8.135),

we can compute its quadrupole power P_2 from its coefficients and use Eq. (8.84) to get $\Omega_{\rm GW}$, like

$$\Omega_{\rm GW} \approx \frac{1}{H_0^2}\langle \delta\dot{\vec{n}}^2\rangle \approx \frac{1}{H_0^2}\frac{6}{5}\frac{1}{4\pi}P_2 = 0.000438\frac{P_2}{(1\ \mu{\rm as/yr})^2}h_{70}^{-2}, \tag{8.188}$$

where we have used $H_0 = 14.76 h_{70}\ \mu$as/yr, matching the normalization in Eq. (2.10). The factor $6/5$ is introduced to compensate the mentioned fraction of quadrupole power with respect to the total, which is $5/6$ (Table 8.3), while the $1/4\pi$ comes from the fact that the proper motion spectrum $\langle \delta\dot{\vec{n}}^2\rangle$ should be normalized with respect to the solid angle volume 4π, which is missing in the definition of the quadrupole power, as we can see in Eq. (8.187). In the final expression, the factor 0.000438 matches the one in our article [4], slightly differing with others in the literature as [140] due to different rounding criteria.

8.8.1 Statistical significance

We now study the statistical properties of the coefficients r_{lm} and power P_l^r. First, we go through the ordinary least squares formalism to get the variance of the coefficients, following [416]. We suppose we are trying to fit a generic, real-valued vector field like the one in Eq. (8.135) to a dataset of size N of positions $\vec{r}_i = (\alpha_i, \delta_i)$, proper motions $\vec{\mu}_i = (\mu_i^\alpha, \mu_i^\delta)$ and associated errors $\Delta\vec{\mu}_i = (\Delta\mu_i^\alpha, \Delta\mu_i^\delta)$, $i = 1, \ldots, N$. Then, we aim to minimize the sum of the residuals ρ_i^2, with

$$\rho_i^2 = \left(\frac{V^\alpha(\vec{r}_i) - \mu_i^\alpha}{\Delta\mu_i^\alpha}\right)^2 + \left(\frac{V^\delta(\vec{r}_i) - \mu_i^\delta}{\Delta\mu_i^\delta}\right)^2. \tag{8.189}$$

For a residual of the form

$$\sum_i \left(y_i - \sum_j a_j X_j(x_i)\right)^2, \tag{8.190}$$

for some data points (x_i, y_i) and basis functions $X_j(x)$, the covariance matrix for the coefficients a_j is proportional to the inverse of the normal matrix, this being

$$(N)_{ij} = \sum_k X_i(x_k)X_j(x_k). \tag{8.191}$$

In our case, things are a bit more complicated because the coefficients and base functions appear in both terms in Eq. (8.189). To simplify things, we will assume that $\Delta\mu_i^\alpha \approx \Delta\mu_i^\delta \equiv \Delta\mu_i$. In this case, our $X_j(x_i)$ in Eq. (8.190) are given by $\vec{R}_{lm}(\vec{r}_i)/\Delta\mu_i$ (even if they are 2D, they play the exact same role), so that the normal matrix would be

$$(N)_{rlm,r'l'm'} = \sum_k \frac{\vec{R}_{lm}(\vec{r}_k)}{\Delta\mu_k}\frac{\vec{R}_{lm}(\vec{r}_k)}{\Delta\mu_k}. \tag{8.192}$$

Now, we assume that the sources are equally distributed in the sky and they have homogeneous proper motion errors. This way, we can take the contraction in the previous equation as an average over the sky (multiplied by the number of sources) and, due to the orthogonality properties of

the vector spherical harmonics, the normal matrix approximately diagonalizes: non-diagonal terms should be low compared with the values in the diagonal. Going to the $\vec{R}_{lm}^{\mathrm{Re/Im}}$ basis for the real vector field case (8.135), we then find out that each diagonal element for r_{lm} is

$$\sum_{i=0}^{N}\left(\frac{\vec{R}_{l0}}{\mu_i^2}\right)^2 \quad \text{for} \quad r_{l0}, \qquad 4\sum_{i=0}^{N}\left(\frac{\vec{R}_{lm}^{\mathrm{Re/Im}}}{\mu_i^2}\right)^2 \quad \text{for} \quad r_{lm}^{\mathrm{Re/Im}}. \tag{8.193}$$

However, the r_{l0} do not depend on α, so their average is 1 over this variable. On the contrary, $r_{lm}^{\mathrm{Re/Im}}$ have factors $\cos^2(m\alpha)$ and $\sin^2(m\alpha)$, which can easily be checked from Eqs. (8.130), (8.131), (8.120), thus averaging to $1/2$ over α. Therefore, under the mentioned idealized conditions, the normal matrix diagonal elements for r_{l0} should be approximately $1/2$ of the ones for $r_{lm}^{\mathrm{Re/Im}}$. As mentioned before, the covariance matrix is proportional to the inverse of the normal matrix, so we then have the inverse relation between variances:

$$\mathrm{Var}(r_{lm}^{\mathrm{Re}}) \approx \mathrm{Var}(r_{lm}^{\mathrm{Im}}) \approx \frac{1}{2}\mathrm{Var}(r_{l0}) \equiv \frac{\sigma_{rl0}^2}{2} \tag{8.194}$$

Assuming that these unknowns behave as Gaussian variables, we notice that the power per multipole order and mode in Eq. (8.184) is a sum of $2l+1$ squared Gaussians with the same variance, given that the factor 2 appearing in the $m \geq 1$ can be re-absorbed into the squared quantity, generating a Gaussian with the same mean multiplied by $\sqrt{2}$ and the variance multiplied by 2. We consider two cases:

- If we assume that the mean is 0, then P_l^r is *the sum of squares of* $2l+1$ *independent, zero mean Gaussian distributions with the same variance* σ_{rl0}. By definition, this is a *chi-squared distribution* of $n = 2l+1$ degrees of freedom rescaled by the factor σ_{rl0}. Therefore, if we rescale each coefficient by their variance, like

$$W_l^r = \left(\frac{r_{l0}}{\sigma_{rl0}}\right)^2 + \sum_{m=1}^{l}\left[\left(\frac{r_{lm}^{\mathrm{Re}}}{\sigma_{rlm}^{\mathrm{Re}}}\right)^2 + \left(\frac{r_{lm}^{\mathrm{Im}}}{\sigma_{rlm}^{\mathrm{Im}}}\right)^2\right], \tag{8.195}$$

  we get *a sum of squares of* $2l+1$ *independent, standard Gaussian distributions (zero mean and unit width) with the same variance* or, in other words, a *chi-squared distribution* of $n = 2l+1$ degrees of freedom, with probability density function

$$f_{\chi_n^2}(x) = \frac{1}{2^{n/2}\Gamma(n/2)}x^{n/2-1}e^{-x/2}, \quad x \in [0,\infty). \tag{8.196}$$

  This will be our null hypothesis. Physically speaking, the coefficients should have approximately zero mean if our data is pure Gaussian noise and our sources are homogeneously distributed in the sky. However, this may not be the case even in the case of noise domination. We will discuss this issue more in depth in Chapter 10.

- If the Gaussians do not have zero mean, the result of Eq. (8.195) will be a *non-central chi-squared distribution* of $n = 2l+1$ degrees of freedom, with probability density function

$$f_{\chi_{n,\lambda}^2}(x) = \frac{1}{2}e^{-\frac{x+\lambda}{2}}\left(\frac{x}{\lambda}\right)^{\frac{n}{4}-\frac{1}{2}} I_{n/2-1}(\sqrt{\lambda x}), \quad x \in [0,\infty), \tag{8.197}$$

where λ is the non-centrality parameter, given by the squared sum of the Gaussian means. Similarly to the previous case, the power P_l^r would behave as the rescaled version of the distribution for W_l^r.

If we have the distribution of the coefficients r_{lm}, for example, from the posteriors after running an MCMC, it is interesting to test how close we are to the first case or, more precisely, how likely it is to be under the null hypothesis. For this purpose, one could use the mean values of r_{lm} and their 1-sigma uncertainties to compute $\overline{W}_l^r$ from Eq. (8.195). Then, one can compute the probability that a χ^2 with $n = 2l + 1$ degrees of freedom produces a value larger than $\overline{W}_l^r$, like

$$P(W_l^r > \overline{W}_l^r) = \int_{\overline{W}_l^r}^{\infty} f_{\chi_n^2}(x)dx \equiv F_{\chi_n^2}(\overline{W}_l^r) \tag{8.198}$$

However, it is also possible to discuss this in terms of sigmas of a Gaussian distribution, which is something widely used in Physics. For this, we can use the following result [419]:

$$\left(\frac{\chi_n^2}{n}\right)^{1/3} \sim N\left(1 - \frac{2}{9n}, \sqrt{\frac{2}{9n}}\right) \tag{8.199}$$

to a good degree of approximation increasing with n, with $N(\mu, \sigma)$ the Gaussian distribution of mean μ and variance σ^2, as we introduced in Subsec. 2.3.1. We can then evaluate how many sigma away our results are from the mean from the following quantity, usually called Z-score [416]:

$$Z_l^r = \sqrt{\frac{9n}{2}}\left[\left(\frac{W_l^r}{n}\right)^{1/3} - \left(1 - \frac{2}{9n}\right)\right] \tag{8.200}$$

In general, the Z-score is given by multipole, which is computed from the previous equation but substituting W_l^r by

$$W_l = W_l^s + W_l^t. \tag{8.201}$$

It can also be extended for several multipoles by following the same logic of summing at the level of W_l. Also, there are different criteria for the definition of W_l^r in Eq. (8.195), one being the one we used and the other, dividing each term by either σ_{rl0}^2 or $\sigma_{rl0}^2/2$ according to their variance in Eq. (8.194). The second definition relies on the idealized conditions explained to obtain Eq. (8.194), so it is less accurate. However, it can easily be computed as $W_l^r = P_l^r/\sigma_{rl0}^2$, which can sometimes be more convenient. In any case, we will use the first definition throughout the thesis.

Therefore, the Z-score gives a measurement of how statistically significant are our results compared to the pure noise hypothesis. As a result, a high Z-score can potentially hint towards a detection, but it may also have other possible explanations, as we will see in Chapter 10.

Chapter 9

The Gaia mission

9.1 Introduction

The Gaia mission was launched by ESA in December 2013 [406] and started its science run in July 2014. The name "GAIA" was originally an acronym for Global Astrometric Interferometer for Astrophysics, but the techniques to be used were changed, making the acronym no longer applicable[1]. As a result, the name Gaia was kept to reflect the continuity of the project, but now without its original acronym meaning. Its nominal science mission was scheduled for 5 years, but it was extended for 10 [420].

The spacecraft is equipped with two telescopes, each of them composed of 3 mirrors. These telescopes are used by the three main instruments, called the astrometric, photometric and spectroscopic instruments. The astrometric instrument takes photometric data from the telescopes in the white, unfiltered, white-light photometric G band (where G stands for Gaia), which covers the range 330-1050 nm: part of the ultraviolet spectrum, the full visible range and part of the infrared spectrum. This high signal-to-noise ratio (SNR) data is then used to derive astrometric information such as positions, proper motions, etc. at different epochs. The sources are selected performing a survey of the sky, instead of using a predefined input catalog as its precursor Hipparcos did [421]. The photometric instrument measures the spectral energy distribution of the same sources at the same epochs, providing astrophysical information. It does it in two frequency ranges: 330–680 nm (blue photometer, BP) and 640-1050 nm (red photometer, RP). Finally, the spectroscopic instrument, or radial-velocity spectrometer, collects spectra in the range 845–872 nm [420] (Calcium triplet region [422]), to produce radial velocities and other astrophysical information on the sources.

The Gaia collaboration releases their data products progressively:

- The first data release, DR1 [423], was published in September 2016 and comprised 1.14 years of data. It included astrometric information and G magnitudes.
- The second data release, DR2 [424], was published in April 2018 and comprised 1.83 years.

[1] https://www.esa.int/Science_Exploration/Space_Science/Gaia_overview

It expanded over the data products of DR1 by including BP and RP photometry, radial velocities and other new astrophysical information.

- The third data release was divided in two, with an early data release (EDR3) [420] in December 2020, with only some astrometric and photometric data, comprising 2.84 years of observation. Later, in June 2022, the third data release DR3 [425] was published, complementing EDR3 with a vast amount of information of the same sources, including everything present in DR2, source classification and redshift determinations. A summary of the quantities present in DR3 can be consulted in [425] and a comparison with previous data releases in [426].

- According to the data release plan [427], DR4 is not expected sooner than the end of 2025. It will comprise 5.5 years of data, including epoch data for all sources. The final data release, DR5, is not expected sooner than the end of 2030 and it will comprise the full observing period of around 10 years, containing all collected data.

In our article [4], we used data from DR3 to set constraints on the SGWB amplitude at low frequencies, as will be detailed in Chapter 10. This data release includes data of 1.81 billion sources, with 1.47 billion having full astrometric measurements According to the EDR3 main article [420], the position uncertainties range from 0.01-0.02 mas for $G < 15$ to ~ 1.0 mas at $G \approx 21$ mag, with the proper motion uncertainties ranging from $0.02 - 0.03$ mas/yr for $G < 15$ to ~ 1.4 mas/yr at $G \approx 21$ mag.

We are interested in working with datasets of quasars, given that they present low intrinsic proper motions, so that a relevant fraction of their correlations can be attributed to a SGWB. We study how to generate these datasets in the next section.

9.2 Generating clean datasets

9.2.1 The QSO candidate sample

Gaia DR3 does not provide a QSO catalog, but rather, a list of sources called *QSO candidates*[2]. The idea of this list was to include all the sources that could reasonably be considered a quasar, even with low probability. It therefore focuses on completeness, disregarding its purity. A source is included in this list according to selection criteria detailed in [430] and in the Gaia DR3 documentation website[3], which we summarize below:

- The main contribution to this catalog is provided by Gaia Discrete Source Classifier (DSC) [431], which classifies sources into five classes: quasar, galaxy, star, white dwarf, and physical binary star. DSC consists of three classifiers: Specmod, which uses BP/RP spectra; Allosmod, which uses other features such as parallax, proper motions, or color indices, and Combmod, which combines the output class probabilities of both of them and assigns a combined probability,

[2] After our publication, a catalog named *Quaia* [428] has been published by an independent team, who use infrared data from the WISE (Wide-field Infrared Survey Explorer) survey [429] to generate a catalog from the QSO candidate sample from Gaia. However, this is not an official catalog from Gaia

[3] Gaia DR3 online documentation: https://www.cosmos.esa.int/web/gaia-users/archive/gdr3-documentation

labeled as `classprob_dsc_combmod_quasar`. We denote this combined probability as p_{QSO} in the following sections.

A source enters the QSO candidate list if any of the three classifiers assign a probability of being a quasar above 0.5. In addition, the Gaia Quasar Classifier module (QSOC) [430, 431] estimates redshifts of quasars from their BP/RP spectra. All sources having reliable [431] estimated redshift also enter the list.

- All sources classified as AGN by the Vari module are included. This module uses photometric light curves to characterise variability.
- The Extended Objects (EO) module analyses surface brightness profiles of sources to look for physical extensions. Quasars analysed by this module are also included.
- All sources used to define the Gaia CRF3 (Celestial Reference Frame 3) [432] are included. These sources are cross-matched between Gaia and several external quasar catalogs and selected according to specific quality metrics.

This sample consists of 6,649,162 sources, of which 6,246,791 have determined proper motions, and many of them are very likely not actual quasars. This becomes obvious when we plot the proper motions of this sample, which are clearly biased by the local behavior in the Milky Way and Magellanic clouds (top left panel of Fig. 9.3. Therefore, we need to clean this sample to generate purer datasets suitable to work with.

HEALPix

It is useful to plot quantities such as proper motions or the density of sources across the sky. To do this, one of the approaches is dividing the sky in a given number of regions of the same area and color them according to the average quantity in each region. For this purpose, we used HEALPix (Hierarchical Equal Area isoLatitude Pixelization)[4], which is one of the most standardized algorithms to tessellate the sky and it has a Python implementation named *healpy* [433, 434]. The HEALPix system initially divides the sky in 12 equal-area cells with their centers forming a dodecahedron. Then, each extra level of refinement subsequently divides every cell in 4 equal-area parts, amounting to $12n^2$ total cells in the refinement level n. This scheme is illustrated in Fig. 9.1. As can be seen in this figure, the points are distributed in equal-latitude levels, hence the *isoLatitude* in the acronym.

Given a HEALPix level, each cell is assigned an index. Therefore, we just need to know to which cell every source belongs to, and then average the desired quantity (or sum, when plotting the number of sources) of all sources in a given cell. This is a way to compress data, which can also be used for analysis purposes as proposed in [408]. Here, however, we will only use it for visualization purposes.

All the plots will be shown in Galactic coordinates, so that the horizontal axis is aligned with the Galactic plane, and using *HEALPix* level 8.

[4] https://healpix.sourceforge.io

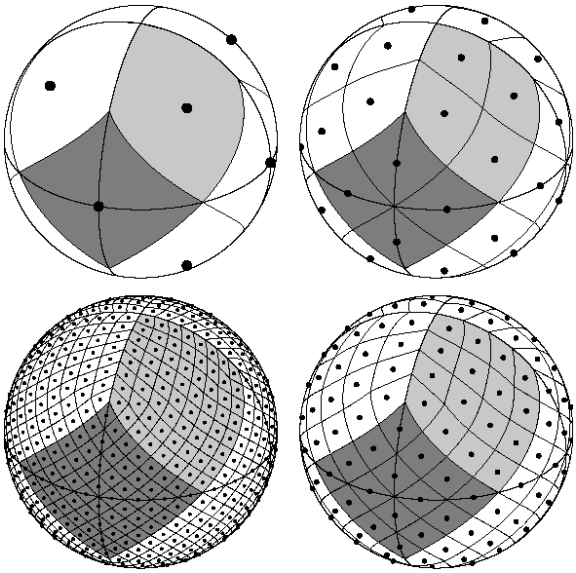

Figure 9.1: Illustration of Healpix levels 1 to 4, corresponding to 12, 48, 192 and 768 pixels, respectively. Credit: Gorski et al. [434]

9.2.2 Filtering and masking

Our first approach to increase the purity of our dataset was to set a threshold in p_{QSO}. We generically refer to this procedure as *filtering*. A low threshold will leave too many non-QSO sources, while a too high threshold may remove too many of the good ones. Therefore, we need to find a correct balance between these two effects.

Given that every source i has a probability $p_{\mathrm{QSO,i}}$ of being a quasar, we can consider it behaves as a Bernoulli distribution. Therefore, its expected value will be $p_{\mathrm{QSO,i}}$. The expected value of the joint distribution of all the sources in a sample of size N will give an estimation of its number of quasars. If we assume that all the sources are independent, the joint expected value is the sum of each individual expected value, $\sum_i p_{\mathrm{QSO,i}}$. Therefore, we can estimate the number of non-QSO sources as $N - \sum_i p_{\mathrm{QSO,i}}$.

As the threshold in p_{QSO} gets more stringent, the resulting dataset will reduce this number of estimated non-QSO sources, as well as the number of sources. This is shown in Fig. 9.2. We decide to set our threshold to the minimum value that reduces the expected number of non-QSO sources to less than 1, as it is also shown in Fig. 9.2.

Applying this process to the QSO candidate list, the threshold in p_{QSO} was found to be 0.99999465, reducing the number of sources to 1,154,431. In the top right panel of Fig. 9.3, the resulting dataset is shown. We can still very clearly see some contamination in the Galactic plane and Magellanic clouds. Therefore, we decided to also apply a mask to this data, which was manually created to cover these areas.

In the bottom left panel in Fig. 9.3, we show the masked QSO candidate dataset, with no

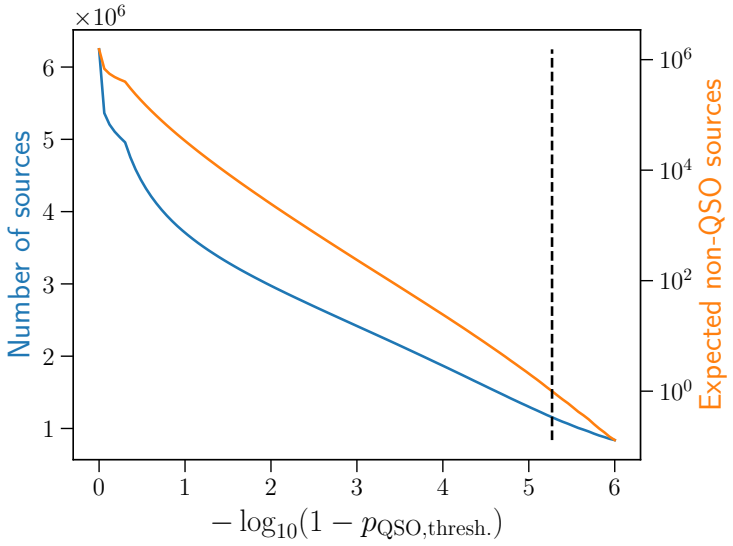

Figure 9.2: Reduction of number of sources (left vertical axis) and expected non-QSO objects (right vertical axis) with a more stringent threshold, in the filtering process for the QSO candidate list. If we denote the quantity plotted in the x axis by k, the threshold is given by $1 - 10^k$. The point where the expected non-QSO sources is 1 corresponds to the x value 5.27, indicated by the dashed, vertical line, which gives a threshold of 0.99999465.

filtering. The number of sources is reduced to 3,240,636.

In order to generate our final dataset, we first apply the mask and, to the resulting dataset, apply the filtering procedure. In the bottom right panel of Fig. 9.3, we show the result after the two-step procedure, which consists of 871,441 sources and has a threshold in $p_{\rm QSO}$ of 0.99998701. We note that this threshold is much less stringent than the previous one due to the preceding masking.

Even if this cleaning process is far from perfect, the result looks more homogeneous and does not show any obvious contamination on visual inspection. We will address the quality of this dataset in the next sections.

9.2.3 Gaia QSO selections

In addition to our masked dataset, we considered other selections suggested in [430]. This reference provides several ways to get higher purity subsamples, of which the ones we used in our article are the following ones:

(i) *Astrometric* selection: sources are accepted or discarded based on astrometry criteria. All the sources in this selection must pass two filters:

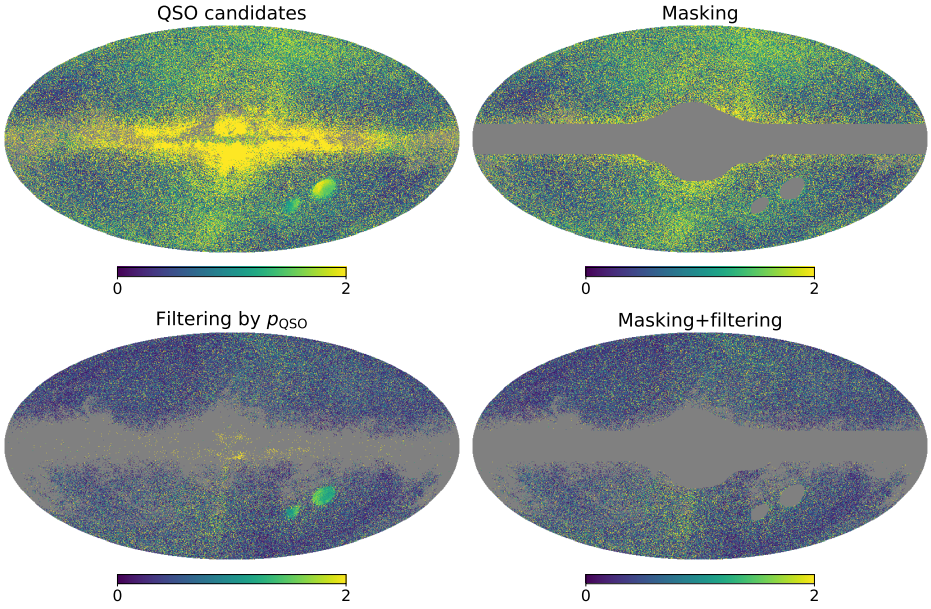

Figure 9.3: Proper motion module (in mas/yr) skymap for different steps. The top left panel shows the full QSO candidates dataset, while the others show the resulting skymap after either of the steps or both.

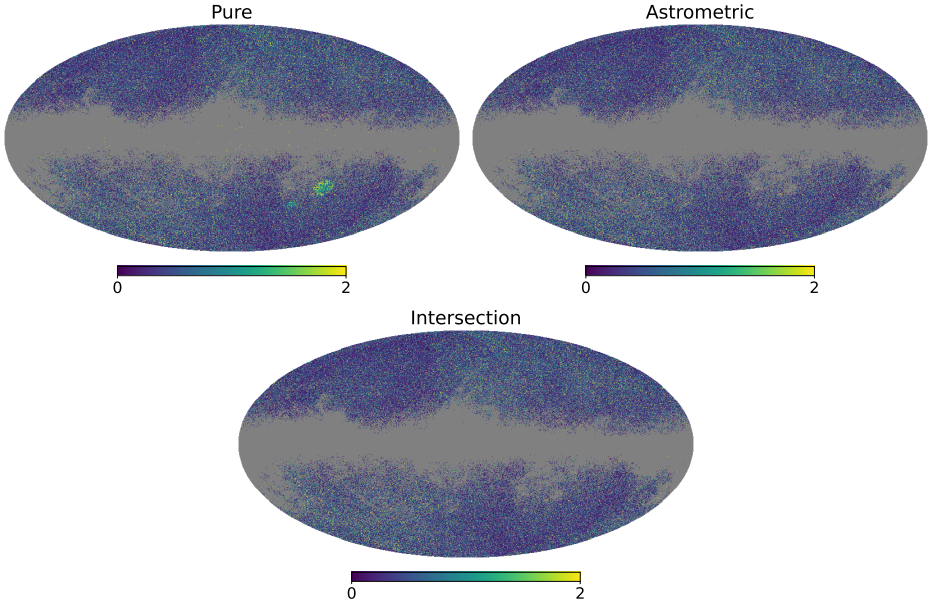

Figure 9.4: Proper motion module (in mas/yr) skymap for different considered datasets.

- First step: individual sources with high-quality astrometric solutions and statistically insignificant parallaxes and proper motions are selected. More than 200 million sources match this criteria, mostly stars from our galaxy [432].
- Second step: samples of sources with near-Gaussian distributions in uncertainty-normalized parallaxes and proper motions are selected.

(ii) *Pure* selection. This refines the criteria used to construct the QSO candidates list:

- All sources from Gaia CRF3 are included.
- Sources from EO (Extended Objects) are included except for those with close neighbours.

  The previous classifiers use lists of quasars identified by other surveys, so their samples are believed to be above 90% pure. On the other hand, the next two classifiers use supervised machine learning to discover new objects just using Gaia data.
- From the DSC sample, sources must be assigned the joint label of *quasar* by the DSC, which requires that both Specmod and Allosmod assign probabilities to be above 0.5 of being a quasar. This subset is believed to have a purity of 62%, increasing to 79% when the Galactic plane ($|b| < 11.54$ deg) is avoided.
- Sources from the Vari sample are included, given that they are considered to have a purity over 90%. These results already exclude the Galactic plane.

The astrometric selection has 1,897,754 sources and around 98% purity or better [430]. The pure one has 1,942,825 sources and a purity of 96%. Their *intersection*, which is also considered as a separate dataset, has 1,801,255 sources.

Given the high number of sources and from the p_{QSO} distribution of these datasets, we conclude there is still significant contamination from non-QSO sources (of order 400,000). Therefore, we apply the same filtering procedure as for the masked dataset, setting a threshold in p_{QSO} to reduce the expected number of non-QSO sources to one. Details on the thresholds and final numbers of sources for each dataset are provided in Table 9.1, together with the minimum constrained frequency, while skymaps are displayed in Fig. 9.4.

We can see that the three selections do a good job removing contamination from our galaxy, but the pure one does not completely remove the contamination from the Magellanic clouds. We do the fits for these three datasets as well as the masked one. However, it is clear that the cleaner dataset we have is the intersection between the astrometric and pure selections, followed by the astrometric one. Therefore, the latter are the two results which should be considered more rigorous.

Color-magnitude and color-color diagrams

In order to test the purity of our final datasets, we plotted their color-magnitude and color-color diagrams, which are shown in Fig 9.5. These diagrams are widely used in Astrophysics and plot the magnitude in some filter against the color index from two filters (color-magnitude), or a given color index against a different one (color-color). The idea of these diagrams is that, by visual inspection, we can see if there are sources which deviate substantially from the general behavior of the majority

Dataset	N	N_z	z_{25}	z_{75}	t_{25} (Gyr)	f_{25} (10^{-18} Hz)	$(1-p_{\mathrm{QSO}}^{\mathrm{min}})$ $\times 10^5$
Masked	871,441	871,438	0.961	2.408	7.52	4.21	1.299
Pure	816,641	816,640	0.967	2.374	7.54	4.20	1.924
Astrometric	786,165	786,164	0.977	2.359	7.58	4.18	1.959
Intersection	773,471	773,470	0.973	2.351	7.57	4.19	2.043
VLBA	711	657	0.57	1.63	5.50	5.76	-
VLBA+Gaia DR1	508	483	0.63	1.64	5.87	5.40	-
SDSS+Gaia EDR3	401,735	392,993	1.032	2.543	7.80	4.06	-

Table 9.1: The number of sources in each considered dataset, along with the number of sources with redshift, the 25th, 50th and 75th percentiles, the time of arrival to the source in the 25th percentile and its corresponding frequency. We also provide the thresholds in p_{QSO} for our four main datasets.

of them. If this is the case, they are likely not to be quasars, so a great number of them can impact our results.

The leftmost areas of the pure dataset diagrams, which are not present in the other datasets, confirm it as the most contaminated one. For the masked one, we can observe some outliers around $G-RP \sim -2$ and $G-RP \sim 5-6$ (see Sec. 9.1 for the filter definitions), but they represent a very small number compared to the O(800,000) total sources. Finally, the astrometric and intersection datasets are clearly the purest, although there are still sources which can be considered outliers at low and high values of the color index $G-RP$. In any case, they are again very few compared to the number of sources, so they are unlikely to bias our results. Therefore, we conclude that our cleaning process is enough. Additional steps we could have applied include setting thresholds in these magnitudes and color indices or in redshift, but based on the plots, we considered them to be unnecessary.

9.3 Other datasets

Given the similarities of our analysis with the ones done by [140] and [407], we also analyzed their datasets to check their results and to test the consistency of our methodology.

Darling et al. [140] use the VLBA catalog in [435] excluding two sources with very high proper motion, which leaves a dataset with 711 sources. This survey monitors radio sources, of which the ones considered in [140] are confirmed quasars. We considered the same sources, with the proper motions published in [435]. In [140], the authors obtain the proper motions from bootstrap-resampled time series, instead of taking them directly from [435], but state that the datasets should be statistically consistent.

In addition, Darling et al. consider an additional dataset based on the previous one but only for sources which have additional data in Gaia DR1. In this case, the authors consider the combined position time series between VLBA and Gaia DR1 and determine the proper motion of each source. With this, they obtain 577 sources, but they discard 69 sources due to the high coordinate offsets between both surveys, getting a dataset of 508 sources. We refer to this sample as the VLBA+Gaia DR1 dataset. The positions of the sources of the VLBA and VLBA+Gaia DR1 datasets are shown

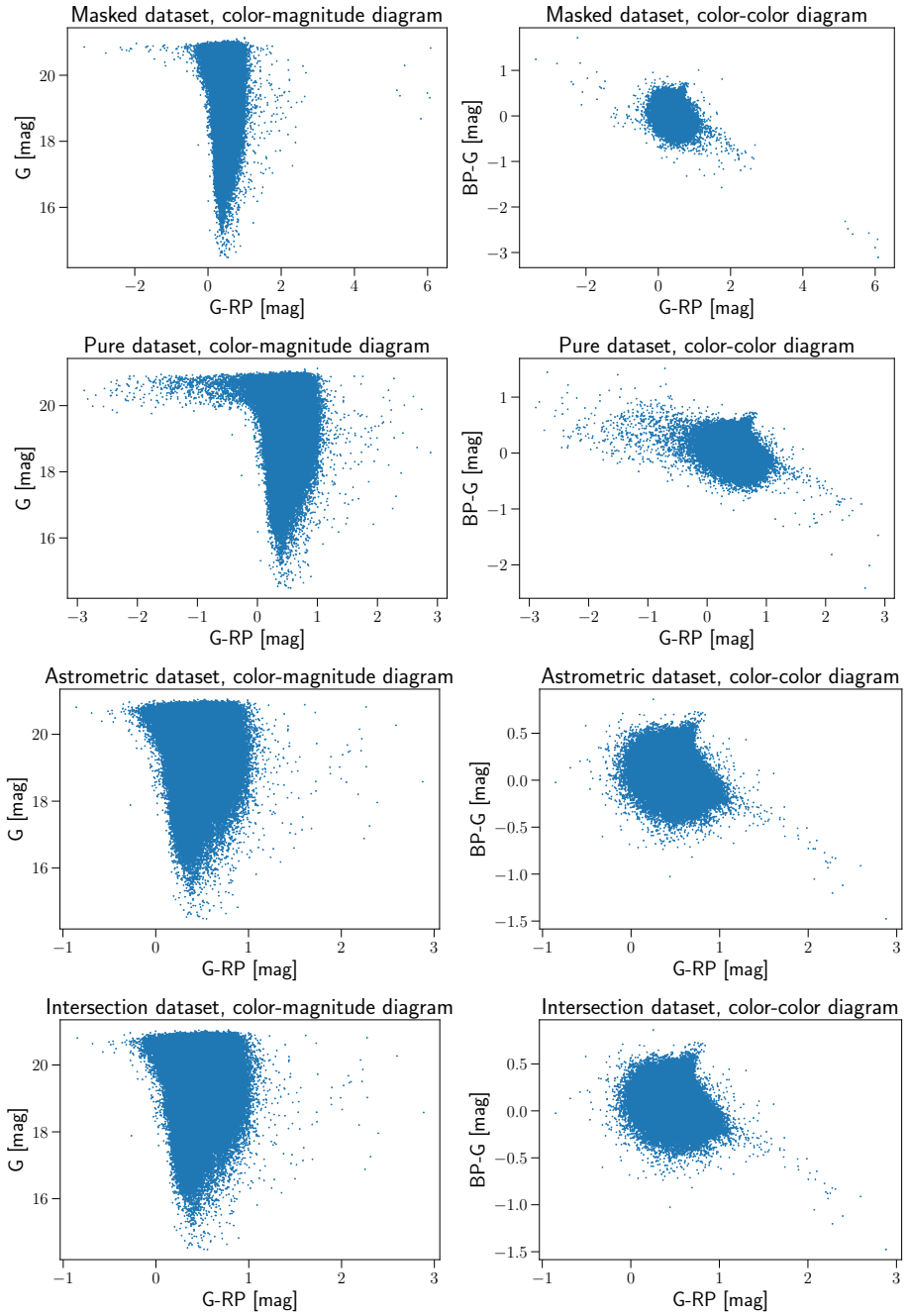

Figure 9.5: Color-magnitude (left) and color-color (right) diagrams for the different considered datasets, using the G band magnitude and its color indices with respect to the RP and BP bands.

in the right panel of Fig. 9.6.

Finally, Aoyama et al. [407] cross-match the 16th data release of the Sloan Digital Sky Survey (SDSS) QSO catalog [436] with the astrometric data in Gaia EDR3. We decided to use the SDSS+Gaia EDR3 cross-matched data provided by the Gaia collaboration[5], although we tried other methods which are detailed in the next section. Regardless, we were not able to get the exact number of sources as in [407], obtaining 401,735 with the SDSS+Gaia EDR3 cross-match. In addition, we did not apply the same filtering procedure as in previous datasets for consistency with the dataset in [407], but in any case, the filtered dataset provides similar results. A skymap of the SDSS+Gaia EDR3 dataset is provided in the left panel of Fig. 9.6.

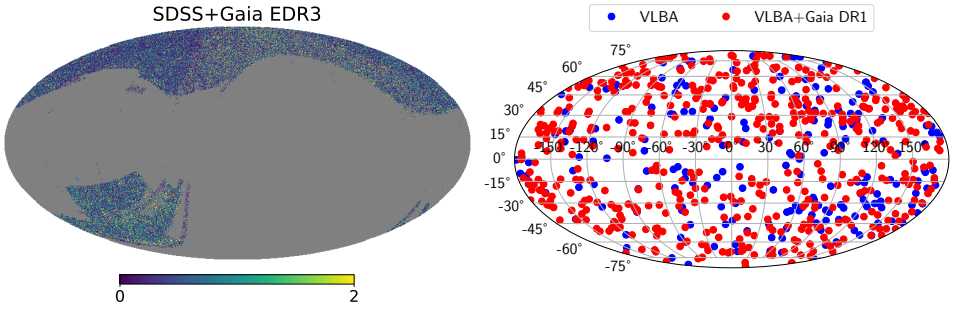

Figure 9.6: Proper motion module (in mas/yr) skymap for the SDSS+Gaia EDR3 dataset (left panel) and source position for VLBA (blue and red) and VLBA+Gaia DR1 (red) datasets (right panel).

9.4 Queries of astronomical databases

9.4.1 Gaia archive

In order to generate the previous datasets, one has to somehow get the data from Gaia. This data can be accessed with standard astronomical query tools such as TOPCAT[6] [437, 438], but it can also be accessed through the Gaia Archive[7]. Our queries will be moderately complex, so it is best to do them through the Astronomical Data Query Language (ADQL). For instance, to download the full QSO candidate dataset, we can do it like

```
SELECT *
FROM gaiadr3.qso_candidates
```

It is relevant to note that the capital letters and line jumps do not alter the query. Nevertheless, it is useful to write them following some rules for readability.

[5] Gaia EDR3 documentation: https://gea.esac.esa.int/archive/documentation/GEDR3/Catalogue_consolidation/chap_crossmatch/sec_crossmatch_externalCat/ssec_crossmatch_sdss.html

[6] http://www.starlink.ac.uk/topcat/

[7] https://gea.esac.esa.int/archive/

The list of tables, such as the `qso_candidates` one, can be checked in the leftmost part of the website, grouped by categories. This one, for instance, is under "Gaia Data Release 3/Extragalactic", and has to be accessed with the `gaiadr3` before. Once we locate the table, we can also check the available quantities, or columns. If we just want some of them instead of the full table, we can generate it like

```
SELECT classprob_dsc_combmod_quasar AS p_qso, redshift_qsoc AS z
FROM gaiadr3.qso_candidates
```

As shown in this query, one can also choose the name that will appear in the header for each variable.

We also want the positions and proper motions, with their errors. However, this information is not in the `qso_candidates` table, but in the main Gaia DR3 one, called `gaia_source` and, again, under `gaiadr3`. We therefore need to somehow establish the correspondence between our sources of interest, which are the ones in the `qso_candidates` table, and the same sources in the `gaia_source` table. We can join the information from both catalogs with the `JOIN` keyword and use the `source_id` column present in both tables to match the sources, with the keyword `ON`:

```
SELECT gaia.ra, gaia.dec, gaia.pmra, gaia.pmdec, gaia.pmra_error,
gaia.pmdec_error, qso.classprob_dsc_combmod_quasar AS p_qso,
qso.redshift_qsoc AS z
FROM gaiadr3.qso_candidates as qso
JOIN gaiadr3.gaia_source as gaia
    ON gaia.source_id=qso.source_id
WHERE gaia.pmra IS NOT NULL
AND gaia.pmdec IS NOT NULL
```

In the two last lines, we used the `WHERE` keyword to add the condition that the proper motions must be determined, since we are not interested in the sources without this information. This reduces the number of sources from 6,649,162 to 6,246,791, as was mentioned in the previous section. The previous query was the one used to generate the QSO candidate dataset we used for masking and filtering in the last section. Except for the mask, the masked dataset can be generated by imposing the threshold condition, with the extra line

```
AND qso.classprob_dsc_combmod_quasar>0.99998701
```

In order to generate the astrometric selection that Gaia provides [430], the boolean flag `astrometric_selection_flag` is included as a column in the `qso_candidates` table. Therefore, to generate our astrometric dataset, we just need to include the condition that this flag is true and use the threshold indicated in the last section,

```
SELECT gaia.ra, gaia.dec, gaia.pmra, gaia.pmdec, gaia.pmra_error,
gaia.pmdec_error, qso.classprob_dsc_combmod_quasar AS p_qso,
qso.redshift_qsoc AS z
FROM gaiadr3.qso_candidates as qso
```

```
JOIN gaiadr3.gaia_source as gaia
    ON gaia.source_id=qso.source_id
WHERE gaia.pmra IS NOT NULL AND gaia.pmdec IS NOT NULL
AND qso.astrometric_selection_flag='true'
AND qso.classprob_dsc_combmod_quasar>0.99998044
```

The pure selection involves several conditions that Gaia provides in [430]. With our threshold in p_{QSO} already applied, we can generate the dataset with the following query:

```
SELECT gaia.ra, gaia.dec, gaia.pmra, gaia.pmdec, gaia.pmra_error,
gaia.pmdec_error, qso.classprob_dsc_combmod_quasar AS p_qso,
qso.redshift_qsoc AS z
FROM gaiadr3.qso_candidates as qso
JOIN gaiadr3.gaia_source as gaia
    ON gaia.source_id=qso.source_id
WHERE gaia.pmra IS NOT NULL AND gaia.pmdec IS NOT NULL
AND (qso.gaia_crf_source='true' OR qso.host_galaxy_flag<6
OR qso.classlabel_dsc_joint='quasar' OR qso.vari_best_class_name='AGN')
AND qso.classprob_dsc_combmod_quasar>0.9999808
```

Finally, the intersection dataset can be generated combining the conditions from the previous two tables, setting the p_{QSO} threshold accordingly:

```
SELECT gaia.ra, gaia.dec, gaia.pmra, gaia.pmdec, gaia.pmra_error,
gaia.pmdec_error, qso.classprob_dsc_combmod_quasar AS p_qso,
qso.redshift_qsoc AS z
FROM gaiadr3.qso_candidates as qso
JOIN gaiadr3.gaia_source as gaia
    ON gaia.source_id=qso.source_id
WHERE gaia.pmra IS NOT NULL AND gaia.pmdec IS NOT NULL
AND qso.astrometric_selection_flag='true'
AND (qso.gaia_crf_source='true' OR qso.host_galaxy_flag<6
OR qso.classlabel_dsc_joint='quasar' OR qso.vari_best_class_name='AGN')
AND gaia.classprob_dsc_combmod_quasar>0.9999796
```

9.4.2 Cross-matching catalogs

Generating the dataset based on Aoyama et al. [407] is a bit more complicated, since it involves another catalog. They considered the 16th data release of the SDSS quasar catalog [436] and cross-match with Gaia to obtain the proper motions of as many SDSS quasars as possible. We did not manage to reproduce the number of sources they claim, among other things, because the number of sources of the SDSS QSO catalog is 750,414, while they quote 817,402. As a result, some discrepancy between our final datasets is expected. In any case, we tried our best to recreate their dataset by following two different methods.

Custom cross-match

In order to get the correspondence between the SDSS catalog and Gaia, one of the options would be to generate the cross-match ourselves. For this purpose, we download the coordinates of all the sources in the SDSS catalog. Then, in the Gaia Archive, we upload this table, that we denote as `sdss_coords` and select the option to cross-match it with another table, which will be the `gaia_source` from EDR3. The reason to choose EDR3 over DR3 is that DR3 was not released at the time of Aoyama et al. paper, but in principle they should be equivalent. The only thing that should difference DR3 from EDR3 are the additional tables, not changes to the existing ones.

We provide 0.5 arcsec as the maximum radius allowed for the cross-match, which is the one used in [407], and the website generates a new table, which we will call `xmatch`, with three columns: the Gaia object identifier, the cross-matched identifiers in our SDSS catalog and the angular separation between their coordinates. Since the SDSS catalog was a user-uploaded table, their identifiers are just the line number of the corresponding source, and they are labeled `sdss_coords_oid`. With this method, the cross-matched sources are 489,392. We can then obtain their proper motions and remove the sources which do not have any with the following query:

```
SELECT gaia.ra, gaia.dec, gaia.pmra, gaia.pmdec, gaia.pmra_error,
gaia.pmdec_error
FROM user_sjaraba.sdss_coords AS sdss_coords,
gaiaedr3.gaia_source AS gaia, user_sjaraba.xmatch AS xmatch
WHERE (xmatch.sdss_coords_sdss_coords_oid = sdss_coords.sdss_coords_oid
AND xmatch.gaia_source_source_id = gaia.source_id)
AND gaia.pmra IS NOT NULL AND gaia.pmdec IS NOT NULL
```

In this query, we also showcase an alternative to the use of `JOIN` and `ON` to combine tables, just using `FROM` and `WHERE`. They are completely equivalent.

The resulting table has 402,334 sources, which does not quite match the 400,894 in [407], but is close enough. In any case, we decided to use another method to cross-match the sources.

Cross-match provided by Gaia

In addition to the cross-match tools of the Gaia Archive, Gaia DR3 provides some tables cross-correlating Gaia sources to other catalogs. One of these catalogs is SDSS DR13 [439], which may lack some data which is present in DR16, but we considered it good enough. There are several of these tables per catalog, among which there is one including all the *good neighbours* (which may include duplicates), defined as "nearby objects in the external catalogue whose position is compatible (within position errors) with the Gaia target", and one indicating only the *best neighbours*, which only takes the best of the good neighbours, according to "the ratio between two opposite models/hypotheses: the counterpart candidate is a match or it is found by chance". We use the latter to avoid duplicates. With this, we upload a table with the identifiers of the SDSS DR16 quasar catalog, which we denote as `sdss_qso`, so that we can generate our table as

```
SELECT gaia.ra, gaia.dec, gaia.pmra, gaia.pmdec, gaia.pmra_error,
gaia.pmdec_error
```

```
FROM user_sjaraba.sdss_qso as sdss
JOIN gaiaedr3.sdssdr13_best_neighbour as gaia_xmatch
    ON sdss.col__objid=gaia_xmatch.original_ext_source_id
JOIN gaiaedr3.gaia_source as gaia
    ON gaia_xmatch.source_id=gaia.source_id
WHERE gaia.pmra IS NOT NULL AND gaia.pmdec IS NOT NULL
```

The result consists of 401,735 sources, which, again, do not exactly match neither the 400,894 in [407] nor the 402,334 from our previous method, but the numbers are really close.

It is important to note that some of these sources, both in the previous case and this one, may not even belong to the QSO candidate sample. This is because we have not used this information, given that it was only released in DR3. If we use it, we can check there are 935 of these sources using this second method, from which we cannot therefore extract quantities like p_{QSO} or the redshift.

9.4.3 VLBA-based datasets

The datasets used by Darling et al. [140] are based on VLBA, so we cannot find them using the Gaia Archive, as we have been doing until now. However, we can use the Table Access Protocol (TAP) via the interface we prefer, such as TOPCAT [437, 438] or some Python packages, for instance. With this, we can access the astronomical databases, including the one from Gaia we have been using until now, but this time not limited to it.

First, we look for the VLBA dataset. In [140], the authors state that their catalog is based on the one in [435]. The proper motions in [140] are obtained from bootstrap-resampled time series, but the authors confirm that these values should be statistically consistent with those in [435], so we take the proper motions directly from this source. In order to find this dataset, we can look for it using the TAP from TOPCAT and searching for the names of the authors. The dataset we look for appears with the title of the article [435], and is labeled as "J/ApJS/233/3/table6". We can do similar queries to the previous cases in Gaia, only that the columns are denoted differently. In addition, in this case, all the sources have proper motions, but in [140], they reject those having proper motions higher than 1 mas/yr. We therefore impose the same condition, taking into account that the proper motion units are given in μas/yr, unlike in the Gaia database:

```
SELECT RAJ2000, DEJ2000, pmRA, pmDE, e_pmRA, e_pmDE, z
FROM "J/ApJS/233/3/table6"
WHERE pmRA*pmRA+pmDE*pmDE<1000000
```

With this, we recover the 711 sources mentioned in [140]. The second dataset they used is given by a cross-match with Gaia DR1, which initially produces 577 sources and can be found labelled as "J/ApJ/861/113/table7". However, when the difference between the proper motions of a given source in either of the coordinates is higher than 3 sigma, the authors decide to exclude it for their analysis. Given that they provide these offsets in sigma units, it is straightforward to write the query to generate the dataset:

```
SELECT RAJ2000, DEJ2000, "pmRA-2", "pmDE-2", "e_pmRA-2", "e_pmDE-2"
FROM "J/ApJ/861/113/table7"
```

```
WHERE dpmRA<3 AND dpmDE<3
```

With this query, we recover the 508 sources mentioned in [140]. The quantities `pmRA-1` and `pmDE-1` provide the proper motions from VLBA, while the ones labeled as `pmRA-2` and `pmDE-2` include the contribution from Gaia DR1. Therefore, we take the latter. The redshift information is not included in this table, but it can be obtained from the previous one by matching the sources, either by coordinates or identifier. A quick way to obtain the table with the redshift is the following one:

```
SELECT vlba_gaia.RAJ2000, vlba_gaia.DEJ2000, vlba_gaia."pmRA-2",
vlba_gaia."pmDE-2", vlba_gaia."e_pmRA-2", vlba_gaia."e_pmDE-2", vlba.z
FROM "J/ApJ/861/113/table7" as vlba_gaia
JOIN "J/ApJS/233/3/table6" as vlba
    ON vlba.Name=vlba_gaia.Name
WHERE vlba_gaia.dpmRA<3 AND vlba_gaia.dpmDE<3
```

Chapter 10

SGWB constraints from Gaia DR3

10.1 Introduction

The constraining potential of the Gaia mission has been a topic of discussion from before its launch in 2013. In [403], the authors estimated its constraining power to $\Omega_{\rm GW} \lesssim 10^{-6}$ based on Eq. (8.86) with $N \approx 10^6$ sources, an angular resolution $\Delta\theta \sim 10$ μas and an observing period $T \approx 1$ year. There were also more optimistic works like [411] in which it was claimed that, by the end of the mission, Gaia could get to $\Omega_{\rm GW} \lesssim 10^{-8}$, by assuming $N \approx 10^9$, $\Delta\theta = 1$ mas and $T = 20$ years. On the opposite side, a prediction based on mock data from a quasar catalog relaxed this limit to $\Omega_{\rm GW} \lesssim 6 \times 10^{-4}$ [140], which better matches our results.

In this chapter, I will explain our article [4] in which we set constraints using real Gaia data, from its third data release. The topic is interesting as a follow-up of the mentioned works, but it is also physically meaningful from the perspective of the possible sources which would contribute to the constrained frequencies ($10^{-18} - 10^{-8}$ Hz). On the astrophysical side, super massive BBH would be the main source in this range [440, 441], but also cosmological sources would leave an imprint, such as cosmic strings [442, 443], phase transitions [444, 445] and PBHs [93, 81, 281]. The advantage of this frequency band is that it partly overlaps with the PTA range [446, 8, 9, 385], which has a better constraining power. Therefore, the sources detected from PTA will likely be found with astrometry much later, which will help better characterizing them. However, since the overlap is only partial, as was already discussed in Chap. 8, other different sources can also be found in the wider frequency range, whenever the sensitivity allows for it.

In Chap. 8, we have already explained the main formalism and part of our methodology. In Chap. 9, we have also detailed the datasets we used in the article. Therefore, all that remains is to explain the rest of our methodology before showing and discussing the results.

10.2 Data analysis

10.2.1 Likelihood

In our article [4], following [447], we use a slightly different likelihood than the standard, Gaussian one which is widely used and was explained in Subsec. 2.3.1. The reason is that the least-squares method is very sensitive to outliers, which can then bias the result significantly. This was good enough for the analyses of Chapters 2 and 3 but, despite our cleaning efforts, there might still be some outliers in our datasets. Therefore, we take the conservative approach of assuming that the experimental uncertainties are only trustworthy as lower bounds of the real one. This does not necessarily mean we do not trust the uncertainties derived by the Gaia collaboration, but rather, that there might be non-negligible intrinsic proper motions in some cases which may bias our results if we are not cautious enough. Following [448], we present the reasoning for a single 1-dimensional data point and then extend it for an arbitrary number of 2D points, as it is the case for proper motion data.

We denote our data point by D, which has an associated error $\sigma_0 > 0$. The value of our model will be given by $M(p)$, where p is a parameter of arbitrary dimension of the model function M. We consider the real error σ to be modelled by a random distribution in the domain $\sigma \geq \sigma_0$. One of the simplest models we can assume is a power law proportional to σ^{-2}, which is the first integer order for which the integral to infinity converges. Therefore, after normalization,

$$P(\sigma|\sigma_0) = \frac{\sigma_0}{\sigma^2}, \quad \sigma \in [\sigma_0, \infty). \tag{10.1}$$

We will therefore have to marginalize over this probability in order to get our likelihood,

$$P(D|M, \sigma_0, p) = \int_{\sigma_0}^{\infty} P(D|M, \sigma, p) P(\sigma|\sigma_0) d\sigma. \tag{10.2}$$

Substituting a Gaussian likelihood for $P(D|M, \sigma, p)$, using the change of variable $u = 1/\sigma$ and denoting $R \equiv (D - M(p))/\sigma_0$ for brevity, we get

$$P(D|M, \sigma_0, p) = \int_{\sigma_0}^{\infty} \frac{\sigma_0}{\sigma^2} \frac{1}{\sqrt{2\pi}\sigma} e^{-\frac{1}{2}\left(\frac{D-M(p)}{\sigma}\right)^2} d\sigma = \frac{\sigma_0}{\sqrt{2\pi}} \int_0^{1/\sigma_0} u e^{-\frac{1}{2}(\sigma_0 R u)^2} du \tag{10.3}$$

$$= \frac{1}{\sqrt{2\pi}\sigma_0} \left[-\frac{1}{R^2} e^{-\frac{1}{2}(\sigma_0 R u)^2} \right]_0^{1/\sigma_0} = \frac{1}{\sqrt{2\pi}\sigma_0} \left[\frac{1 - e^{-R^2/2}}{R^2} \right] \tag{10.4}$$

If we extend this result to a 1D dataset of size N, we would get N independent distributions for σ_i, dependent on their corresponding $\sigma_{0,i}$, that would be marginalized with N integrals similar to the one-point case. Given that the likelihood is an exponential of the sum of residuals, we can divide it in separate factors which are integrated independently, obtaining a product of factors of the form in Eq. (10.4). Therefore, the log-likelihood would be

$$\ln \mathcal{L} = \text{const.} + \sum_{i=1}^{n} \ln \left[\frac{1 - e^{-\rho_i^2/2}}{\rho_i^2} \right] \tag{10.5}$$

where, for a 2D dataset as one consisting of proper motions, the residual ρ_i can be computed as in Eq. (8.189).

If there are significant outliers, a likelihood like the one in Eq. (10.5) can drastically improve the fit. This can be observed in Fig. 10.1, which shows the difference of behaviors between the least-squares and permissive fit approaches for a well-behaved case and one with significant outliers. However, even if the likelihood in Eq. (10.5) recovers the least-squares solution for a well-behaved case, it also broadens its posteriors, around a factor 50% according to [448]. In fact, one can easily check that, for small ρ_i, one recovers

$$\ln \mathcal{L} \approx \text{const.} - \sum_{i=1} \frac{\rho_i^2}{4}, \tag{10.6}$$

which corresponds to the Gaussian likelihood with errors multiplied by $\sqrt{2}$. This broadening of the posteriors is expected from the assumption on the experimental errors in Eq. (10.1). In the end, it is up to the analyst to decide whether this behavior is compensated by the improvement of the outlier exclusion or not, which will depend on the nature of the dataset. In our case, we decide to use it, both to be more conservative with our constraints and to match the existing literature [140].

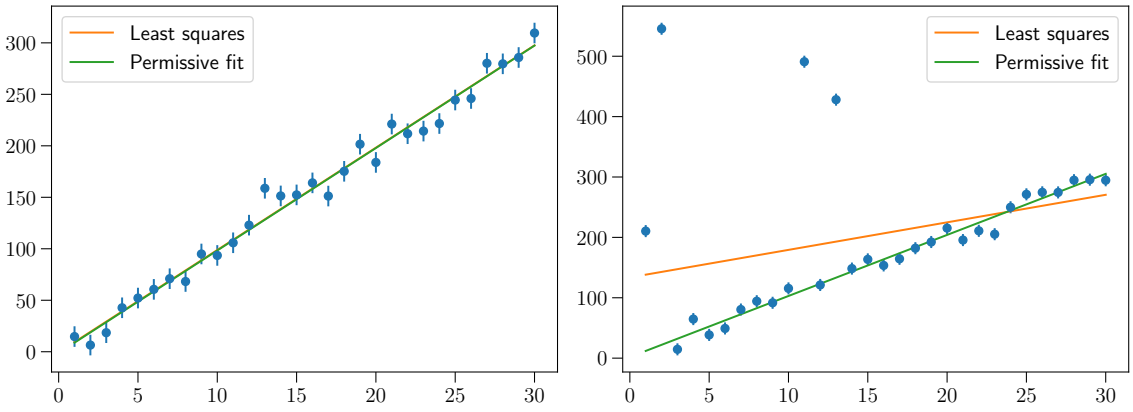

Figure 10.1: Difference of behaviors of the usual, least-squares method and the permissive fit given by the likelihood in Eq. (10.5). The left panel shows a well-behaved case, where both approaches coincide. The right panel shows a case with some outliers that bias the least-squares method, which do not significantly impact the permissive fit approach.

10.2.2 Parameter estimation

Using Eq. (10.5), we run our parameter estimation with the *emcee* sampler [131], which does an MCMC over the data. We jointly fit the dipole and quadrupole with the decomposition in the form (8.135), which makes a total of $n = 16$ parameters. For all of them, we set uniform priors in the $[-100, 100]$ μas/yr range, and we use $10n = 160$ walkers. In order to confirm the convergence, we compute the autocorrelation times [133] and run the MCMCs for at least a hundred times the shorter autocorrelation time, which was usually around 20,000 iterations.

From the posteriors, we derive the 95% credible level upper bound for $\Omega_{\rm GW}$, as well as compute its Z-score from Eq. (8.200) to address its statistical significance. Also, we plot the difference distributions discussed in Subsec. 8.8.1 in Fig. 10.2, for the astrometric dataset.

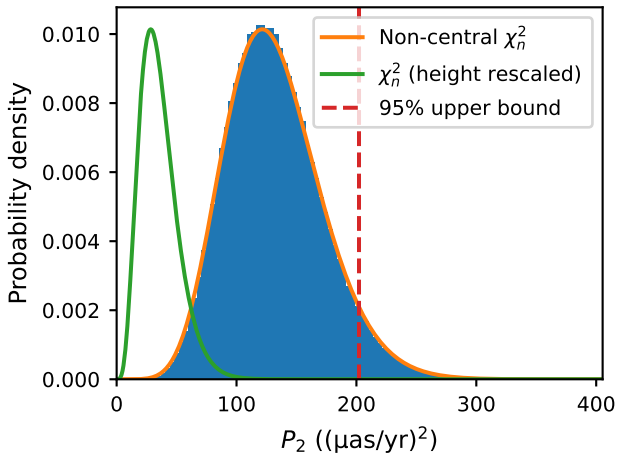

Figure 10.2: Posterior distribution for the quadrupole power P_2 for the astrometric dataset, with the corresponding chi-square and non-centered chi-square distributions superimposed.

In addition, we also compute the Bayes factors by assuming Gaussian posteriors, which is a good approximation in this case, following the formalism explained in Subsec. 2.3.3. From these posteriors, we get the maximum likelihood $\mathcal{L}_{12}$ and covariance matrix Σ_{12}. As our null hypothesis, we suppose an only-dipole case and use for the likelihood $\mathcal{L}_1$ the one computed from the dipole of our maximum likelihood estimate. As covariance matrix, we use the $(l = 1, l = 1)$ submatrix $\Sigma_1 \subset \Sigma_{12}$. From Eq. (2.81), the Bayes factor can be computed as

$$\mathcal{B}_1^{12} \approx \frac{\mathcal{L}_{12}}{\mathcal{L}_1} \left(\frac{\sqrt{2\pi}}{2L}\right)^{n_{12}-n_1} \left(\frac{\det(\Sigma_{12})}{\det(\Sigma_1)}\right)^{1/2}, \tag{10.7}$$

where L is the posterior half-width, $L = 100$ μas/yr.

We run this procedure over all the datasets described in Chapter 9. The one based on Gaia DR3 that we trust for our final constraints is the intersection one, but we also derive the constraints for the other three as control cases, to check that our constraints are robust under dataset choice. In addition, we also run them for the additional datasets described in this chapter: VLBA, VLBA+Gaia DR1 and SDSS+Gaia DR3. For all the datasets, the minimum frequencies were indicated in Table 9.1, while the maximum ones are given by the inverse of the observing period. For the Gaia DR3-based cases, this frequency is $f_{\rm max} \approx 1.1 \times 10^{-8}$ Hz ($T = 2.84$ years), while for the VLBA-based cases, it is $f_{\rm max} \approx 1.4 \times 10^{-9}$ ($T = 22.2$ years).

10.3 Results

The main results of our article are presented in Table 10.1, which shows the fitted total power of the quadrupole moment, Z scores for $l = 2$ (Z_2), Bayes factors $\mathcal{B}_1^{12}$ between the dipole+quadrupole and only dipole hypotheses, the best-fit $\Omega_{\rm GW}$ value corresponding to the quadrupole power, and the 95% upper bound on $\Omega_{\rm GW}$.

Dataset	$\sqrt{P_2}$ (μas/yr)	Z_2	$\ln \mathcal{B}_1^{12}$	$h_{70}^2\Omega_{\rm GW}$	$h_{70}^2\Omega_{\rm GW}^{\rm up}$ (95%)
Masked	12.51(1.81)	4.19	-17.2	0.069(0.021)	0.114
Pure	23.15(2.01)	10.21	34.4	0.235(0.040)	0.295
Astrometric	10.13(1.73)	3.10	-23.2	0.045(0.017)	0.089
Intersection	9.53(1.73)	2.68	-23.5	0.040(0.017)	0.087
VLBA	2.73(1.23)	-1.93	-42.3	0.0033(0.0056)	0.024
VLBA+Gaia DR1	5.30(1.36)	0.57	-14.7	0.0123(0.0077)	0.034
SDSS+Gaia EDR3	52.48(10.88)	4.70	69.6	1.21(0.54)	2.43

Table 10.1: The total quadrupole power obtained from the dipole+quadrupole fits, together with the Z score corresponding to the quadrupole, the Bayes factor between the dipole+quadrupole and only dipole hypotheses, and the $\Omega_{\rm GW}$ estimations (best-fit and 95% CL upper limit values). The values correspond to the maximum likelihood estimates and the 1-sigma errors are provided in brackets.

In addition, the fitted multipole coefficients for our four main datasets are presented in Table 10.2, as well as the vector field for the intersection dataset in Fig. 10.3. In App. D, I also include the corner plots showing the posterior distribution of the multipole coefficients, as well as the posteriors of $\Omega_{\rm GW}$ for all datasets. We also show the full correlation matrices for all runs.

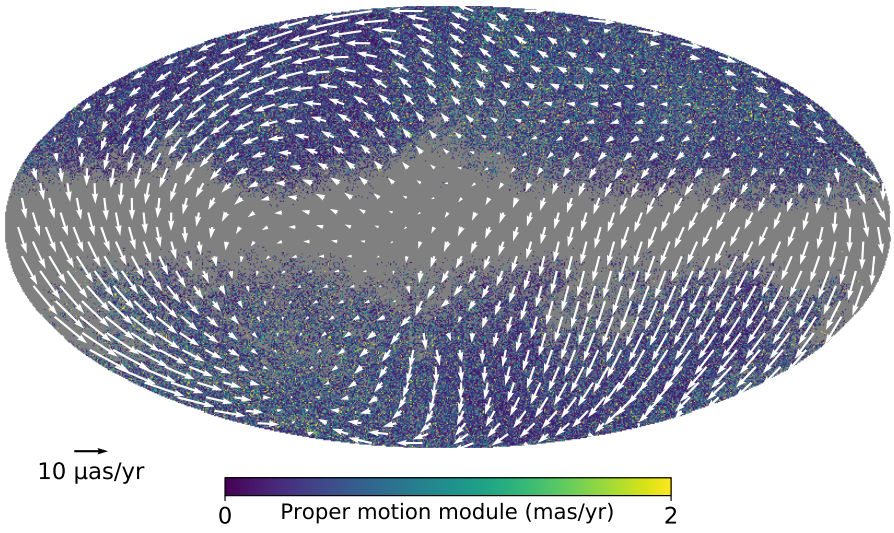

Figure 10.3: Fitted vector field skymap for the intersection dataset.

	Masked	Pure	Astrometric	Intersection
s_{10}	-39.92(1.92)	-4.40(1.89)	-5.72(1.89)	-4.79(1.88)
s_{11}^{Re}	11.92(1.49)	4.64(1.44)	0.31(1.46)	0.18(1.44)
s_{11}^{Im}	3.74(1.45)	-6.02(1.42)	-8.86(1.43)	-9.06(1.42)
t_{10}	-14.01(2.09)	-5.81(2.04)	-0.31(2.04)	-0.20(2.06)
t_{11}^{Re}	-14.19(1.44)	-6.48(1.39)	-1.57(1.38)	-1.60(1.41)
t_{11}^{Im}	5.91(1.33)	9.96(1.29)	3.74(1.30)	3.41(1.31)
$\sqrt{P_1^s}$	43.65(1.91)	11.60(1.70)	13.78(1.88)	13.68(1.74)
$\sqrt{P_1^t}$	25.86(2.12)	17.78(1.96)	5.75(1.80)	5.32(1.82)
$\sqrt{P_1}$	50.74(2.13)	21.23(1.99)	14.93(1.95)	14.68(1.94)
s_{20}	3.84(1.88)	-8.65(1.81)	-5.79(1.81)	-5.15(1.82)
s_{21}^{Re}	-0.85(1.28)	-8.33(1.24)	2.29(1.24)	2.10(1.24)
s_{21}^{Im}	5.16(1.37)	-0.91(1.33)	1.85(1.33)	1.91(1.34)
s_{22}^{Re}	2.15(1.40)	4.49(1.37)	-0.65(1.38)	-0.50(1.37)
s_{22}^{Im}	1.77(1.41)	5.29(1.38)	2.63(1.37)	2.01(1.38)
t_{20}	5.25(1.98)	-1.69(1.94)	3.63(1.93)	3.74(1.95)
t_{21}^{Re}	-1.09(1.39)	3.40(1.36)	-0.29(1.35)	0.72(1.36)
t_{21}^{Im}	3.59(1.43)	-6.74(1.41)	1.72(1.41)	1.84(1.41)
t_{22}^{Re}	-1.59(1.32)	-7.16(1.29)	-2.56(1.29)	-2.82(1.29)
t_{22}^{Im}	-2.33(1.34)	-1.52(1.31)	1.52(1.30)	0.97(1.31)
$\sqrt{P_2^s}$	9.21(1.86)	17.65(1.97)	8.10(1.63)	7.15(1.70)
$\sqrt{P_2^t}$	8.46(2.02)	14.97(2.25)	6.08(1.80)	6.28(2.01)
$\sqrt{P_2}$	12.51(1.81)	23.15(2.01)	10.13(1.73)	9.53(1.73)

Table 10.2: Fitted multipole coefficients, in μas/yr, for the four main considered datasets. The values correspond to the maximum likelihood estimates and the 1-sigma errors are provided in brackets.

We first take a look at the statistical significance of our results. Most of the datasets show Z-scores above 2.5, which can be interpreted as sigma deviations (see Sec. 8.8.1). This means there is more than just pure isotropic Gaussian noise in them, but does not necessarily imply a detection. Indeed, these numbers can be explained by biases in the datasets, such as contamination of intrinsic proper motions. This point is reinforced by the fact that our pure dataset, which is the most contaminated one, especially by the Magellanic clouds, has the highest Z score.

The Bayes factors can be interpreted in a similar way. In general, they disfavour the quadrupole detection, except for the pure dataset and the SDSS+Gaia EDR3, in which cases the quadrupole arises from the contamination and inhomogeneity of the datasets. In fact, the SDSS+Gaia EDR3 case shows strong dipole-quadrupole correlations, as can be seen in Appendix D (Fig. D.4), which makes the Bayes factor computation unreliable. Furthermore, for this dataset, if we take as null hypothesis the lack of any signal, the log-Bayes factor turns negative, reinforcing the idea of a non-detection.

Having established that we do not get any detection, we now turn our attention to the upper bounds. For the Gaia DR3-based datasets, our final upper bound is the one set for the intersection dataset, $h_{70}^2\Omega_{\mathrm{GW}} \lesssim 0.087$ for 4.2×10^{-18} Hz $\lesssim f \lesssim 1.1\times10^{-8}$ Hz. The rest of the cases behave as

expected: the upper bound based on the astrometric dataset is very similar, due to its similarity with the intersection dataset; the one derived from the masked dataset is within 30%, which was expected from the slightly lower purity; and the pure dataset sets a considerably higher constraint due to its contamination, but still within a factor 4. Therefore, we conclude that our results are robust under the choice of dataset, which means that our constraint of 0.087 is not likely to be lowered by using the same algorithm with a different dataset based on Gaia DR3 alone.

Another thing we notice from the results in table 10.2 is that the power in the toroidal dipole is, in general, less than the 1/4 of the one in the spheroidal dipole. While, for the higher multipoles, it is expected that both have a similar value if they come from a gravitational wave background (see Subsec. 8.7.3), a high toroidal dipole indicates a spurious rotation. The fact that toroidal dipoles are related to rotations is given by their definition, and illustrated by the $\vec{T}_{11}$ vector spherical harmonic in Fig. 8.2. Having the toroidal dipole under control is a good indication of the purity of our data. Again, the pure dataset breaks this trend due to its contamination.

With respect to the VLBA and VLBA+Gaia DR1 datasets, we get $h_{70}^2\Omega_{\rm GW} \lesssim 0.024$ for 5.76×10^{-18} Hz $\lesssim f \lesssim 1.4 \times 10^{-9}$ and $h_{70}^2\Omega_{\rm GW} \lesssim 0.034$ for 5.40×10^{-18} Hz $\lesssim f \lesssim 1.4 \times 10^{-9}$, respectively. These are more pessimistic results than the ones in [140], also for the Z-scores, due to a different implementation of the likelihood (10.5) which underestimated the errors on their side [447], as well as our simultaneous fit to the dipole and quadrupole, which they did it separately. Still, they stand as the best astrometric constraints to date.

For the SDSS+Gaia EDR3 dataset, we did not manage to reproduce the results in [407]. Given its poor sky coverage shown in Fig. 9.4 and the high correlations seen in Figs. D.3 and D.4, such a significantly higher upper bound is to be expected. For an only-quadrupole fit, this constraint is reduced to $h_{70}^2\Omega_{\rm GW} \lesssim 0.40$, which is much more reasonable, but it does not make sense to ignore the dipole with this method and, in any case, it is much higher than the results of order 10^{-4} they claim. This is likely explained by the narrow prior range they choose, although there could be other factors explained by the different methodology.

To conclude this section, we should discuss why the derived constraints from Gaia DR3 are still worse than those from VLBA. As discussed in Subsec. 8.6.1, we can use Eq. (8.86) to roughly get an expected upper bound for a mission with resolution $\Delta\theta$, observing time T and number of sources N. As we are working with proper motion, we can assume that the mean uncertainty in proper motion is roughly given by $\Delta\mu \sim \Delta\theta/T$ and rewrite

$$\Omega_{\rm GW} \lesssim \frac{\Delta\mu^2}{NH_0^2}. \tag{10.8}$$

Our Gaia DR3-based datasets have around 1000 times more sources, which is good for a constraint, but the uncertainties in proper motions are larger than in VLBA ($\langle\Delta\mu\rangle \approx 670$ μas/yr versus 20 μas/yr), compensating this effect. In addition, Eq. (10.8) assumes that all sources have a rms proper motion of order $\Delta\mu/\sqrt{N}$, which is not true neither for the Gaia DR3-based datasets nor for the VLBA datasets. Furthermore, the real numbers differ more from this hypothesis as the number of sources increases and the sky coverage is less isotropic. Both reasons make the Gaia DR3 datasets perform a bit worse overall.

10.4 Future prospects

From Gaia DR3, we have obtained the upper bound for the SGWB amplitude $h_{70}^2\Omega_{\rm GW} \lesssim 0.087$ for 4.2×10^{-18} Hz $\lesssim f \lesssim 1.1\times10^{-8}$ Hz. This is worse than the ones obtained for the VLBA-based datasets in [140], which we reanalyzed to obtain $h_{70}^2\Omega_{\rm GW} \lesssim 0.024$ for 5.76×10^{-18} Hz $\lesssim f \lesssim 1.4\times10^{-9}$ for the VLBA dataset. As has been commented, part of the worse performance from Gaia comes from its worse resolution, which partly derives from its lower observing period (2.84 years for Gaia DR3 versus 22.2 years for VLBA).

Future Gaia releases will use longer observing periods, increasing the SNR and reducing the uncertainty in proper motions. According to [425, 449], the coordinate and parallax resolution increases proportionally to $\sqrt{T}$, expecting improvement factors of 1.4 and 1.9 for Gaia DR4 (5.5 years) and DR5 (10 years), respectively. Furthermore, the proper motions increase their resolution proportionally to $T^{3/2}$, which means improvement factors of 2.7 and 6.6 for DR4 and DR5, respectively. Also, $\Omega_{\rm GW}$ decreases with the error in proper motion squared, which translates into a decrease proportional to T^3, or a 7.2 and 44 improvement factors for DR4 and DR5, respectively. Extrapolating our current constraints, this would imply constraints of order $\Omega_{\rm GW} \lesssim 0.012$ and 0.0020 for DR4 and DR5, respectively, with the maximum constrained frequencies being lowered a bit, since they are given by T^{-1}. In addition, the number of sources will likely increase, which means we will likely be able to get to 10^{-4} in the final data release.

Also, the next data releases will include the full time series of each source. This will allow to make more sophisticated analyses and, particularly, to constrain the $f \gtrsim 1/T \approx 3.2\times10^{-9}$ Hz range, as discussed in Subsec. 8.6.2.

Once Gaia finishes releasing their data, the hopes to further refine these constraints will be set in future generation astrometric missions such as Theia [450, 451]. In [411], it is proposed that Theia will improve the proper motion resolution in a factor 60 and observe 100 times more sources. Using our Eq. (10.8) and our predictions for Gaia DR5, this would imply a constraint of order 10^{-10}.

As detailed in the introduction, achieving better sensitivities is the key to constrain stochastic backgrounds such as super massive black hole binaries, cosmic strings, phase transitions and primordial black holes. This field will likely follow behind what happens in the PTA range, but it is nevertheless absolutely important to keep updating the astrometric constraints, first, for confirmation of these signals and, more importantly, to look for extra signals in the wider frequency range that neither CMB nor PTAs can reach.

Chapter 11

Conclusions

The field of Gravitational Waves is living a revolution from their first detection almost a decade ago. As a physicist, this is one of the most exciting areas to which one can contribute from a wide variety of topics and methodologies: theoretical predictions, data analysis or numerical simulations are some of the options which we explored in this thesis. The fast improvements in GW detection sensitivity, as well as the new frequency windows that new missions will probe, imply an increasingly overwhelming amount of observational data of great relevance to Astrophysics and Cosmology. From the point of view of Theoretical Physics, gravitational waves present a unique opportunity to make predictions which can be confronted with data in only a matter of years, which will surely make our understanding of the Universe drastically progress in the coming decades, similarly to how the CMB did over the last half century.

In this thesis, we have studied several aspects related to gravitational waves, in the areas of Stochastic Gravitational Wave Backgrounds, Primordial Black Holes, Numerical Relativity and Astrometry. In Chapter 1, we started with a broad introduction to GW theory, covering the main ideas of energy radiation and GW production, and applying the formalism to two-body systems, from the points of view of CBCs and hyperbolic encounters.

We continued our approach to GWs by delving into SGWBs in Chapter 2, including an introduction to parameter estimation and concluding with a review of current constraints and with a work [5] in which we constrained the SIGW background assuming non-Gaussianities. In Chapter 3, we relaxed the isotropic SGWB assumption to study the formalism for its anisotropies, concluding with a work [3] which developed a spherical-harmonic decomposition formalism and applied it to several test cases of interest.

In Chapter 4, we incorporated PBHs to the thesis, which would be relevant in subsequent chapters. The introduction to their formation mechanisms was followed by a detailed explanation on how to compute the overdensity thresholds required for the PBH collapse. This was done with a numerical approach, which served as a first contact with Numerical Relativity, with some of the concepts introduced in this section reappearing in the NR chapters. Finally, we presented the two main scenarios for BBH production, together with the merger rate in the late binary approach, which connects to the next chapter.

In Chapter 5, we computed the PBH contribution to the SGWB from their close hyperbolic

interactions, as we did in the article [2]. For reference, we applied the same procedure to the PBH contribution from BBHs, and compared both components. We discovered that introducing a redshift-dependent event rate leads to significant changes in the shape of the CHE contribution, while the BBH component is only enhanced slightly. From this fact, we concluded that a good characterization of the CHE background would lead to significant findings on the PBH clustering across the Universe, as well as their relative abundance with respect to ABHs. However, the detection prospects are more pessimistic than for the standard BBH component, although this would depend on the exact properties of PBH clusters.

In Chapter 6, we turned our attention to Numerical Relativity, with a brief introduction to the field and a broader presentation of the used software, the Einstein Toolkit, as well as some of the issues that arise in these simulations. The chapter concluded with a practical overview of the Einstein Toolkit capacities, both from a BBH simulation and three runs for black hole CHEs, showing some of the outputs that can be derived from them.

In Chapter 7, our article on spin induction from BH CHEs [1] was presented, in which we used NR simulations to characterize this effect. We studied how two initially non-spinnning black holes acquire significant spins after their interaction in a CHE, and explored the parameter space of initial momenta, incidence angles and mass ratios. In addition, we addressed some of the technical difficulties to extend these studies to lower mass ratios, illustrating it with a simulation of $q = 0.1$. From this study, we concluded that this effect is a viable mechanism for PBHs to acquire spins, which could explain GW signals generated by intermediate-mass BHs with relevant spins, such as GW190521.

We arrived to the final topic in Chapter 8, where we saw a broad introduction on how to use astrometric measurements to set constraints on the SGWB amplitude. These upper bounds are imposed on the frequency range below the nHz, where no other probe has access to. Therefore, systematic and rigorous work on this topic is required to obtain the maximum information possible from the SGWB in all frequencies. As the chapter came to the end, we shifted from the theoretical formalism to more practical considerations which are necessary to bear in mind for a data analysis work on this topic.

In Chapter 9, we gave an overview of the Gaia mission, including how to obtain some of the data, how to clean it according to different criteria and showing the necessary queries in ADQL. Finally, in Chapter 10, we used the datasets obtained in the previous chapter to set constraints to the SGWB amplitude, following our article [4]. Aside from setting constraints using Gaia data, we updated existing constraints from VLBA, as well as outlined the future prospects we expect from subsequent data releases of Gaia.

This thesis provides an overview of some of the different research areas available to the Gravitational Wave field. In doing so, it highlights my contributions to these areas during the four years of my PhD, as well as suggests some possible avenues that could be pursued in the future. Nevertheless, the field of Gravitational Waves is immersed in a constant evolution due to its drastic progress, which comes from the increasing amount of observations due to the improvements in detector sensitivity, the reports of evidences of SGWB from PTAs and the addition of new detectors in the short (KAGRA, LIGO-India) and medium (LISA, ET, CE) term, only to name a few. The future of gravitational waves is as uncertain as exciting, offering a unique framework for physicists to contribute to the scientific progress and promising to revolutionize our understanding of the Universe in the coming decades.

Conclusiones

El campo de las Ondas Gravitacionales está viviendo una revolución desde su primera detección hace casi una década. Como físico, esta es una de las áreas más apasionantes en las que se puede contribuir desde una amplia variedad de temas y metodologías: predicciones teóricas, análisis de datos o simulaciones numéricas son algunas de las opciones que exploramos en esta tesis. Las rápidas mejoras en la sensibilidad de detección de GWs, así como las nuevas ventanas de frecuencia que explorarán las nuevas misiones, implican una cantidad cada vez más abrumadora de datos observacionales de gran relevancia para la Astrofísica y la Cosmología. Desde el punto de vista de la Física Teórica, las ondas gravitacionales presentan una oportunidad única para realizar predicciones que puedan ser contrastadas con datos en solo cuestión de años, lo que seguramente hará que nuestra comprensión del Universo avance drásticamente en las próximas décadas, de manera similar a la revolución que ha causado el CMB durante el último medio siglo.

En esta tesis hemos estudiado varios aspectos relacionados con las ondas gravitacionales, en las áreas de Fondos Estocásticos de Ondas Gravitacionales, Agujeros Negros Primordiales, Relatividad Numérica y Astrometría. En el Capítulo 1, comenzamos con una amplia introducción a la teoría de GW, cubriendo las ideas principales de la radiación de energía y producción de GWs, y aplicando el formalismo a sistemas de dos cuerpos, desde el punto de vista de los CBCs y los encuentros hiperbólicos.

Continuamos nuestra aproximación a los GWs profundizando en el SGWB en el Capítulo 2, incluyendo una introducción a la estimación de parámetros y concluyendo con una revisión de los límites observacionales actuales y con un trabajo [5] en el que ponemos límites al fondo de ondas gravitacionales inducidas por escalares asumiendo no-Gaussianidades. En el Capítulo 3, relajamos el la suposición de isotropía en el SGWB para estudiar el formalismo de sus anisotropías, concluyendo con un trabajo [3] en el que desarrollamos un formalismo de descomposición en armónicos esféricos y lo aplicamos a varios casos de prueba de interés.

En el Capítulo 4, incorporamos PBHs a la tesis, dada su relevancia en capítulos posteriores. La introducción a sus mecanismos de formación ha continuado con una explicación detallada sobre cómo calcular los valores límite para la sobredensidad necesaria para producir el colapso de un PBH. Esto se ha hecho con un enfoque numérico, que ha servido como un primer contacto con la Relatividad Numérica, reapareciendo algunos de los conceptos introducidos en esta sección en los capítulos de NR. Finalmente, presentamos los dos escenarios principales para la producción de BBH, junto con los ritmos de fusión para la hipótesis de binarias tardías, lo cual conecta con el siguiente capítulo.

En el Capítulo 5, hemos calculado la contribución de los PBHs al SGWB a partir de sus inter-

acciones hiperbólicas cercanas, tal como lo hicimos en el artículo [2]. Como referencia, aplicamos el mismo procedimiento a la contribución de PBH de BBH y comparamos ambos componentes. Encontramos que la introducción de una tasa de eventos dependiente del corrimiento al rojo conduce a cambios significativos en la forma de la contribución de CHE, mientras que la componente BBH solo aumenta ligeramente. De ello concluimos que una buena caracterización del fondo de CHE conduciría a hallazgos significativos sobre las agrupaciones de PBH en todo el Universo, así como su abundancia relativa con respecto de los ABH. Sin embargo, las perspectivas de detección son más pesimistas que para la componente usual de BBHs, aunque esto dependería de las propiedades exactas de estas agrupaciones de PBHs.

En el Capítulo 6, centramos nuestra atención en la Relatividad Numérica, con una breve introducción al campo y una presentación más amplia del software utilizado, el Einstein Toolkit, así como algunos de los problemas que surgen en estas simulaciones. El capítulo concluye con una descripción práctica de las capacidades del Einstein Toolkit, tanto de una simulación BBH como de tres ejemplos para CHEs de agujeros negros, mostrando algunos de los resultados que se pueden obtener de ellos.

En el Capítulo 7, se ha presentado nuestro artículo sobre la inducción de espín a partir de CHEs de BHs [1], en el que utilizamos simulaciones de NR para caracterizar este efecto. Estudiamos cómo dos agujeros negros que inicialmente no giraban adquieren espines significativos después de su interacción en un CHE, y exploramos el espacio de parámetros de los momentos iniciales, ángulos de incidencia y cociente de masas. Además, abordamos algunas de las dificultades técnicas que surgen al extender estos estudios a cocientes de masa más bajos, ilustrándolo con una simulación con $q = 0.1$. A partir de este estudio, llegamos a la conclusión de que este efecto es un mecanismo viable para que los PBHs adquieran espines, lo que podría explicar las señales de GW generadas por BHs de masa intermedia con espines relevantes, como GW190521.

Llegamos al tema final en el Capítulo 8, donde hemos visto una amplia introducción sobre cómo usar mediciones astrométricas para establecer límites sobre la amplitud del SGWB. Estos límites superiores se imponen en el rango de frecuencia por debajo de los nHz, al que ningún otro experimento tiene acceso. Por lo tanto, se requiere un trabajo sistemático y riguroso en este tema para obtener la máxima información posible del SGWB en todas las frecuencias. Al llegar al final del capítulo, pasamos del formalismo teórico a consideraciones más prácticas que es necesario tener en cuenta para realizar análisis de datos sobre este tema.

En el Capítulo 9, se proporciona una descripción general de la misión Gaia, incluyendo cómo obtener algunos de los datos, cómo limpiarlos según diferentes criterios y mostrando las consultas necesarias en lenguaje ADQL. Finalmente, en el Capítulo 10, utilizamos los datos obtenidos en el capítulo anterior para obtener límites sobre la amplitud del SGWB, siguiendo nuestro artículo [4]. Además de establecer estos límites utilizando los datos de Gaia, actualizamos las restricciones existentes a partir de VLBA y describimos las perspectivas futuras que esperamos de las siguientes publicaciones de datos de Gaia.

Esta tesis proporciona una descripción general de algunas de las diferentes áreas de investigación disponibles para el campo de las ondas gravitacionales. Al hacerlo, se destacan mis contribuciones a estas áreas durante los cuatro años de mi doctorado, además de sugerir algunas posibles vías que se podrían explorar en el futuro. Sin embargo, el campo de las Ondas Gravitacionales está inmerso en una constante evolución debido a su drástico progreso, que proviene del creciente número de observaciones debido a las mejoras en la sensibilidad de los detectores, los informes de evidencias

de SGWB por parte de los PTAs y la incorporación de nuevos detectores en el corto (KAGRA, LIGO-India) y el medio plazo (LISA, ET, CE), solo por nombrar algunas causas. El futuro de las ondas gravitacionales es tan incierto como apasionante, que ofrece un marco único para que los físicos contribuyan al progreso científico y promete revolucionar nuestra comprensión del Universo en las próximas décadas.

Appendix A

Scalar-induced gravitational wave formalism

In this appendix chapter, we will briefly review the scalar-induced gravitational wave theory which was necessary for our article [5], explained in Sect. 2.5. This chapter is mainly taken from this article, whose formalism is based on [154, 153, 152].

We start from the perturbed metric in the conformal Newtonian gauge, which can be written as

$$ds^2 = a(\tau)^2 \left[-(1+2\Phi(\tau,\vec{x}))d\tau^2 + \left((1-2\Phi(\tau,\vec{x}))\delta_{ij} + \frac{1}{2}h_{ij}\right) dx^i\, dx^j\right] \tag{A.1}$$

where τ represents the conformal time, $\Phi(\tau,\vec{x})$ is the curvature perturbation in the Newtonian gauge and h_{ij} is the transverse traceless tensor perturbation described in Chapter 1. We neglect vector perturbations and the scalar anisotropic stress.

As we saw in Chapter 1, h_{ij} can be expanded in Fourier modes as

$$h_{ij}(\tau,\vec{x}) = \sum_{A=+,\times} \int d^3\vec{k} e^{i\vec{k}\cdot\vec{x}} e^A_{ij}(\vec{k}) h_A(\tau,\vec{k}), \tag{A.2}$$

where we take the $e^A_{ij}(\vec{k})$ basis tensors to be normalized as $e^A_{ij}e^{A'}_{ij} = \delta^{AA'}$. Note that there is a factor 2 of difference with the definition in Eq. (1.35). In addition, unlike in the rest of the thesis, we will not use a tilde to express Fourier-space quantities, to make the notation simpler.

We start by reviewing the SIGW theory for the Gaussian case.

A.1 Scalar induced gravitational waves

At the second order, the Fourier modes of a gravitational wave follow the equation of motion

$$h''_A(\tau,\vec{k}) + 2\mathcal{H}h'_A(\tau,\vec{k}) + k^2 h_A(\tau,\vec{k}) = 4S_A(\tau,\vec{k})\,, \tag{A.3}$$

where the prime denotes derivative with respect to τ, $\mathcal{H} = a(\tau)H(\tau)$ is the conformal Hubble parameter and $S_A(\tau, \vec{k})$ is a source term. In terms of the primordial curvature perturbation ζ, this source term can be expressed as

$$S_A(\tau, \vec{k}) = \int\!\!\int \frac{d^3\vec{q}}{(2\pi)^3} Q_A(\vec{k}, \vec{q}) f\left(\vec{k} - \vec{q}, q, \tau\right) \zeta(\vec{q})\zeta(\vec{k} - \vec{q}), \tag{A.4}$$

where $Q_A(\vec{k}, \vec{q})$ is a projection factor given by

$$Q_A(\vec{k}, \vec{q}) = e^A_{ij}(\vec{k}) q^i q^j, \tag{A.5}$$

where the polarization basis tensors are normalized, in this formalism, as $e^A_{ij} e^{A'}_{ij} = \delta^{AA'}$, so there is a factor 2 of difference with respect to our definitions in Eq. (1.35).

Here, we set $\vec{k}$ to be in the z direction. The source factor $f(p, q, \tau)$ appearing in Eq. (A.4), assuming radiation domination, is given by

$$f(p, q, \tau) = 3\phi(p\tau)\phi(q\tau) + \frac{d\phi(p\tau)}{d\ln(p\tau)} \frac{d\phi(q\tau)}{d\ln(q\tau)} + \left(\phi(p\tau)\frac{d\phi(q\tau)}{d\ln(q\tau)} + \frac{d\phi(p\tau)}{d\ln(p\tau)}\phi(q\tau)\right)\left(\tag{A.6}$$

where $\phi(x)$ is the linear transfer function between Φ in the Newtonian gauge and ζ

$$\Phi(\tau, \vec{k}) = \phi(k\tau)\zeta(\vec{k}). \tag{A.7}$$

In this work, we consider adiabatic scalar perturbations, so that, in the radiation-dominated era,

$$\phi(x) = -\frac{2}{3}\frac{9}{x^2} \quad \frac{\sin(x/\sqrt{3})}{x/\sqrt{3}} - \cos(x/\sqrt{3})\Bigg). \tag{A.8}$$

For isocurvature perturbations, this transfer function changes (see e.g. [452]).

Then, the equation of motion (A.3) can be solved using a Green's function, similar to the discussion for Eq. (1.19) in Chapter 1, so that

$$h_A(\tau, \vec{k}) = \frac{4}{a(\tau)} \int\!\!\int d\tilde{\tau} G_{\vec{k}}(\tau, \tilde{\tau}) a(\tilde{\tau}) S_A(\tilde{\tau}, \vec{k}), \tag{A.9}$$

with the Green's function given by

$$G_{\vec{k}}(\tau, \tilde{\tau}) = \frac{\sin k(\tau - \tilde{\tau})}{k}. \tag{A.10}$$

Substituting Eq. (A.4) into Eq. (A.9), the two-point estimator for the induced gravitational waves is

$$\langle h_A(\tau, \vec{k}_1) h_{A'}(\tau, \vec{k}_2)\rangle = \int\!\!\int \frac{d^3\vec{q}_1}{(2\pi)^3}\frac{d^3\vec{q}_2}{(2\pi)^3} Q_{A_1}(\vec{k_1}, \vec{q}_1) Q_{A_2}(\vec{k_2}, \vec{q}_2) \tag{A.11}$$

$$\times I_k\left(\vec{k}_1 - \vec{q}_1, q_1, \tau\right) I_k\left(\vec{k}_2 - \vec{q}_2, q_2, \tau\right)\left(\tag{A.12}$$

$$\times \langle\zeta(\vec{q}_1)\zeta(\vec{k}_1 - \vec{q}_1)\zeta(\vec{q}_2)\zeta(\vec{k}_2 - \vec{q}_2)\rangle, \tag{A.13}$$

with the kernel function given by

$$I_k(p, q, \tau) = 4 \int\!\!\int d\tilde{\tau}\, G_{\vec{k}}(\tau, \tilde{\tau}) \frac{a(\tilde{\tau})}{a(\tau)} f(p, q, \tilde{\tau}). \tag{A.14}$$

A.2 Gravitational waves induced by non-Gaussian curvature perturbations

Let us now consider the scalar-induced gravitational wave formalism with non-Gaussian primordial curvature perturbations. As explained in Sec. 2.5, we consider a quadratic local-type non-Gaussianity parametrized as Eq. (2.83), while the Gaussian curvature perturbation has a monochromatic spectrum given by Eq. (2.85).

We now have to substitute the non-Gaussian parametrization of ζ given by Eq. (2.83) into the two-point function in Eq. (A.9). In order to do so, we first define a dimensionless power spectrum $\mathcal{P}_{AA'}(\tau,k)$ as

$$\langle h_A(\tau,\vec{k})h_{A'}(\tau,\vec{k})\rangle \equiv (2\pi)^3\delta^3(\vec{k}+\vec{k}')\frac{2\pi^2}{k^3}\mathcal{P}_{AA'}(\tau,k). \tag{A.15}$$

This power spectrum $\mathcal{P}_{AA'}(\tau,k)$ will be the sum of seven components,

$$\mathcal{P}_{AA'}(\tau,k)=\sum_{n=1}^{7}\mathcal{P}^{(n)}_{AA}(\tau,k)\delta_{AA'}, \tag{A.16}$$

which can be computed as [154, 153]

$$\mathcal{P}^{(1)}_{AA}(\tau,k)=2\,\mathcal{I}_{AA}(\tau,\vec{k}\,|\,\vec{q},\vec{q}\,|\,\vec{q},\vec{k}-\vec{q}), \tag{A.17}$$

$$\mathcal{P}^{(2)}_{AA}(\tau,k)=2^2\,(2!F_{\rm NL})^2\mathcal{I}_{AA}(\tau,\vec{k}\,|\,\vec{q}_1,\vec{q}_2\,|\,\vec{q}_2,\vec{k}-\vec{q}_2,\vec{q}_1-\vec{q}_2), \tag{A.18}$$

$$\mathcal{P}^{(3)}_{AA}(\tau,k)=2^2\,(2!F_{\rm NL})^2\mathcal{I}_{AA}(\tau,\vec{k}\,|\,\vec{q}_1,\vec{q}_2\,|\,\vec{q}_1,\vec{q}_2,\vec{k}-\vec{q}_1-\vec{q}_2), \tag{A.19}$$

$$\mathcal{P}^{(4)}_{AA}(\tau,k)=2^2\,\frac{(2!F_{\rm NL})^2}{2!}\mathcal{I}_{AA}(\tau,\vec{k}\,|\,\vec{q}_1,\vec{q}_1\,|\,\vec{k}-\vec{q}_1,\vec{q}_2,\vec{q}_1-\vec{q}_2), \tag{A.20}$$

$$\mathcal{P}^{(5)}_{AA}(\tau,k)=2\,\frac{(2!F_{\rm NL})^4}{(2!)^2}\mathcal{I}_{AA}(\tau,\vec{k}\,|\,\vec{q}_1,\vec{q}_1\,|\,\vec{q}_1-\vec{k}+\vec{q}_3,\vec{q}_3,\vec{q}_2,\vec{q}_2-\vec{q}_1), \tag{A.21}$$

$$\mathcal{P}^{(6)}_{AA}(\tau,k)=2\,(2!F_{\rm NL})^4\mathcal{I}_{AA}(\tau,\vec{k}\,|\,\vec{q}_1,\vec{q}_2\,|\,\vec{q}_1-\vec{q}_3,\vec{q}_2-\vec{q}_3,\vec{q}_3,\vec{q}_3-\vec{k}), \tag{A.22}$$

$$\mathcal{P}^{(7)}_{AA}(\tau,k)=(2!F_{\rm NL})^4\mathcal{I}_{AA}(\tau,\vec{k}\,|\,\vec{q}_1,\vec{q}_2\,|\,\vec{q}_1-\vec{k}+\vec{q}_2-\vec{q}_3,\vec{q}_1-\vec{q}_3,\vec{q}_2-\vec{q}_3,\vec{q}_3)\,, \tag{A.23}$$

with

$$\begin{aligned}\mathcal{I}_{AA'}(\tau,\vec{k}\,|\,\vec{q}_1,\vec{q}_2\,|\,\vec{k}_1,\vec{k}_2,\cdots)=&\frac{k^3}{2\pi^2}\int\!\!\int\frac{d^3\vec{q}_1}{(2\pi)^3}\frac{d^3\vec{q}_2}{(2\pi)^3}\cdots Q_A(\vec{k},\vec{q}_1)Q_{A'}(\vec{k},\vec{q}_2)\\ &\times I_k\left(\vec{k}-\vec{q}_1\ ,q_1,\tau\right)I_k\left(\vec{k}-\vec{q}_2\ ,q_2,\tau\right)P_g(k_1)P_g(k_2)\ldots,\end{aligned} \tag{A.24}$$

with the power spectrum $P_g(k)$ of the Gaussian curvature perturbation ζ_g defined in Eq. (2.84), which takes the form of Eq. (2.85) in the monochromatic case.

Here, we can see that the constant parameters A_g and $F_{\rm NL}$ can be taken out from the integrals in $\mathcal{I}_{AA'}$. As a result, the order of each contribution is $\mathcal{P}^{(1)}_{AA}=O(F^0_{\rm NL}A^2_g)$, $\mathcal{P}^{(2,3,4)}_{AA}=O(F^2_{\rm NL}A^3_g)$,

and $\mathcal{P}_{AA}^{(5,6,7)} = O(F_{\rm NL}^4 A_g^4)$. These are the seven terms which were referred to in Sec. 2.5 and were reduced to three due to the common parameter dependence of $\mathcal{P}_{AA}^{(2,3,4)}$ and $\mathcal{P}_{AA}^{(5,6,7)}$.

We must now convert this result into an energy density parameter $\Omega_{\rm GW}(f)$. Given that $f \propto k$ via Eq. (2.86), the energy density parameter can be computed as

$$\Omega_{\rm GW}(\tau, k) \equiv \frac{1}{\rho_c}\frac{d\rho_{\rm GW}}{d\ln k} = \frac{1}{48}\left(\frac{k}{\mathcal{H}(\tau)}\right)^2 \sum_{A,A'=+,\times} \overline{\mathcal{P}_{AA'}(\tau, k)}\,, \tag{A.25}$$

where the overline denotes oscillation average. In the radiation-dominated era, the source term of GW given by Eq. (A.4) becomes negligible soon after the curvature perturbation re-enters the horizon, so that scalar-induced gravitational waves behave as the radiation without the source. If we denote the energy density parameter in the subhorizon limit during the RD era as $\Omega_{\rm GW}^{\rm RD}(k)$, then the present density parameter can be described as [453]

$$\Omega_{\rm GW}(\tau_0, k) = \Omega_{r,0}\frac{g^*(\tau_i)}{g_0^*}\left(\frac{g_{s,0}^*}{g_s^*(\tau_i)}\right)^{4/3} \Omega_{\rm GW}^{\rm RD}(k)\,, \tag{A.26}$$

where the subscript "0" denotes the present value, Ω_r is the radiation density parameter, g^* and g_s^* represent the effective number of relativistic degrees of freedom contributing to the energy and entropy densities, respectively, and τ_i is the conformal time when the SIGW start to behave as radiation. Here, we assume $g^*(\tau_i) = g_s^*(\tau_i) = 106.75$, which corresponds to the epoch in which the relevant scales for LVK band re-entered the horizon. For a more detailed description of numerically computing $\Omega_{\rm GW}^{\rm RD}(k)$, one can refer to [154, 153]. To conclude the computation, one would have to convert the scale k to frequency with the relation given by Eq. (2.86).

Eq. (A.26) is the final expression we used in our article [5], summarized in Sect. 2.5. We can see its shape for different $F_{\rm NL}$ values in Fig. 2.5.

Appendix B

Derivation of dipole artifact due to Doppler shift

In this appendix chapter, I include the derivation of the dipole artifact caused in a SGWB by the Doppler shift due to the observer's relative motion, included in the article [3]. This is based on similar derivations for the CMB [197, 198].

We denote by S a rest frame in which the SGWB is isotropic, and by S' the observer's system, which is traveling at a constant relative speed $v = \beta c$ with respect to S. The parameters of S' will be denoted with a prime. Both $\theta = 0$ and $\theta' = 0$ are defined so that they point towards the direction of motion, so it will be necessary to rotate the final result to align it with the Earth's rotation axis.

The Lorentz transformation between θ and θ' is then

$$\cos\theta' = \frac{\cos\theta + \beta}{1 + \beta\cos\theta}. \tag{B.1}$$

Then, for a gravitational wave signal coming from θ in S, the observed gravitational wave frequency f' relates to the emitted one f as

$$f' = \frac{1 + \beta\cos\theta}{\sqrt{1-\beta^2}} f = \frac{\sqrt{1-\beta^2}}{1 - \beta\cos\theta'} f. \tag{B.2}$$

This equation differs from the standard expressions for the Doppler shift by a minus sign, $\beta \mapsto -\beta$, due to the different setup. We now write the series expansion of Eq. (B.2) in β up to the second order,

$$\frac{f'}{f} = 1 + \beta\cos\theta' + \beta^2\left(\cos^2\theta' - \frac{1}{2}\right) + \mathcal{O}(\beta^3). \tag{B.3}$$

The term with $\cos^2\theta'$ implies that this order of approximation leads to multipoles $l \leq 2$, so the Doppler effect is not a pure dipole, as it is commonly assumed.

In order to compute the angular distribution of the SGWB observed in S', we look for an expression for $\Omega'_{\rm gw}(f', \theta')$ in terms of $\Omega_{\rm gw}(f', \theta)$, with the same frequency in both cases. The GW

energy density can be computed as the number density of gravitational quanta times the energy of each of them, which is proportional to the frequency. Similar to Eq. (1) in [197], we define a spectral number density $n(f,\theta)$, with units of $\mathrm{m}^{-1}\mathrm{sr}^{-1}\mathrm{Hz}^{-1}$. Then, the energy density satisfies

$$\frac{d\rho_{\mathrm{gw}}}{df\, d^2\Omega} \propto f \times n(f,\theta), \tag{B.4}$$

which can be understood as an energy flux or intensity. According to Eq. (7) in [197], which reads $n(f',\theta') = n(f)(f'/f)^2$, then the definition of $\Omega_{\mathrm{gw}}(f,\vec{n})$ in Eq. (3.3) and the previous Eq. (B.4) imply

$$\Omega'_{\mathrm{gw}}(f',\theta') = \left(\frac{f'}{f}\right)^4 \Omega_{\mathrm{gw}}(f,\theta). \tag{B.5}$$

From now on, we omit the angular dependence notation for brevity. Substituting Eq. (B.3) into Eq. (B.5), we get

$$\frac{\Omega'_{\mathrm{gw}}(f')}{\Omega_{\mathrm{gw}}(f)} = \left(\frac{f'}{f}\right)^4 \approx 1 + 4\beta\cos\theta' + \beta^2\left(10\cos^2\theta' - 2\right) \tag{B.6}$$

We now make another series expansion to relate $\Omega_{\mathrm{gw}}(f)$ to $\Omega_{\mathrm{gw}}(f')$,

$$\begin{aligned}\Omega_{\mathrm{gw}}(f) &\approx \Omega_{\mathrm{gw}}\left(f'\left[1 - \beta\cos\theta' + \frac{\beta^2}{2}\right]\right)\\ &\approx \Omega_{\mathrm{gw}}(f')\left\{1 + \alpha\left(\beta\cos\theta' + \frac{\beta^2}{2}\right) + \frac{A}{2}\beta^2\cos^2\theta'\right\}\end{aligned} \tag{B.7}$$

where

$$\alpha = \frac{f}{\Omega_{\mathrm{gw}}}\frac{\partial\Omega_{\mathrm{gw}}}{\partial f}, \quad A = \frac{f^2}{\Omega_{\mathrm{gw}}}\frac{\partial^2\Omega_{\mathrm{gw}}}{\partial f^2}. \tag{B.8}$$

The expressions appearing in this equation for α and A should use f' instead of f. However, since the difference is a constant factor, as shown in Eq. (B.3), the results are identical in either case. In particular, if $\Omega_{\mathrm{gw}} \propto f^m$, then $\alpha = m$ (hence the notation) and $A = \alpha(\alpha-1)$.

Therefore, we can therefore compute $\Omega'_{\mathrm{gw}}(f',\theta')$ in terms of $\Omega_{\mathrm{gw}}(f')$ by substituting Eq. (B.7) into Eq. (B.6) up to $O(\beta^2)$, so that

$$\Omega'_{\mathrm{gw}}(f',\theta') = \Omega_{\mathrm{gw}}(f')\left\{1 + \beta\cos\theta'(4-\alpha) + \beta^2\left[\cos^2\theta'\left(10 - 4\alpha + \frac{A}{2}\right) + \frac{\alpha}{2} - 2\right]\right\} \tag{B.9}$$

In particular, when $\alpha = 4$, it follows that $A = 12$ and the above equation reduces to $\Omega'_{\mathrm{gw}}(f',\theta') = \Omega_{\mathrm{gw}}(f')$. This is due to the Lorentz invariance of $\Omega_{\mathrm{gw}}(f)/f^4$, and explains the dip observed in Fig. 3.5.

Using the spherical harmonics in Table 8.1 for the standard spherical coordinates (θ,ϕ) instead of (α,δ),

$$Y_{00}(\theta,\phi) = \sqrt{\frac{1}{4\pi}}, \quad Y_{10}(\theta,\phi) = \sqrt{\frac{3}{4\pi}}\cos\theta, \tag{B.10}$$

$$Y_{20}(\theta,\phi) = \sqrt{\frac{5}{4\pi}}\left(\frac{3}{2}\cos^2\theta - \frac{1}{2}\right) \tag{B.11}$$

we can derive the $\mathcal{P}_{lm}$ coefficients from Eq. (B.9):

$$\mathcal{P}_{00} = \left(1 + \beta^2 \left[\frac{4}{3} - \frac{5}{6}\mu + \frac{1}{6}A\right]\right)\sqrt{4\pi}, \tag{B.12}$$

$$\mathcal{P}_{10} = \beta(4-\mu)\sqrt{\frac{4\pi}{3}}, \tag{B.13}$$

$$\mathcal{P}_{20} = \beta^2 \left(10 - 4\mu + \frac{A}{2}\right)\frac{2}{3}\sqrt{\frac{4\pi}{5}}, \tag{B.14}$$

with the rest of $\mathcal{P}_{\ell m} = 0$. Given that the dipole points to the $\theta = 0$ direction by hypothesis, only the $\mathcal{P}_{l0}$ are non-zero. However, as indicated at the beginning of this chapter, the actual implementation requires a rotation to make the dipole direction correspond to the direction of the relative motion shown in Fig. 3.4, which we take from Planck's measurements. This populates the other $\mathcal{P}_{lm}(m \neq 0)$ components.

Appendix C

Analytic estimate of the induced spins

In this appendix chapter, analytic expressions for the induced spins are derived using frame dragging. Nevertheless, in order to get an accurate estimations, one would have to resort to the fourth order of the post-Newtonian formalism [278, 383]. The derived expressions are therefore only valid as a simple qualitative approach.

For this purpose, the main idea is to interpret the precession vectors from frame dragging as the angular speeds which are induced on the corresponding inertial frames.

C.1 Ring approximation

From the rest frame of a black hole, a close encounter with another one with a certain mass m is just a point mass current following a certain trajectory $\vec{r}(t)$, which is exactly a hyperbola in the Keplerian limit. This situation is analogous to a black hole located at the center of a massive ring of mass m, with a time-varying radius following the equation $R(t) = |\vec{r}(t)|$ and rotating so that the speed of each of its points matches the velocity that the point mass would have. To simplify things, we take a stationary situation in which R and ω are constant, with their values corresponding to the point of closest approach.

First, we consider a thin ring of certain mass m_1 and radius R, which rotates around its axis at a certain angular speed ω. From the PPN(1.5) formalism, the rotation angular momentum of the central black hole undergoes a certain precession given by the vector

$$\vec{\Omega} = \frac{2}{r^3}\vec{J}_1, \tag{C.1}$$

where $\vec{J}_1$ is the angular momentum of the ring. This expression is the same one as for the precession of the orbital angular momentum of a test particle orbiting a rotating black hole, an effect which is known as Lense-Thirring precession [454].

For a thin ring, the moment of inertia with respect to the center is just $I = m_1 R^2$. Therefore,

$$\vec{\Omega} = \frac{2}{r^3}\vec{J}_1 = \frac{2}{R^3} m_1 R^2 \vec{\omega} = \frac{2m_1}{R}\vec{\omega}, \tag{C.2}$$

which relates the angular speed of the ring with that of the induced inertial frame at its center. The same relation between $\vec{\Omega}$ and $\vec{\omega}$ can be obtained from the equations in [455] in the thin-ring approximation.

We now compute the dimensionless spin that would correspond to a black hole of certain mass m_2 located at the center of the ring. For this purpose, we assume that the frame-dragging speed Ω is completely transferred to the central black hole, which rotates with this angular speed. Taking the black hole as a solid sphere whose radius coincides with its Schwarzschild radius $R_{S,2}$, its moment of inertia is

$$I_2 = \frac{2}{5} m_2 R_{S,2}^2 = \frac{2}{5} m_2 (2m_2)^2 = \frac{8}{5} m_2^3. \tag{C.3}$$

With this, we can get the dimensionless spin,

$$\chi = \frac{a}{m_2} = \frac{J}{m_2^2} = \frac{I_2 \Omega}{m_2^2} = \frac{16}{5}\frac{m_1 m_2}{R}\omega. \tag{C.4}$$

Finally, we want to extrapolate this result to the hyperbolic motion of a black hole of mass m_1 around a black hole of mass m_2. For this purpose, we express ω and R in terms of two parameters which characterize the hyperbolic motion: the velocity at the point of closest approach, v_0, and the eccentricity of the orbit, e.

First of all, we take the radius of the ring, R, to be the distance between both black holes at the moment of closest approach. As we saw in Eq. (1.202), this distance is given in hyperbolic motion by $R = a(e-1)$, where a is the semi-major axis of the hyperbola and must not be confused with the dimensionless spin a.

Second, when we substitute the ring by a black hole, we keep the same angular momentum. Therefore,

$$L_{\text{ring}} = L_{\text{BH}} \quad \Rightarrow \quad m_2 R^2 \omega = m_2 R v_0 \quad \Rightarrow \quad \omega = v_0/R. \tag{C.5}$$

Using the expression for v_0 in terms of a given by Eq. (1.205), we can substitute the ω in Eq. (C.5) into the expression for χ in Eq. (C.4) to get

$$\chi = \frac{16}{5}\frac{m_1 m_2}{R^2} v_0 = \frac{16}{5}\frac{m_1 m_2}{a^2 (e-1)^2} v_0 = \frac{16}{5}\frac{m_1 m_2}{M^2}\frac{1}{(e+1)^2} v_0^5. \tag{C.6}$$

For the particular case $m_1 = m_2$, the previous expression is just

$$\chi = \frac{4}{5}\frac{1}{(e+1)^2} v_0^5. \tag{C.7}$$

For the approach in the next section, it is useful to note that, in order to convert from Ω to χ, we have just multiplied by a factor

$$\frac{\chi}{\Omega} = \frac{I}{m_2^2} = \frac{8}{5} m_2. \tag{C.8}$$

C.2 Mass current

Another possible approach to compute the spin is introducing a mass m_1 current at a position $\tilde{\vec{r}}$ with speed $\tilde{\vec{v}}$. We start by writing the angular velocity of an inertial frame within the gravitational potentials ϕ and $\vec{g}$, which can be taken from the equation (9.6.12) in Ref. [456],

$$\vec{\Omega} = -\frac{1}{2}\nabla \times \vec{g} - \frac{3}{2}\vec{v} \times \nabla\phi. \tag{C.9}$$

The second term corresponds to the de Sitter effect, coming from the gravitoelectric part of the potential. If we assume that the mass current is symmetrically distributed within a ring, then the potential ϕ at the center is constant and we can safely ignore this component.

Therefore, we just have to compute $\vec{g}$, which can be done with the expression

$$\vec{g} = -4G \iint\!\!\!\iint d^3\vec{r'}\, \frac{\rho(\vec{r'})\vec{v}(\vec{r'})}{|\vec{r} - \vec{r'}|}. \tag{C.10}$$

We will now substitute ρ and $\vec{v}$ by the ones corresponding to a point mass current at position $\vec{\tilde{r}}(\varphi)$, where φ is an angular variable that parametrizes the trajectory. Distributing this mass within a ring at the same distance does not have an effect over the first term in (C.9), which is a vector parallel to the symmetry axis. We would just do the integration at a later stage.

$$\vec{g} = -4G \iint\!\!\!\iint d^3\vec{r'}\, \frac{m_1\delta^3(\vec{r'} - \vec{\tilde{r}}(\varphi))\vec{\tilde{v}}(\varphi)}{|\vec{r} - \vec{r'}|} = -\frac{4Gm_1\,\vec{\tilde{v}}(\varphi)}{|\vec{r} - \vec{\tilde{r}}(\varphi)|}. \tag{C.11}$$

We now use Eq. (C.9), first noting that

$$\nabla \times \left(\frac{\vec{\tilde{v}}(\varphi)}{|\vec{r} - \vec{\tilde{r}}(\varphi)|}\right) = -\vec{\tilde{v}}(\varphi) \times \nabla \cdot \left(\frac{1}{|\vec{r} - \vec{\tilde{r}}(\varphi)|}\right) = \vec{\tilde{v}}(\varphi) \times \frac{\vec{r} - \vec{\tilde{r}}(\varphi)}{|\vec{r} - \vec{\tilde{r}}(\varphi)|^3}, \tag{C.12}$$

where the first equality comes from the vector identity $\nabla \times (f\vec{a}) = (\nabla f) \times \vec{a} + f(\nabla \times \vec{a})$, where in this case the second term is zero.

Taking this into account, we can use Eq. (C.9) to get

$$\vec{\Omega} = 2m_1\nabla \times \left(\frac{\vec{\tilde{v}}(\varphi)}{|\vec{r} - \vec{\tilde{r}}(\varphi)|}\right) = 2m_1\vec{\tilde{v}}(\varphi) \times \frac{\vec{r} - \vec{\tilde{r}}(\varphi)}{|\vec{r} - \vec{\tilde{r}}(\varphi)|^3}. \tag{C.13}$$

We can get rid of the $\vec{r}$ by staying at the coordinate origin, $\vec{r} = 0$, and thus get (dropping the tildes and the φ dependence)

$$\vec{\Omega} = 2m_1\frac{\vec{r} \times \vec{v}}{r^3}. \tag{C.14}$$

Now, we use several equations from hyperbolic motion, namely

$$r = a(e\cosh(E) - 1), \qquad \vec{r} \times \vec{v} = a(e-1)v_0, \tag{C.15}$$

where the second expression comes from angular momentum conservation and E is the eccentric anomaly, related to the true anomaly by [48, 49]

$$\tan^2\left(\frac{\varphi-\varphi_0}{2}\right)=\frac{e+1}{e-1}\tanh^2\left(\frac{E}{2}\right). \tag{C.16}$$

As a result,

$$\vec{\Omega}=2m_1\frac{(e-1)v_0}{a^2(e\cosh(E)-1)^3}=\frac{2m_1}{M^2}\frac{1}{(e\cosh(E)-1)^3}\frac{(e-1)^3}{(e+1)^2}v_0^5. \tag{C.17}$$

If we impose $E=0$, corresponding to the point of closest approach, $\varphi=\varphi_0$, and compute χ, we get

$$\chi=\frac{8}{5}m_2\frac{2m_1}{M^2}\frac{1}{(e+1)^2}v_0^5=\frac{16}{5}\frac{m_1m_2}{M^2}\frac{1}{(e+1)^2}v_0^5, \tag{C.18}$$

which is, remarkably, the same expression we have obtained for the ring case, Eq. (C.6).

C.3 From spin-orbit equations at PPN(1.5)

Alternatively to the previous approaches, we can use some equations from [457]. In this reference, the spins of two black holes in hyperbolic motion both follow precession dynamics given by the vectors

$$\vec{\Omega}_i=\frac{\hat{k}}{M}\frac{\overline{\xi}^{5/3}\sqrt{e_t^2-1}}{(e_t\cosh(E)-1)^3}\delta_i, \tag{C.19}$$

for $i=1,2$, where $\hat{k}$ is the unit vector perpendicular to the orbital angular momentum and

$$\overline{\xi}=M\overline{n},\quad \delta_{1,2}=\frac{\eta}{2}+\frac{3}{4}(1\mp\sqrt{1-4\eta}), \tag{C.20}$$

$$\eta=m_1m_2/M^2,\quad m_1\geq m_2, \tag{C.21}$$

with $\overline{n}$ being the mean motion of the hyperbolic orbit and E its eccentric anomaly. Both e_t and $\overline{n}$ are deviations of the keplerian case, taken at PPN(1.5) order. In our case, we will take them as if they were the exact Newtonian values: $\overline{n}=n$, $e_t=e$. In standard hyperbolic motion, n is given by the expression $n^2a^3=M$.

If we now substitute these expressions, we get

$$\begin{aligned}\Omega_i&=\frac{1}{M}\frac{(M/a)^{5/2}\sqrt{e^2-1}}{(e\cosh(E)-1)^3}\delta_i=\frac{1}{M}\frac{\sqrt{e^2-1}}{(e\cosh(E)-1)^3}\frac{(e-1)^{5/2}}{(e+1)^{5/2}}\delta_i v_0^5\\&=\frac{1}{M}\frac{1}{(e\cosh(E)-1)^3}\frac{(e-1)^3}{(e+1)^2}\delta_i v_0^5,\end{aligned} \tag{C.22}$$

which is somewhat similar to the expression (C.17). The difference is a factor

$$\frac{M}{2m_i}\delta_i. \tag{C.23}$$

We can now compute the dimensionless spins, which in this case we have to split into two separate expressions. We also evaluate at $E = 0$:

$$\chi_1 = \left[\frac{4}{5}\eta + \frac{6}{5}\left(1 - \sqrt{1-4\eta}\right)\right]\left(\frac{m_1}{M}\frac{1}{(e+1)^2}v_0^5, \tag{C.24}$$

$$\chi_2 = \left[\frac{4}{5}\eta + \frac{6}{5}\left(1 + \sqrt{1-4\eta}\right)\right]\left(\frac{m_2}{M}\frac{1}{(e+1)^2}v_0^5. \tag{C.25}$$

The comparison with the ring expression is difficult, due to factors dependent on the masses that were not present before. However, for the case $m_1 = m_2$, both spins are equal and we get

$$\chi = \frac{7}{10}\frac{1}{(e+1)^2}v_0^5, \tag{C.26}$$

which is formally identical to the ring case but with a factor $7/8$ difference.

C.4 Differences between expressions

In order to better understand the differences between the three expressions (C.6), (C.24) and (C.25), we can plot the factors f that appear in these expressions before the $v_0^5/(e+1)^2$, which are given by Eqs. (C.6), (C.24) and (C.25). These values are shown in Fig. C.1.

We have also plotted the asymptotic values to which each curve tends to for $q \to 0$. These can easily be found from the expressions of each factor in the limit $q \ll 1$,

$$f_{\rm ring}, f_{\rm 1.5PN,1} \to \frac{16}{5}q, \qquad f_{\rm 1.5PN,2} \to \frac{12}{5}q. \tag{C.27}$$

Interestingly, for the PPN(1.5) approximation, the induced spin on the most massive black hole approaches the same trend as that of the ring. Also, in the PPN(1.5) case, the highest spin is induced on the most massive black hole.

Fig. C.1 also shows that the order of magnitude of the computed spins is essentially the same, independent of the method that we use. In particular, the maximum difference between the different cases is a factor $4/3$.

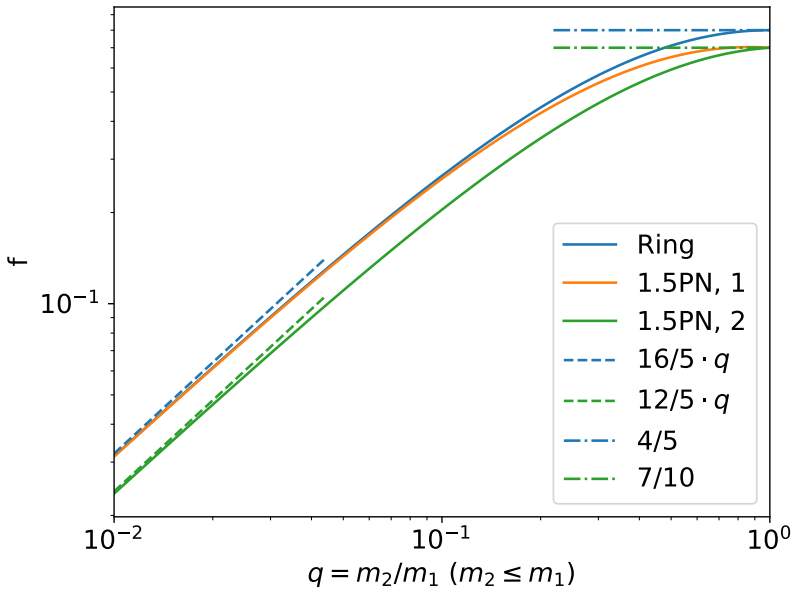

Figure C.1: Factor f versus mass ratio $q = m_2/m_1$ ($m_2 \leq m_1$). The trends for $q \to 0, 1$ are also provided for each curve.

Appendix D

Corner plots for SGWB constraints from Gaia DR3

This appendix chapter includes complementary plots for Chapter 10. Figs. D.1-D.3 show the marginalized 1 and 2-dimensional posterior distributions for the multipole coefficients r_{lm} of the VSH decomposition of the proper motion field, as well as the derived posterior distribution for $\Omega_{\rm GW}$. I Fig. D.4, the covariance matrices from our analysis are also shown.

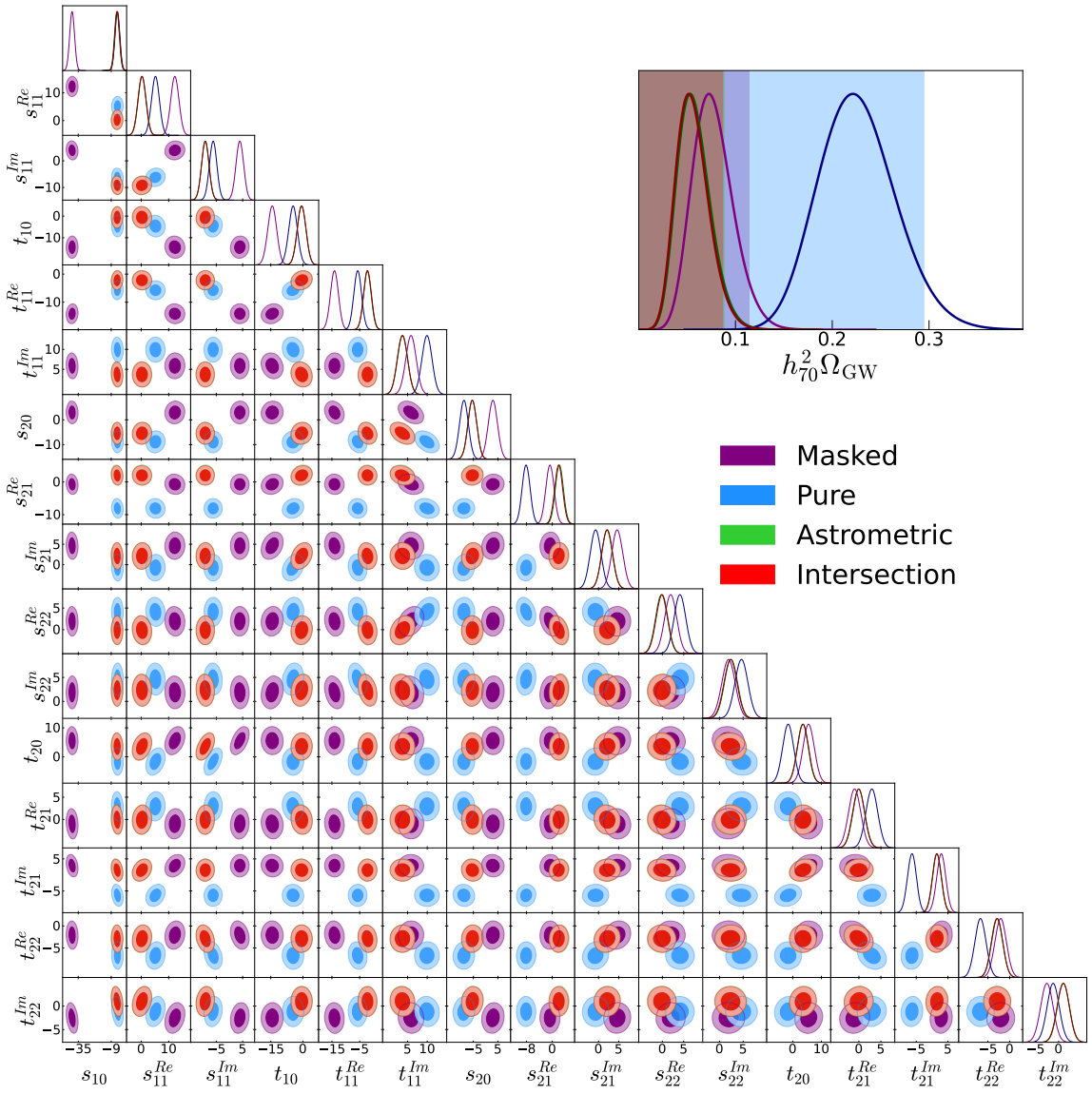

Figure D.1: Posteriors for the masked, pure, astrometric and intersection datasets. The results of the intersection and astrometric datasets considerably overlap.

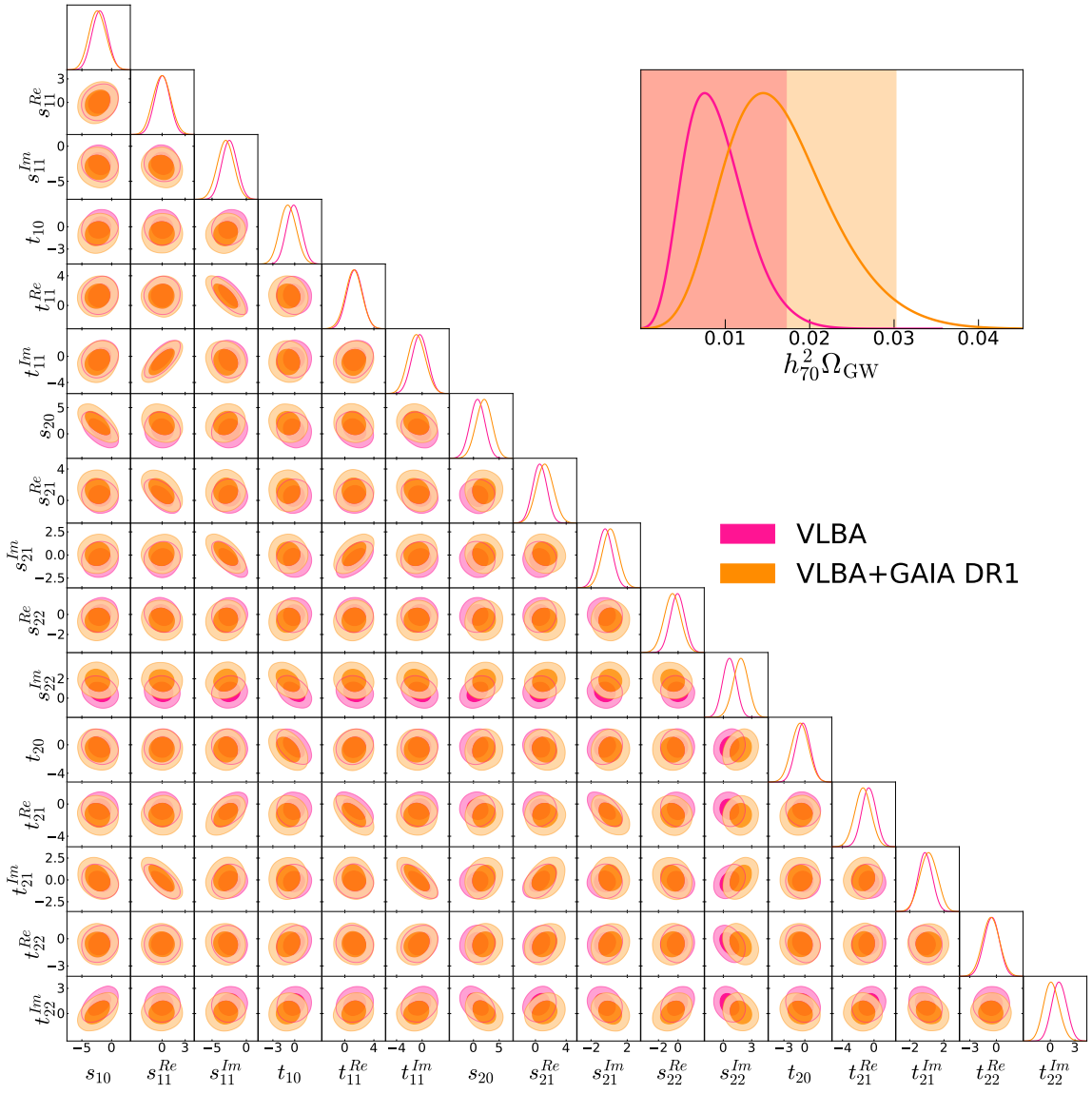

Figure D.2: Posteriors for the VLBA and VLBA+Gaia DR1 datasets.

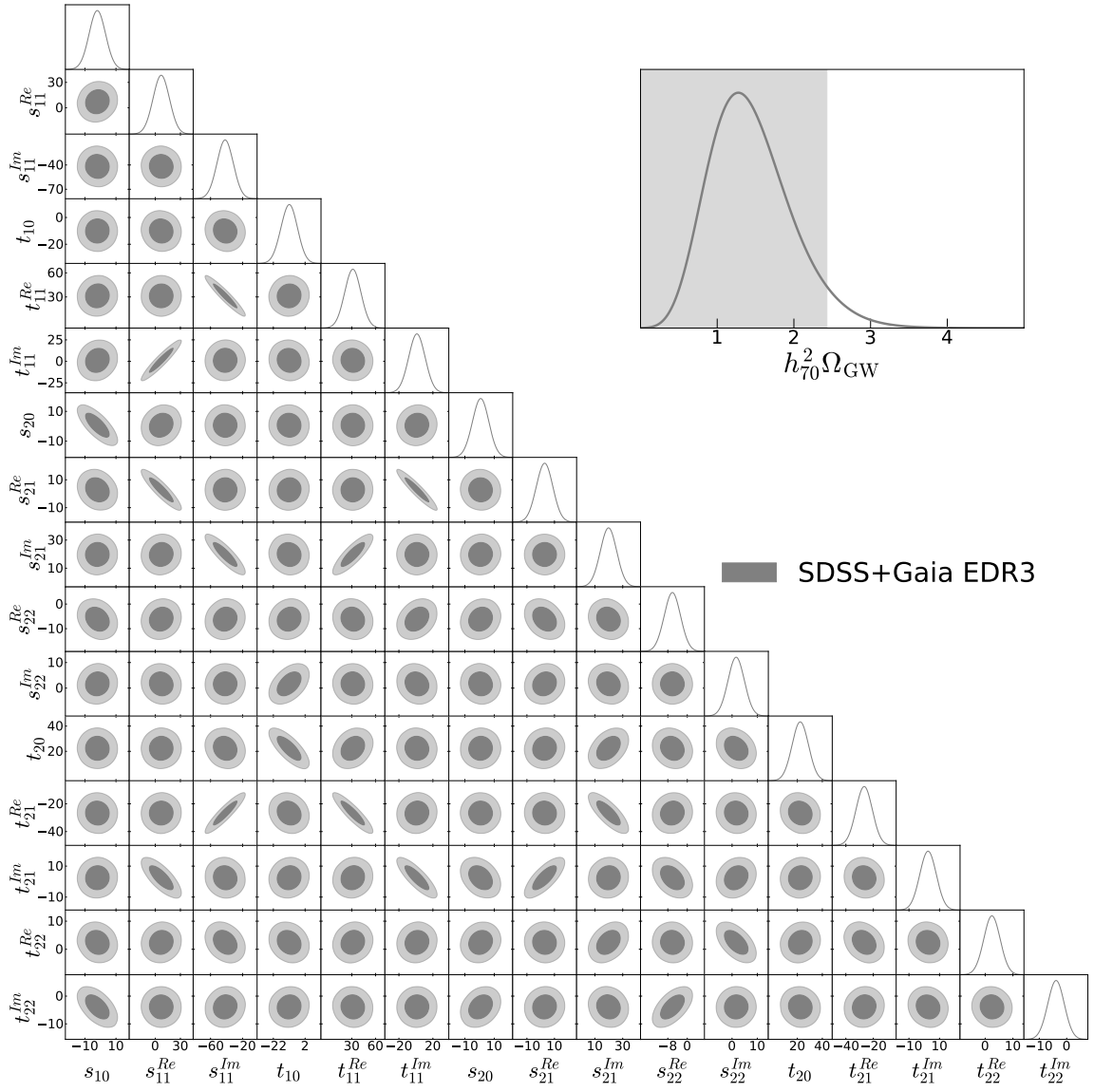

Figure D.3: Posteriors for the SDSS+Gaia EDR3 dataset.

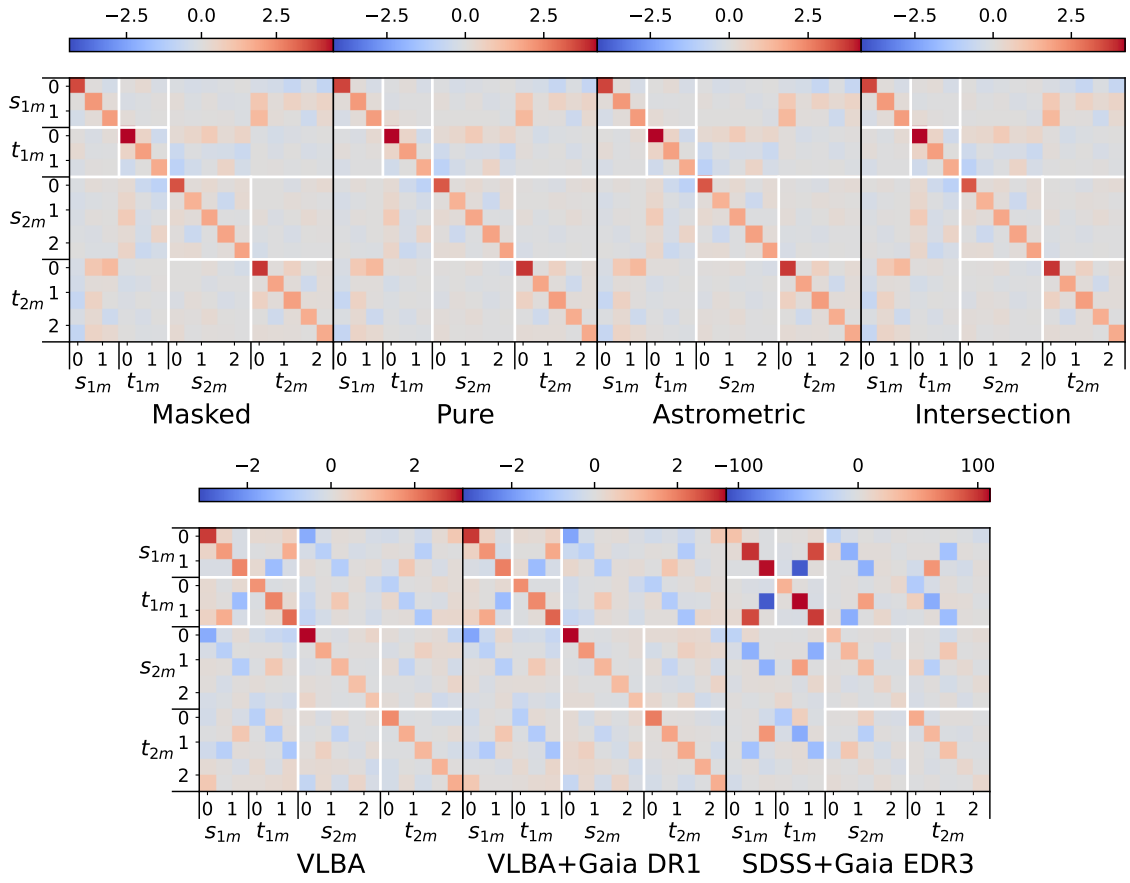

Figure D.4: Covariance matrices for all the considered datasets, with units $(\mu\text{as/yr})^2$.

List of Figures

1.1 Effect of the polarizations plus (+) and cross (×) on a circle consisting of test masses. 13

1.2 Illustration of the distances involved in Eqs. (1.86) and (1.87), where $\vec{x}$ is the distance from the source to the observer and $\vec{x}'$ is an internal distance of the source distribution. In the limit in which the distance from the source to the observer is much larger than the internal distances, $|\vec{x}| \gg |\vec{x}'|$, we can see how $\vec{x} - \vec{x'} \approx \vec{x}$. . . . 21

1.3 Gravitational-wave strain (left) and black hole trajectories (right) during a CBC, showing the inspiral, merger and ringdown in different colors. 24

1.4 Ellipse with its relevant points, distances and angle. C indicates the center of the ellipse, while F indicates the focus which is taken as the origin of the coordinate system, while the other focus would be in the symmetric position. P indicates a generic point in the ellipse with radial coordinate r and phase φ. The semimajor and semiminor axes a and b are also shown, as well as the distance c from the center to the focus. 26

1.5 Left branch of a hyperbola with its relevant points, distances and angles. C indicates the center of the hyperbola, A is the branch vertex and F its focus, which is taken as the origin of the coordinate system. P indicates a generic point in the left branch with radial coordinate r and phase φ. The semimajor axis a is also shown, representing the distance from the center to the vertex, as well as the distance c from the center to the focus. The dash-dotted lines represent the asymptotes of the hyperbola, while φ_0 is the angle they form with the major axis. Finally, the impact parameter b indicates the distance from the focus to the asymptotes. 39

2.1 SGWB spectra for several cosmological models (colored solid curves) compared to current upper limits (shaded in gray) and expected sensitivities of future experiments (black dashed lines), taken from [98]. The figure includes signals from inflation (R^2 inflation [76]) along with their modification by a stiff equation of state [77], but one should note that the amplitude and spectral behavior of these signals heavily depend on the model parameters. The GW spectrum of cosmic string loops [78, 79] is also presented, as well as the electroweak phase transition [80]. Current constraints include the Advanced-LIGO O3 upper limit [28], constraints based on Big Bang nucleosynthesis and CMB observations [99], pulsar timing, the astrometric measurements by Gaia explained in Chapter 10, CMB temperature and polarization observations [100], and pulsar timing arrays [11]. Future expected sensitivities include the final sensitivity of Advanced-LIGO [101], ET [102], DECIGO [23], LISA [103], SKA [104], and LiteBIRD [105]. An observing period of 3 years is assumed for interferometer experiments and 20 years for SKA. The blue-shaded band indicates the expected amplitude of the SGWB due to the cosmic population of CBCs, based on the observed individual events in the O3 catalog [106], while the expected spectral amplitude is extrapolated to the LISA frequency band assuming the $f^{2/3}$ dependence of the inspiral phase (Eq. (1.196)). However, the lower frequencies could be modified by the effects of eccentricity and precession at the time of binary formation [107, 108]. 44

2.2 Example of a Monte Carlo method for the computation of π. N denotes the number of points, while $N_{\rm in}$ is the number of them inside the radius $x^2 + y^2 = 1$ (black line). The exact value of π is given by $4A_{\rm circle}/A_{\rm square}$, so an approximation is given by $4N_{\rm in}/N$. For each realization, we can see the number of used points and their approximation of π, which statistically gets better as N increases. 58

2.3 Gaussian PDF illustrating the 1-sigma (blue), 2-sigma (orange+blue) and 3-sigma (green+orange+blue) regions, covering the 68%, 95% and 99.7% of the total central probability, respectively. The dashed, vertical line also marks the 95% credible-level upper bound. 61

2.4 Corner plot for the parameter estimation run by LVK with a Gaussian prior for α and log-uniform prior for Ω_α, denoted here by $\Omega_{\rm ref}$. Figure taken from [28]. 66

2.5 $\Omega_{\rm GW}(f)$ spectrum for different $F_{\rm NL}$ values, with $A_g = 0.001$. 67

2.6 Posterior distributions for the combined SIGW and CBC search, where the blue and light blue contours correspond to the 68 and 95% CL regions, respectively. For reference, we plot the red line corresponding to $F_{\rm NL}^2 A_g = 1$, which is the boundary where the non-Gaussian terms start to dominate over the Gaussian contribution in the $\Omega_{\rm gw}(f)$ power spectrum (Eq. (2.87)). The orange line corresponds to the asymptotic behavior at large $F_{\rm NL}$ values, following $F_{\rm NL} A_g = 0.380$. 69

2.7 Posterior 95% CL contours for $A_g - k_*$, obtained from the fixed $F_{\rm NL}$ runs. The 95% CL region corresponds to the area under these curves. 70

2.8 Posterior 95% CL contours for $A_g - F_{\rm NL}$ plane (solid lines), obtained from the fixed k_* runs. The dashed lines represent the asymptotic behavior for large non-Gaussianity (orange) and the red one marks the boundary where non-Gaussian term start to dominate over the Gaussian contribution in $\Omega_{\rm gw}(f)$, similar to the lines in Fig. 2.6. Dotted lines correspond to analytically derived relations between $F_{\rm NL}$ and A_g which show the limit at which PBHs make up 100% of the dark matter, showing small differences between different values of k_*. 71

3.1 Example posterior for an injected and recovered broken power-law model, with $\ln \mathcal{B}^{\rm BPL}_{\rm PL} = 417$. The recovery is consistent with the injection, indicated by the red markers and lines. 82

3.2 Heatmap showing the Bayes factor for the broken power-law versus power-law $\bar{H}(f)$ recovery models, for different injected values of ϵ and α_2 with $f_0 = 100$ Hz and $\alpha_1 = 2/3$. 82

3.3 Heatmap showing the Bayes factor for the Galactic plane versus isotropic $\mathcal{P}_{lm}$ recovery models, for different injected values of ϵ and α and an injected Galactic plane $\mathcal{P}_{lm}$ model. 83

3.4 Sky map of the dipole artifact for $\alpha = 2/3$ and Planck values for the relative speed and direction, plotted in a Mollweide projection. The color map represents an arbitrary scale. 84

3.5 Heatmap showing the Bayes factor for the dipole artifact $\mathcal{P}_{lm}$ model versus the isotropic one. 85

4.1 Higgs potential $V(x)$ defined in Eq. (4.9), with the parameters from Eq. (4.11), as indicated in [211]. 90

4.2 Normalized power spectrum of overdensity perturbations for a Gaussian primordial curvature power spectrum, as well as other distributions from quantum diffusion models (Elliptic2 and Elliptic4), effective descriptions using $f_{\rm NL}$ parameters and a lognormal power spectrum. The free parameters of the distributions are set so that the behavior around the peak is similar. Figure taken from [150], where we refer to for additional details on these shapes. 91

4.3 Time evolution of the compaction function $C(r)$ for an initial overdensity of $\delta_m = 0.57$, leading to the formation of a black hole (left), and $\delta_m = 0.45$, for which the pertubation decays away (right). In both cases, a radiation fluid is considered, $\omega = 1/3$. 101

4.4 Thresholds δ_c and $\delta_{0,c}$ for δ_m and δ_0, respectively, as functions of the equation of state parameter ω. 102

4.5 Relativistic degrees of freedom g_* (left) and equation of state parameter ω (right) evolution with temperature, showing the particles whose decoupling caused the changes. Figures taken from [168] and [200]. 103

4.6 Left panel: density fraction of PBHs at formation (β_f defined in Eq. (4.1)) for the different PBH masses. Right panel: dark matter fraction of PBHs today. In both cases, two models are considered, where the first one comes from Refs. [241, 242] and the second one corresponds to Refs. [243, 244]. Figures taken from [168] and [200]. . 104

5.1 Comparison of the SGWB spectrum originating from BBHs and CHEs, both for $\beta = 0$ (solid lines) and 1.28 (dashed lines). The power-law integrated sensitivity curves of several GW detectors are also plotted for a signal-to-noise ratio of 10 and an observation time of 1 year, following the formalism in [282]. For the BBH curves, we take $m_1 = m_2 = 100 - 300\ M_\odot$ and $v_\infty = 30$km/s. The CHE curves correspond to the same range of masses with $a_0 = 5$AU, $y_0 = 2 \times 10^{-3}$ for $\sim$ 10Hz, and $a_0 = 5 \cdot 10^7$AU, $y_0 = 10^{-5}$ for the mHz range. For all cases, we take $\sigma_a, \sigma_y = 0.1$, $\sigma_m = 0.5$, and $f_{\rm PBH} = 1$. For a smaller fraction of PBHs, the GW spectral amplitude simply scales as $\Omega_{\rm GW} \propto f_{\rm PBH}^2$. 112

6.1 Initial conditions for numerical BBH simulations, where we take $m_1 \geq m_2$ and $\vec{p}_1 = -\vec{p}_2$. 118

6.2 Real part of the Weyl scalar Ψ_4 defined in Eq. (6.14) in the xy plane for four different instants of the BBH simulation described in Sec. 6.2. It illustrates the junk radiation (second panel) generated when the initial conditions (first panel) relax to an equilibrium configuration (third panel). For reference, the fourth panel shows the physical gravitational waves generated at the merger. 119

6.3 Adaptive mesh refinement scheme in the xy plane for different instants of the BBH simulation described in Sec. 6.2. Each color represents a different refinement level, for a total of seven in both panels. The inset plots show the transition from one refinement level to the following one. 120

6.4 Apparent horizons (dashed lines) for some iterations of the GW150914 simulation (left panel) and for the hyperbolic simulation with $\theta_2 = 3.12°$ described in Sec. 6.3 (right panel), with their positions (solid lines) plotted for reference. The blue lines denote the heaviest initial black hole, while the orange one denotes the lightest one. In the case of GW150914, the red dotted line marks the joint apparent horizon around its formation time, and the green line is also the joint horizon, after some relaxation time. 124

6.5 Spin component on the z axis of the two parent black holes of GW150914 before their merger, which is indicated by the dashed vertical line, and of the final black hole after the fusion. 125

6.6 Weyl scalar Ψ_4 (left) and strain amplitudes for each polarization, h_+, $h_\times$ (right), for the GW150914 simulation. These quantities are provided for the multipoles (l, l), $2 \leq l \leq 4$. 128

6.7 Black hole positions for the three hyperbolic simulations described in Sec. 6.3, from the most open to the closest one. 130

6.8 Gravitational-wave strains for the three hyperbolic simulations described in Sec. 6.3, from the most open to the closest one. 131

6.9 Spin component on the z axis for both black holes of the hyperbolic simulation described in Sec. 6.3 with $\theta_2 = 3.12°$. The two curves overlap due to the symmetry of the simulation. 131

7.1 Strain of the emitted gravitational wave from the $l = k = 2$ multipole (upper panel) and spin evolution (lower) during a hyperbolic encounter with $p/M = 0.49$, $q = 1$ and $\theta = 3.12°$. 137

7.2 Spin evolution during a hyperbolic encounter with $p/M = 0.49$, $q = 1$ and different values of θ. 139

7.3 Final spin for hyperbolic encounters with different momenta and $q = 1$ versus θ, as well as their fit to a power law. 139

7.4 Same as Fig. 7.3, with the curves normalized by the maximum spin-up value and subtracting $\theta_{\rm min}$ to θ. 140

7.5 Spin evolution during a hyperbolic encounter with $p/M = 0.49$, $\theta = 3.12°$ and different values of q. 141

7.6 Final spin for hyperbolic encounters with different initial momenta and θ corresponding to the $q = 1$ highest spin-up versus the black hole mass, as well as their linear fits. 141

7.7 Same as Fig. 7.6, where we divided each value of χ by the one corresponding to the same initial momentum and $q = 1$. The points are now open in order to better see the overlapping values, and the linear fits now have the restriction to pass through the central, common point. 142

7.8 All the relevant points and quantities involved in the transformation of the Weyl scalar from the sphere S_0 to the sphere $S_{\rm CM}$, for an arbitrary space-time point $p_3 = (t, \vec{r}_3)$, $r_3 \in S_{\rm CM}(t - R)$. The dotted line represents the light ray which passes through the three relevant points p_i, $i = 1, 2, 3$. 144

7.9 Strain amplitudes of the $q = 0.1$ simulation for the modes $l = k \leq 4$ (upper panel), together with the spin evolution (lower), where the first black hole is the most massive one. The dashed, vertical lines separate the periods before and after the merger. . . 144

8.1 Illustration of the concept of angular deflection. In the absence of a GW, the star at source S is observed in the direction of the unitary vector $\vec{n}$. With the passage of a gravitational wave, this position is deflected to $\vec{n}'$ (gray), with the angular deflection being $\delta\vec{n} = \vec{n}' - \vec{n}$ (red). The gravitational wave is represented by its propagation direction $\vec{p}$ and plane wavefronts (cyan). 150

8.2 Several vector spherical harmonics. Each row presents the spheroidal (left) and toroidal (right) modes for the same multipole indices l and m. 171

9.1 Illustration of Healpix levels 1 to 4, corresponding to 12, 48, 192 and 768 pixels, respectively. Credit: Gorski et al. [434] 188

9.2 Reduction of number of sources (left vertical axis) and expected non-QSO objects (right vertical axis) with a more stringent threshold, in the filtering process for the QSO candidate list. If we denote the quantity plotted in the x axis by k, the threshold is given by $1 - 10^k$. The point where the expected non-QSO sources is 1 corresponds to the x value 5.27, indicated by the dashed, vertical line, which gives a threshold of 0.99999465. 189

9.3 Proper motion module (in mas/yr) skymap for different steps. The top left panel shows the full QSO candidates dataset, while the others show the resulting skymap after either of the steps or both. 190

9.4 Proper motion module (in mas/yr) skymap for different considered datasets. 190

9.5 Color-magnitude (left) and color-color (right) diagrams for the different considered datasets, using the G band magnitude and its color indices with respect to the RP and BP bands. 193

9.6 Proper motion module (in mas/yr) skymap for the SDSS+Gaia EDR3 dataset (left panel) and source position for VLBA (blue and red) and VLBA+Gaia DR1 (red) datasets (right panel). 194

10.1 Difference of behaviors of the usual, least-squares method and the permissive fit given by the likelihood in Eq. (10.5). The left panel shows a well-behaved case, where both approaches coincide. The right panel shows a case with some outliers that bias the least-squares method, which do not significantly impact the permissive fit approach. 203

10.2 Posterior distribution for the quadrupole power P_2 for the astrometric dataset, with the corresponding chi-square and non-centered chi-square distributions superimposed. 204

10.3 Fitted vector field skymap for the intersection dataset. 205

C.1 Factor f versus mass ratio $q = m_2/m_1$ ($m_2 \leq m_1$). The trends for $q \to 0, 1$ are also provided for each curve. 228

D.1 Posteriors for the masked, pure, astrometric and intersection datasets. The results of the intersection and astrometric datasets considerably overlap. 230

D.2 Posteriors for the VLBA and VLBA+Gaia DR1 datasets. 231

D.3 Posteriors for the SDSS+Gaia EDR3 dataset. 232

D.4 Covariance matrices for all the considered datasets, with units $(\mu\text{as/yr})^2$. 233

List of Tables

2.1 Broadband estimates $\hat{\Omega}_\alpha$ given by Eq. (2.65), for a power-law $\Omega_{\rm gw}$ of exponent α and reference frequency $f_{\rm ref} = 25$ Hz. A separate estimate is provided for O1 [139], O2 [122] and O3 [28] LVK data, in this last case separated by baseline, together with the joint O1+O2+O3 estimates. 64

2.2 95% credible-level upper bounds for the amplitude Ω_α of a power-law $\Omega_{\rm gw}(f)$ of exponent α and reference frequency $f_{\rm ref} = 25$ Hz. A separate estimate is provided for uniform and log-uniform priors and for the different datasets, consisting on O1 [139], O1+O2 [122] and O1+O2+O3 [28] LVK data. Three fixed-α cases are provided, as well as one with free α. 65

2.3 Prior distributions used for the parameter estimation. 68

7.1 Ranges of θ considered for each initial momentum, as well as the equivalent minimum distances and fitted impact parameters and eccentricities. 138

7.2 Fitted parameters for Fig. 7.3 to a power law $\chi = (\theta/\theta_0)^n$, as well as $\theta_{\rm min}$ for reference and the linear correlation coefficient r^2 for the $(\log(\theta), \log(\chi))$ data to the corresponding linear function. 138

7.3 Fitted parameters for Fig. 7.7, with their linear correlation coefficient r^2 and values of the central spin. 142

8.1 Spherical harmonics up to $l = 2$ given by Eq. (8.120). 169

8.2 Vector spherical harmonics up to $l = 3$ given by Eqs. (8.130), (8.131). 172

8.3 Exact and numerical values for α_l^r in Eq. (8.181) for the first multipoles up to $l = 11$. 180

9.1 The number of sources in each considered dataset, along with the number of sources with redshift, the 25th, 50th and 75th percentiles, the time of arrival to the source in the 25th percentile and its corresponding frequency. We also provide the thresholds in $p_{\rm QSO}$ for our four main datasets. 192

10.1 The total quadrupole power obtained from the dipole+quadrupole fits, together with the Z score corresponding to the quadrupole, the Bayes factor between the dipole+quadrupole and only dipole hypotheses, and the $\Omega_{\rm GW}$ estimations (best-fit and 95% CL upper limit values). The values correspond to the maximum likelihood estimates and the 1-sigma errors are provided in brackets. 205

10.2 Fitted multipole coefficients, in μas/yr, for the four main considered datasets. The values correspond to the maximum likelihood estimates and the 1-sigma errors are provided in brackets. 206

Bibliography

[1] S. Jaraba and J. García-Bellido, *Black hole induced spins from hyperbolic encounters in dense clusters*, *Phys. Dark Univ.* **34** (2021) 100882 [2106.01436].

[2] J. García-Bellido, S. Jaraba and S. Kuroyanagi, *The stochastic gravitational wave background from close hyperbolic encounters of primordial black holes in dense clusters*, *Phys. Dark Univ.* **36** (2022) 101009 [2109.11376].

[3] L. Tsukada, S. Jaraba, D. Agarwal and E. Floden, *Bayesian parameter estimation for targeted anisotropic gravitational-wave background*, *Phys. Rev. D* **107** (2023) 023024 [2208.14421].

[4] S. Jaraba, J. García-Bellido, S. Kuroyanagi, S. Ferraiuolo and M. Braglia, *Stochastic gravitational wave background constraints from Gaia DR3 astrometry*, *Mon. Not. Roy. Astron. Soc.* **524** (2023) 3609–3622 [2304.06350].

[5] R. Inui, S. Jaraba, S. Kuroyanagi and S. Yokoyama, *Constraints on Non-Gaussian primordial curvature perturbation from the LIGO-Virgo-KAGRA third observing run*, 2311.05423.

[6] LIGO Scientific collaboration, *Advanced LIGO*, *Class. Quant. Grav.* **32** (2015) 074001 [1411.4547].

[7] LIGO Scientific, Virgo collaboration, *Observation of Gravitational Waves from a Binary Black Hole Merger*, *Phys. Rev. Lett.* **116** (2016) 061102 [1602.03837].

[8] NANOGrav collaboration, *The NANOGrav 15 yr Data Set: Evidence for a Gravitational-wave Background*, *Astrophys. J. Lett.* **951** (2023) L8 [2306.16213].

[9] EPTA collaboration, *The second data release from the European Pulsar Timing Array - I. The dataset and timing analysis*, *Astron. Astrophys.* **678** (2023) A48 [2306.16224].

[10] D. J. Reardon et al., *Search for an Isotropic Gravitational-wave Background with the Parkes Pulsar Timing Array*, *Astrophys. J. Lett.* **951** (2023) L6 [2306.16215].

[11] International Pulsar Timing Array collaboration, *Comparing recent PTA results on the nanohertz stochastic gravitational wave background*, 2309.00693.

[12] VIRGO collaboration, *Advanced Virgo: a second-generation interferometric gravitational wave detector*, *Class. Quant. Grav.* **32** (2015) 024001 [1408.3978].

[13] KAGRA collaboration, *Overview of KAGRA: Detector design and construction history*, *PTEP* **2021** (2021) 05A101 [2005.05574].

[14] KAGRA, VIRGO, LIGO Scientific collaboration, *GWTC-3: Compact Binary Coalescences Observed by LIGO and Virgo during the Second Part of the Third Observing Run*, *Phys. Rev. X* **13** (2023) 041039 [2111.03606].

[15] LIGO Scientific, Virgo collaboration, *GW170817: Observation of Gravitational Waves from a Binary Neutron Star Inspiral*, *Phys. Rev. Lett.* **119** (2017) 161101 [1710.05832].

[16] LIGO Scientific, Virgo collaboration, *GW190521: A Binary Black Hole Merger with a Total Mass of* $150M_{\odot}$, *Phys. Rev. Lett.* **125** (2020) 101102 [2009.01075].

[17] M. Punturo et al., *The Einstein Telescope: A third-generation gravitational wave observatory*, *Class. Quant. Grav.* **27** (2010) 194002.

[18] D. Reitze et al., *Cosmic Explorer: The U.S. Contribution to Gravitational-Wave Astronomy beyond LIGO*, *Bull. Am. Astron. Soc.* **51** (2019) 035 [1907.04833].

[19] KAGRA, LIGO Scientific, VIRGO collaboration, *Prospects for Observing and Localizing Gravitational-Wave Transients with Advanced LIGO, Advanced Virgo and KAGRA*, *Living Rev. Rel.* **21** (2018) 3 [1304.0670].

[20] LISA collaboration, *Laser Interferometer Space Antenna*, 1702.00786.

[21] TianQin collaboration, *TianQin: a space-borne gravitational wave detector*, *Class. Quant. Grav.* **33** (2016) 035010 [1512.02076].

[22] W.-R. Hu and Y.-L. Wu, *The Taiji Program in Space for gravitational wave physics and the nature of gravity*, *Natl. Sci. Rev.* **4** (2017) 685–686.

[23] S. Kawamura et al., *Current status of space gravitational wave antenna DECIGO and B-DECIGO*, *PTEP* **2021** (2021) 05A105 [2006.13545].

[24] Y. B. Zel'dovich and I. D. Novikov, *The Hypothesis of Cores Retarded during Expansion and the Hot Cosmological Model*, *Sov. Astron.* **10** (1967) 602.

[25] S. Hawking, *Gravitationally collapsed objects of very low mass*, *Mon. Not. Roy. Astron. Soc.* **152** (1971) 75.

[26] B. J. Carr and S. W. Hawking, *Black holes in the early Universe*, *Mon. Not. Roy. Astron. Soc.* **168** (1974) 399–415.

[27] B. J. Carr, *The Primordial black hole mass spectrum*, *Astrophys. J.* **201** (1975) 1–19.

[28] KAGRA, Virgo, LIGO Scientific collaboration, *Upper limits on the isotropic gravitational-wave background from Advanced LIGO and Advanced Virgo's third observing run*, *Phys. Rev. D* **104** (2021) 022004 [2101.12130].

[29] T. Regimbau, *The astrophysical gravitational wave stochastic background*, *Res. Astron. Astrophys.* **11** (2011) 369–390 [1101.2762].

[30] H. Estellés, M. Colleoni, C. García-Quirós, S. Husa, D. Keitel, M. Mateu-Lucena et al., *New twists in compact binary waveform modeling: A fast time-domain model for precession*, *Phys. Rev. D* **105** (2022) 084040 [2105.05872].

[31] G. Pratten et al., *Computationally efficient models for the dominant and subdominant harmonic modes of precessing binary black holes*, *Phys. Rev. D* **103** (2021) 104056 [2004.06503].

[32] J. E. Thompson, E. Hamilton, L. London, S. Ghosh, P. Kolitsidou, C. Hoy et al., *PhenomXO4a: a phenomenological gravitational-wave model for precessing black-hole binaries with higher multipoles and asymmetries*, *Phys. Rev. D* **109** (2024) 063012 [2312.10025].

[33] F. Pretorius, *Evolution of binary black hole spacetimes*, *Phys. Rev. Lett.* **95** (2005) 121101 [gr-qc/0507014].

[34] M. Campanelli, C. O. Lousto, P. Marronetti and Y. Zlochower, *Accurate evolutions of orbiting black-hole binaries without excision*, *Phys. Rev. Lett.* **96** (2006) 111101 [gr-qc/0511048].

[35] J. G. Baker, J. Centrella, D.-I. Choi, M. Koppitz and J. van Meter, *Gravitational wave extraction from an inspiraling configuration of merging black holes*, *Phys. Rev. Lett.* **96** (2006) 111102 [gr-qc/0511103].

[36] A. Ramos-Buades, A. Buonanno, H. Estellés, M. Khalil, D. P. Mihaylov, S. Ossokine et al., *Next generation of accurate and efficient multipolar precessing-spin effective-one-body waveforms for binary black holes*, *Phys. Rev. D* **108** (2023) 124037 [2303.18046].

[37] A. Nagar, P. Rettegno, R. Gamba, S. Albanesi, A. Albertini and S. Bernuzzi, *Analytic systematics in next generation of effective-one-body gravitational waveform models for future observations*, *Phys. Rev. D* **108** (2023) 124018 [2304.09662].

[38] L. D. Landau and E. M. Lifschitz, *The Classical Theory of Fields*, vol. 2 of *Course of Theoretical Physics*. Pergamon Press, Oxford, 1975.

[39] M. Maggiore, *Gravitational Waves. Vol. 1: Theory and Experiments*. Oxford University Press, 2007, 10.1093/acprof:oso/9780198570745.001.0001.

[40] M. Maggiore, *Gravitational Waves. Vol. 2: Astrophysics and Cosmology*. Oxford University Press, 3, 2018.

[41] L. Bianchi, *Sui simboli a quattro indici e sulla curvatura di Riemann*, *Rend. Acc. Naz. Lincei* **11** (1902) 3–7.

[42] J. Stewart, *Calculus: early transcendentals*. Brooks/Cole, Cengage Learning, 2012.

[43] S. Chandrasekhar, *The Post-Newtonian Equations of Hydrodynamics in General Relativity.*, *Astrophys. J.* **142** (1965) 1488–1512.

[44] T. Damour, *Gravitational scattering, post-Minkowskian approximation and Effective One-Body theory*, *Phys. Rev. D* **94** (2016) 104015 [1609.00354].

[45] L. Blanchet, *Gravitational Radiation from Post-Newtonian Sources and Inspiralling Compact Binaries*, *Living Rev. Rel.* **17** (2014) 2 [1310.1528].

[46] E. Hamilton, L. London and M. Hannam, *Ringdown frequencies in black holes formed from precessing black-hole binaries*, *Phys. Rev. D* **107** (2023) 104035 [2301.06558].

[47] E. W. Leaver, *An Analytic representation for the quasi normal modes of Kerr black holes*, *Proc. Roy. Soc. Lond. A* **402** (1985) 285–298.

[48] M. Capderou, *Satellites: Orbits and Missions*. Springer, 2005.

[49] O. Montenbruck and E. Gill, *Satellite Orbits: Models, Methods and Applications*. Springer Verlag Berlin, 2000.

[50] P. C. Peters and J. Mathews, *Gravitational radiation from point masses in a Keplerian orbit*, *Phys. Rev.* **131** (1963) 435–439.

[51] P. C. Peters, *Gravitational Radiation and the Motion of Two Point Masses*, *Phys. Rev.* **136** (1964) B1224–B1232.

[52] R. Courant and D. Hilbert, *Methods of mathematical physics, vol. I*. New York: Interscience Publishers, 1953.

[53] J. Garcia-Bellido and S. Nesseris, *Gravitational wave bursts from Primordial Black Hole hyperbolic encounters*, *Phys. Dark Univ.* **18** (2017) 123–126 [1706.02111].

[54] J. García-Bellido and S. Nesseris, *Gravitational wave energy emission and detection rates of Primordial Black Hole hyperbolic encounters*, *Phys. Dark Univ.* **21** (2018) 61–69 [1711.09702].

[55] S. Mukherjee, S. Mitra and S. Chatterjee, *Gravitational wave observatories may be able to detect hyperbolic encounters of black holes*, *Mon. Not. Roy. Astron. Soc.* **508** (2021) 5064–5073 [2010.00916].

[56] R. Gamba, M. Breschi, G. Carullo, S. Albanesi, P. Rettegno, S. Bernuzzi et al., *GW190521 as a dynamical capture of two nonspinning black holes*, *Nature Astron.* **7** (2023) 11–17 [2106.05575].

[57] G. Morrás, J. García-Bellido and S. Nesseris, *Search for black hole hyperbolic encounters with gravitational wave detectors*, *Phys. Dark Univ.* **35** (2022) 100932 [2110.08000].

[58] A. Chowdhuri, R. K. Singh, K. Kangsabanik and A. Bhattacharyya, *Gravitational radiation from hyperbolic encounters in the presence of dark matter*, 2306.11787.

[59] M. Caldarola, S. Kuroyanagi, S. Nesseris and J. Garcia-Bellido, *Effects of orbital precession on hyperbolic encounters*, *Phys. Rev. D* **109** (2024) 064001 [2307.00915].

[60] A. Roskill, M. Caldarola, S. Kuroyanagi and S. Nesseris, *Mass octupole and current quadrupole corrections to gravitational wave emission from close hyperbolic encounters*, 2310.07439.

[61] S. Bini, S. Tiwari, Y. Xu, L. Smith, M. Ebersold, G. Principe et al., *Search for hyperbolic encounters of compact objects in the third LIGO-Virgo-KAGRA observing run*, *Phys. Rev. D* **109** (2024) 042009 [2311.06630].

[62] M. Kerachian, S. Mukherjee, G. Lukes-Gerakopoulos and S. Mitra, *Detectability of stochastic gravitational wave background from weakly hyperbolic encounters*, *Astron. Astrophys.* **684** (2024) A17 [2311.16634].

[63] M. Teuscher, A. Barrau and K. Martineau, *Elementary considerations on gravitational waves from hyperbolic encounters*, 2402.10706.

[64] A. Barrau, J. García-Bellido, K. Martineau and M. Teuscher, *Prospects for detection of ultra high frequency gravitational waves from hyperbolic encounters with resonant cavities*, 2404.08379.

[65] J. García-Bellido and S. Clesse, *Constraints from microlensing experiments on clustered primordial black holes*, *Phys. Dark Univ.* **19** (2018) 144–148 [1710.04694].

[66] M. S. Turner, *Detectability of inflation produced gravitational waves*, *Phys. Rev. D* **55** (1997) R435–R439 [astro-ph/9607066].

[67] S. Capozziello, M. De Laurentis, F. De Paolis, G. Ingrosso and A. Nucita, *Gravitational waves from hyperbolic encounters*, *Mod. Phys. Lett. A* **23** (2008) 99–107 [0801.0122].

[68] L. De Vittori, P. Jetzer and A. Klein, *Gravitational wave energy spectrum of hyperbolic encounters*, *Phys. Rev. D* **86** (2012) 044017 [1207.5359].

[69] M. Turner, *Gravitational radiation from point-masses in unbound orbits: Newtonian results.*, *Astrophys. J.* **216** (1977) 610-619.

[70] K. Crocker, T. Prestegard, V. Mandic, T. Regimbau, K. Olive and E. Vangioni, *Systematic study of the stochastic gravitational-wave background due to stellar core collapse*, *Phys. Rev. D* **95** (2017) 063015 [1701.02638].

[71] M. Arimoto et al., *Gravitational Wave Physics and Astronomy in the nascent era*, 2104.02445.

[72] S. Marassi, R. Schneider and V. Ferrari, *Gravitational wave backgrounds and the cosmic transition from Population III to Population II stars*, *Mon. Not. Roy. Astron. Soc.* **398** (2009) 293 [0906.0461].

[73] B. Allen and J. D. Romano, *Detecting a stochastic background of gravitational radiation: Signal processing strategies and sensitivities*, *Phys. Rev. D* **59** (1999) 102001 [gr-qc/9710117].

[74] M. R. Adams and N. J. Cornish, *Detecting a Stochastic Gravitational Wave Background in the presence of a Galactic Foreground and Instrument Noise*, *Phys. Rev. D* **89** (2014) 022001 [1307.4116].

[75] P. Amaro-Seoane et al., *Low-frequency gravitational-wave science with eLISA/NGO*, *Class. Quant. Grav.* **29** (2012) 124016 [1202.0839].

[76] A. A. Starobinsky, *A New Type of Isotropic Cosmological Models Without Singularity*, *Phys. Lett. B* **91** (1980) 99–102.

[77] M. Giovannini, *Gravitational waves constraints on postinflationary phases stiffer than radiation*, *Phys. Rev. D* **58** (1998) 083504 [hep-ph/9806329].

[78] T. Damour and A. Vilenkin, *Gravitational wave bursts from cosmic strings*, *Phys. Rev. Lett.* **85** (2000) 3761–3764 [gr-qc/0004075].

[79] T. Damour and A. Vilenkin, *Gravitational wave bursts from cusps and kinks on cosmic strings*, *Phys. Rev. D* **64** (2001) 064008 [gr-qc/0104026].

[80] A. Kosowsky and M. S. Turner, *Gravitational radiation from colliding vacuum bubbles: envelope approximation to many bubble collisions*, *Phys. Rev. D* **47** (1993) 4372–4391 [astro-ph/9211004].

[81] J. Garcia-Bellido, M. Peloso and C. Unal, *Gravitational Wave signatures of inflationary models from Primordial Black Hole Dark Matter*, *JCAP* **09** (2017) 013 [1707.02441].

[82] A. Linde, S. Mooij and E. Pajer, *Gauge field production in supergravity inflation: Local non-Gaussianity and primordial black holes*, *Phys. Rev. D* **87** (2013) 103506 [1212.1693].

[83] E. Bugaev and P. Klimai, *Axion inflation with gauge field production and primordial black holes*, *Phys. Rev. D* **90** (2014) 103501 [1312.7435].

[84] V. Domcke, F. Muia, M. Pieroni and L. T. Witkowski, *PBH dark matter from axion inflation*, *JCAP* **07** (2017) 048 [1704.03464].

[85] J. Garcia-Bellido, M. Peloso and C. Unal, *Gravitational waves at interferometer scales and primordial black holes in axion inflation*, *JCAP* **12** (2016) 031 [1610.03763].

[86] O. Özsoy and Z. Lalak, *Primordial black holes as dark matter and gravitational waves from bumpy axion inflation*, *JCAP* **01** (2021) 040 [2008.07549].

[87] O. Özsoy, *Synthetic Gravitational Waves from a Rolling Axion Monodromy*, *JCAP* **04** (2021) 040 [2005.10280].

[88] C. T. Byrnes, P. S. Cole and S. P. Patil, *Steepest growth of the power spectrum and primordial black holes*, *JCAP* **06** (2019) 028 [1811.11158].

[89] T. Nakama, *Stochastic gravitational waves associated with primordial black holes formed during an early matter era*, *Phys. Rev. D* **101** (2020) 063519.

[90] C. Ünal, E. D. Kovetz and S. P. Patil, *Multimessenger probes of inflationary fluctuations and primordial black holes*, *Phys. Rev. D* **103** (2021) 063519 [2008.11184].

[91] K. N. Ananda, C. Clarkson and D. Wands, *The Cosmological gravitational wave background from primordial density perturbations*, *Phys. Rev. D* **75** (2007) 123518 [gr-qc/0612013].

[92] D. Baumann, P. J. Steinhardt, K. Takahashi and K. Ichiki, *Gravitational Wave Spectrum Induced by Primordial Scalar Perturbations*, *Phys. Rev. D* **76** (2007) 084019 [hep-th/0703290].

[93] R. Saito and J. Yokoyama, *Gravitational wave background as a probe of the primordial black hole abundance*, *Phys. Rev. Lett.* **102** (2009) 161101 [0812.4339].

[94] G. Domènech, *Scalar Induced Gravitational Waves Review*, *Universe* **7** (2021) 398 [2109.01398].

[95] K. Inomata and T. Nakama, *Gravitational waves induced by scalar perturbations as probes of the small-scale primordial spectrum*, *Phys. Rev. D* **99** (2019) 043511 [1812.00674].

[96] S. J. Kapadia, K. Lal Pandey, T. Suyama, S. Kandhasamy and P. Ajith, *Search for the Stochastic Gravitational-wave Background Induced by Primordial Curvature Perturbations in LIGO's Second Observing Run*, *Astrophys. J. Lett.* **910** (2021) L4 [2009.05514].

[97] A. Romero-Rodriguez, M. Martinez, O. Pujolàs, M. Sakellariadou and V. Vaskonen, *Search for a Scalar Induced Stochastic Gravitational Wave Background in the Third LIGO-Virgo Observing Run*, *Phys. Rev. Lett.* **128** (2022) 051301 [2107.11660].

[98] A. Romero-Rodriguez and S. Kuroyanagi, *LVK constraints on PBHs from stochastic gravitational wave background searches*, 2024.

[99] T.-H. Yeh, J. Shelton, K. A. Olive and B. D. Fields, *Probing physics beyond the standard model: limits from BBN and the CMB independently and combined*, *JCAP* **10** (2022) 046 [2207.13133].

[100] BICEP, Keck collaboration, *Improved Constraints on Primordial Gravitational Waves using Planck, WMAP, and BICEP/Keck Observations through the 2018 Observing Season*, *Phys. Rev. Lett.* **127** (2021) 151301 [2110.00483].

[101] LIGO Scientific, Virgo collaboration, *GW150914: Implications for the stochastic gravitational wave background from binary black holes*, *Phys. Rev. Lett.* **116** (2016) 131102 [1602.03847].

[102] LIGO Scientific collaboration, *Exploring the Sensitivity of Next Generation Gravitational Wave Detectors*, *Class. Quant. Grav.* **34** (2017) 044001 [1607.08697].

[103] M. Colpi et al., *LISA Definition Study Report*, 2402.07571.

[104] P. E. Dewdney, P. J. Hall, R. T. Schilizzi and T. J. L. W. Lazio, *The Square Kilometre Array*, in *Proceedings of the IEEE*, vol. 97, pp. 1482–1496, 8, 2009, DOI.

[105] LiteBIRD collaboration, *LiteBIRD: JAXA's new strategic L-class mission for all-sky surveys of cosmic microwave background polarization*, *Proc. SPIE Int. Soc. Opt. Eng.* **11443** (2020) 114432F [2101.12449].

[106] KAGRA, VIRGO, LIGO Scientific collaboration, *Population of Merging Compact Binaries Inferred Using Gravitational Waves through GWTC-3*, *Phys. Rev. X* **13** (2023) 011048 [2111.03634].

[107] D. J. D'Orazio and J. Samsing, *Black Hole Mergers From Globular Clusters Observable by LISA II: Resolved Eccentric Sources and the Gravitational Wave Background*, *Mon. Not. Roy. Astron. Soc.* **481** (2018) 4775–4785 [1805.06194].

[108] Y. Zhao and Y. Lu, *Stochastic Gravitational Wave Background and Eccentric Stellar Compact Binaries*, *Mon. Not. Roy. Astron. Soc.* **500** (2020) 1421–1436 [2009.01436].

[109] A. I. Renzini, B. Goncharov, A. C. Jenkins and P. M. Meyers, *Stochastic Gravitational-Wave Backgrounds: Current Detection Efforts and Future Prospects*, *Galaxies* **10** (2022) 34 [2202.00178].

[110] A. I. Renzini et al., *pygwb: A Python-based Library for Gravitational-wave Background Searches*, *Astrophys. J.* **952** (2023) 25 [2303.15696].

[111] E. Thrane, S. Ballmer, J. D. Romano, S. Mitra, D. Talukder, S. Bose et al., *Probing the anisotropies of a stochastic gravitational-wave background using a network of ground-based laser interferometers*, *Phys. Rev. D* **80** (2009) 122002 [0910.0858].

[112] J. D. Romano and N. J. Cornish, *Detection methods for stochastic gravitational-wave backgrounds: a unified treatment*, *Living Rev. Rel.* **20** (2017) 2 [1608.06889].

[113] M. Rouaud, *Probability, statistics and estimation*, *Propagation of uncertainties* **191** (2013) 1110.

[114] J. L. Cook and L. Sorbo, *Particle production during inflation and gravitational waves detectable by ground-based interferometers*, *Phys. Rev. D* **85** (2012) 023534 [1109.0022].

[115] B. F. Schutz, *Networks of gravitational wave detectors and three figures of merit*, *Class. Quant. Grav.* **28** (2011) 125023 [1102.5421].

[116] LIGO Scientific, VIRGO collaboration, *Searching for stochastic gravitational waves using data from the two colocated LIGO Hanford detectors*, *Phys. Rev. D* **91** (2015) 022003 [1410.6211].

[117] P. M. Meyers, K. Martinovic, N. Christensen and M. Sakellariadou, *Detecting a stochastic gravitational-wave background in the presence of correlated magnetic noise*, *Phys. Rev. D* **102** (2020) 102005 [2008.00789].

[118] I. Kowalska-Leszczynska et al., *Globally coherent short duration magnetic field transients and their effect on ground based gravitational-wave detectors*, *Class. Quant. Grav.* **34** (2017) 074002 [1612.01102].

[119] M. W. Coughlin et al., *Measurement and subtraction of Schumann resonances at gravitational-wave interferometers*, *Phys. Rev. D* **97** (2018) 102007 [1802.00885].

[120] E. Thrane, N. Christensen and R. Schofield, *Correlated magnetic noise in global networks of gravitational-wave interferometers: observations and implications*, *Phys. Rev. D* **87** (2013) 123009 [1303.2613].

[121] E. Thrane, N. Christensen, R. M. S. Schofield and A. Effler, *Correlated noise in networks of gravitational-wave detectors: subtraction and mitigation*, *Phys. Rev. D* **90** (2014) 023013 [1406.2367].

[122] LIGO Scientific, Virgo collaboration, *Search for the isotropic stochastic background using data from Advanced LIGO's second observing run*, *Phys. Rev. D* **100** (2019) 061101 [1903.02886].

[123] D. R. Cox, *Principles of Statistical Inference*. Cambridge University Press, 2006.

[124] G. Ashton et al., *BILBY: A user-friendly Bayesian inference library for gravitational-wave astronomy*, *Astrophys. J. Suppl.* **241** (2019) 27 [1811.02042].

[125] R. E. Kass and A. E. Raftery, *Bayes factors*, *Journal of the American Statistical Association* **90** (1995) 773-795.

[126] E. Thrane and C. Talbot, *An introduction to Bayesian inference in gravitational-wave astronomy: parameter estimation, model selection, and hierarchical models*, *Publ. Astron. Soc. Austral.* **36** (2019) e010 [1809.02293].

[127] N. Metropolis, A. W. Rosenbluth, M. N. Rosenbluth, A. H. Teller and E. Teller, *Equation of state calculations by fast computing machines*, *J. Chem. Phys.* **21** (1953) 1087–1092.

[128] W. K. Hastings, *Monte Carlo Sampling Methods Using Markov Chains and Their Applications*, *Biometrika* **57** (1970) 97–109.

[129] N. Metropolis and S. Ulam, *The monte carlo method*, *Journal of the American Statistical Association* **44** (1949) 335–341.

[130] N. Metropolis, *The Beginning of the Monte Carlo Method*, in *Los Alamos Science Special Issue*, vol. 15, pp. 125–130, 1987.

[131] D. Foreman-Mackey, D. W. Hogg, D. Lang and J. Goodman, *emcee: The MCMC Hammer*, *Publ. Astron. Soc. Pac.* **125** (2013) 306–312 [1202.3665].

[132] A.-P. Oriol, A. Virgile, C. Colin, D. Larry, F. C. J., K. Maxim et al., *Pymc: A modern and comprehensive probabilistic programming framework in python*, *PeerJ Computer Science* **9** (2023) e1516.

[133] J. Goodman and J. Weare, *Ensemble samplers with affine invariance*, *Communications in Applied Mathematics and Computational Science* **5** (2010) 65-80.

[134] J. Skilling, *Nested Sampling*, *AIP Conf. Proc.* **735** (2004) 395.

[135] J. Buchner, A. Georgakakis, K. Nandra, L. Hsu, C. Rangel, M. Brightman et al., *X-ray spectral modelling of the AGN obscuring region in the CDFS: Bayesian model selection and catalogue*, *Astron. Astrophys.* **564** (2014) A125 [1402.0004].

[136] W. J. Handley, M. P. Hobson and A. N. Lasenby, *PolyChord: nested sampling for cosmology*, *Mon. Not. Roy. Astron. Soc.* **450** (2015) L61–L65 [1502.01856].

[137] W. J. Handley, M. P. Hobson and A. N. Lasenby, *polychord: next-generation nested sampling*, *Mon. Not. Roy. Astron. Soc.* **453** (2015) 4385–4399 [1506.00171].

[138] J. S. Speagle, *dynesty: a dynamic nested sampling package for estimating Bayesian posteriors and evidences*, *Mon. Not. Roy. Astron. Soc.* **493** (2020) 3132–3158 [1904.02180].

[139] LIGO Scientific, Virgo collaboration, *Upper Limits on the Stochastic Gravitational-Wave Background from Advanced LIGO's First Observing Run*, *Phys. Rev. Lett.* **118** (2017) 121101 [1612.02029].

[140] J. Darling, A. E. Truebenbach and J. Paine, *Astrometric Limits on the Stochastic Gravitational Wave Background*, *Astrophys. J.* **861** (2018) 113 [1804.06986].

[141] "*Note about sigmas* in corner python package documentation." https://corner.readthedocs.io/en/latest/pages/sigmas/.

[142] J. García-Bellido, *An analytical approach to Bayesian evidence computation*, *Universe* **9** (2023) 118 [2301.13783].

[143] J. T. Whelan, E. L. Robinson, J. D. Romano and E. H. Thrane, *Treatment of Calibration Uncertainty in Multi-Baseline Cross-Correlation Searches for Gravitational Waves*, *J. Phys. Conf. Ser.* **484** (2014) 012027 [1205.3112].

[144] A. A. Starobinsky, *Spectrum of relict gravitational radiation and the early state of the universe*, *JETP Lett.* **30** (1979) 682–685.

[145] A. Matas, I. Dvorkin, T. Regimbau, and A. Romero. https://dcc.ligo.org/T2000512/public, 2021.

[146] LIGO Scientific collaboration, *Searching for a Stochastic Background of Gravitational Waves with LIGO*, *Astrophys. J.* **659** (2007) 918–930 [astro-ph/0608606].

[147] https://pypi.org/project/pygwb.

[148] J. M. Ezquiaga and J. García-Bellido, *Quantum diffusion beyond slow-roll: implications for primordial black-hole production*, *JCAP* **08** (2018) 018 [1805.06731].

[149] J. M. Ezquiaga, J. García-Bellido and V. Vennin, *The exponential tail of inflationary fluctuations: consequences for primordial black holes*, *JCAP* **03** (2020) 029 [1912.05399].

[150] J. M. Ezquiaga, J. García-Bellido and V. Vennin, *Massive Galaxy Clusters Like El Gordo Hint at Primordial Quantum Diffusion*, *Phys. Rev. Lett.* **130** (2023) 121003 [2207.06317].

[151] M. Biagetti, G. Franciolini, A. Kehagias and A. Riotto, *Primordial Black Holes from Inflation and Quantum Diffusion*, *JCAP* **07** (2018) 032 [1804.07124].

[152] K. Kohri and T. Terada, *Semianalytic calculation of gravitational wave spectrum nonlinearly induced from primordial curvature perturbations*, *Phys. Rev. D* **97** (2018) 123532 [1804.08577].

[153] K. T. Abe, R. Inui, Y. Tada and S. Yokoyama, *Primordial black holes and gravitational waves induced by exponential-tailed perturbations*, *JCAP* **05** (2023) 044 [2209.13891].

[154] P. Adshead, K. D. Lozanov and Z. J. Weiner, *Non-Gaussianity and the induced gravitational wave background*, *JCAP* **10** (2021) 080 [2105.01659].

[155] R.-g. Cai, S. Pi and M. Sasaki, *Gravitational Waves Induced by non-Gaussian Scalar Perturbations*, *Phys. Rev. Lett.* **122** (2019) 201101 [1810.11000].

[156] C. Unal, *Imprints of Primordial Non-Gaussianity on Gravitational Wave Spectrum*, *Phys. Rev. D* **99** (2019) 041301 [1811.09151].

[157] LIGO Scientific, Virgo collaboration, *Open data from the first and second observing runs of Advanced LIGO and Advanced Virgo*, *SoftwareX* **13** (2021) 100658 [1912.11716].

[158] KAGRA, VIRGO, LIGO Scientific collaboration, *Open Data from the Third Observing Run of LIGO, Virgo, KAGRA, and GEO*, *Astrophys. J. Suppl.* **267** (2023) 29 [2302.03676].

[159] J. M. Bardeen, J. R. Bond, N. Kaiser and A. S. Szalay, *The Statistics of Peaks of Gaussian Random Fields*, *Astrophys. J.* **304** (1986) 15–61.

[160] C.-M. Yoo, T. Harada, J. Garriga and K. Kohri, *Primordial black hole abundance from random Gaussian curvature perturbations and a local density threshold*, *PTEP* **2018** (2018) 123E01 [1805.03946].

[161] C.-M. Yoo, J.-O. Gong and S. Yokoyama, *Abundance of primordial black holes with local non-Gaussianity in peak theory*, *JCAP* **09** (2019) 033 [1906.06790].

[162] N. Kitajima, Y. Tada, S. Yokoyama and C.-M. Yoo, *Primordial black holes in peak theory with a non-Gaussian tail*, *JCAP* **10** (2021) 053 [2109.00791].

[163] Y.-F. Cai, X. Chen, M. H. Namjoo, M. Sasaki, D.-G. Wang and Z. Wang, *Revisiting non-Gaussianity from non-attractor inflation models*, *JCAP* **05** (2018) 012 [1712.09998].

[164] V. Atal, J. Cid, A. Escrivà and J. Garriga, *PBH in single field inflation: the effect of shape dispersion and non-Gaussianities*, *JCAP* **05** (2020) 022 [1908.11357].

[165] H. V. Ragavendra, *Accounting for scalar non-Gaussianity in secondary gravitational waves*, *Phys. Rev. D* **105** (2022) 063533 [2108.04193].

[166] S. Pi and M. Sasaki, *Primordial Black Hole Formation in Non-Minimal Curvaton Scenario*, 2112.12680.

[167] Y.-F. Cai, X.-H. Ma, M. Sasaki, D.-G. Wang and Z. Zhou, *One small step for an inflaton, one giant leap for inflation: A novel non-Gaussian tail and primordial black holes*, *Phys. Lett. B* **834** (2022) 137461 [2112.13836].

[168] LISA Cosmology Working Group collaboration, *Cosmology with the Laser Interferometer Space Antenna*, *Living Rev. Rel.* **26** (2023) 5 [2204.05434].

[169] S. Pi and M. Sasaki, *Logarithmic Duality of the Curvature Perturbation*, *Phys. Rev. Lett.* **131** (2023) 011002 [2211.13932].

[170] LIGO Scientific collaboration, *Directional limits on persistent gravitational waves using LIGO S5 science data*, *Phys. Rev. Lett.* **107** (2011) 271102 [1109.1809].

[171] KAGRA, Virgo, LIGO Scientific collaboration, *All-sky, all-frequency directional search for persistent gravitational waves from Advanced LIGO's and Advanced Virgo's first three observing runs*, *Phys. Rev. D* **105** (2022) 122001 [2110.09834].

[172] LIGO Scientific collaboration, *Analysis of first LIGO science data for stochastic gravitational waves*, *Phys. Rev. D* **69** (2004) 122004 [gr-qc/0312088].

[173] Planck collaboration, *Planck 2018 results. I. Overview and the cosmological legacy of Planck*, *Astron. Astrophys.* **641** (2020) A1 [1807.06205].

[174] Planck collaboration, *Planck 2018 results. VII. Isotropy and Statistics of the CMB*, *Astron. Astrophys.* **641** (2020) A7 [1906.02552].

[175] S. W. Ballmer, *A Radiometer for stochastic gravitational waves*, *Class. Quant. Grav.* **23** (2006) S179–S186 [gr-qc/0510096].

[176] S. Ballmer, *LIGO interferometer operating at design sensitivity with application to gravitational radiometry*, Ph.D. thesis, Massachusetts Institute of Technology, 2006.

[177] S. Mitra, S. Dhurandhar, T. Souradeep, A. Lazzarini, V. Mandic, S. Bose et al., *Gravitational wave radiometry: Mapping a stochastic gravitational wave background*, *Phys. Rev. D* **77** (2008) 042002 [0708.2728].

[178] B. Allen and A. C. Ottewill, *Detection of anisotropies in the gravitational wave stochastic background*, *Phys. Rev. D* **56** (1997) 545–563 [gr-qc/9607068].

[179] C. R. Contaldi, *Anisotropies of gravitational wave backgrounds: A line of sight approach*, *Physics Letters B* **771** (2017) 9-12 [1609.08168].

[180] A. C. Jenkins, R. O'Shaughnessy, M. Sakellariadou and D. Wysocki, *Anisotropies in the astrophysical gravitational-wave background: The impact of black hole distributions*, *Phys. Rev. Lett.* **122** (2019) 111101 [1810.13435].

[181] A. C. Jenkins and M. Sakellariadou, *Shot noise in the astrophysical gravitational-wave background*, *Phys. Rev. D* **100** (2019) 063508 [1902.07719].

[182] A. C. Jenkins, J. D. Romano and M. Sakellariadou, *Estimating the angular power spectrum of the gravitational-wave background in the presence of shot noise*, *Phys. Rev. D* **100** (2019) 083501 [1907.06642].

[183] D. Bertacca, A. Ricciardone, N. Bellomo, A. C. Jenkins, S. Matarrese, A. Raccanelli et al., *Projection effects on the observed angular spectrum of the astrophysical stochastic gravitational wave background*, *Phys. Rev. D* **101** (2020) 103513 [1909.11627].

[184] G. Cusin, C. Pitrou and J.-P. Uzan, *Anisotropy of the astrophysical gravitational wave background: Analytic expression of the angular power spectrum and correlation with cosmological observations*, *Phys. Rev. D* **96** (2017) 103019 [1704.06184].

[185] G. Cusin, C. Pitrou and J.-P. Uzan, *The signal of the gravitational wave background and the angular correlation of its energy density*, *Phys. Rev.* **D97** (2018) 123527 [1711.11345].

[186] G. Cusin, I. Dvorkin, C. Pitrou and J.-P. Uzan, *First predictions of the angular power spectrum of the astrophysical gravitational wave background*, *Phys. Rev. Lett.* **120** (2018) 231101 [1803.03236].

[187] G. Cusin, I. Dvorkin, C. Pitrou and J.-P. Uzan, *Properties of the stochastic astrophysical gravitational wave background: astrophysical sources dependencies*, *Phys. Rev. D* **100** (2019) 063004 [1904.07797].

[188] C. Pitrou, G. Cusin and J.-P. Uzan, *Unified view of anisotropies in the astrophysical gravitational-wave background*, *Phys. Rev. D* **101** (2020) 081301 [1910.04645].

[189] G. Cañas Herrera, O. Contigiani and V. Vardanyan, *Cross-correlation of the astrophysical gravitational-wave background with galaxy clustering*, *Phys. Rev. D* **102** (2020) 043513 [1910.08353].

[190] M. Geller, A. Hook, R. Sundrum and Y. Tsai, *Primordial Anisotropies in the Gravitational Wave Background from Cosmological Phase Transitions*, *Phys. Rev. Lett.* **121** (2018) 201303 [1803.10780].

[191] LIGO Scientific Collaboration and Virgo Collaboration collaboration, *An upper limit on the stochastic gravitational-wave background of cosmological origin*, *Nature* **460** (2009) 990-994.

[192] LIGO Scientific, Virgo collaboration, *Directional Limits on Persistent Gravitational Waves from Advanced LIGO's First Observing Run*, *Phys. Rev. Lett.* **118** (2017) 121102 [1612.02030].

[193] LIGO Scientific, Virgo collaboration, *Directional limits on persistent gravitational waves using data from Advanced LIGO's first two observing runs*, *Phys. Rev. D* **100** (2019) 062001 [1903.08844].

[194] KAGRA, Virgo, LIGO Scientific collaboration, *Search for anisotropic gravitational-wave backgrounds using data from Advanced LIGO and Advanced Virgo's first three observing runs*, *Phys. Rev. D* **104** (2021) 022005 [2103.08520].

[195] A. K.-W. Chung, A. C. Jenkins, J. D. Romano and M. Sakellariadou, *Targeted search for the kinematic dipole of the gravitational-wave background*, *Phys. Rev. D* **106** (2022) 082005 [2208.01330].

[196] D. Agarwal, J. Suresh, V. Mandic, A. Matas and T. Regimbau, *Targeted search for the stochastic gravitational-wave background from the galactic millisecond pulsar population*, *Phys. Rev. D* **106** (2022) 043019 [2204.08378].

[197] P. J. E. Peebles and D. T. Wilkinson, *Comment on the Anisotropy of the Primeval Fireball*, *Phys. Rev.* **174** (1968) 2168–2168.

[198] A. Kogut et al., *Dipole anisotropy in the COBE DMR first year sky maps*, *Astrophys. J.* **419** (1993) 1 [astro-ph/9312056].

[199] G. F. Chapline, *Cosmological effects of primordial black holes*, *Nature* **253** (1975) 251–252.

[200] LISA Cosmology Working Group collaboration, *Primordial black holes and their gravitational-wave signatures*, 2310.19857.

[201] I. Musco, *Threshold for primordial black holes: Dependence on the shape of the cosmological perturbations*, *Phys. Rev. D* **100** (2019) 123524 [1809.02127].

[202] I. Musco, V. De Luca, G. Franciolini and A. Riotto, *Threshold for primordial black holes. II. A simple analytic prescription*, *Phys. Rev. D* **103** (2021) 063538 [2011.03014].

[203] A. G. Polnarev and I. Musco, *Curvature profiles as initial conditions for primordial black hole formation*, *Class. Quant. Grav.* **24** (2007) 1405–1432 [gr-qc/0605122].

[204] A. Escrivà, *Simulation of primordial black hole formation using pseudo-spectral methods*, *Phys. Dark Univ.* **27** (2020) 100466 [1907.13065].

[205] A. Escrivà, C. Germani and R. K. Sheth, *Universal threshold for primordial black hole formation*, *Phys. Rev. D* **101** (2020) 044022 [1907.13311].

[206] A. Dolgov and J. Silk, *Baryon isocurvature fluctuations at small scales and baryonic dark matter*, *Phys. Rev. D* **47** (1993) 4244–4255.

[207] B. J. Carr and J. E. Lidsey, *Primordial black holes and generalized constraints on chaotic inflation*, *Phys. Rev. D* **48** (1993) 543–553.

[208] B. J. Carr, J. H. Gilbert and J. E. Lidsey, *Black hole relics and inflation: Limits on blue perturbation spectra*, *Phys. Rev. D* **50** (1994) 4853–4867 [astro-ph/9405027].

[209] P. Ivanov, P. Naselsky and I. Novikov, *Inflation and primordial black holes as dark matter*, *Phys. Rev. D* **50** (1994) 7173–7178.

[210] J. Garcia-Bellido, A. D. Linde and D. Wands, *Density perturbations and black hole formation in hybrid inflation*, *Phys. Rev. D* **54** (1996) 6040–6058 [astro-ph/9605094].

[211] J. M. Ezquiaga, J. Garcia-Bellido and E. Ruiz Morales, *Primordial Black Hole production in Critical Higgs Inflation*, *Phys. Lett. B* **776** (2018) 345–349 [1705.04861].

[212] J. García-Bellido, *Massive Primordial Black Holes as Dark Matter and their detection with Gravitational Waves*, *J. Phys. Conf. Ser.* **840** (2017) 012032 [1702.08275].

[213] A. D. Linde, *Hybrid inflation*, *Phys. Rev. D* **49** (1994) 748–754 [astro-ph/9307002].

[214] E. J. Copeland, A. R. Liddle, D. H. Lyth, E. D. Stewart and D. Wands, *False vacuum inflation with Einstein gravity*, *Phys. Rev. D* **49** (1994) 6410–6433 [astro-ph/9401011].

[215] S. Clesse and J. García-Bellido, *Massive Primordial Black Holes from Hybrid Inflation as Dark Matter and the seeds of Galaxies*, *Phys. Rev. D* **92** (2015) 023524 [1501.07565].

[216] V. Vennin and D. Wands, *Quantum diffusion and large primordial perturbations from inflation*, 2402.12672.

[217] B. Carr, S. Clesse and J. García-Bellido, *Primordial black holes from the QCD epoch: Linking dark matter, baryogenesis and anthropic selection*, *Mon. Not. Roy. Astron. Soc.* **501** (2021) 1426–1439 [1904.02129].

[218] K. Jedamzik, *Primordial black hole formation during the QCD epoch*, *Phys. Rev. D* **55** (1997) 5871–5875 [astro-ph/9605152].

[219] M. Khlopov, B. A. Malomed and I. B. Zeldovich, *Gravitational instability of scalar fields and formation of primordial black holes*, *Mon. Not. Roy. Astron. Soc.* **215** (1985) 575–589.

[220] A. Polnarev and R. Zembowicz, *Formation of Primordial Black Holes by Cosmic Strings*, *Phys. Rev. D* **43** (1991) 1106–1109.

[221] J. Garcia-Bellido and E. Ruiz Morales, *Primordial black holes from single field models of inflation*, *Phys. Dark Univ.* **18** (2017) 47–54 [1702.03901].

[222] K. Inomata, M. Braglia, X. Chen and S. Renaux-Petel, *Questions on calculation of primordial power spectrum with large spikes: the resonance model case*, *JCAP* **04** (2023) 011 [2211.02586].

[223] D. K. Nadezhin, I. D. Novikov and A. G. Polnarev, *The hydrodynamics of primordial black hole formation*, *Sov. Astron.* **22** (1978) 129-138.

[224] G. V. Bicknell and R. N. Henriksen, *Formation of primordial black holes.*, *Astrophys. J.* **232** (1979) 670-682.

[225] I. D. Novikov and A. G. Polnarev, *The Hydrodynamics of Primordial Black Hole Formation - Dependence on the Equation of State*, *Sov. Astron.* **24** (1980) 147-151.

[226] M. W. Choptuik, *Universality and scaling in gravitational collapse of a massless scalar field*, *Phys. Rev. Lett.* **70** (1993) 9–12.

[227] K. Jedamzik and J. C. Niemeyer, *Primordial black hole formation during first order phase transitions*, *Phys. Rev. D* **59** (1999) 124014 [astro-ph/9901293].

[228] M. Shibata and M. Sasaki, *Black hole formation in the Friedmann universe: Formulation and computation in numerical relativity*, *Phys. Rev. D* **60** (1999) 084002 [gr-qc/9905064].

[229] I. Hawke and J. M. Stewart, *The dynamics of primordial black hole formation*, *Class. Quant. Grav.* **19** (2002) 3687–3707.

[230] I. Musco, J. C. Miller and L. Rezzolla, *Computations of primordial black hole formation*, *Class. Quant. Grav.* **22** (2005) 1405–1424 [gr-qc/0412063].

[231] I. Musco, J. C. Miller and A. G. Polnarev, *Primordial black hole formation in the radiative era: Investigation of the critical nature of the collapse*, *Class. Quant. Grav.* **26** (2009) 235001 [0811.1452].

[232] I. Musco and J. C. Miller, *Primordial black hole formation in the early universe: critical behaviour and self-similarity*, *Class. Quant. Grav.* **30** (2013) 145009 [1201.2379].

[233] C. W. Misner and D. H. Sharp, *Relativistic equations for adiabatic, spherically symmetric gravitational collapse*, *Phys. Rev.* **136** (1964) B571–B576.

[234] W. C. Hernandez and C. W. Misner, *Observer Time as a Coordinate in Relativistic Spherical Hydrodynamics*, *Astrophys. J.* **143** (1966) 452.

[235] M. M. May and R. H. White, *Hydrodynamic Calculations of General-Relativistic Collapse*, *Phys. Rev.* **141** (1966) 1232–1241.

[236] D. H. Lyth, K. A. Malik and M. Sasaki, *A General proof of the conservation of the curvature perturbation*, *JCAP* **05** (2005) 004 [astro-ph/0411220].

[237] P. Virtanen et al., *SciPy 1.0–Fundamental Algorithms for Scientific Computing in Python*, *Nature Meth.* **17** (2020) 261 [1907.10121].

[238] J. P. Boyd, *Chebyshev and Fourier Spectral Methods*. Dover, 2000.

[239] L. N. Trefethen, *Spectral Methods in MATLAB*. SIAM, 2000.

[240] I. Musco, K. Jedamzik and S. Young, *Primordial black hole formation during the QCD phase transition: Threshold, mass distribution, and abundance*, *Phys. Rev. D* **109** (2024) 083506 [2303.07980].

[241] B. Carr, S. Clesse, J. García-Bellido and F. Kühnel, *Cosmic conundra explained by thermal history and primordial black holes*, *Phys. Dark Univ.* **31** (2021) 100755 [1906.08217].

[242] S. Clesse and J. Garcia-Bellido, *GW190425, GW190521 and GW190814: Three candidate mergers of primordial black holes from the QCD epoch*, *Phys. Dark Univ.* **38** (2022) 101111 [2007.06481].

[243] V. De Luca, G. Franciolini and A. Riotto, *NANOGrav Data Hints at Primordial Black Holes as Dark Matter*, *Phys. Rev. Lett.* **126** (2021) 041303 [2009.08268].

[244] C. T. Byrnes, M. Hindmarsh, S. Young and M. R. S. Hawkins, *Primordial black holes with an accurate QCD equation of state*, *JCAP* **08** (2018) 041 [1801.06138].

[245] S. Clesse and J. García-Bellido, *The clustering of massive Primordial Black Holes as Dark Matter: measuring their mass distribution with Advanced LIGO*, *Phys. Dark Univ.* **15** (2017) 142–147 [1603.05234].

[246] T. Nakamura, M. Sasaki, T. Tanaka and K. S. Thorne, *Gravitational waves from coalescing black hole MACHO binaries*, *Astrophys. J. Lett.* **487** (1997) L139–L142 [astro-ph/9708060].

[247] M. Sasaki, T. Suyama, T. Tanaka and S. Yokoyama, *Primordial Black Hole Scenario for the Gravitational-Wave Event GW150914*, *Phys. Rev. Lett.* **117** (2016) 061101 [1603.08338].

[248] M. Raidal, C. Spethmann, V. Vaskonen and H. Veermäe, *Formation and Evolution of Primordial Black Hole Binaries in the Early Universe*, *JCAP* **02** (2019) 018 [1812.01930].

[249] S. S. G.D. Quinlan, *Dynamical evolution of dense clusters of compact stars*, *Astrophys. J.* **343** (1989) 725-749.

[250] H. Mouri and Y. Taniguchi, *Runaway merging of black holes: analytical constraint on the timescale*, *Astrophys. J. Lett.* **566** (2002) L17–L20 [astro-ph/0201102].

[251] S. Clesse and J. García-Bellido, *Detecting the gravitational wave background from primordial black hole dark matter*, *Phys. Dark Univ.* **18** (2017) 105-114 [1610.08479].

[252] G. Hütsi, M. Raidal, V. Vaskonen and H. Veermäe, *Two populations of LIGO-Virgo black holes*, *JCAP* **03** (2021) 068 [2012.02786].

[253] V. De Luca, G. Franciolini, P. Pani and A. Riotto, *Primordial Black Holes Confront LIGO/Virgo data: Current situation*, *JCAP* **06** (2020) 044 [2005.05641].

[254] Y. Ali-Haïmoud, E. D. Kovetz and M. Kamionkowski, *Merger rate of primordial black-hole binaries*, *Phys. Rev. D* **96** (2017) 123523 [1709.06576].

[255] B. Kocsis, T. Suyama, T. Tanaka and S. Yokoyama, *Hidden universality in the merger rate distribution in the primordial black hole scenario*, *Astrophys. J.* **854** (2018) 41 [1709.09007].

[256] Y. N. Eroshenko, *Gravitational waves from primordial black holes collisions in binary systems*, *J. Phys. Conf. Ser.* **1051** (2018) 012010 [1604.04932].

[257] V. Vaskonen and H. Veermäe, *Lower bound on the primordial black hole merger rate*, *Phys. Rev. D* **101** (2020) 043015 [1908.09752].

[258] LIGO Scientific, Virgo collaboration, *GWTC-2: Compact Binary Coalescences Observed by LIGO and Virgo During the First Half of the Third Observing Run*, *Phys. Rev. X* **11** (2021) 021053 [2010.14527].

[259] K. Jedamzik, *Primordial Black Hole Dark Matter and the LIGO/Virgo observations*, *JCAP* **09** (2020) 022 [2006.11172].

[260] K. Jedamzik, *Consistency of Primordial Black Hole Dark Matter with LIGO/Virgo Merger Rates*, *Phys. Rev. Lett.* **126** (2021) 051302 [2007.03565].

[261] A. Hall, A. D. Gow and C. T. Byrnes, *Bayesian analysis of LIGO-Virgo mergers: Primordial vs. astrophysical black hole populations*, *Phys. Rev. D* **102** (2020) 123524 [2008.13704].

[262] G. Franciolini, V. Baibhav, V. De Luca, K. K. Y. Ng, K. W. K. Wong, E. Berti et al., *Searching for a subpopulation of primordial black holes in LIGO-Virgo gravitational-wave data*, *Phys. Rev. D* **105** (2022) 083526 [2105.03349].

[263] N. Fernandez and S. Profumo, *Unraveling the origin of black holes from effective spin measurements with LIGO-Virgo*, *JCAP* **08** (2019) 022 [1905.13019].

[264] J. García-Bellido, J. F. Nuño Siles and E. Ruiz Morales, *Bayesian analysis of the spin distribution of LIGO/Virgo black holes*, *Phys. Dark Univ.* **31** (2021) 100791 [2010.13811].

[265] E. Bugaev and P. Klimai, *Induced gravitational wave background and primordial black holes*, *Phys. Rev. D* **81** (2010) 023517 [0908.0664].

[266] R. Saito and J. Yokoyama, *Gravitational-Wave Constraints on the Abundance of Primordial Black Holes*, *Prog. Theor. Phys.* **123** (2010) 867–886 [0912.5317].

[267] V. Mandic, S. Bird and I. Cholis, *Stochastic Gravitational-Wave Background due to Primordial Binary Black Hole Mergers*, *Phys. Rev. Lett.* **117** (2016) 201102 [1608.06699].

[268] M. Raidal, V. Vaskonen and H. Veermäe, *Gravitational Waves from Primordial Black Hole Mergers*, *JCAP* **09** (2017) 037 [1707.01480].

[269] Z.-C. Chen, F. Huang and Q.-G. Huang, *Stochastic Gravitational-wave Background from Binary Black Holes and Binary Neutron Stars and Implications for LISA*, *Astrophys. J.* **871** (2019) 97 [1809.10360].

[270] S. Wang, T. Terada and K. Kohri, *Prospective constraints on the primordial black hole abundance from the stochastic gravitational-wave backgrounds produced by coalescing events and curvature perturbations*, *Phys. Rev. D* **99** (2019) 103531 [1903.05924].

[271] S. Wang, Y.-F. Wang, Q.-G. Huang and T. G. F. Li, *Constraints on the Primordial Black Hole Abundance from the First Advanced LIGO Observation Run Using the Stochastic Gravitational-Wave Background*, *Phys. Rev. Lett.* **120** (2018) 191102 [1610.08725].

[272] S. Mukherjee and J. Silk, *Can we distinguish astrophysical from primordial black holes via the stochastic gravitational wave background?*, *Mon. Not. Roy. Astron. Soc.* **506** (2021) 3977–3985 [2105.11139].

[273] M. Saleem et al., *The science case for LIGO-India*, *Class. Quant. Grav.* **39** (2022) 025004 [2105.01716].

[274] B. Kocsis, M. E. Gaspar and S. Marka, *Detection rate estimates of gravity-waves emitted during parabolic encounters of stellar black holes in globular clusters*, *Astrophys. J.* **648** (2006) 411–429 [astro-ph/0603441].

[275] R. M. O'Leary, B. Kocsis and A. Loeb, *Gravitational waves from scattering of stellar-mass black holes in galactic nuclei*, *Mon. Not. Roy. Astron. Soc.* **395** (2009) 2127–2146 [0807.2638].

[276] M. Gröbner, P. Jetzer, M. Haney, S. Tiwari and W. Ishibashi, *A note on the gravitational wave energy spectrum of parabolic and hyperbolic encounters*, *Class. Quant. Grav.* **37** (2020) 067002 [2001.05187].

[277] M. Trashorras, J. García-Bellido and S. Nesseris, *The clustering dynamics of primordial black boles in N-body simulations*, *Universe* **7** (2021) 18 [2006.15018].

[278] P. E. Nelson, Z. B. Etienne, S. T. McWilliams and V. Nguyen, *Induced Spins from Scattering Experiments of Initially Nonspinning Black Holes*, *Phys. Rev. D* **100** (2019) 124045 [1909.08621].

[279] J. Healy, J. Levin and D. Shoemaker, *Zoom-Whirl Orbits in Black Hole Binaries*, *Phys. Rev. Lett.* **103** (2009) 131101 [0907.0671].

[280] P. Ajith et al., *Inspiral-merger-ringdown waveforms for black-hole binaries with non-precessing spins*, *Phys. Rev. Lett.* **106** (2011) 241101 [0909.2867].

[281] M. Braglia, J. Garcia-Bellido and S. Kuroyanagi, *Testing Primordial Black Holes with multi-band observations of the stochastic gravitational wave background*, *JCAP* **12** (2021) 012 [2110.07488].

[282] E. Thrane and J. D. Romano, *Sensitivity curves for searches for gravitational-wave backgrounds*, *Phys. Rev. D* **88** (2013) 124032 [1310.5300].

[283] T. Regimbau, M. Evans, N. Christensen, E. Katsavounidis, B. Sathyaprakash and S. Vitale, *Digging deeper: Observing primordial gravitational waves below the binary black hole produced stochastic background*, *Phys. Rev. Lett.* **118** (2017) 151105 [1611.08943].

[284] Z.-C. Liang, Y.-M. Hu, Y. Jiang, J. Cheng, J.-d. Zhang and J. Mei, *Science with the TianQin Observatory: Preliminary Results on Stochastic Gravitational-Wave Background*, 2107.08643.

[285] G. Wang, W.-T. Ni, W.-B. Han, P. Xu and Z. Luo, *Alternative LISA-TAIJI networks*, *Phys. Rev. D* **104** (2021) 024012 [2105.00746].

[286] G. Wang and W.-B. Han, *Alternative LISA-TAIJI networks: detectability to isotropic stochastic gravitational wave background*, 2108.11151.

[287] N. Aggarwal et al., *Challenges and opportunities of gravitational-wave searches at MHz to GHz frequencies*, *Living Rev. Rel.* **24** (2021) 4 [2011.12414].

[288] S. Kuroyanagi, T. Chiba and T. Takahashi, *Probing the Universe through the Stochastic Gravitational Wave Background*, *JCAP* **11** (2018) 038 [1807.00786].

[289] C. Caprini, D. G. Figueroa, R. Flauger, G. Nardini, M. Peloso, M. Pieroni et al., *Reconstructing the spectral shape of a stochastic gravitational wave background with LISA*, *JCAP* **11** (2019) 017 [1906.09244].

[290] G. Cusin, I. Dvorkin, C. Pitrou and J.-P. Uzan, *Stochastic gravitational wave background anisotropies in the mHz band: astrophysical dependencies*, *Mon. Not. Roy. Astron. Soc.* **493** (2020) L1–L5 [1904.07757].

[291] C. R. Contaldi, M. Pieroni, A. I. Renzini, G. Cusin, N. Karnesis, M. Peloso et al., *Maximum likelihood map-making with the Laser Interferometer Space Antenna*, *Phys. Rev. D* **102** (2020) 043502 [2006.03313].

[292] S. Mukherjee and J. Silk, *Time-dependence of the astrophysical stochastic gravitational wave background*, *Mon. Not. Roy. Astron. Soc.* **491** (2020) 4690–4701 [1912.07657].

[293] R. J. E. Smith, C. Talbot, F. Hernandez Vivanco and E. Thrane, *Inferring the population properties of binary black holes from unresolved gravitational waves*, *Mon. Not. Roy. Astron. Soc.* **496** (2020) 3281–3290 [2004.09700].

[294] A. Buonanno and T. Damour, *Effective one-body approach to general relativistic two-body dynamics*, *Phys. Rev. D* **59** (1999) 084006 [gr-qc/9811091].

[295] Y. Pan, A. Buonanno, J. G. Baker, J. Centrella, B. J. Kelly, S. T. McWilliams et al., *A Data-analysis driven comparison of analytic and numerical coalescing binary waveforms: Nonspinning case*, *Phys. Rev. D* **77** (2008) 024014 [0704.1964].

[296] P. Ajith et al., *Phenomenological template family for black-hole coalescence waveforms*, *Class. Quant. Grav.* **24** (2007) S689–S700 [0704.3764].

[297] V. Varma, S. E. Field, M. A. Scheel, J. Blackman, D. Gerosa, L. C. Stein et al., *Surrogate models for precessing binary black hole simulations with unequal masses*, *Phys. Rev. Research.* **1** (2019) 033015 [1905.09300].

[298] J. Yoo et al., *Numerical relativity surrogate model with memory effects and post-Newtonian hybridization*, *Phys. Rev. D* **108** (2023) 064027 [2306.03148].

[299] A. Dhani, S. Völkel, A. Buonanno, H. Estelles, J. Gair, H. P. Pfeiffer et al., *Systematic Biases in Estimating the Properties of Black Holes Due to Inaccurate Gravitational-Wave Models*, 2404.05811.

[300] V. Kapil, L. Reali, R. Cotesta and E. Berti, *Systematic bias from waveform modeling for binary black hole populations in next-generation gravitational wave detectors*, 2404.00090.

[301] F. Loffler et al., *The Einstein Toolkit: A Community Computational Infrastructure for Relativistic Astrophysics*, *Class. Quant. Grav.* **29** (2012) 115001 [1111.3344].

[302] "The Einstein Toolkit." https://einsteintoolkit.org.

[303] S. G. Hahn and R. W. Lindquist, *The two-body problem in geometrodynamics*, *Annals of Physics* **29** (1964) 304-331.

[304] C. W. Misner and J. A. Wheeler, *Classical physics as geometry: Gravitation, electromagnetism, unquantized charge, and mass as properties of curved empty space*, *Annals Phys.* **2** (1957) 525–603.

[305] C. Palenzuela, *Introduction to Numerical Relativity*, *Front. Astron. Space Sci.* **7** (2020) 58 [2008.12931].

[306] M. Zilhão and F. Löffler, *An Introduction to the Einstein Toolkit*, *Int. J. Mod. Phys. A* **28** (2013) 1340014 [1305.5299].

[307] R. L. Arnowitt, S. Deser and C. W. Misner, *The Dynamics of general relativity*, *Gen. Rel. Grav.* **40** (2008) 1997–2027 [gr-qc/0405109].

[308] L. Witten and J. E. Romain, *Gravitation: An introduction to current research*, *Physics Today* **16** (1963) 70-72.

[309] J. W. York, Jr., *Kinematics and Dynamics of General Relativity*, in *Workshop on Sources of Gravitational Radiation*, pp. 83–126, 1978.

[310] M. Shibata and T. Nakamura, *Evolution of three-dimensional gravitational waves: Harmonic slicing case*, *Phys. Rev. D* **52** (1995) 5428–5444.

[311] T. W. Baumgarte and S. L. Shapiro, *On the numerical integration of Einstein's field equations*, *Phys. Rev. D* **59** (1998) 024007 [gr-qc/9810065].

[312] M. Bezares, C. Palenzuela and C. Bona, *Final fate of compact boson star mergers*, *Phys. Rev. D* **95** (2017) 124005 [1705.01071].

[313] D. R. Brill and R. W. Lindquist, *Interaction energy in geometrostatics*, *Phys. Rev.* **131** (1963) 471–476.

[314] A. M. Abrahams and R. H. Price, *Black hole collisions from Brill-Lindquist initial data: Predictions of perturbation theory*, *Phys. Rev. D* **53** (1996) 1972–1976 [gr-qc/9509020].

[315] J. M. Bowen and J. W. York, Jr., *Time asymmetric initial data for black holes and black hole collisions*, *Phys. Rev. D* **21** (1980) 2047–2056.

[316] S. Brandt and B. Bruegmann, *A Simple construction of initial data for multiple black holes*, *Phys. Rev. Lett.* **78** (1997) 3606–3609 [gr-qc/9703066].

[317] M. Ansorg, B. Bruegmann and W. Tichy, *A Single-domain spectral method for black hole puncture data*, *Phys. Rev. D* **70** (2004) 064011 [gr-qc/0404056].

[318] K. Clough, P. Figueras, H. Finkel, M. Kunesch, E. A. Lim and S. Tunyasuvunakool, *GRChombo : Numerical Relativity with Adaptive Mesh Refinement*, *Class. Quant. Grav.* **32** (2015) 245011 [1503.03436].

[319] T. Andrade et al., *GRChombo: An adaptable numerical relativity code for fundamental physics*, *J. Open Source Softw.* **6** (2021) 3703 [2201.03458].

[320] "GRChombo." https://www.grchombo.org.

[321] G. Lovelace, *Reducing spurious gravitational radiation in binary-black-hole simulations by using conformally curved initial data*, *Class. Quant. Grav.* **26** (2009) 114002 [0812.3132].

[322] V. Varma, M. A. Scheel and H. P. Pfeiffer, *Comparison of binary black hole initial data sets*, *Phys. Rev. D* **98** (2018) 104011 [1808.08228].

[323] K. Higginbotham, B. Khamesra, J. P. McInerney, K. Jani, D. M. Shoemaker and P. Laguna, *Coping with spurious radiation in binary black hole simulations*, *Phys. Rev. D* **100** (2019) 081501 [1907.00027].

[324] A. Sommerfeld, *Die greensche funktion der schwingungslgleichung.*, *Jahresbericht der Deutschen Mathematiker-Vereinigung* **21** (1912) 309-352.

[325] M. Alcubierre, B. Bruegmann, P. Diener, M. Koppitz, D. Pollney, E. Seidel et al., *Gauge conditions for long term numerical black hole evolutions without excision*, *Phys. Rev. D* **67** (2003) 084023 [gr-qc/0206072].

[326] I. Ruchlin, Z. B. Etienne and T. W. Baumgarte, *SENR/NRPy+: Numerical Relativity in Singular Curvilinear Coordinate Systems*, *Phys. Rev. D* **97** (2018) 064036 [1712.07658].

[327] "NRPy+." https://nrpyplus.net.

[328] M. D. Duez, F. Foucart, L. E. Kidder, H. P. Pfeiffer, M. A. Scheel and S. A. Teukolsky, *Evolving black hole-neutron star binaries in general relativity using pseudospectral and finite difference methods*, *Phys. Rev. D* **78** (2008) 104015 [0809.0002].

[329] "The Spectral Einstein Code." https://www.black-holes.org/code/SpEC.html.

[330] B. Bruegmann, J. A. Gonzalez, M. Hannam, S. Husa, U. Sperhake and W. Tichy, *Calibration of Moving Puncture Simulations*, *Phys. Rev. D* **77** (2008) 024027 [gr-qc/0610128].

[331] N. Choustikov, *The Einstein Toolkit: A Student's Guide*, 2011.13314.

[332] T. Goodale, G. Allen, G. Lanfermann, J. Massó, T. Radke, E. Seidel et al., *The Cactus framework and toolkit: Design and applications*, in *Vector and Parallel Processing – VECPAR'2002, 5th International Conference, Lecture Notes in Computer Science*, (Berlin), Springer, 2003, http://edoc.mpg.de/3341.

[333] "Cactus Computational Toolkit." http://www.cactuscode.org/.

[334] E. Schnetter, S. H. Hawley and I. Hawke, *Evolutions in 3-D numerical relativity using fixed mesh refinement*, *Class. Quantum Grav.* **21** (2004) 1465-1488 [arXiv:gr-qc/0310042].

[335] Carpet: Adaptive Mesh Refinement for the Cactus Framework.

[336] D. Pollney, C. Reisswig, E. Schnetter, N. Dorband and P. Diener, *High accuracy binary black hole simulations with an extended wave zone*, *Phys. Rev.* **D83** (2011) 044045 [0910.3803].

[337] V. Paschalidis, Z. B. Etienne, R. Gold and S. L. Shapiro, *An efficient spectral interpolation routine for the TwoPunctures code*, 1304.0457.

[338] J. D. Brown, P. Diener, O. Sarbach, E. Schnetter and M. Tiglio, *Turduckening black holes: An Analytical and computational study*, *Phys. Rev. D* **79** (2009) 044023 [0809.3533].

[339] C. Reisswig, C. D. Ott, U. Sperhake and E. Schnetter, *Gravitational Wave Extraction in Simulations of Rotating Stellar Core Collapse*, *Phys. Rev. D* **83** (2011) 064008 [1012.0595].

[340] "McLachlan, a public BSSN code." http://www.cct.lsu.edu/~eschnett/McLachlan/.

[341] S. Husa, I. Hinder and C. Lechner, *Kranc: a Mathematica application to generate numerical codes for tensorial evolution equations*, *Comput. Phys. Commun.* **174** (2006) 983-1004 [arXiv:gr-qc/0404023].

[342] "Kranc assembles numerical code." http://kranccode.org/.

[343] M. Thomas and E. Schnetter, *Simulation factory: Taming application configuration and workflow on high-end resources*, in *Grid Computing (GRID), 2010 11th IEEE/ACM International Conference on*, pp. 369 –378, oct., 2010, DOI [arXiv:1008.4571 [cs.DC]].

[344] B. Wardell, I. Hinder and E. Bentivegna, *Simulation of GW150914 binary black hole merger using the Einstein Toolkit*, Sept., 2016. 10.5281/zenodo.155394.

[345] J. Thornburg, *A Fast apparent horizon finder for three-dimensional Cartesian grids in numerical relativity*, *Class. Quant. Grav.* **21** (2004) 743–766 [gr-qc/0306056].

[346] O. Dreyer, B. Krishnan, D. Shoemaker and E. Schnetter, *Introduction to isolated horizons in numerical relativity*, *Phys. Rev. D* **67** (2003) 024018 [arXiv:gr-qc/0206008].

[347] W. Rindler, *Visual Horizons in World Models*, *Mon. Not. Roy. Astron. Soc.* **116** (1956) 662–677.

[348] S. W. Hawking and G. F. R. Ellis, *The Large Scale Structure of Space-Time*, Cambridge Monographs on Mathematical Physics. Cambridge University Press, 2, 2023, 10.1017/9781009253161.

[349] J. M. M. Senovilla, *Trapped surfaces*, *Int. J. Mod. Phys. D* **20** (2011) 2139 [1107.1344].

[350] E. Altas and B. Tekin, *Basics of Apparent horizons in black hole physics*, *J. Phys. Conf. Ser.* **2191** (2022) 012002 [2108.05119].

[351] J. Thornburg, *Finding apparent horizons in numerical relativity*, *Phys. Rev. D* **54** (1996) 4899–4918 [gr-qc/9508014].

[352] M. Alcubierre et al., *Dynamical evolution of quasi-circular binary black hole data*, *Phys. Rev. D* **72** (2005) 044004 [gr-qc/0411149].

[353] D. Christodoulou, *Reversible and irreversible transforations in black hole physics*, *Phys. Rev. Lett.* **25** (1970) 1596–1597.

[354] E. Schnetter, B. Krishnan and F. Beyer, *Introduction to dynamical horizons in numerical relativity*, *Phys. Rev. D* **74** (2006) 024028 [gr-qc/0604015].

[355] L. B. Szabados, *Quasi-Local Energy-Momentum and Angular Momentum in GR: A Review Article*, *Living Rev. Rel.* **7** (2004) 4.

[356] E. Newman and R. Penrose, *An Approach to gravitational radiation by a method of spin coefficients*, *J. Math. Phys.* **3** (1962) 566–578.

[357] C. Reisswig and D. Pollney, *Notes on the integration of numerical relativity waveforms*, *Class. Quant. Grav.* **28** (2011) 195015 [1006.1632].

[358] J. Calderon Bustillo, I. C. F. Wong, N. Sanchis-Gual, S. H. W. Leong, A. Torres-Forne, K. Chandra et al., *Gravitational-Wave Parameter Inference with the Newman-Penrose Scalar*, *Phys. Rev. X* **13** (2023) 041048 [2205.15029].

[359] E. T. Newman and R. Penrose, *Note on the Bondi-Metzner-Sachs group*, *J. Math. Phys.* **7** (1966) 863–870.

[360] J. J. G. Scanio, *Spin-weighted spherical harmonics and electromagnetic multipole expansions*, *American Journal of Physics* **45** (1977) 173-178.

[361] J. N. Goldberg, A. J. Macfarlane, E. T. Newman, F. Rohrlich and E. C. G. Sudarshan, *Spin-s Spherical Harmonics and ð*, *Journal of Mathematical Physics* **8** (1967) 2155-2161.

[362] K. S. Thorne, *Multipole Expansions of Gravitational Radiation*, *Rev. Mod. Phys.* **52** (1980) 299–339.

[363] G. Bozzola, *kuibit: Analyzing Einstein Toolkit simulations with Python*, *J. Open Source Softw.* **6** (2021) 3099 [2104.06376].

[364] C. O. Lousto and J. Healy, *Exploring the Small Mass Ratio Binary Black Hole Merger via Zeno's Dichotomy Approach*, *Phys. Rev. Lett.* **125** (2020) 191102 [2006.04818].

[365] J. Healy and C. O. Lousto, *Fourth RIT binary black hole simulations catalog: Extension to eccentric orbits*, *Phys. Rev. D* **105** (2022) 124010 [2202.00018].

[366] J. Healy, C. O. Lousto, H. Nakano and Y. Zlochower, *Post-Newtonian Quasicircular Initial Orbits for Numerical Relativity*, *Class. Quant. Grav.* **34** (2017) 145011 [1702.00872].

[367] S. Habib, A. Ramos-Buades, E. A. Huerta, S. Husa, R. Haas and Z. Etienne, *Initial Data and Eccentricity Reduction Toolkit for Binary Black Hole Numerical Relativity Waveforms*, *Class. Quant. Grav.* **38** (2021) 125007 [2011.08878].

[368] M. A. Shaikh, V. Varma, H. P. Pfeiffer, A. Ramos-Buades and M. van de Meent, *Defining eccentricity for gravitational wave astronomy*, *Phys. Rev. D* **108** (2023) 104007 [2302.11257].

[369] T. Islam, V. Varma, J. Lodman, S. E. Field, G. Khanna, M. A. Scheel et al., *Eccentric binary black hole surrogate models for the gravitational waveform and remnant properties: comparable mass, nonspinning case*, *Phys. Rev. D* **103** (2021) 064022 [2101.11798].

[370] A. Nagar et al., *Time-domain effective-one-body gravitational waveforms for coalescing compact binaries with nonprecessing spins, tides and self-spin effects*, *Phys. Rev. D* **98** (2018) 104052 [1806.01772].

[371] A. Nagar and S. Albanesi, *Toward a gravitational self-force-informed effective-one-body waveform model for nonprecessing, eccentric, large-mass-ratio inspirals*, *Phys. Rev. D* **106** (2022) 064049 [2207.14002].

[372] X. Liu, Z. Cao and Z.-H. Zhu, *A higher-multipole gravitational waveform model for an eccentric binary black holes based on the effective-one-body-numerical-relativity formalism*, *Class. Quant. Grav.* **39** (2022) 035009 [2102.08614].

[373] H. Yu, J. Roulet, T. Venumadhav, B. Zackay and M. Zaldarriaga, *Accurate and efficient waveform model for precessing binary black holes*, *Phys. Rev. D* **108** (2023) 064059 [2306.08774].

[374] S. Schmidt et al., *Searching for gravitational-wave signals from precessing black hole binaries with the GstLAL pipeline*, 2403.17186.

[375] T. Dietrich, T. Hinderer and A. Samajdar, *Interpreting Binary Neutron Star Mergers: Describing the Binary Neutron Star Dynamics, Modelling Gravitational Waveforms, and Analyzing Detections*, *Gen. Rel. Grav.* **53** (2021) 27 [2004.02527].

[376] LIGO Scientific, Virgo collaboration, *Properties and Astrophysical Implications of the 150 $M_\odot$ Binary Black Hole Merger GW190521*, *Astrophys. J. Lett.* **900** (2020) L13 [2009.01190].

[377] R. Farmer, M. Renzo, S. E. de Mink, P. Marchant and S. Justham, *Mind the gap: The location of the lower edge of the pair instability supernovae black hole mass gap*, *Astrophys. J.* **887** (2019) 53 [1910.12874].

[378] M. Shibata, K. Kiuchi, S. Fujibayashi and Y. Sekiguchi, *Alternative possibility of GW190521: Gravitational waves from high-mass black hole-disk systems*, *Phys. Rev. D* **103** (2021) 063037 [2101.05440].

[379] S. Clesse and J. García-Bellido, *Seven Hints for Primordial Black Hole Dark Matter*, *Phys. Dark Univ.* **22** (2018) 137-146 [1711.10458].

[380] T. Chiba and S. Yokoyama, *Spin Distribution of Primordial Black Holes*, *PTEP* **2017** (2017) 083E01 [1704.06573].

[381] V. De Luca, V. Desjacques, G. Franciolini, P. Pani and A. Riotto, *GW190521 Mass Gap Event and the Primordial Black Hole Scenario*, *Phys. Rev. Lett.* **126** (2021) 051101 [2009.01728].

[382] W. Kastaun, "PyCactus tools." https://github.com/wokast/PyCactus.

[383] E. Poisson and M. Sasaki, *Gravitational radiation from a particle in circular orbit around a black hole. 5: Black hole absorption and tail corrections*, *Phys. Rev. D* **51** (1995) 5753–5767 [gr-qc/9412027].

[384] Planck collaboration, *Planck 2018 results. X. Constraints on inflation*, *Astron. Astrophys.* **641** (2020) A10 [1807.06211].

[385] P. D. Lasky et al., *Gravitational-wave cosmology across 29 decades in frequency*, *Phys. Rev. X* **6** (2016) 011035 [1511.05994].

[386] T. Namikawa, S. Saga, D. Yamauchi and A. Taruya, *CMB Constraints on the Stochastic Gravitational-Wave Background at Mpc scales*, *Phys. Rev. D* **100** (2019) 021303 [1904.02115].

[387] R. L. Forward, *Multidirectional, multipolarization antennas for scalar and tensor gravitational radiation*, *Gen. Rel. Grav.* **2** (1971) 149–159.

[388] O. D. Aguiar, *The Past, Present and Future of the Resonant-Mass Gravitational Wave Detectors*, *Res. Astron. Astrophys.* **11** (2011) 1–42 [1009.1138].

[389] M. Goryachev and M. E. Tobar, *Gravitational Wave Detection with High Frequency Phonon Trapping Acoustic Cavities*, *Phys. Rev. D* **90** (2014) 102005 [1410.2334].

[390] M. Gertsenshtein, *Wave resonance of light and gravitional waves*, *Sov Phys JETP* **14** (1962) 84–85.

[391] D. Boccaletti, V. De Sabbata, P. Fortini and C. Gualdi, *Conversion of photons into gravitons and vice versa in a static electromagnetic field*, *Nuovo Cim. B* **70** (1970) 129–146.

[392] A. Füzfa, *Electromagnetic Gravitational Waves Antennas for Directional Emission and Reception*, 1702.06052.

[393] E. V. Linder, *Relativistic scattering coherence*, *Phys. Rev. D* **34** (1986) 1759.

[394] E. V. Linder, *Clustering Correlations and Limits on Cosmological Gravitational Waves*, *Astrophys. J.* **328** (1988) 77.

[395] V. B. Braginsky, N. S. Kardashev, I. D. Novikov and A. G. Polnarev, *Propagation of electromagnetic radiation in a random field of gravitational waves and space radio interferometry*, *Nuovo Cim. B* **105** (1990) 1141–1158.

[396] R. Fakir, *Gravity wave watching*, *Astrophys. J.* **426** (1994) 74–78 [gr-qc/9304003].

[397] E. E. Flanagan, *The Sensitivity of the laser interferometer gravitational wave observatory (LIGO) to a stochastic background, and its dependence on the detector orientations*, *Phys. Rev. D* **48** (1993) 2389–2407 [astro-ph/9305029].

[398] T. Pyne, C. R. Gwinn, M. Birkinshaw, T. M. Eubanks and D. N. Matsakis, *Gravitational radiation and very long baseline interferometry*, *Astrophys. J.* **465** (1996) 566–577 [astro-ph/9507030].

[399] N. Kaiser and A. H. Jaffe, *Bending of light by gravity waves*, *Astrophys. J.* **484** (1997) 545–554 [astro-ph/9609043].

[400] T. Damour and G. Esposito-Farese, *Light deflection by gravitational waves from localized sources*, *Phys. Rev. D* **58** (1998) 044003 [gr-qc/9802019].

[401] A. H. Jaffe, *Observing gravitational radiation with QSO proper motions and the SKA*, *New Astron. Rev.* **48** (2004) 1483–1485 [astro-ph/0409637].

[402] B. F. Schutz, *Astrometric and timing effects of gravitational waves*, *IAU Symp.* **261** (2010) 234–239.

[403] L. G. Book and E. E. Flanagan, *Astrometric Effects of a Stochastic Gravitational Wave Background*, *Phys. Rev. D* **83** (2011) 024024 [1009.4192].

[404] C. R. Gwinn, T. M. Eubanks, T. Pyne, M. Birkinshaw and D. N. Matsakis, *Quasar proper motions and low frequency gravitational waves*, *Astrophys. J.* **485** (1997) 87–91 [astro-ph/9610086].

[405] O. Titov, S. B. Lambert and A. M. Gontier, *VLBI measurement of the secular aberration drift*, *Astron. Astrophys.* **529** (2011) A91 [1009.3698].

[406] Gaia collaboration, *The Gaia Mission*, *Astron. Astrophys.* **595** (2016) A1 [1609.04153].

[407] S. Aoyama, D. Yamauchi, M. Shiraishi and M. Ouchi, *Gaia 400,894 QSO constraint on the energy density of low-frequency gravitational waves*, 2105.04039.

[408] C. J. Moore, D. P. Mihaylov, A. Lasenby and G. Gilmore, *Astrometric Search Method for Individually Resolvable Gravitational Wave Sources with Gaia*, *Phys. Rev. Lett.* **119** (2017) 261102 [1707.06239].

[409] D. P. Mihaylov, C. J. Moore, J. R. Gair, A. Lasenby and G. Gilmore, *Astrometric Effects of Gravitational Wave Backgrounds with non-Einsteinian Polarizations*, *Phys. Rev. D* **97** (2018) 124058 [1804.00660].

[410] D. P. Mihaylov, C. J. Moore, J. Gair, A. Lasenby and G. Gilmore, *Astrometric effects of gravitational wave backgrounds with nonluminal propagation speeds*, *Phys. Rev. D* **101** (2020) 024038 [1911.10356].

[411] J. García-Bellido, H. Murayama and G. White, *Exploring the early Universe with Gaia and Theia*, *JCAP* **12** (2021) 023 [2104.04778].

[412] R. M. Wald, *General Relativity*. Chicago Univ. Pr., Chicago, USA, 1984, 10.7208/chicago/9780226870373.001.0001.

[413] D. Blas and A. C. Jenkins, *Detecting stochastic gravitational waves with binary resonance*, *Phys. Rev. D* **105** (2022) 064021 [2107.04063].

[414] R. Olinde, *De l'attraction des spheroides*, *Correspondence sur l'École Imperiale Polytechnique* **3** (1816) 361–385.

[415] E. Condon and G. Shortley, *The Theory of Atomic Spectra*, Cambridge Univ.Pr.209. Cambridge University Press, 1935.

[416] F. Mignard and S. Klioner, *Analysis of astrometric catalogues with vector spherical harmonics*, *Astron. Astrophys.* **547** (2012) A59 [1207.0025].

[417] A. Unsöld, *Beiträge zur quantenmechanik der atome*, *Annalen der Physik* **387** (1927) 355-393.

[418] Planck collaboration, *Planck 2018 results. VI. Cosmological parameters*, *Astron. Astrophys.* **641** (2020) A6 [1807.06209].

[419] E. B. Wilson and M. M. Hilferty, *The Distribution of Chi-Square*, *Proc. of the National Academy of Sciences of the United States of America* **17** (1931) 684-688.

[420] Gaia collaboration, *Gaia early data release 3 - summary of the contents and survey properties*, *Astron. Astrophys.* **649** (2021) A1 [2012.01533].

[421] C. Turon, M. Creze, D. Egret, A. Gomez, M. Grenon, H. Jahreiß et al., *Version 2 of the HIPPARCOS input catalogue*, *Bulletin d'information du Centre de données astronomiques de Strasbourg* **43** (1993) 5–6.

[422] M. Cropper, D. Katz, P. Sartoretti, T. Prusti, J. De Bruijne, F. Chassat et al., *Gaia data release 2-gaia radial velocity spectrometer*, *Astronomy & Astrophysics* **616** (2018) A5.

[423] Gaia collaboration, *Gaia Data Release 1: Summary of the astrometric, photometric, and survey properties*, *Astron. Astrophys.* **595** (2016) A2 [1609.04172].

[424] Gaia collaboration, *Gaia Data Release 2: Summary of the contents and survey properties*, *Astron. Astrophys.* **616** (2018) A1 [1804.09365].

[425] Gaia collaboration, *Gaia Data Release 3: Summary of the content and survey properties*, *Astron. Astrophys.* **674** (2023) A1 [2208.00211].

[426] "Gaia data release 3 documentation." https://www.cosmos.esa.int/web/gaia/dr3.

[427] "Gaia data release scenario." https://www.cosmos.esa.int/web/gaia/release.

[428] K. Storey-Fisher, D. W. Hogg, H.-W. Rix, A.-C. Eilers, G. Fabbian, M. R. Blanton et al., *Quaia, the Gaia-unWISE Quasar Catalog: An All-sky Spectroscopic Quasar Sample*, *Astrophys. J.* **964** (2024) 69 [2306.17749].

[429] D. Lang, *unwise: Unblurred coadds of the wise imaging*, *The Astronomical Journal* **147** (2014) 108.

[430] Gaia collaboration, *Gaia Data Release 3 - The extragalactic content*, *Astron. Astrophys.* **674** (2023) A41 [2206.05681].

[431] L. Delchambre et al., *Gaia Data Release 3 - Apsis. III. Non-stellar content and source classification*, *Astron. Astrophys.* **674** (2023) A31 [2206.06710].

[432] Gaia collaboration, *Gaia Early Data Release 3 - The celestial reference frame (Gaia-CRF3)*, *Astron. Astrophys.* **667** (2022) A148 [2204.12574].

[433] A. Zonca, L. Singer, D. Lenz, M. Reinecke, C. Rosset, E. Hivon et al., *healpy: equal area pixelization and spherical harmonics transforms for data on the sphere in Python*, *Journal of Open Source Software* **4** (2019) 1298.

[434] K. M. Górski, E. Hivon, A. J. Banday, B. D. Wandelt, F. K. Hansen, M. Reinecke et al., *HEALPix - A Framework for high resolution discretization, and fast analysis of data distributed on the sphere*, *Astrophys. J.* **622** (2005) 759–771 [astro-ph/0409513].

[435] A. E. Truebenbach and J. Darling, *The VLBA Extragalactic Proper Motion Catalog and a Measurement of the Secular Aberration Drift*, *Astrophys. J. Suppl.* **233** (2017) 3 [1710.02099].

[436] B. W. Lyke et al., *The Sloan Digital Sky Survey Quasar Catalog: Sixteenth Data Release*, *Astrophys. J. Suppl.* **250** (2020) 8 [2007.09001].

[437] M. B. Taylor, *TOPCAT & STIL: Starlink Table/VOTable Processing Software*, in *Astronomical Data Analysis Software and Systems XIV*, P. Shopbell, M. Britton and R. Ebert, eds., vol. 347 of *Astronomical Society of the Pacific Conference Series*, p. 29, Dec., 2005.

[438] M. B. Taylor, *STILTS - A Package for Command-Line Processing of Tabular Data*, in *Astronomical Data Analysis Software and Systems XV*, C. Gabriel, C. Arviset, D. Ponz and S. Enrique, eds., vol. 351 of *Astronomical Society of the Pacific Conference Series*, p. 666, July, 2006.

[439] eBOSS collaboration, *The 13th Data Release of the Sloan Digital Sky Survey: First Spectroscopic Data from the SDSS-IV Survey Mapping Nearby Galaxies at Apache Point Observatory*, *Astrophys. J. Suppl.* **233** (2017) 25 [1608.02013].

[440] A. Sesana, A. Vecchio and C. N. Colacino, *The stochastic gravitational-wave background from massive black hole binary systems: implications for observations with Pulsar Timing Arrays*, *Mon. Not. Roy. Astron. Soc.* **390** (2008) 192 [0804.4476].

[441] S. Burke-Spolaor et al., *The Astrophysics of Nanohertz Gravitational Waves*, *Astron. Astrophys. Rev.* **27** (2019) 5 [1811.08826].

[442] J. J. Blanco-Pillado, K. D. Olum and X. Siemens, *New limits on cosmic strings from gravitational wave observation*, *Phys. Lett. B* **778** (2018) 392–396 [1709.02434].

[443] Y. Matsui and S. Kuroyanagi, *Gravitational wave background from kink-kink collisions on infinite cosmic strings*, *Phys. Rev. D* **100** (2019) 123515 [1902.09120].

[444] C. Caprini, R. Durrer and X. Siemens, *Detection of gravitational waves from the QCD phase transition with pulsar timing arrays*, *Phys. Rev. D* **82** (2010) 063511 [1007.1218].

[445] A. Brandenburg, E. Clarke, Y. He and T. Kahniashvili, *Can we observe the QCD phase transition-generated gravitational waves through pulsar timing arrays?*, *Phys. Rev. D* **104** (2021) 043513 [2102.12428].

[446] NANOGrav collaboration, *The NANOGrav 12.5 yr Data Set: Search for an Isotropic Stochastic Gravitational-wave Background*, *Astrophys. J. Lett.* **905** (2020) L34 [2009.04496].

[447] J. Darling. personal communication, 2023.

[448] D. S. Sivia and J. Skilling, *Data Analysis: A Bayesian Tutorial*. Oxford University Press, 2 ed., 2006.

[449] A. G. Brown, *Microarcsecond astrometry: Science highlights from gaia*, *Annual Review of Astronomy and Astrophysics* **59** (2021) 59-115 [2102.11712].

[450] Theia collaboration, *Theia: Faint objects in motion or the new astrometry frontier*, 1707.01348.

[451] F. Malbet et al., *Theia : science cases and mission profiles for high precision astrometry in the future*, in *SPIE Astronomical Telescopes + Instrumentation 2022*, 7, 2022, 2207.12540.

[452] G. Domènech, S. Passaglia and S. Renaux-Petel, *Gravitational waves from dark matter isocurvature*, *JCAP* **03** (2022) 023 [2112.10163].

[453] K. Ando, K. Inomata and M. Kawasaki, *Primordial black holes and uncertainties in the choice of the window function*, *Phys. Rev. D* **97** (2018) 103528 [1802.06393].

[454] J. Lense and H. Thirring, *Ueber den Einfluss der Eigenrotation der Zentralkoerper auf die Bewegung der Planeten und Monde nach der Einsteinschen Gravitationstheorie*, *Phys. Z.* **19** (1918) 156–163.

[455] S. Horatschek and D. Petroff, *Uniformly Rotating Homogeneous Rings in post-Newtonian Gravity*, *Mon. Not. Roy. Astron. Soc.* **408** (2010) 1749 [1005.0294].

[456] S. Weinberg, *Gravitation and Cosmology. Principles and applications of the General Theory of Relativity*. John Wiley & Sons, Inc., 1972.

[457] L. De Vittori, A. Gopakumar, A. Gupta and P. Jetzer, *Gravitational waves from spinning compact binaries in hyperbolic orbits*, *Phys. Rev. D* **90** (2014) 124066 [1410.6311].